Cronfa
Swansea University's Research Repository

# A New Updated Reference Lagrangian Smooth Particle Hydrodynamics Framework for Large Strain Solid Dynamics and its Extension to Dynamic Fracture

**Paulo Roberto Refachinho de Campos**

Submitted to the Faculty of Science and Engineering in partial fulfilment of the requirements for the Degree of

Doctor of Philosophy

Swansea University

2022

Copyright: The author, Paulo R. Refachinho de Campos, 2023. Released under the terms of a Creative Commons Attribution-Only (CC-BY) License. Third party content is excluded for use under the license terms.

# Declarations

This work has not previously been accepted in substance for any degree and is not being concurrently submitted in candidature for any degree.

Signed ................[redacted]

Date ...................................................06/12/2022.....................................................

This thesis is the result of my own investigations, except where otherwise stated. Other sources are acknowledged by footnotes giving explicit references. A bibliography is appended.

Signed ...................[redacted]

Date ...................................................06/12/2022.....................................................

I hereby give consent for my thesis, if accepted, to be available for photocopying and for interlibrary loan, and for the title and summary to be made available to outside organisations.

Signed ..................[redacted]

Date ...................................................06/12/2022.....................................................

The University's ethical procedures have been followed and, where appropriate, that ethical approval has been granted.

Signed .....................[redacted]

Date ...................................................06/12/2022.................................................

# Acknowledgements

I would like to acknowledge firstly the financial support received through the project Marie Skłodowska-Curie ITN-EJD ProTechTion, funded by the European Union Horizon 2020 research and innovation program with grant number 764636.

Secondly, I would like to express my profound gratitude to my supervisors, for trusting me to conduct this research and also for being supportive in all aspects of my PhD. In particular, I want to thank Professor Antonio J. Gil and Dr Chun Hean Lee for the uncountable hours dedicated to supporting my work. From teaching non-linear continuum mechanics through deriving novel formulations to debugging code. The combination of these interactions led me to great achievements, which are now compiled in this thesis and in the other publications made along the PhD journey or reflected in my professional profile. I also thank my supervisors at Universitat Politècnica de Catalunya, Professor Antonio Huerta and Dr Matteo Giacomini, who hosted me during my secondment in this institution.

Finally, I would like to dedicate this work to my parents and to my sister, for supporting me always and for understanding my choice of moving abroad to pursue my personal and professional objectives. I also dedicate the work to my wife, who entered my life during my PhD and is a source of motivation to me since then. I am also grateful to the friends who contributed either to the technical aspects of the PhD, or to my well-being during this period of my life. All of that was very meaningful.

# Abstract

This work presents a new updated reference Lagrangian Smooth Particle Hydrodynamics algorithm for the analysis of large deformation by introducing a novel system of first order conservation laws. Both isothermal and thermally-coupled scenarios are considered within the elasticity and elasto-plasticity domains. Taking as point of departure a total Lagrangian setting and considering as referential configuration an intermediate configuration of the deformation process, the equation of conservation of linear momentum and three geometric conservation laws (for the deformation gradient, its cofactor and its determinant) are rewritten leading to a very generic (incremental) system of first order conservation laws, which can be degenerated into a total Lagrangian system or into a purely updated Lagrangian system. The key feature of the formulation is a suitable multiplicative decomposition of the conservation variables, leading to a very simple final set of equations with striking similarities to the conventional total Lagrangian system albeit rewritten in terms of incremental updated conservation variables which are evolved in time. Taking advantage of this new updated reference Lagrangian formalism, a second order (in space and time) entropy-stable upwiding stabilisation method derived by means of the use of the Rankine Hugoniot jump conditions is introduced. No ad-hoc algorithmic regularisation procedures are needed. To demonstrate the robustness and applicability of the methodology, a wide spectrum of challenging problems are presented and compared, including benchmarks in hyperelasticity, elasto-plasticity and dynamic fracture problems. A new dynamic fracture approach is proposed in this work. The spark for fracture is based on the maximum principal stresses. Once fracture takes place, the particle is split into two new particles and post-fracture velocities and deformation gradients are computed locally, ensuring conservation of mass, linear momentum and total energy. The work explores the use of a series of novel expressions for the evaluation of kernels and the gradients of kernels, all leading to equally robust results and circumventing the issues faced by classic isotropic (spherical) kernels in the presence of strong anisotropic changes in volume.

*“if you’re going to try, go all the*
*way.*
*otherwise, don’t even start.”*
— Charles Bukowski, *Roll the Dice*

# Contents

# List of Figures

# List of Tables

# Acronyms

| | |
|---|---|
| **CAD** | Computer Aided Design. |
| **CAE** | Computer Aided Engineering. |
| **CFL** | Courant–Friedrichs–Lewy. |
| **EFG** | Element Free Galerkin. |
| **FEM** | Finite Element Method. |
| **FSI** | Fluid Structure Interaction. |
| **FVPM** | Finite Volume Particle Method. |
| **LHS** | Left Hand Side. |
| **PDE** | Partial Differential Equation. |
| **SPH** | Smooth Particle Hydrodynamics. |
| **TLF** | Total Lagrangian Formulation. |
| **ULF** | Updated Lagrangian Formulation. |
| **XFEM** | Extended Finite Element Method. |

# List of Symbols

## Greek Symbols

| | |
|---|---|
| $\alpha$ | Thermal expansion coefficient |
| $\alpha_a$ | Correction parameter for a kernel function |
| $\alpha_{CFL}$ | Courant–Friedrichs–Lewy stability number |
| $\boldsymbol{\beta}$ | Parameter used in the computation of post-fracture $\boldsymbol{F}$ |
| $\boldsymbol{\beta}_a$ | Correction parameter for the gradient of a kernel function |
| $\Gamma_0$ | Mie-Grüneisen material parameter |
| $\Delta_\gamma$ | Incremental plastic multiplier |
| $\Delta_t$ | Time step increment |
| $\Delta_{\boldsymbol{v}}$ | Post-fracture increment in velocity |
| $\delta$ | Saturation exponent for the nonlinear hardening law |
| $\delta_N$ | Crack opening (displacement jump) |
| $\delta_{\max}$ | Critical crack opening |
| $\delta_{ij}$ | Kronecker-delta |
| $\tilde{\mathcal{E}}$ | Internal energy in thermo-mechanical context |
| $\tilde{\mathcal{E}}_R$ | Energy measured per unit of initial volume at reference temperature |
| $\bar{\epsilon}_p$ | Equivalent plastic strain |
| $\dot{\bar{\epsilon}}$ | Plastic strain rate |
| $\dot{\bar{\epsilon}}_0$ | Reference strain rate |
| $\tilde{\eta}$ | Entropy density |
| $\tilde{\eta}_R$ | Entropy density measured at reference temperature |
| $\hat{\theta}$ | Non-dimensional temperature |
| $\theta$ | Current temperature |
| $\theta_{\text{melt}}$ | Melting temperature |

| | |
|---|---|
| $\theta_R$ | Reference temperature |
| $\theta_{\text{transition}}$ | Transition temperature |
| $\kappa$ | Bulk modulus |
| $\lambda$ | Lamé first parameter |
| $\lambda_{e,\alpha}$ | Elastic principal stretches |
| $\mu$ | Shear modulus |
| $\nu$ | Poisson's ratio |
| $\dot{\Pi}_{\boldsymbol{b}_0}$ | Power of body forces |
| $\dot{\Pi}_{\text{ext}}$ | Power of external forces |
| $\dot{\Pi}_{\text{int}_{\boldsymbol{P}}}$ | Power of internal forces in terms of the first Piola-Kirchhoff stress tensor |
| $\dot{\Pi}_{\text{int}_{\boldsymbol{\sigma}}}$ | Power of internal forces in terms of the Cauchy stress tensor |
| $\dot{\Pi}_{\text{int}_{\boldsymbol{S}}}$ | Power of internal forces in terms of the second Piola-Kirchhoff stress tensor |
| $\dot{\Pi}_{\boldsymbol{t}_0}$ | Power of traction forces |
| $\rho$ | Current specific mass |
| $\rho_0$ | Initial specific mass |
| $\rho_{\boldsymbol{\chi}}$ | Intermediate specific mass |
| $\boldsymbol{\Sigma}_{\boldsymbol{F}}$ | Conjugate stress with respect to $\boldsymbol{F}$ |
| $\boldsymbol{\Sigma}_{\boldsymbol{f}}$ | Conjugate stress with respect to $\boldsymbol{f}$ |
| $\boldsymbol{\Sigma}_{\boldsymbol{H}}$ | Conjugate stress with respect to $\boldsymbol{H}$ |
| $\boldsymbol{\Sigma}_{\boldsymbol{h}}$ | Conjugate stress with respect to $\boldsymbol{h}$ |
| $\Sigma_J$ | Conjugate stress with respect to $J$ |
| $\Sigma_j$ | Conjugate stress with respect to $j$ |
| $\boldsymbol{\sigma}$ | Cauchy stress tensor |
| $\boldsymbol{\sigma}_n$ | Normal stress vector |
| $\boldsymbol{\sigma}_s$ | Shear stress vector |
| $\boldsymbol{\sigma}_{\boldsymbol{\chi}}$ | Updated reference stress tensor |
| $\sigma_{1,2,3}$ | Principal stresses |
| $\sigma_{\max}$ | Maximum principal stress |
| $\sigma^0_{\max}$ | Maximum allowable principal stress |

| | |
|---|---|
| $\sigma_v$ | von Mises equivalent stress |
| $\boldsymbol{\tau}$ | Kirchhoff stress tensor |
| $\boldsymbol{\tau}'$ | Deviatoric part of Kirchhoff stress tensor |
| $\tau_{\max}$ | Maximum normal traction |
| $\bar{\tau}_y$ | Yield stress |
| $\tau_y^0$ | Initial yield stress |
| $\tau_y^\infty$ | Residual yield stress |
| $\upsilon_\alpha$ | Direction vector in a return mapping algorithm |
| $\boldsymbol{\phi}$ | Mapping function between initial and current configurations |
| $\boldsymbol{\chi}$ | Position vector of a generic particle in the intermediate configuration |
| $\Psi$ | Strain energy per unit of initial volume |
| $\hat{\Psi}$ | Deviatoric component of the strain energy per unit of initial volume |
| $\Psi_{\boldsymbol{X}}$ | Multivariable strain energy per unit of initial volume |
| $\hat{\Psi}_{\boldsymbol{X}}$ | Deviatoric component of the multivariable strain energy per unit of initial volume |
| $\Omega_V$ | Initial domain |
| $\Omega_{V\chi}$ | Intermediate domain |
| $\Omega_v$ | Current domain |

**Latin Symbols**

| | |
|---|---|
| $\boldsymbol{A}_G$ | Angular momentum about mass centre |
| $A$ | Yield stress parameter in a Johnson-Cook model |
| $\boldsymbol{b}$ | Body force per unit of current volume |
| $\boldsymbol{b}_e$ | Elastic Left Cauchy-Green deformation tensor |
| $\boldsymbol{b}_0$ | Body force per unit of initial volume |
| $\boldsymbol{b}_{\boldsymbol{\chi}}$ | Body force per unit of intermediate volume |
| $b$ | Hardening parameter in a Johnson-Cook model |
| $\boldsymbol{C}$ | Right Cauchy-Green deformation tensor |
| $\boldsymbol{C}_{ab}^{\boldsymbol{\chi}}$ | Pseudo area vector in updated reference Lagrangian SPH |
| $\boldsymbol{C}_{ab}^{\boldsymbol{X}}$ | Pseudo area vector in Total Lagrangian SPH |

| | |
|---|---|
| $\boldsymbol{C}_p$ | Plastic right Cauchy-Green deformation tensor |
| $\boldsymbol{\mathcal{C}}_{\boldsymbol{NN}}$ | Acoustic tensor |
| $\boldsymbol{\mathcal{C}}_{\boldsymbol{NN}}^{\mathrm{lin}}$ | Acoustic tensor in linear elasticity |
| $C_v$ | Specific heat capacity |
| $c$ | Strain rate coefficient in a Johnson-Cook model |
| $\bar{c}_p$ | Linear pressure wave speed in the initial configuration |
| $c_p$ | Nonlinear pressure wave speed |
| $\bar{c}_s$ | Linear shear wave speed in the initial configuration |
| $c_s$ | Nonlinear shear wave speed |
| $c_v$ | Volumetric heat capacity |
| $\boldsymbol{D}_{ab}^{\boldsymbol{p}_{\boldsymbol{\chi}}}$ | Numerical dissipation in the linear momentum equation |
| $D_{ab}^{j}$ | Numerical dissipation in the incremental volume map equation |
| $\boldsymbol{d}$ | Rate of deformation tensor |
| $dA$ | Element of area in the initial configuration |
| $dA^{\boldsymbol{\chi}}$ | Element of area in the intermediate configuration |
| $da$ | Element of area in the current configuration |
| $d\boldsymbol{L}$ | Arbitrary vector in the initial configuration |
| $d\boldsymbol{l}$ | Arbitrary vector in the current configuration |
| $dm$ | Mass of a single point in the current configuration |
| $d\boldsymbol{p}$ | Resultant force on an element of area $da$ |
| $dV$ | Element of volume in the initial configuration |
| $dV^{\boldsymbol{\chi}}$ | Element of volume in the intermediate configuration |
| $dv$ | Element of volume in the current configuration |
| $\boldsymbol{E}$ | Lagrangian or Green strain tensor |
| $E$ | Total energy per unit of initial volume |
| $E_{\boldsymbol{\chi}}$ | Total energy per unit of intermediate volume |
| $\boldsymbol{e}$ | Eulerian or Almansi strain tensor |
| $\boldsymbol{F}$ | Deformation gradient |
| $\boldsymbol{F}_e$ | Elastic component of the deformation gradient |

| | |
|---|---|
| $\boldsymbol{F}_p$ | Plastic component of the deformation gradient |
| $\boldsymbol{F}_{\boldsymbol{\chi}}$ | Intermediate deformation gradient |
| $\boldsymbol{f}$ | Incremental deformation gradient |
| $\boldsymbol{f}_{\text{ext}}$ | Resultant of external forces |
| $f$ | Yield function |
| $f_h$ | Smoothing length factor |
| $G_f$ | Fracture energy |
| $\boldsymbol{H}$ | Area map (co-factor of $\boldsymbol{F}$ in exact continuum mechanics) |
| $\boldsymbol{H}_{\boldsymbol{\chi}}$ | Intermediate area map (co-factor of $\boldsymbol{F}_{\boldsymbol{\chi}}$ in exact continuum mechanics) |
| $H$ | Hardening modulus |
| $\boldsymbol{h}$ | Incremental area map (co-factor of $\boldsymbol{f}$ in exact continuum mechanics) |
| $h$ | Smoothing length |
| $\boldsymbol{I}$ | Identity tensor |
| $J$ | Volume map (Jacobian of $\boldsymbol{F}$ in exact continuum mechanics) |
| $J_{\boldsymbol{\chi}}$ | Intermediate volume map (Jacobian of $\boldsymbol{F}_{\boldsymbol{\chi}}$ in exact continuum mechanics) |
| $j$ | Incremental volume map (Jacobian of $\boldsymbol{f}$ in exact continuum mechanics) |
| $\boldsymbol{K}$ | Conductivity tensor in the material configuration |
| $\boldsymbol{K}_{\boldsymbol{\chi}}$ | Conductivity tensor in the intermediate configuration |
| $K$ | Kinetic energy |
| $k$ | Thermal conductivity |
| $\boldsymbol{L}$ | Linear momentum |
| $\boldsymbol{L}_a$ | Gradient correction matrix |
| $\boldsymbol{l}$ | Velocity gradient |
| $\boldsymbol{m}_{\text{ext}}$ | Resultant of external moments |
| $m$ | Temperature exponent in a Johnson-Cook model |
| $m_i$ | Mass of particle $i$ |
| $\boldsymbol{N}$ | Outward pointing unit normal in the initial configuration |
| $\boldsymbol{N}^{\boldsymbol{\chi}}$ | Outward pointing unit normal in the intermediate configuration |
| $\boldsymbol{n}$ | Outward pointing unit normal in the current configuration |

| | |
|---|---|
| $n'$ | Hardening exponent in a Johnson-Cook model |
| $\boldsymbol{P}$ | First Piola-Kirchhoff stress tensor |
| $\boldsymbol{p}$ | Linear momentum per unit of initial volume |
| $\boldsymbol{p}_{\boldsymbol{\chi}}$ | Linear momentum per unit of intermediate volume |
| $p$ | Pressure |
| $\bar{p}$ | Temperature-dependent pressure |
| $\boldsymbol{Q}$ | Lagrangian heat flux vector |
| $\boldsymbol{Q}_{\boldsymbol{\chi}}$ | Heat flux vector in the intermediate configuration |
| $q$ | Dimensionless Mie-Grüneisen parameter |
| $\boldsymbol{R}$ | Orthogonal rotation tensor |
| $\boldsymbol{S}$ | Second Piola-Kirchhoff stress tensor |
| $S_{ab}^{j}$ | Stabilisation for incremental volume map |
| $\boldsymbol{S}_{ab}^{\boldsymbol{p}_{\boldsymbol{\chi}}}$ | Stabilisation tensor for linear momentum |
| $\boldsymbol{s}_0$ | Heat source per unit of initial volume |
| $\boldsymbol{s}_{\boldsymbol{\chi}}$ | Heat source per unit of intermediate volume |
| $\boldsymbol{T}_{ab}$ | Pair-wise interacting force between particle $a$ and particle $b$ in TLF |
| $\boldsymbol{T}_{ab}^{\boldsymbol{\chi}}$ | Updated reference pair-wise interacting force between particle $a$ and particle $b$ |
| $\boldsymbol{t}$ | Traction force per unit of current area |
| $\boldsymbol{t}_0$ | Traction force per unit of initial area |
| $\boldsymbol{t}_{\boldsymbol{\chi}}$ | Traction force per unit of intermediate area |
| $t$ | Time |
| $\boldsymbol{U}$ | Material stretch tensor |
| $U$ | Volumetric component of the strain energy per unit of initial volume |
| $\boldsymbol{u}$ | Displacement vector |
| $\boldsymbol{V}$ | Spatial stretch tensor |
| $\boldsymbol{v}$ | Velocity field |
| $\tilde{W}$ | Corrected kernel function |
| $W$ | Kernel function |

| | |
|---|---|
| $W_p$ | Plastic dissipation |
| $w_p$ | Plastic dissipation per unit of initial volume |
| $\boldsymbol{X}$ | Position vector of a generic particle in the initial configuration |
| $\boldsymbol{x}$ | Position vector of a generic particle in the current configuration |

**Operators**

| | |
|---|---|
| $\boldsymbol{\mathcal{C}}_*$ | Kernel gradient correction operator |
| $\mathcal{C}_*$ | Kernel correction operator |
| $\partial\Omega_V$ | Initial boundary surface |
| $\partial\Omega_{V\boldsymbol{\chi}}$ | Intermediate boundary surface |
| $\partial\Omega_v$ | Current boundary surface |
| $\tilde{\boldsymbol{\nabla}}_{\boldsymbol{X}}$ | Corrected gradient with respect to the initial configuration |
| $\boldsymbol{\nabla}_{\boldsymbol{X}}$ | Gradient with respect to the initial configuration |
| $\tilde{\boldsymbol{\nabla}}_{\boldsymbol{\chi}}$ | Corrected gradient with respect to the intermediate configuration |
| $\boldsymbol{\nabla}_{\boldsymbol{\chi}}$ | Gradient with respect to the intermediate configuration |
| $\boldsymbol{\nabla}$ | Gradient with respect to the current configuration |
| $\boldsymbol{\phi}_*$ | Push forward operation applied to the gradient of a kernel function |
| $\phi_*$ | Push forward operation applied to a kernel function |

# List of author's publications

- **Journals**

**P. R. Refachinho de Campos**, A. J. Gil, C. H. Lee, J. Bonet. *A New Updated Reference Lagrangian Smooth Particle Hydrodynamics algorithm for dynamic fracture*. Under preparation.

**P. R. Refachinho de Campos**, C. H. Lee, A. J. Gil, J. Bonet. *A New Updated Reference Lagrangian Smooth Particle Hydrodynamics algorithm for thermo-elasticity and thermo-visco-plasticity*. Under preparation.

**P. R. Refachinho de Campos**, A. J. Gil, C. H. Lee, M. Giacomini, J. Bonet. *A New Updated Reference Lagrangian Smooth Particle Hydrodynamics algorithm for isothermal elasticity and elasto-plasticity*. In: *Comput. Methods Appl. Mech. Engrg.* 392.1 (2022), pp. 114680. DOI: 10.1016/j.cma.2022.114680.

- **Conferences and Congresses**

**P. R. Refachinho de Campos**, A. J. Gil, C. H. Lee, A. Huerta, M. Giacomini. *Stabilised Updated Lagrangian SPH for Fast Solid Dynamics*. ADMOS 2021: Gothenburg, Sweden, 2021.

**P. R. Refachinho de Campos**, A. J. Gil, C. H. Lee, A. Huerta, M. Giacomini. *Robust Updated Lagrangian Smooth Particle Hydrodynamics for Fast Solid Dynamics*. UKACM 2021: Loughborough, England, 2021.

C. H. Lee, **P. R. Refachinho de Campos**, A. J. Gil and J. Bonet. *A First Order Conservation Law Framework for Fast Solid Dynamics*. UKACM 2021: Loughborough, England, 2021.

**P. R. Refachinho de Campos**, A. J. Gil, C. H. Lee, A. Huerta, M. Giacomini, J. Bonet. *Stabilised Updated Lagrangian SPH for Fast Solid Dynamics*. WCCM & ECCOMAS 2020: Virtual Congress, 2021.

**P. R. Refachinho de Campos**, A. J. Gil, C. H. Lee, A. Huerta, M. Giacomini, J. Bonet. *Towards a new dynamic fragmentation solver in Engineering*. ADMOS 2019: Alicante, Spain, 2019.

- **Workshops**

**P. R. Refachinho de Campos**, A. J. Gil, C. H. Lee, A. Huerta, M. Giacomini. *Stabilised Updated Lagrangian SPH for Fast Solid Dynamics*. ZCCE Postgraduate Workshop: Swansea, Wales, 2021.

**P. R. Refachinho de Campos**, A. J. Gil, C. H. Lee, A. Huerta, M. Giacomini. *Stabilised Updated Lagrangian SPH for Fast Solid Dynamics*. ZCCE Postgraduate Workshop: Swansea, Wales, 2020.

# Part I

# Preliminaries

# Chapter 1

# Introduction

## 1.1 Motivation

Numerical methods that do not require connection between nodes or the creation of sub-regions (elements) in the process of discretisation compose a large family of methods called meshless (or meshfree) methods. Belytschko et al. [1], Huerta et al. [2] and Chen et al. [3] provide in-depth presentations of meshfree methods. The main objective of such techniques is to eliminate some of the limitations related to the mesh dependence of conventional computational methods. Since the approximations are constructed in terms of nodes (particles) and not based on elements, which distortion may degrade accuracy, meshfree methods can address a range of problems much wider than mesh-based methods. Moreover, meshfree methods have the potential of circumventing some difficulties usually faced in the pre-processing stage, i.e., meshfree methods eliminate the standard mesh generation process, making the integration between Computer Aided Engineering (CAE) and Computer Aided Design (CAD) easier.

Computational methods in fast solid dynamics, which is the branch of computational mechanics that deals with the simulation of relatively short-duration dynamic events, where large deformations, high energy impacts, fracture and fragmentation can take place, can benefit from the advantages of not having interconnected elements. For example, when it comes to the modelling of fracture, the introduction of domain discontinuities seems to be more naturally achieved with meshless methods. In the past years, different meshless methods have been used for this purpose, the Smooth Particle Hydrodynamics (SPH) [4, 5] and the Element Free Galerkin (EFG) [6] are two examples strongly present in this context. In practical terms, the ability of accurately modelling this class of phenomena can contribute to a better understanding of the structural behaviour of mechanical systems subjected to extreme loading conditions, leading to the development of more reliable products and safer operations. The spectrum of applications is very wide and comprises the most diverse fields. One can think about forensic engineering, for example, where numerical methods are employed in the investigation of accidents, usually involving failure and rupture of materials [7]. A completely different example is found in life sciences engineering, in the studies performed to improve medical procedures, such as the extracorporeal shock-wave lithotripsy used in the comminution of kidney stones [8]. A few other possible applications are illustrated in figure 1.1.

Therefore, meshless methods are potential candidates when deciding between

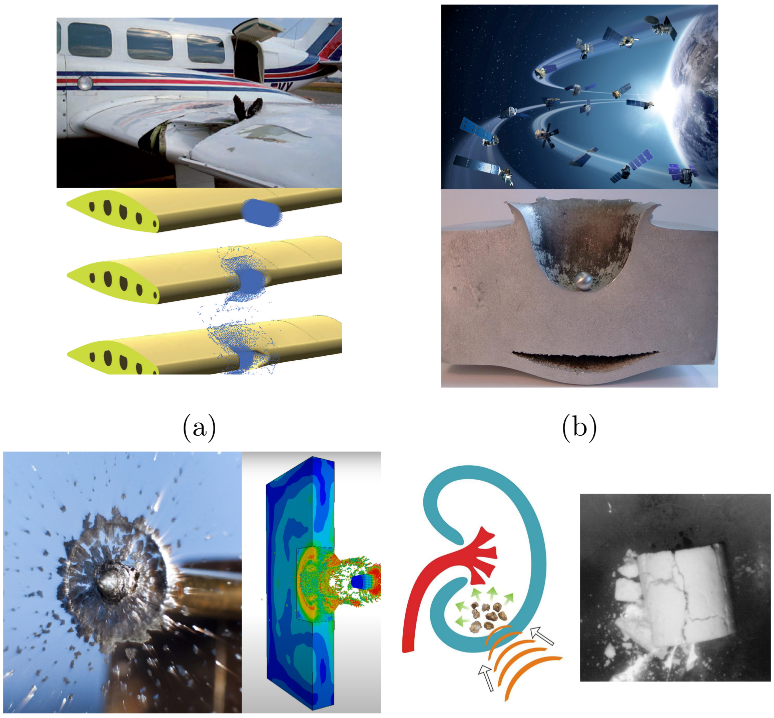

(a) (b)

(c) (d)

Figure 1.1: Examples of applications for fast solid dynamics. (a) Aircraft bird impact. (b) Space debris impact. (c) Ballistic. (d) Shock-wave lithotripsy.

modelling techniques to tackle problems in fast solid dynamics. The SPH method, in particular, has a long history of development and is very attractive because of its simplicity, low computational cost and versatility. However, in its original version, the SPH method lacks robustness and can present, among other issues, numerical instabilities [9]. This behaviour may lead to the development of spurious modes, non-physical results and even to the occurrence of numerical fracture, i.e., the clumping of the particles caused by numerical instabilities can lead to non-physical cracks. The present work is driven by the interest of having a robust tool for computer simulations in fast solid dynamics and aims at laying the foundations for approaching complex phenomena such as contact and dynamic fracture employing the SPH method. As an outcome, a new stabilised updated reference Lagrangian SPH framework will be presented and employed in the solution of challenging benchmark problems.

## 1.2 State of the art

### 1.2.1 Smooth Particle Hydrodynamics method for solids

One of the earliest meshfree methods is the Smooth Particle Hydrodynamics (SPH), first presented for astrophysical applications in 1977 by Gingold et al. [4] and Lucy [5]. Libersky et al. [10, 11] were among the firsts to use the SPH method in the context of strength of materials in 1990, and dynamic solid mechanics in 1993. The SPH method gives numerical solutions to initial-boundary value problems defined by conservation laws of continuum mechanics, combined to constitutive relations for the materials involved. It is important to emphasise that SPH is not based on discrete particles colliding with each other or presenting cohesive-like behaviour. Instead of this, SPH is a Lagrangian modelling scheme that permits the discretisation of continuum Partial Differential Equation (PDE) through the approximation of properties at a set of points distributed over the domain, without the need of defining a spatial mesh. The Lagrangian nature of the method, and its ability to keep accurate histories of the events, associated with its meshless characteristic represent the main advantages of SPH. A massive number of publications regarding the SPH method is available in the literature. The works by Monaghan [12], Swegle et al. [13] and Vignjevic et al. [14] provide comprehensive reviews of the theme.

Nevertheless, the classical updated Lagrangian displacement-based SPH suffers from a number of drawbacks reported by many authors, namely: numerical instabilities such as spurious zero-energy modes and tensile instability [9, 15–27], lack of consistency [19, 21, 28, 29], loss of conservation [25, 30, 31] and reduced order of convergence for derived variables such as stresses and strains [25]. The stability analysis of the SPH method was addressed for the first time by Swegle et al. [9] and their results indicated an instability in the tensile regime of the standard SPH, even though the method appeared to be stable in compression. In [20] a unified stability analysis of meshless particle methods is presented with the objective of clearly identifying different types of instabilities and the effectiveness of various stabilisation techniques. Notice that the tensile instability is not present in total Lagrangian approaches [20, 23, 32], and therefore, the majority of recent advancements for solid mechanics in SPH were proposed in a total Lagrangian setting.

Since its inception, many research groups proposed solutions for the different issues faced in SPH, some recent works tackling SPH in the context of solids include [22, 24, 27, 33–38]. Some interesting work has also been reported in [35, 39] where a hourglass control based stabilisation algorithm is employed for the description of elasto- and visco-plastic continuum. Enhanced SPH formulations for solids were also developed in the context of Fluid Structure Interaction (FSI). In [40], a Hamiltonian SPH structural model was coupled with an enhanced version of incompressible SPH allowing conservative simulations of laminated composite elastic structures. An accurate multi-resolution hydroelastic FSI solver, comprising an SPH structural model that preserves linear and angular momenta was presented in [41]. Other authors combined SPH with similar meshless techniques, e.g. Finite Volume Particle Method (FVPM) [42] and the Vector-based Discrete Element Model [43], in order to produce a robust meshless SPH model for Fluid Structure Interaction.

In the work by Lee et al. [27], as a result of the evolution of previous works, an alternative Riemann-based stabilisation strategy for a mixed-based SPH framework for large strain explicit solid dynamics was presented. The resulting mixed methodology is in the form of a system of total Lagrangian first order conservation laws, where the equation of the conservation of the linear momentum $\boldsymbol{p}$ is supplemented with three geometric conservation laws, namely, the conservation of the deformation gradient $\boldsymbol{F}$, of the volume map $J$ (Jacobian) and of the area map $\boldsymbol{H}$ (co-factor). The new stabilised total Lagrangian SPH methodology introduced in [27] aims at the removal of spurious zero-energy modes and improved order of convergence of variables such as stresses and strains. Moreover, in their approach, linear consistency is fulfilled by performing kernel and gradient corrections, as proposed in [29]. Global conservation of angular momentum is ensured with the introduction of a monolithic angular momentum projection algorithm, first presented in [25]. The stabilisation methodology presented in [27] has as one of its main advantages the fact that it does not require user-defined artificial stabilisation parameters, instead of this, it is based on the physical pressure and shear wave speeds.

One of the main characteristics of the framework proposed in [27] is the fact that the conservation of the linear momentum is solved along with the conservation equations for the deformation gradient and its minors. In previous works, but in different contexts, Lee et al. [44, 45] proposed other methodologies which had as unknowns the linear momentum, the deformation gradient and the total energy. With both the linear momentum and the deformation gradient tensor being primary variables of the problem, stresses converge at the same rate as the velocities and displacements. Moreover, the new formulation was shown to be efficient in nearly incompressible and bending dominated scenarios. However, in case of extreme deformations in the incompressible limit, the $\boldsymbol{p}-\boldsymbol{F}$ formulation lacks robustness. In [46], in the context of the Finite Element Method (FEM), Gil et al. enhanced the formulation for nearly and truly incompressible deformations with the novelty of introducing a conservation law for the Jacobian $J$ of the deformation gradient, providing extra flexibility to the scheme. In [47], a new geometric conservation law for the co-factor $\boldsymbol{H}$ of the deformation gradient was also added to the framework, leading to an enhanced mixed-formulation. The development of this new conservation equation was possible due to the simplification introduced by the use of a tensor cross product operation, presented for the first time in the context of solid mechanics in [48] and further explained in [49].

Even though considerable progress was made in the SPH method in recent years, further improvements still need to be done in order to achieve a robust updated Lagrangian SPH methodology, which is needed for taking into account topological changes that take place in fracture and fragmentation scenarios.

### 1.2.2 Meshfree methods in fracture mechanics

In the class of meshless techniques, the Smooth Particle Hydrodynamics (SPH) has been widely used for computational fracture mechanics [18, 50–56]. Other method appearing very often in this field is the Element Free Galerkin (EFG) [57–61]. The recent work by Rabczuk et al. [62] dedicates an entire chapter to the topic, titled in that work as “extended meshfree methods”, in analogy to the Extended Finite Element Method (XFEM) [63, 64]. It is also noticeable the recent interest of researchers in the so-called peridynamics [65], a non-local type continuum mechanics formulation, originally introduced to predict fracture [66, 67] and often discretised using meshfree schemes. Nonetheless, Ganzenmüller et al. [68] have shown the equivalence of peridynamics and classic SPH, if nodal integration is used.

Generally speaking, four main ingredients are necessary to computational fracture mechanics in meshfree methods, they are:

1. A failure criterion.
2. A procedure to obtain the new domains of influence once fracture takes place.
3. A traction-crack opening law (also referred as a cohesive law).
4. An updated description of the governing equations (Updated Lagrangian Formulation).

Among the options available for the first item of this list, the simplest approach is the Rankine criterion, where a crack is introduced when the principal tensile stress reaches the uniaxial tensile strength at a particle and the crack is initiated perpendicular to the direction of the principal tensile stress. Another option employed is the loss of hyperbolicity criterion on a softening model [69], where the change of the type of the Partial Differential Equation (PDE) (for rate-independent materials) leads to a localisation of deformation and the displacement field develops a discontinuity as a consequence. Loss of material stability, which can be identified when the minimum eigenvalue of the acoustic tensor is smaller than zero [70] can also be used as a failure criterion.

Referring back to the very first works where SPH was employed for computational fracture mechanics, in [18] Randles and Libersky give a gentle overview of their approach to fracture. The strategy was to alter the pair-wise interaction between two particles, once they have both accumulated significant damage projection towards each other. For doing so, a damage interaction factor is introduced directly into the kernel estimate for the linear momentum equation, as a multiplicative factor (see equation 55 in reference [18]). This factor is obtained from a function expressed in terms of the accumulated damage of each particle, computed using a damage model and is defined in such a way to result equal to 1 when there is no damage and equal to 0 when the total accumulated damage reaches 1. The effect is that the dynamic interaction of the particles is reduced when they have significant damage projected towards one another, up to the point of having absolutely no interaction (damage interaction factor equal to 0). In this approach there is no splitting of particles and the domains of influence of each particle will be affected as new standard 2h searches are performed. In a much more recent work, the idea of having a damage interaction factor is employed again. In [55], Chakraborty and Shaw introduce the concept of having pseudo-springs connecting neighbouring particles. In their methodology, the damage is associated to the pseudo-springs, rather than to the particles themselves. The search for neighbours is performed only once and the pseudo-springs are added between immediate neighbouring particles. Fracture is characterised then by the "breakage" of the pseudo-springs. The authors point out the benefit of rezoning or discontinuous enrichments being not needed for this model.

Following a different line, in [57], the approach entitled "cracking particles" is described in the context of meshfree methods. The model is initially applied to 2D problems. The work was originally motivated by the work of Remmers et al. [71], where a crack was represented by a set of overlapping cohesive segments, i.e., the discontinuity is modelled by unconnected piecewise linear segments in such a way that a representation of the crack surface is not required. Extending this idea to meshfree methods, in [57] a continuous crack consists of a set of contiguous cracked particles. As pointed out by the authors, the cracking particles method is applicable to many particles methods, including the Smooth Particle Hydrodynamics (SPH). The formulation employed is displacement based and in addition to the standard Dirichlet and Neumann boundary conditions, cohesive forces across the crack are considered. The discrete equations are developed mainly in a Total Lagrangian Formulation (TLF) form. However, boundary terms on the crack surface are evaluated in the current configuration. The discontinuity is described by decomposing the displacement field into continuous and discontinuous parts. The discontinuous part of the displacement is also called enrichment. In the cracking particles method, each crack line (or plane in 3D) is restricted to always pass through a particle and only cracked nodes are enriched. In the initial configuration, the crack surface on a cracked particle denotes a single surface, but in the current configuration it becomes two surfaces.

In the original cracking particles method from [57], the deformation gradient $\boldsymbol{F}$ is also decomposed into continuous and discontinuous parts $\boldsymbol{F} = \hat{\boldsymbol{F}} + \tilde{\boldsymbol{F}}$, where $\hat{\boldsymbol{F}}$ is continuous and $\tilde{\boldsymbol{F}}$ is discontinuous. Cubic B-spline is used for the kernel function with a cylindrical compact support. The same shape functions are used for the enrichment but usually with a support size larger than the support of the continuous approximation. Stress point integration is used in order to remove the instabilities caused by rank deficiency which appears in a pure nodal integration. The cohesive nodal forces are computed in the current configuration and for this purpose, Nanson's rule is used to obtain the current normal. For the constitutive model, a damage plasticity model, the Lemaitre[1] model and also a linear elastic model are used. A discrete crack is introduced when the criterion for loss of continuity is met at a particle, the Rankine criterion and a loss of hyperbolicity criterion are both tested.

Further research was conducted in the cracking particles method, for instance, in [59], the methodology presented in [57] was extended to the three-dimensional space with the crack still being modelled as a set of cracked particles. An $h$-adaptivity method is implemented together with the cracking particles in the Element Free Galerkin (EFG) context, this provides the method with more accuracy around the crack tip. Another contribution of [59] is the development of a methodology for switching between total and updated Lagrangian kernels at the nodes that are cracked. The term Eulerian kernel is employed in [59] to refer to kernels expressed in terms of spatial coordinates and with support sizes that can vary in time. Due to the fact that the neighbours do not change in a total Lagrangian approach, the domain of influence can become extremely distorted with time. This limits the magnitude of the deformation that can be represented and therefore, an Updated Lagrangian Formulation (ULF) is essential when modelling fracture and fragmentation. In [59], the simulation always starts with total Lagrangian kernels. However, after introducing a discontinuity, when the particles have separated or if the cohesive tractions have decayed to zero, the kernel is switched to an updated kernel. The main cracking criteria used by Rabczuk and Belytschko [59] is the loss of material stability criterion, where material stability is checked by conditions on the acoustic tensor. For a rate-independent material, the momentum equation stays hyperbolic as long as the minimum eigenvalue of the acoustic tensor remains positive (see, e.g. [70]).

In [61], a three-dimensional cracking particles formulation without enrichment is proposed, i.e., no additional unknowns are needed to capture the displacement discontinuity. When cracking is detected, a cohesive surface is introduced and the particle is split into two particles lying on opposite sides of the crack. The method is developed within the EFG context, with the cubic B-spline chosen as window function. The size of the crack segment is determined by the size of the compact support of the cracked particle. To capture the jump in displacements, the shape functions are cut across the crack boundary using the so-called visibility method.

---

[1] The Lemaitre model is an elastic model with isotropic damage, developed for brittle materials such as concrete.

In order to deal correctly with interior boundaries such as cracks and holes, the domain of influence of a particle cannot cross a boundary adjacent to that point, i.e., only points that can be connected to the target particle, without intersecting any boundary, can be included in the domain of influence. The need of this kind of treatment was presented in [6] and a possible methodology is the one that employs the visibility criterion [72]. The following, very elucidative, analogy is extracted from [1] and explains the visibility method:

"*The boundaries of the body and any interior lines of discontinuity are considered opaque when constructing the weight functions. By opacity, we mean that when the domain of influence for the weight function is constructed, the line from a point to a node is imagined to be a ray of light. If the ray encounters an opaque surface, such as the boundary of a body or an interior discontinuity, it is terminated and the point is not included in the domain of influence.*"

The cracking particles method, as first presented in [57] suffers from spurious crack nucleation when a crack propagates. As pointed out in [60, 61], this can be avoided with the introduction of some criteria to distinguish between crack nucleation, crack propagation and crack branching. The distinction is possible by searching for existing cracked nodes in the vicinity of a new cracked node, crack initiation is assumed when no cracked node is detected in the vicinity. Spurious cracking can occur adjacent to an existing crack or near the crack tip, each case receives a different treatment.

## 1.3 Novelties of the thesis

The purpose of this work is to develop and test a new and robust updated reference Lagrangian SPH framework, aiming at applications in the field of fast solid dynamics with extended capabilities, such as thermal-stress analysis and fracture mechanics. The aim is to obtain a versatile formulation, that can be degenerated into a standard Total Lagrangian Formulation (TLF) or into a truly Updated Lagrangian Formulation (ULF), taking full advantage of both approaches. The SPH framework proposed in this thesis is inspired by the works of Vidal et al. [24] and Lee et al. [27].

The highlights of the work include:

1. System of first order conservation laws
2. Updated reference Lagrangian formulation
3. Anisotropic kernel functions
4. Entropy stable stabilisation scheme

The updated reference Lagrangian approach, based on the multiplicative decomposition of the deformation process, allows for updates on the reference configuration to be performed only when required, for example, when topological changes take place. Moreover, the mixed-based nature of the formulation adds to the robustness of the scheme and ensures that strains converge at the same rate as the velocities. Novel methodologies for obtaining updated kernels and gradients are also introduced, the deformation gradient and its minors allow anisotropic compact supports to be accurately obtained. Another novelty is the introduction of a consistent Riemann-based stabilisation scheme in the context of an Updated Lagrangian Formulation. The stabilisation terms are based on the physics of the problem, i.e., the numerical dissipation depends on the pressure and shear wave speeds of the underlying material, and are developed in such a manner to satisfy the second law of thermodynamics.

## 1.4 Outline

In order to elaborate the objectives indicated in the previous section, this thesis is organised as follows:

- Part I opens and motivates the work.

- Part II presents the formulation in the continuum level. It consists of chapter 2, where the key features of an updated reference Lagrangian formulation are discussed and a mixed-based set of first-order conservation laws is introduced in an isothermal context. Followed by chapter 3, where the first law of thermodynamics written in terms of the total energy is added to the set of conservation laws. The purpose is to extend the formulation to a thermal-coupled context.

- Part III presents the numerical aspects of the formulation in the discrete level. It consists of chapter 4, where the key ingredients of the Smooth Particle Hydrodynamics (SPH) are discussed. Followed by chapter 5, which is devoted to the development of the updated reference Lagrangian SPH framework. The system of updated reference Lagrangian equations is discretised using the SPH method, consistent stabilisation terms are developed, a time-integration scheme and an angular momentum preserving algorithm are provided. Part III ends with chapters 6 and 7, where all aspects of the formulation are explored through challenging numerical examples in isothermal and thermo-mechanical contexts.

- Part IV presents the extension of the framework to the context of fracture mechanics. It consists of chapter 8, where by making full use of the characteristics of the proposed formulation, the post-fracture velocity and deformation gradient are derived. Afterwards, the numerical aspects of the particle splitting capability are detailed, including the fracture criteria adopted. Part IV is then concluded with chapter 9, presenting numerical examples in fracture mechanics.

- Part V consists of chapter 10, only. It concludes the thesis by summarising the main points and indicating some suggestions for future research works.

It is noteworthy the importance of the content of the appendices in part VI, as follows:

- Appendix A brings altogether the mathematical definitions and identities used throughout the thesis.

- Appendix B summarises the fundamental concepts of nonlinear solid mechanics with the objective to ease the reading of the thesis.

- Appendix C presents the fundamental developments and mathematical manipulations of the equations that are used to form the mixed-based set of conservation laws. The transition between total Lagrangian and updated Lagrangian formulations is well detailed in this appendix.

- Appendix D gives further details on the development of the angular momentum projection algorithm used in conjunction with the three-stages Runge-Kutta time integrator employed in this work.

## 1.5 A note about the numerical examples

Each of the three main topics covered in this thesis, i.e., the updated reference formulation in SPH and its extension into thermo and fracture mechanics contexts, has a corresponding chapter presenting numerical examples aiming at testing the proposed formulation. Different test cases are analysed comprising a variety of geometries and constitutive models. The frequency of updating the reference configuration is chosen in such a way that: 1) A Total Lagrangian Formulation is retrieved, i.e., no updates are performed and the simulation is based on the initial geometry, these examples will be identified as TLF. 2) A truly Updated Lagrangian Formulation is retrieved, i.e., the reference configuration is updated at every time step and the simulation evolves based on a new (deformed) geometry, these examples will be identified as ULF. 3) Intermediate states between TLF and ULF, where the reference configuration is updated from time to time, are also performed. For these cases, the updating frequency may be arbitrarily chosen or can be based in some criteria, (e.g. a plastic strain threshold, fracture, etc.). Details will be presented together with the respective example when this technique is employed.

The models presented in this work were created using a conventional finite element pre-processor. The position of the nodes of 8-, 6- and/or 4-nodes elements were extracted and used as the particles coordinates. The coordinates are the only information required from the mesh. As a characteristic of corrected SPH methods, the present formulation does not require any special orientation or distribution for the particles. Therefore, any structured or unstructured mesh would serve for the purpose of obtaining the initial particle coordinates. The number of particles for each model was arbitrarily chosen to provide a good coverage of the domain and allow successive model refinements. Unless specified differently, only one layer of immediate neighbouring particles was considered. The same set of neighbours is kept constant throughout the simulation, with the smoothing length parameter defined individually for each domain of influence as a function of the most distant neighbour within that support. The different alternatives for computation of kernels and gradients presented in chapter 4 are used without a preferred method, yielding equally robust results.

It is well known that the ratio between the smoothing length and the distance between particles is problem dependent and calibration of $h$ for practical applications remains a major challenge in meshless methods [2, 38, 73]. For all examples solved using the methodology presented in this work, the factor $f_h$ employed with the quadratic kernel function was $f_h = 0.6$, while for the cubic spline smoothing function a factor $f_h = 0.8$ was used. All examples were elaborated in the International System of units.

# Part II

# Conservation Equations for Solid Dynamics

# Chapter 2

# Isothermal deformation process

## 2.1 Introduction

In this chapter the updated reference Lagrangian set of equations that forms the basis of the framework developed in this work is presented in the continuum level. The chapter introduces a mixed-based set of first order conservation laws, also presenting the concepts behind the Total Lagrangian Formulation (TLF) and the Updated Lagrangian Formulation (ULF). The step-by-step development of the equations presented in this chapter is included in Appendix C. The constitutive models available within the framework are also presented, namely a nearly incompressible neo-Hookean model and a rate-independent von Mises plasticity model.

## 2.2 Elastodynamics

Consider the three dimensional deformation of an isothermal body of material density $\rho_0$ moving from its initial undeformed configuration $\Omega_V$, with boundary $\partial\Omega_V$, to a current deformed configuration $\Omega_v$ at time $t$, with boundary $\partial\Omega_v$ (see figure 2.1). In the absence of non-smooth solutions, the time dependent motion[1] $\boldsymbol{\phi}$ which satisfies a set of Total Lagrangian first order conservation laws was well explored in [25–27]. The term Total Lagrangian Formulation (TLF) refers to the fact that the equations for the conservation laws are expressed in terms of the initial undeformed configuration $\Omega_V$ as

$$\frac{\partial \boldsymbol{p}}{\partial t} - \mathrm{DIV}\boldsymbol{P} = \boldsymbol{b}_0, \tag{2.1}$$

$$\frac{\partial \boldsymbol{F}}{\partial t} - \mathrm{DIV}(\boldsymbol{v} \otimes \boldsymbol{I}) = \boldsymbol{0}, \tag{2.2}$$

$$\frac{\partial \boldsymbol{H}}{\partial t} - \mathrm{CURL}\,(\boldsymbol{v} \times \boldsymbol{F}) = \boldsymbol{0}, \tag{2.3}$$

$$\frac{\partial J}{\partial t} - \mathrm{DIV}\left(\boldsymbol{H}^T \boldsymbol{v}\right) = 0. \tag{2.4}$$

where DIV and CURL represent the material divergence and curl operators carried out with respect to the material configuration, and the symbol $\times$ represents the

---

[1] See section B.2 of Appendix B for a detailed review on kinematics.

tensor cross product between vectors and/or second order tensors, see appendix A and [49]. In addition to this, $\boldsymbol{p} = \rho_0 \boldsymbol{v}$ is the linear momentum per unit of initial volume, $\boldsymbol{b}_0$ is the body force per unit of initial volume, $\boldsymbol{P}$ is the first Piola-Kirchhoff stress tensor, $\boldsymbol{F}$ is the deformation gradient, $\boldsymbol{H}$ is the area map (co-factor of $\boldsymbol{F}$), $J$ is the volume map (Jacobian of $\boldsymbol{F}$) and the involutions $\text{CURL}\boldsymbol{F} = \boldsymbol{0}$ and $\text{DIV}\boldsymbol{H} = \boldsymbol{0}$ are satisfied[2].

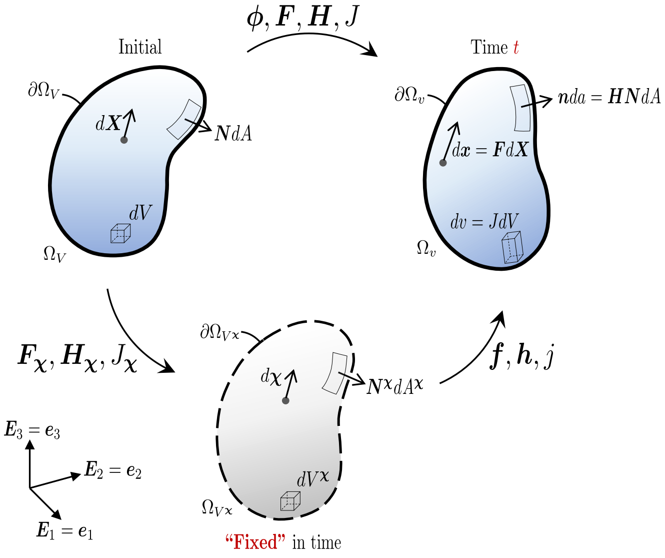

Figure 2.1: Deformation of a solid body.

**Remark 1** *It is important to emphasise the following aspect of the present formulations: the conservation law for the linear momentum is solved along with the equations for the deformation gradient and its minors (area and volume maps). Therefore, the geometric compatibility conditions*

$$\boldsymbol{F} = \boldsymbol{\nabla}_{\boldsymbol{X}} \boldsymbol{\phi}, \tag{2.5}$$

$$\boldsymbol{H} = \det\left(\boldsymbol{\nabla}_{\boldsymbol{X}} \boldsymbol{\phi}\right) \left(\boldsymbol{\nabla}_{\boldsymbol{X}} \boldsymbol{\phi}\right)^{-T}, \tag{2.6}$$

$$J = \det\left(\boldsymbol{\nabla}_{\boldsymbol{X}} \boldsymbol{\phi}\right), \tag{2.7}$$

*with $\boldsymbol{\nabla}_{\boldsymbol{X}}$ representing the material gradient with respect to $\boldsymbol{X}$, which are strongly satisfied in exact continuum mechanics (see Appendix B), are not necessarily true in the context of approximate solutions in mixed-based formulations. Precisely, this means that the three deformation measures $\boldsymbol{F}$, $\boldsymbol{H}$ and $J$ are independent from each other and only indirectly related through a weak enforcement of geometric compatibility conditions [49].*

The set of total Lagrangian conservation laws can be alternatively written in hyperbolic form as

$$\frac{\partial \boldsymbol{\mathcal{U}}}{\partial t} + \sum_{I=1}^{3} \frac{\partial \boldsymbol{\mathcal{F}}_I}{\partial X_I} = \boldsymbol{\mathcal{S}}, \tag{2.8}$$

---

[2] The curl of a gradient is zero, as well as the divergence of its cofactor is also zero, see [49]. Notice that the material curl of a second order tensor is defined as $[\text{CURL}\boldsymbol{A}]_{iI} = \varepsilon_{IJK} \frac{\partial A_{iK}}{\partial X_J}$.

where

$$\boldsymbol{\mathcal{U}} = \begin{bmatrix} \boldsymbol{p} \\ \boldsymbol{F} \\ \boldsymbol{H} \\ J \end{bmatrix}, \quad \boldsymbol{\mathcal{F}}_I = - \begin{bmatrix} \boldsymbol{P}\boldsymbol{E}_I \\ \boldsymbol{v} \otimes \boldsymbol{E}_I \\ \boldsymbol{F} \boldsymbol{\times} (\boldsymbol{v} \otimes \boldsymbol{E}_I) \\ \boldsymbol{H} \colon (\boldsymbol{v} \otimes \boldsymbol{E}_I) \end{bmatrix}, \quad \boldsymbol{\mathcal{S}} = \begin{bmatrix} \boldsymbol{b}_0 \\ \boldsymbol{0} \\ \boldsymbol{0} \\ 0 \end{bmatrix}, \tag{2.9}$$

with $\boldsymbol{E}_I :=$ $I$th unit vector of the Cartesian basis.

Alternatively, these equations can be expressed in terms of the current deformed configuration $\Omega_v$, known as Updated Lagrangian Formulation (ULF), that is obtained by pushing the total Lagrangian equations forward as

$$J^{-1}\frac{\partial \boldsymbol{\mathcal{U}}}{\partial t} + \sum_{i=1}^{3} \frac{\partial \left(\boldsymbol{\mathcal{F}}\boldsymbol{H}^{-1}\right)_i}{\partial x_i} = J^{-1}\boldsymbol{\mathcal{S}}, \qquad \text{in} \quad \Omega_v, \tag{2.10}$$

resulting in

$$J^{-1}\frac{\partial \boldsymbol{p}}{\partial t} - \text{div}\boldsymbol{\sigma} = \boldsymbol{b}, \tag{2.11}$$

$$J^{-1}\frac{\partial \boldsymbol{F}}{\partial t} - \text{div}\big(\boldsymbol{v} \otimes \boldsymbol{H}^{-1}\big) = \boldsymbol{0}, \tag{2.12}$$

$$J^{-1}\frac{\partial \boldsymbol{H}}{\partial t} - \text{div}\left(\boldsymbol{F} \boldsymbol{\times} \left(\boldsymbol{v} \otimes \boldsymbol{H}^{-1}\right)\right) = \boldsymbol{0} \tag{2.13}$$

$$J^{-1}\frac{\partial J}{\partial t} - \text{div}\boldsymbol{v} = 0, \tag{2.14}$$

where the involutions $\text{curl}\boldsymbol{F}^{-1} = \boldsymbol{0}$ and $\text{div}\boldsymbol{H}^{-1} = \boldsymbol{0}$ are satisfied, with div and curl representing the spatial divergence and curl operators carried out with respect to the spatial configuration, $\boldsymbol{b} = J^{-1}\boldsymbol{b}_0$ is the body force per unit of current volume and $\boldsymbol{\sigma}$ is the Cauchy stress tensor.

Following the idea of having an updated reference Lagrangian scheme from [24], a new approach is proposed in this work, where the set of first order conservation laws for $[\boldsymbol{p}, \boldsymbol{F}, \boldsymbol{H}, J]$ is now expressed in terms of the intermediate configuration $\Omega_{V\boldsymbol{\chi}}$ (see figure 2.1) as

$$J_{\boldsymbol{\chi}}^{-1}\frac{\partial \boldsymbol{\mathcal{U}}}{\partial t} + \sum_{i=1}^{3} \frac{\partial \left(\boldsymbol{\mathcal{F}}\boldsymbol{H}_{\boldsymbol{\chi}}^{-1}\right)_i}{\partial \chi_i} = J_{\boldsymbol{\chi}}^{-1}\boldsymbol{\mathcal{S}}, \qquad \text{in} \quad \Omega_{V\boldsymbol{\chi}}, \tag{2.15}$$

resulting in

$$J_{\boldsymbol{\chi}}^{-1}\frac{\partial \boldsymbol{p}}{\partial t} - \text{div}_{\boldsymbol{\chi}}\left(\boldsymbol{P}\boldsymbol{H}_{\boldsymbol{\chi}}^{-1}\right) = J_{\boldsymbol{\chi}}^{-1}\boldsymbol{b}_0, \tag{2.16}$$

$$J_{\boldsymbol{\chi}}^{-1}\frac{\partial \boldsymbol{F}}{\partial t} - \text{div}_{\boldsymbol{\chi}}\big(\boldsymbol{v} \otimes \boldsymbol{H}_{\boldsymbol{\chi}}^{-1}\big) = \boldsymbol{0}, \tag{2.17}$$

$$J_{\boldsymbol{\chi}}^{-1}\frac{\partial \boldsymbol{H}}{\partial t} - \text{div}_{\boldsymbol{\chi}}\left(\boldsymbol{F} \boldsymbol{\times} \left(\boldsymbol{v} \otimes \boldsymbol{H}_{\boldsymbol{\chi}}^{-1}\right)\right) = \boldsymbol{0}, \tag{2.18}$$

$$J_{\boldsymbol{\chi}}^{-1}\frac{\partial J}{\partial t} - \text{div}_{\boldsymbol{\chi}}\left(\boldsymbol{H}_{\boldsymbol{\chi}}^{-T}\boldsymbol{H}^{T}\boldsymbol{v}\right) = 0, \tag{2.19}$$

where the involutions $\text{curl}_{\boldsymbol{\chi}}\left(\boldsymbol{F}\boldsymbol{F}_{\boldsymbol{\chi}}^{-1}\right) = \boldsymbol{0}$ and $\text{div}_{\boldsymbol{\chi}}\left(\boldsymbol{H}\boldsymbol{H}_{\boldsymbol{\chi}}^{-1}\right) = \boldsymbol{0}$ are satisfied, with $\text{div}_{\boldsymbol{\chi}}$ and $\text{curl}_{\boldsymbol{\chi}}$ representing the divergence and curl operators carried out with respect to the intermediate (updated) configuration.

The above equation 2.16 represents the conservation of linear momentum, whilst the rest of the system equations 2.17-2.19 represent a supplementary set of equations for the geometric strain measures $[\boldsymbol{F}, \boldsymbol{H}, J]$. Notice however that the fluxes in the above equations are highly nonlinear and the use of the multiplicative decompositions $\boldsymbol{F} := \boldsymbol{f}\boldsymbol{F}_{\boldsymbol{\chi}}$, $\boldsymbol{H} := \boldsymbol{h}\boldsymbol{H}_{\boldsymbol{\chi}}$ and $J := jJ_{\boldsymbol{\chi}}$ enables equations (2.16-2.19) to be rewritten as

$$\frac{\partial \boldsymbol{p}_{\boldsymbol{\chi}}}{\partial t} - \text{div}_{\boldsymbol{\chi}}\boldsymbol{\sigma}_{\boldsymbol{\chi}} = \boldsymbol{b}_{\boldsymbol{\chi}}, \tag{2.20}$$

$$\frac{\partial \boldsymbol{f}}{\partial t} - \text{div}_{\boldsymbol{\chi}}\left(\boldsymbol{v} \otimes \boldsymbol{I}\right) = \boldsymbol{0}, \tag{2.21}$$

$$\frac{\partial \boldsymbol{h}}{\partial t} - \text{curl}_{\boldsymbol{\chi}}\left(\boldsymbol{v} \times \boldsymbol{f}\right) = \boldsymbol{0}, \tag{2.22}$$

$$\frac{\partial j}{\partial t} - \text{div}_{\boldsymbol{\chi}}\left(\boldsymbol{h}^T\boldsymbol{v}\right) = 0, \tag{2.23}$$

where $\boldsymbol{b}_{\boldsymbol{\chi}} = J_{\boldsymbol{\chi}}^{-1}\boldsymbol{b}_0 = j\boldsymbol{b}$ is the body force per unit of intermediate volume, $\boldsymbol{p}_{\boldsymbol{\chi}} = J_{\boldsymbol{\chi}}^{-1}\boldsymbol{p} = J_{\boldsymbol{\chi}}^{-1}\rho_0\boldsymbol{v} = \rho_{\boldsymbol{\chi}}\boldsymbol{v} = j\rho\boldsymbol{v}$ is the linear momentum per unit of intermediate volume[3] and the stress tensor $\boldsymbol{\sigma}_{\boldsymbol{\chi}} = J_{\boldsymbol{\chi}}^{-1}\boldsymbol{P}\boldsymbol{F}_{\boldsymbol{\chi}}^T$ can alternatively be seen as[4] $\boldsymbol{\sigma}_{\boldsymbol{\chi}} = \boldsymbol{P}\boldsymbol{H}_{\boldsymbol{\chi}}^{-1} = \boldsymbol{P}\boldsymbol{H}^{-1}\boldsymbol{h} = \boldsymbol{\sigma}\boldsymbol{h}$.

The system of equations (2.20-2.23) can be summarised in a concise manner as

$$\frac{\partial \boldsymbol{\mathcal{U}}_{\boldsymbol{\chi}}}{\partial t} + \sum_{i=1}^{3}\frac{\partial \boldsymbol{\mathcal{F}}_{\boldsymbol{\chi}}^i}{\partial \chi_i} = \boldsymbol{\mathcal{S}}_{\boldsymbol{\chi}}, \tag{2.24}$$

where

$$\boldsymbol{\mathcal{U}}_{\boldsymbol{\chi}} = \begin{bmatrix} \boldsymbol{p}_{\boldsymbol{\chi}} \\ \boldsymbol{f} \\ \boldsymbol{h} \\ j \end{bmatrix}, \quad \boldsymbol{\mathcal{F}}_{\boldsymbol{\chi}}^i = -\begin{bmatrix} \boldsymbol{\sigma}_{\boldsymbol{\chi}}\boldsymbol{e}_i \\ \boldsymbol{v} \otimes \boldsymbol{e}_i \\ \boldsymbol{f} \times (\boldsymbol{v} \otimes \boldsymbol{e}_i) \\ \boldsymbol{h} : (\boldsymbol{v} \otimes \boldsymbol{e}_i) \end{bmatrix}, \quad \boldsymbol{\mathcal{S}}_{\boldsymbol{\chi}} = \begin{bmatrix} \boldsymbol{b}_{\boldsymbol{\chi}} \\ \boldsymbol{0} \\ \boldsymbol{0} \\ 0 \end{bmatrix}, \tag{2.25}$$

with $\boldsymbol{e}_i :=$ $i$th unit vector of the Cartesian basis.

Further simplification can be achieved by imposing satisfaction of the involutions $\text{curl}_{\boldsymbol{\chi}}\boldsymbol{f} = \boldsymbol{0}$ and $\text{div}_{\boldsymbol{\chi}}\boldsymbol{h} = \boldsymbol{0}$ on equations 2.22 and 2.23 to give

---

[3] Note that

$$\rho_0 = J\rho = J_{\boldsymbol{\chi}}\rho_{\boldsymbol{\chi}} \rightarrow \rho_{\boldsymbol{\chi}} = J_{\boldsymbol{\chi}}^{-1}\rho_0 = JJ_{\boldsymbol{\chi}}^{-1}\rho = j\rho.$$

[4] Refer to Appendix B for the definitions of the first Piola-Kirchhoff ($\boldsymbol{P}$) and the Cauchy ($\boldsymbol{\sigma}$) stress tensors, as well as the relationship between them.

$$\frac{\partial \boldsymbol{p}_{\boldsymbol{\chi}}}{\partial t} = \mathrm{div}_{\boldsymbol{\chi}} \boldsymbol{\sigma}_{\boldsymbol{\chi}} + \boldsymbol{b}_{\boldsymbol{\chi}}, \tag{2.26}$$

$$\frac{\partial \boldsymbol{f}}{\partial t} = \boldsymbol{\nabla}_{\boldsymbol{\chi}} \boldsymbol{v}, \tag{2.27}$$

$$\frac{\partial \boldsymbol{h}}{\partial t} = \boldsymbol{f} \boldsymbol{\times} \boldsymbol{\nabla}_{\boldsymbol{\chi}} \boldsymbol{v}, \tag{2.28}$$

$$\frac{\partial j}{\partial t} = \boldsymbol{h} \colon \boldsymbol{\nabla}_{\boldsymbol{\chi}} \boldsymbol{v}, \tag{2.29}$$

where $\boldsymbol{\nabla}_{\boldsymbol{\chi}}$ represents the gradient with respect to $\boldsymbol{\chi}$, carried out in the intermediate (updated) configuration.

## 2.3 Constitutive models

The closure of the system of equations requires the introduction of a suitable constitutive law relating the stress tensor $\boldsymbol{\sigma}_{\boldsymbol{\chi}}$ to the incremental strain measures $[\boldsymbol{f}, \boldsymbol{h}, j]$. In classic continuum mechanics a strain energy $\Psi\left(\boldsymbol{\nabla}_{\boldsymbol{X}} \boldsymbol{\phi}\right)$ is defined so that it is possible to express the virtual internal work as

$$D\Psi\left(\boldsymbol{\nabla}_{\boldsymbol{X}} \boldsymbol{\phi}\right)[\delta \boldsymbol{v}] = \frac{\partial \Psi}{\partial \boldsymbol{\nabla}_{\boldsymbol{X}} \boldsymbol{\phi}} \colon D\boldsymbol{\nabla}_{\boldsymbol{X}} \boldsymbol{x}\,[\delta \boldsymbol{v}], \tag{2.30a}$$

$$= \frac{\partial \Psi}{\partial \boldsymbol{\nabla}_{\boldsymbol{X}} \boldsymbol{x}} \colon \boldsymbol{\nabla}_{\boldsymbol{X}} \delta \boldsymbol{v}, \tag{2.30b}$$

$$= \boldsymbol{P} \colon \boldsymbol{\nabla}_{\boldsymbol{X}} \delta \boldsymbol{v}. \tag{2.30c}$$

In a mixed-based Total Lagrangian Formulation, a multi-variable strain energy $\Psi_{\boldsymbol{X}}\left(\boldsymbol{F}, \boldsymbol{H}, J\right)$ is defined and the virtual internal work is expressed in a similar way as

$$D\Psi_{\boldsymbol{X}}\left(\boldsymbol{F}, \boldsymbol{H}, J\right)[\delta \boldsymbol{v}] = \frac{\partial \Psi_{\boldsymbol{X}}}{\partial \boldsymbol{F}} \colon D\boldsymbol{F}\,[\delta \boldsymbol{v}] + \frac{\partial \Psi_{\boldsymbol{X}}}{\partial \boldsymbol{H}} \colon D\boldsymbol{H}\,[\delta \boldsymbol{v}] + \frac{\partial \Psi_{\boldsymbol{X}}}{\partial J} DJ\,[\delta \boldsymbol{v}], \tag{2.31a}$$

$$= \frac{\partial \Psi_{\boldsymbol{X}}}{\partial \boldsymbol{F}} \colon \boldsymbol{\nabla}_{\boldsymbol{X}} \delta \boldsymbol{v} + \frac{\partial \Psi_{\boldsymbol{X}}}{\partial \boldsymbol{H}} \colon \left(\boldsymbol{F} \boldsymbol{\times} \boldsymbol{\nabla}_{\boldsymbol{X}} \delta \boldsymbol{v}\right) + \frac{\partial \Psi_{\boldsymbol{X}}}{\partial J} \left(\boldsymbol{H} \colon \boldsymbol{\nabla}_{\boldsymbol{X}} \delta \boldsymbol{v}\right), \tag{2.31b}$$

$$= \left(\frac{\partial \Psi_{\boldsymbol{X}}}{\partial \boldsymbol{F}} + \frac{\partial \Psi_{\boldsymbol{X}}}{\partial \boldsymbol{H}} \boldsymbol{\times} \boldsymbol{F} + \frac{\partial \Psi_{\boldsymbol{X}}}{\partial J} \boldsymbol{H}\right) \colon \boldsymbol{\nabla}_{\boldsymbol{X}} \delta \boldsymbol{v}, \tag{2.31c}$$

$$= \underbrace{\left(\boldsymbol{\Sigma}_{\boldsymbol{F}} + \boldsymbol{\Sigma}_{\boldsymbol{H}} \boldsymbol{\times} \boldsymbol{F} + \Sigma_J \boldsymbol{H}\right)}_{\boldsymbol{P}} \colon \boldsymbol{\nabla}_{\boldsymbol{X}} \delta \boldsymbol{v}, \tag{2.31d}$$

where

$$\boldsymbol{\Sigma}_{\boldsymbol{F}} := \frac{\partial \Psi_{\boldsymbol{X}}}{\partial \boldsymbol{F}}, \qquad \boldsymbol{\Sigma}_{\boldsymbol{H}} := \frac{\partial \Psi_{\boldsymbol{X}}}{\partial \boldsymbol{H}} \quad \text{and} \quad \Sigma_J := \frac{\partial \Psi_{\boldsymbol{X}}}{\partial J}. \tag{2.32}$$

The derivation of the stress tensor in the updated reference Lagrangian formulation can be done by a push-forward of the first Piola-Kirchhoff stress tensor, that is

$$J_{\chi}\boldsymbol{\sigma}_{\chi} = \boldsymbol{P}\boldsymbol{F}_{\chi}^{T}. \tag{2.33}$$

Substituting the definition of $\boldsymbol{P}$ given in equation 2.31d into equation 2.33

$$J_{\chi}\boldsymbol{\sigma}_{\chi} = \boldsymbol{\Sigma_F}\boldsymbol{F}_{\chi}^{T} + (\boldsymbol{\Sigma_H} \times \boldsymbol{F})\,\boldsymbol{F}_{\chi}^{T} + \Sigma_J\boldsymbol{H}\boldsymbol{F}_{\chi}^{T}, \tag{2.34}$$

and performing further operations, taking into account the multiplicative decomposition, leads to

$$\boldsymbol{\sigma}_{\chi} = J_{\chi}^{-1}\boldsymbol{\Sigma_F}\boldsymbol{F}_{\chi}^{T} + J_{\chi}^{-1}\boldsymbol{\Sigma_H}\boldsymbol{H}_{\chi}^{T} \times \boldsymbol{f} + \Sigma_J\boldsymbol{h}, \tag{2.35a}$$

$$= \boldsymbol{\Sigma_f} + \boldsymbol{\Sigma_h} \times \boldsymbol{f} + \Sigma_j\boldsymbol{h}, \tag{2.35b}$$

where

$$\boldsymbol{\Sigma_f} = J_{\chi}^{-1}\boldsymbol{\Sigma_F}\boldsymbol{F}_{\chi}^{T}, \qquad \boldsymbol{\Sigma_h} = J_{\chi}^{-1}\boldsymbol{\Sigma_H}\boldsymbol{H}_{\chi}^{T} \quad \text{and} \quad \Sigma_j = \Sigma_J. \tag{2.36}$$

### 2.3.1 Nearly incompressible neo-Hookean material

For the particular case of a nearly incompressible neo-Hookean material, the multi-variable strain energy $\Psi_{\boldsymbol{X}}(\boldsymbol{F}, \boldsymbol{H}, J)$ can be decomposed into the summation of deviatoric $\hat{\Psi}_{\boldsymbol{X}}$ and volumetric $U$ contributions as [74]

$$\Psi_{\boldsymbol{X}} = \hat{\Psi}_{\boldsymbol{X}}(\boldsymbol{F}, J) + U(J), \tag{2.37}$$

where

$$\hat{\Psi}_{\boldsymbol{X}} = \frac{\mu}{2}\left[J^{-2/3}(\boldsymbol{F} : \boldsymbol{F}) - 3\right], \tag{2.38}$$

and

$$U = \frac{\kappa}{2}(J-1)^2, \tag{2.39}$$

with the shear modulus $\mu$ and the bulk modulus $\kappa$ given in terms of the Young's modulus $E$ and Poisson's ratio $\nu$ as $\mu = \frac{E}{2(1+\nu)}$ and $\kappa = \frac{E}{3(1-2\nu)}$, respectively.

The conjugate stresses $\boldsymbol{\Sigma_F}$ and $\Sigma_J$ with respect to $\boldsymbol{F}$ and $J$ are then given as

$$\boldsymbol{\Sigma_F} = \mu J^{-2/3}\boldsymbol{F}, \tag{2.40}$$

and

$$\Sigma_J = \hat{\Sigma}_J + p, \tag{2.41}$$

with

$$\hat{\Sigma}_J := \frac{\partial\hat{\Psi}_{\boldsymbol{X}}}{\partial J} = -\frac{\mu}{3}J^{-5/3}(\boldsymbol{F} : \boldsymbol{F}), \qquad p := \frac{\partial U}{\partial J} = \kappa(J-1). \tag{2.42}$$

Note that for a nearly incompressible neo-Hookean material the conjugate stress $\boldsymbol{\Sigma_H} := \frac{\partial\hat{\Psi}_{\boldsymbol{X}}}{\partial\boldsymbol{H}}$ results null. Therefore, using equations 2.40 and 2.42, the first Piola-Kirchhoff stress tensor is given by

$$\boldsymbol{P}(\boldsymbol{F}, \boldsymbol{H}, J) = \boldsymbol{\Sigma_F} + \Sigma_J\boldsymbol{H}, \tag{2.43}$$

from which $\boldsymbol{\sigma}_{\chi}$ can be obtained.

### 2.3.2 Rate-independent Hencky model with von Mises plasticity

An isothermal rate-independent von Mises plasticity model with isotropic hardening is now presented. For this material model, the deformation gradient can be decomposed into elastic and plastic components $\boldsymbol{F} = \boldsymbol{F}_e\boldsymbol{F}_p$, where the elastic left strain tensor is defined as $\boldsymbol{b}_e = \boldsymbol{F}\boldsymbol{C}_p^{-1}\boldsymbol{F}^T$ and the plastic right Cauchy Green tensor as $\boldsymbol{C}_p = \boldsymbol{F}_p^T\boldsymbol{F}_p$. In the same way as equation 2.37, the strain energy functional can be decomposed in deviatoric and volumetric contributions, which are defined in terms of the elastic principal stretches as

$$\hat{\Psi} = \mu\left[(\ln\lambda_{e,1})^2 + (\ln\lambda_{e,2})^2 + (\ln\lambda_{e,3})^2\right] - \frac{\mu}{3}(\ln J)^2\,, \tag{2.44}$$

and

$$U = \frac{\kappa}{2}(\ln J)^2\,, \qquad \ln J = \sum_{\alpha}^{3}\ln\lambda_{e,\alpha}. \tag{2.45}$$

The yield surface is defined as a function of the Kirchhoff stress tensor $\boldsymbol{\tau}$, a yield stress $\bar{\tau}_y$ and a hardening variable $\bar{\epsilon}_p$. The pressure $p$ (mean stress) is computed as a function of the volume map $J$ and the bulk modulus of the material $\kappa$, as

$$p = \left(\frac{\kappa\ln J}{J}\right). \tag{2.46}$$

From the plastic right Cauchy-Green tensor $\boldsymbol{C}_p$, a trial left elastic Cauchy-Green tensor can be computed as

$$\boldsymbol{b}_e^{\text{trial}} = \boldsymbol{F}\boldsymbol{C}_p^{-1}\boldsymbol{F}^T, \tag{2.47}$$

and performing the spectral decomposition of $\boldsymbol{b}_e^{\text{trial}}$, the trial stretches and principal directions are obtained

$$\boldsymbol{b}_e^{\text{trial}} = \sum_{\alpha}^{3}\left(\lambda_{e,\alpha}^{\text{trial}}\right)^2\left(\boldsymbol{n}_\alpha^{\text{trial}}\otimes\boldsymbol{n}_\alpha^{\text{trial}}\right). \tag{2.48}$$

The components of a trial deviatoric Kirchhoff stress tensor are now expressed as

$$\tau_{\alpha\alpha}'^{\text{trial}} = 2\mu\ln\lambda_{e,\alpha}^{\text{trial}} - \frac{2}{3}\mu\ln J \tag{2.49}$$

The check for yielding is done by verifying that the yield function is less than or equal to zero, that is

$$f\left(\boldsymbol{\tau}^{\text{trial}},\bar{\epsilon}_p\right) \leq 0, \tag{2.50}$$

for the von Mises model presented here

$$f\left(\boldsymbol{\tau}^{\text{trial}},\bar{\epsilon}_p\right) = \sqrt{\frac{3}{2}\left(\boldsymbol{\tau}'^{\text{trial}} : \boldsymbol{\tau}'^{\text{trial}}\right)} - \bar{\tau}_y \leq 0, \tag{2.51}$$

where, assuming the hypothesis of linear hardening, $\bar{\tau}_y$ is given by:

$$\bar{\tau}_y = \tau_y^0 + H\bar{\epsilon}_p, \tag{2.52}$$

with $\tau_y^0$ being the initial yield stress of the material and $H$ being the hardening modulus.

For the case in which $f > 0$, a radial return mapping approach is followed. It starts with the computation of the direction vector $\upsilon_\alpha$

$$\upsilon_\alpha = \frac{\tau'^{\,\mathrm{trial}}_{\alpha\alpha}}{\sqrt{\frac{2}{3}}\|\boldsymbol{\tau}^{\mathrm{trial}}\|}, \tag{2.53}$$

and then the incremental plastic multiplier $\Delta_\gamma$

$$\Delta_\gamma = \frac{f\left(\boldsymbol{\tau}^{\mathrm{trial}}, \bar{\epsilon}_p\right)}{3\mu + H}. \tag{2.54}$$

If no yielding is observed, the incremental plastic multiplier is null $\Delta_\gamma = 0$.

The computation of logarithmic elastic stretches is possible with

$$\ln \lambda_{e,\alpha} = \ln \lambda_{e,\alpha}^{\mathrm{trial}} - \Delta_\gamma \upsilon_\alpha, \tag{2.55}$$

and the current deviatoric Kirchhoff stresses are obtained by

$$\tau'_{\alpha\alpha} = \left(1 - \frac{2\mu\Delta_\gamma}{\sqrt{2/3}\|\boldsymbol{\tau}'^{\,\mathrm{trial}}\|}\right)\tau'^{\mathrm{trial}}_{\alpha\alpha}. \tag{2.56}$$

The elastic left Cauchy-Green tensor can be updated by

$$\boldsymbol{b}_e = \sum_{\alpha=1}^{3} \left(\lambda_{e,\alpha}\right)^2 \boldsymbol{n}_\alpha \otimes \boldsymbol{n}_\alpha, \tag{2.57}$$

with $\boldsymbol{n}_\alpha = \boldsymbol{n}_\alpha^{\mathrm{trial}}$.

The principal Kirchhoff stresses, obtained as

$$\tau_{\alpha\alpha} = \tau'_{\alpha\alpha} + Jp, \tag{2.58}$$

allow the computation of the updated Kirchhoff stress tensor as

$$\boldsymbol{\tau} = \sum_{\alpha=1}^{3} \tau_{\alpha\alpha} \boldsymbol{n}_\alpha \otimes \boldsymbol{n}_\alpha. \tag{2.59}$$

The first Piola-Kirchhoff stress tensor is then obtained as $\boldsymbol{P} = \boldsymbol{\tau}\boldsymbol{F}^{-T}$, from which $\boldsymbol{\sigma}_{\boldsymbol{\chi}}$ can be obtained as shown in the previous section.

The final step is to update the plastic right Cauchy-Green tensor

$$\boldsymbol{C}_p^{-1} = \boldsymbol{F}^{-1}\boldsymbol{b}_e\boldsymbol{F}^{-T}, \tag{2.60}$$

and the equivalent plastic strain

$$\bar{\epsilon}_p = \bar{\epsilon}_p + \Delta_\gamma. \tag{2.61}$$

The plastic dissipation per unit of initial volume $w_p$ can be computed as

$$w_p = \sigma_v \Delta_\gamma, \tag{2.62}$$

where $\sigma_v$ is the von Mises equivalent stress given as $\sigma_v = \sqrt{\frac{3}{2}\left(\boldsymbol{\tau}'\colon \boldsymbol{\tau}'\right)}$.

An algorithmic representation of the principal direction formulation for the Hencky model with von Mises plasticity with linear hardening described above is given in algorithm 1.

Alternatively, an isotropic nonlinear hardening model can be obtained, for instance, rewriting equation 2.52 as

$$\bar{\tau}_y = \left(\tau_y^{\infty} - \tau_y^{0}\right)\left[1 - e^{(-\delta\bar{\epsilon}_p)}\right] + H\bar{\epsilon}_p, \tag{2.63}$$

with $\tau_y^{\infty}$ being the residual yield stress and $\delta$ the saturation exponent, parameters that need to be calibrated using experimental test data (see e.g. [75]).

Notice however, that for the nonlinear hardening case, the incremental plastic multiplier $\Delta_\gamma$ needs to be obtained iteratively, for example using the Newton-Raphson method, with the following expression

$$\Delta_\gamma^{k+1} = \Delta_\gamma^{k} - \frac{T - F}{3\mu + H + \left(\tau_y^{\infty} - \tau_y^{0}\right)\delta e^{-\delta\left(\bar{\epsilon}_p^{n} + \Delta_\gamma^{k}\right)}}, \tag{2.64}$$

where

$$T = 3\mu\Delta_\gamma^{k} + \bar{\tau}_y\left(\bar{\epsilon}_p^{n} + \Delta_\gamma^{k}\right), \tag{2.65}$$

and

$$F = f_{n+1}^{\text{trial}} + \bar{\tau}_y\left(\bar{\epsilon}_p^{n}\right). \tag{2.66}$$

The Newton-Raphson method described above is illustrated in algorithm 2.

## 2.4 Conclusion

This chapter introduced the mixed-based system of conservation laws employed to describe the motion of solid bodies in an isothermal context. The system of equations was presented in terms of different configurations, i.e., total Lagrangian, updated Lagrangian and the new updated reference Lagrangian formulations. The chapter serves therefore to clarify these concepts and also to explore the aspects of mixed-based formulations. The introduction of the multiplicative decomposition of the deformation process was key in obtaining a system of equations that shares the versatility of the updated Lagrangian formulation while still maintaining the simplicity of the Total Lagrangian formulation. Finally, a stress tensor suitable for the new formulation was derived and constitutive models in elasticity and elasto-plasticity were presented.

**Algorithm 1:** Principal Direction formulation for Hencky model with von Mises plasticity with linear hardening

```
Input  : $\boldsymbol{F}^{n+1}, \boldsymbol{H}^{n+1}, J^{n+1}, \left[\boldsymbol{C}_p^{-1}\right]^n, \bar{\epsilon}_p^n$
Output: $\boldsymbol{P}^{n+1}, \left[\boldsymbol{C}_p^{-1}\right]^{n+1}, \bar{\epsilon}_p^{n+1}$

(1) Evaluate pressure: $p^{n+1} = \kappa \frac{\ln J^{n+1}}{J^{n+1}}$
(2) Compute trial elastic left strain tensor: $\boldsymbol{b}_e^{\text{trial}} = \boldsymbol{F}^{n+1}\left[\boldsymbol{C}_p^{-1}\right]^n\left[\boldsymbol{F}^T\right]^{n+1}$
(3) Spectral decomposition of $\boldsymbol{b}_e^{\text{trial}}$: $\boldsymbol{b}_e^{\text{trial}} = \sum_{\alpha=1}^{3}\left(\lambda_{e,\alpha}^{\text{trial}}\right)^2\left(\boldsymbol{n}_\alpha^{n+1} \otimes \boldsymbol{n}_\alpha^{n+1}\right)$
(4) Obtain trial deviatoric Kirchoff stress tensor:
    $\tau'^{\,\text{trial}}_{\alpha\alpha} = 2\mu \ln \lambda_{e,\alpha}^{\text{trial}} - \frac{2}{3}\mu \ln J^{n+1}$
(5) Obtain yield criterion: $f\left(\tau'^{\,\text{trial}}_{\alpha\alpha}, \bar{\epsilon}_p^n\right) = \left[\frac{3}{2}\sum_{\beta=1}^{3}\left(\tau'^{\,\text{trial}}_{\beta\beta}\right)^2\right]^{1/2} - \bar{\tau}_y^n$;
    $\bar{\tau}_y^n = \tau_y^0 + H\bar{\epsilon}_p^n$
(6) Compute direction vector and plastic multiplier:
    if $f\left(\tau'^{\,trial}_{\alpha\alpha}, \bar{\epsilon}_p^n\right) > 0$ then
        Direction vector: $\upsilon_\alpha^{n+1} = \frac{\tau'^{\,\text{trial}}_{\alpha\alpha}}{\left[\frac{2}{3}\sum_{\beta=1}^{3}\left(\tau'^{\,\text{trial}}_{\beta\beta}\right)^2\right]^{1/2}}$
        Plastic multiplier: $\Delta\gamma = \frac{f\left(\tau'^{\,\text{trial}}_{\alpha\alpha}, \bar{\epsilon}_p^n\right)}{3\mu + H}$
    else
        $\upsilon_\alpha^{n+1} = \Delta_\gamma = 0$
    end
(7) Update deviatoric Kirchoff stresss tensor:
    $\boldsymbol{\tau}'^{\,n+1} = \tau'^{\,n+1}_{\alpha\alpha}\boldsymbol{n}^{n+1} \otimes \boldsymbol{n}^{n+1}$;    $\tau'^{\,n+1}_{\alpha\alpha} = \tau'^{\,\text{trial}}_{\alpha\alpha} - 2\mu\Delta_\gamma \upsilon_\alpha^{n+1}$
(8) Evaluate first Piola Kirchoff stress tensor:
    $\boldsymbol{P}^{n+1} = \boldsymbol{\tau}'^{\,n+1}\left[\boldsymbol{F}^{-T}\right]^{n+1} + p^{n+1}\boldsymbol{H}^{n+1}$
(9) Update elastic left Cauchy strain tensor:
    $\boldsymbol{b}_e^{n+1} = \sum_{\alpha=1}^{3}\left(\lambda_{e,\alpha}^{n+1}\right)^2\left(\boldsymbol{n}_\alpha^{n+1} \otimes \boldsymbol{n}_\alpha^{n+1}\right)$;    $\ln \lambda_{e,\alpha}^{n+1} = \ln \lambda_{e,\alpha}^{\text{trial}} - \Delta_\gamma \upsilon_\alpha^{n+1}$
(10) Compute plastic right Cauchy Green tensor:
    $\left[\boldsymbol{C}_p^{-1}\right]^{n+1} = \left[\boldsymbol{F}^{-1}\right]^{n+1}\boldsymbol{b}_e^{n+1}\left[\boldsymbol{F}^{-T}\right]^{n+1}$
(11) Update plastic strain: $\bar{\epsilon}_p^{n+1} = \bar{\epsilon}_p^n + \Delta_\gamma$
```

**Algorithm 2:** Newton-Raphson iteration for the evaluation of nonlinear hardening

```
Input   :
Output:
(1) Compute constant value $F$
(2) Assume $\Delta_\gamma = \frac{f\left(\tau'^{\,\text{trial}}_{\alpha\alpha}, \bar{\epsilon}^n_p\right)}{3\mu+H}$
(3) Assign $TOL = 1e^{-6}$ and $Err = 2 \times TOL$
while $Err \geq TOL$ do
    (4) Evaluate $T(\Delta_\gamma)$
    (5) Evaluate $\mathrm{R} = -\frac{T-F}{3\mu+H+(\tau_\infty-\tau^0_y)\delta e^{-\delta(\bar{\epsilon}^n_p+\Delta_\gamma)}}$
    (6) $\Delta_\gamma = \Delta_\gamma + \mathrm{R}$
    (7) $Err = |\mathrm{R}|$
end
```

# Chapter 3

# Thermo-mechanics

## 3.1 Introduction

In this chapter the formulation presented in chapter 2 is extended to the context of thermo-mechanics. The aim is to further extend the work to account for possible strongly thermally-coupled scenarios, through the consideration of constitutive models in both thermo-elasticity and thermo-plasticity. For this purpose, the system of first order conservation laws previously presented is now supplemented with the first law of thermodynamics, written in terms of the total energy $E_{\boldsymbol{\chi}}$, which is solved along with the set of equations for $\{\boldsymbol{p}_{\boldsymbol{\chi}}, \boldsymbol{f}, \boldsymbol{h}, j\}$.

## 3.2 First law of thermodynamics

In order to consider thermal effects, the first law of thermodynamics, written in terms of the total energy of the system $E$, needs to be solved in addition to the conservation of linear momentum and the geometric conservation laws. In a TLF approach, as presented in [76], the equation is given as

$$\frac{\partial E}{\partial t} - \mathrm{DIV}\left(\boldsymbol{P}^T\boldsymbol{v} - \boldsymbol{Q}\right) = \boldsymbol{b}_0 \cdot \boldsymbol{v} + s_0, \tag{3.1}$$

where $E$ is the total energy per unit of undeformed volume, $\boldsymbol{P}$ represents the first Piola-Kirchhoff stress tensor, $\boldsymbol{Q}$ represents the Lagrangian heat flux vector, $s_0$ denotes a possible heat source term, $\boldsymbol{b}_0$ is the body force per unit of initial volume and $\boldsymbol{v} = \rho_0^{-1}\boldsymbol{p}$ is the velocity.

In the present work, the conservation laws are expressed in terms of the intermediate configuration, and the same process of transformation (refer to Appendix C for a detailed derivation) is followed for equation 3.1, leading to

$$\frac{\partial E_{\boldsymbol{\chi}}}{\partial t} - \mathrm{div}_{\boldsymbol{\chi}}\left(\boldsymbol{\sigma}_{\boldsymbol{\chi}}^T\boldsymbol{v} - \boldsymbol{Q}_{\boldsymbol{\chi}}\right) = \boldsymbol{b}_{\boldsymbol{\chi}} \cdot \boldsymbol{v} + s_{\boldsymbol{\chi}}, \tag{3.2}$$

where $E_{\boldsymbol{\chi}}$ is the total energy per unit of intermediate volume, the stress tensor $\boldsymbol{\sigma}_{\boldsymbol{\chi}} = J_{\boldsymbol{\chi}}^{-1}\boldsymbol{P}\boldsymbol{F}_{\boldsymbol{\chi}}^T$, $s_{\boldsymbol{\chi}}$ denotes a possible heat source term, $\boldsymbol{b}_{\boldsymbol{\chi}}$ is the body force per unit of intermediate volume, $\boldsymbol{v} = \rho_{\boldsymbol{\chi}}^{-1}\boldsymbol{p}_{\boldsymbol{\chi}}$ is the velocity and $\boldsymbol{Q}_{\boldsymbol{\chi}}$ represents the heat flux vector in the intermediate configuration, given as

$$\boldsymbol{Q}_{\boldsymbol{\chi}} = -\boldsymbol{K}_{\boldsymbol{\chi}}\boldsymbol{\nabla}_{\boldsymbol{\chi}}\theta, \qquad \boldsymbol{K}_{\boldsymbol{\chi}} = j^{-1}k\boldsymbol{h}^T\boldsymbol{h}, \tag{3.3}$$

with $k$ being the thermal conductivity of the material.

In general, the Calorimetry relationships between internal energy $E$, temperature $\theta$ and entropy $\eta$ can be derived from the definition of the specific heat at constant volume $c_v$

$$c_v = \frac{\partial \tilde{\mathcal{E}}\left(\boldsymbol{\mathcal{X}}_\theta\right)}{\partial \theta}, \tag{3.4}$$

with $c_v = \rho_R C_v > 0$, where $\rho_R$ is the density measured at the reference temperature $\theta_R$ and $C_v$ the specific heat per unit mass. The internal energy density $\tilde{\mathcal{E}}\left(\boldsymbol{\mathcal{X}}_\theta\right)$ is defined in terms of the triplet of deformation and the temperature, i.e., $\boldsymbol{\mathcal{X}}_\theta = [\boldsymbol{\mathcal{X}}, \theta] = [\boldsymbol{F}, \boldsymbol{H}, J, \theta]$.

Integration of equation 3.4 with respect to temperature between the limits $\theta_R$ and a given value $\theta$ gives

$$\int_{\tilde{\mathcal{E}}_R(\boldsymbol{\mathcal{X}})}^{\tilde{\mathcal{E}}(\boldsymbol{\mathcal{X}}_\theta)} d\mathcal{E} = c_v \int_{\theta_R}^{\theta} d\theta, \tag{3.5}$$

which yields

$$\tilde{\mathcal{E}}\left(\boldsymbol{\mathcal{X}}_\theta\right) = \tilde{\mathcal{E}}_R\left(\boldsymbol{\mathcal{X}}\right) + c_v\left(\theta - \theta_R\right), \tag{3.6}$$

where $\tilde{\mathcal{E}}_R\left(\boldsymbol{\mathcal{X}}\right)$ represents the energy per unit of material volume caused by the deformation after the temperature has been allowed to return back to the reference value $\theta_R$ and is computed according to the material model. Recall that the internal energy can be expressed as $\tilde{\mathcal{E}}\left(\boldsymbol{\mathcal{X}}_\theta\right) = E - \frac{\rho_0}{2}\boldsymbol{v}\cdot\boldsymbol{v}$ and therefore, the temperature update can be obtained re-arranging equation 3.6 as

$$\theta = \theta_R + \frac{1}{c_v}\left[E - \frac{\rho_0}{2}\boldsymbol{v}\cdot\boldsymbol{v} - \tilde{\mathcal{E}}_R\right], \tag{3.7a}$$

$$= \theta_R + \frac{1}{c_v}\left[J_{\boldsymbol{\chi}} E_{\boldsymbol{\chi}} - \frac{J_{\boldsymbol{\chi}}\rho_{\boldsymbol{\chi}}}{2}\boldsymbol{v}\cdot\boldsymbol{v} - \tilde{\mathcal{E}}_R\right]. \tag{3.7b}$$

**Remark 2** *Note that the internal energy can be expressed as a function of* $\boldsymbol{\mathcal{X}}_\eta = [\boldsymbol{\mathcal{X}}, \eta] = [\boldsymbol{F}, \boldsymbol{H}, J, \eta]$, *and given the fact that* $\theta = \frac{\partial \tilde{\mathcal{E}}(\boldsymbol{\mathcal{X}}_\eta)}{\partial \eta}$ *[76], using the chain rule in equation 3.4 yields*

$$\frac{c_v}{\theta} = \frac{\partial \tilde{\eta}\left(\boldsymbol{\mathcal{X}}_\theta\right)}{\partial \theta}, \tag{3.8}$$

*which can be integrated with respect to temperature changes as*

$$\int_{\tilde{\eta}_R(\boldsymbol{\mathcal{X}})}^{\tilde{\eta}(\boldsymbol{\mathcal{X}}_\theta)} d\eta = c_v \int_{\theta_R}^{\theta} \frac{1}{\theta} d\theta, \tag{3.9}$$

*leading to a relationship between entropy density and temperature*

$$\tilde{\eta}\left(\boldsymbol{\mathcal{X}}_\theta\right) = \tilde{\eta}_R\left(\boldsymbol{\mathcal{X}}\right) + c_v \ln\left(\frac{\theta}{\theta_R}\right), \tag{3.10}$$

*where* $\tilde{\eta}_R\left(\boldsymbol{\mathcal{X}}\right)$ *depends on the material model and denotes the entropy measured at reference temperature* $\theta_R$. *Clearly, a reverse relationship can also be derived from equation 3.10*

$$\theta = \theta_R \exp^{\frac{\tilde{\eta}-\tilde{\eta}_R}{c_v}}. \tag{3.11}$$

**Remark 3** *The reader interested in revisiting the second law of thermodynamics when written in terms of the ballistic free energy is referred to section 3.1 of [76].*

## 3.3 Constitutive models for thermal-stress analysis

In this work, the well-established thermo-elastic Mie-Grüneisen equation of state is used as presented in [76]. Using equations 3.6 and 3.11 derived in the previous section, the internal energy in a thermo-mechanical context can be expressed as

$$\tilde{\mathcal{E}} = \tilde{\mathcal{E}}_R + c_v\theta_R \left(\exp^{\frac{\tilde{\eta}-\tilde{\eta}_R}{c_v}} - 1\right), \tag{3.12}$$

where, assuming a Mie-Grüneisen model, the reference entropy is computed as

$$\tilde{\eta}_R = \frac{c_v\Gamma_0}{q}\left(J^q - 1\right), \tag{3.13}$$

where $q$ is a dimensionless coefficient that varies from zero (for a perfect gas) to one (for solid materials) and the material parameter $\Gamma_0$ can be calibrated against those of linear elasticity (shear modulus $\mu$, bulk modulus $\kappa$ and thermal expansion coefficient $\alpha$) as

$$\alpha = \frac{c_v\Gamma_0}{3\kappa}. \tag{3.14}$$

The deviatoric-volumetric expression for the internal energy density, at the reference temperature, considering the Mie-Grüneisen material is given as [76]

$$\tilde{\mathcal{E}}_R = \Psi_R + c_v\theta_R\Gamma_0\left(J - 1\right), \tag{3.15}$$

where $\Psi_R$ is defined according to the constitutive model.

The stress conjugates in a thermal context can be obtained from equation 3.12, similarly to the derivation developed in section 2.3 of chapter 2

$$\begin{aligned} &\boldsymbol{\Sigma}_{\boldsymbol{F}} := \frac{\partial\tilde{\mathcal{E}}}{\partial\boldsymbol{F}} = \frac{\partial\Psi_R}{\partial\boldsymbol{F}}, \qquad \boldsymbol{\Sigma}_{\boldsymbol{H}} := \frac{\partial\tilde{\mathcal{E}}}{\partial\boldsymbol{H}} = \frac{\partial\Psi_R}{\partial\boldsymbol{H}} \quad \text{and} \\ &\Sigma_J := \frac{\partial\tilde{\mathcal{E}}}{\partial J} = \frac{\partial\Psi_R}{\partial J} - c_v\Gamma_0\left(J^{q-1}\theta - \theta_R\right), \end{aligned} \tag{3.16}$$

allowing the stress tensor $\boldsymbol{\sigma}_{\boldsymbol{\chi}}$ to be obtained (see equation 2.35b).

For the nearly-incompressible neo-Hookean material model

$$\Psi_R = \frac{\mu}{2}J^{-2/3}\left(\boldsymbol{F} : \boldsymbol{F}\right) - \frac{3\mu}{2} + \frac{1}{2}\left(\kappa - c_v\theta_R\Gamma_0\left(1-q\right)\right)\left(J-1\right)^2, \tag{3.17}$$

Therefore, developing equations 3.16 further leads to $\boldsymbol{\Sigma}_{\boldsymbol{F}}$ and $\boldsymbol{\Sigma}_{\boldsymbol{H}}$ identical to the ones obtained in an isothermal context (see chapter 2) but $\Sigma_J$ being modified by the temperature change

$$\Sigma_J = -\frac{\mu}{3} J^{-5/3} \left(\boldsymbol{F} \colon \boldsymbol{F}\right) + \underbrace{\left(\kappa - c_v \theta_R \Gamma_0 \left(1 - q\right)\right) \left(J - 1\right) - c_v \Gamma_0 \left(J^{q-1}\theta - \theta_R\right)}_{\bar{p}} \tag{3.18}$$

where $\bar{p}$ is the pressure.

### 3.3.1 Thermally-coupled Hencky model with von Mises plasticity and Johnson-Cook hardening law

For the logarithmic-strain von Mises elasto-plastic model

$$\Psi_R = \mu \left[\left(\ln \lambda_{e,1}\right)^2 + \left(\ln \lambda_{e,2}\right)^2 + \left(\ln \lambda_{e,3}\right)^2\right] - \frac{\mu}{3} \left(\ln J\right)^2 + \frac{1}{2} \left(\kappa - c_v \theta_R \Gamma_0 \left(1 - q\right)\right) \left(\ln J\right)^2 , \tag{3.19}$$

and therefore the pressure in a thermal context is computed as

$$\bar{p} = \left(\kappa - c_v \theta_R \Gamma_0 \left(1 - q\right)\right) \frac{\ln J}{J} - c_v \Gamma_0 \left(J^{q-1}\theta - \theta_R\right) . \tag{3.20}$$

Within a thermal context, the plasticity model can be further enhanced to take into account the material temperature dependence. For this purpose, the rate- and temperature-dependent Johnson-Cook hardening law [77–79] is introduced. The equivalent yield stress is expressed now as

$$\bar{\tau}_y = \left(A + b \left(\bar{\epsilon}_p\right)^{n'}\right) \left[1 + c \ln\left(\frac{\dot{\bar{\epsilon}}_p}{\dot{\bar{\epsilon}}_0}\right)\right] \left(1 - \hat{\theta}^m\right) , \tag{3.21}$$

where $\bar{\epsilon}_p$ is the equivalent plastic strain, and $\dot{\bar{\epsilon}}_p$ and $\dot{\bar{\epsilon}}_0$ represent the plastic strain rate and the reference strain rate, respectively. The first parenthesis gives the stress as a function of the strain for $\frac{\dot{\bar{\epsilon}}_p}{\dot{\bar{\epsilon}}_0} = 1$ and $\hat{\theta} = 0$. The second expression, within square brackets, represents the effects of the strain rate, while the last parenthesis is related to the temperature effects. The five material constants (measured below the transition temperature) are interpreted as: the yield stress $A$, hardening parameter $b$, hardening exponent $n'$, strain rate coefficient $c$, temperature exponent $m$.

The non-dimensional temperature $\hat{\theta}$ is defined as

$$\hat{\theta} = \begin{cases} 0 & \text{for} \quad \theta < \theta_{\text{transition}}, \\ \left(\theta - \theta_{\text{transition}}\right) / \left(\theta_{\text{melt}} - \theta_{\text{transition}}\right) & \text{for} \quad \theta_{\text{transition}} \leq \theta \leq \theta_{\text{melt}}, \\ 1 & \text{for} \quad \theta > \theta_{\text{melt}}, \end{cases} \tag{3.22}$$

where $\theta$ is the current temperature, $\theta_{\text{melt}}$ is the melting temperature of the material, and $\theta_{\text{transition}}$ is the temperature at or below which there is no temperature dependence of the yield stress. Note that when $\theta > \theta_{\text{melt}}$, the material is assumed to melt and behave like a fluid, offering no shear resistance since $\bar{\tau}_y = 0$.

Notice that the Newton-Raphson method presented for a nonlinear hardening is slightly different for a Johnson-Cook hardening law. The plastic multiplier $\Delta_\gamma$ will need to be expressed as

$$\Delta_\gamma^{k+1} = \Delta_\gamma^k - \frac{T - F}{3\mu + b n' \left(\bar{\epsilon}_p^n + \Delta_\gamma^k\right)^{n'-1} g(\dot{\bar{\epsilon}}_p^n) f(\theta^{n+1})} .$$

Here, $g(\dot{\bar{\epsilon}}_p^n) = \left[1 + c\ln\left(\frac{\dot{\bar{\epsilon}}_p^n}{\dot{\epsilon}_0}\right)\right]$ and $f(\theta^{n+1}) = \left(1 - \hat{\theta}^m\right)$ are used to simplify the notation.

$T = 3\mu\Delta_\gamma^k + \left[A + b\left(\bar{\epsilon}_p^n + \Delta_\gamma^k\right)^{n'}\right] f(\theta^{n+1})g(\dot{\bar{\epsilon}}_p^n)$ and $F = f\left(\tau'^{\,\mathrm{trial}}_{\alpha\alpha}, \bar{\epsilon}_p^n, \dot{\bar{\epsilon}}_p^n, \theta^{n+1}\right) + \bar{\tau}_y^n(\bar{\epsilon}_p^n, \dot{\bar{\epsilon}}_p^n, \theta^{n+1})$.

**Remark 4** *During the iterative process, the plastic multiplier $\Delta_\gamma^k$ may become negative (before convergence is achieved). Such scenario would be non-physical and lead to the non-convergence of the algorithm. One alternative solution to circumvent this issue is to redefine the variable as*

$$\mathrm{X} = \left(\bar{\epsilon}_p^n + \Delta_\gamma\right)^{n'}, \tag{3.23}$$

*the Newton-Raphson iteration algorithm then becomes*

$$\mathrm{X}^{k+1} = \mathrm{X}^k - \frac{\hat{T} - F}{\frac{3\mu}{n'}{\mathrm{X}^k}^{\frac{1-n'}{n'}} + bg(\dot{\bar{\epsilon}}_p^n)f(\theta^{n+1})}, \tag{3.24}$$

*with $\hat{T} = 3\mu\left(\left(\mathrm{X}^k\right)^{1/n'} - \bar{\epsilon}_p^n\right) + \left[A + b\mathrm{X}^k\right] g(\dot{\bar{\epsilon}}_p^n)f(\theta^{n+1})$.*

The Newton-Raphson method described above is illustrated in algorithm 3.

**Algorithm 3:** Newton-Raphson iteration for the evaluation of Johnson-Cook hardening

```
(1) Compute constant value $F$
(2) Assume $\mathrm{X} = 0$
(3) Assign $TOL = 1e^{-6}$ and $Err = 2 \times TOL$
while $Err \geq TOL$ do
    (4) Evaluate $\hat{T}(\mathrm{X})$
    (5) Evaluate $\mathrm{R}(\mathrm{X}) = -\frac{\hat{T}(\mathrm{X}) - F}{\frac{3\mu}{n'}\mathrm{X}^{\frac{1-n'}{n'}} + bg(\dot{\bar{\epsilon}}_p^n)f(\theta^{n+1})}$
    (6) $\mathrm{X} = \mathrm{X} + \mathrm{R}(\mathrm{X})$
    (7) $Err = |\mathrm{R}|$
end
(8) $\Delta_\gamma = \mathrm{X}^{1/n'} - \bar{\epsilon}_p^n$.
```

An algorithmic representation of the Hencky model with von Mises thermoplasticity described in this section is given in algorithm 4.

## 3.4 Conclusion

This chapter extended the new updated reference Lagrangian formulation to the context of thermo-mechanics. The first law of thermodynamics was written in terms of the total energy. Thermally-coupled constitutive models were also presented. The

**Algorithm 4:** Principal Direction formulation for Hencky model with von Mises thermoplasticity

```
Input  : $\boldsymbol{F}^{n+1}, \boldsymbol{H}^{n+1}, J^{n+1}, \theta^{n+1}, \left[\boldsymbol{C}_p^{-1}\right]^n, \bar{\epsilon}_p^n$
Output: $\boldsymbol{P}^{n+1}, \left[\boldsymbol{C}_p^{-1}\right]^{n+1}, \bar{\epsilon}_p^{n+1}$

(1) Evaluate pressure: $p^{n+1} = \kappa \frac{\ln J^{n+1}}{J^{n+1}} - c_v \Gamma_0(\theta^{n+1} - \theta_R)$; assuming
    Mie-Gruneisen coefficient is unity
(2) Compute trial elastic left strain tensor: $\boldsymbol{b}_e^{\text{trial}} = \boldsymbol{F}^{n+1} \left[\boldsymbol{C}_p^{-1}\right]^n \left[\boldsymbol{F}^T\right]^{n+1}$
(3) Spectral decomposition of $\boldsymbol{b}_e^{\text{trial}}$: $\boldsymbol{b}_e^{\text{trial}} = \sum_{\alpha=1}^3 \left(\lambda_{e,\alpha}^{\text{trial}}\right)^2 (\boldsymbol{n}_\alpha^{n+1} \otimes \boldsymbol{n}_\alpha^{n+1})$
(4) Obtain trial deviatoric Kirchoff stress tensor:
    $\tau'^{\text{trial}}_{\alpha\alpha} = 2\mu \ln \lambda_{e,\alpha}^{\text{trial}} - \frac{2}{3}\mu \ln J^{n+1}$
(5) Obtain yield criterion:
    $f\left(\tau'^{\text{trial}}_{\alpha\alpha}, \bar{\epsilon}_p^n, \dot{\bar{\epsilon}}_p^n, \theta^{n+1}\right) = \left[\frac{3}{2}\sum_{\beta=1}^3 \left(\tau'^{\text{trial}}_{\beta\beta}\right)^2\right]^{1/2} - \bar{\tau}_y^n(\bar{\epsilon}_p^n, \dot{\bar{\epsilon}}_p^n, \theta^{n+1})$;
    $\bar{\tau}_y^n(\bar{\epsilon}_p^n, \dot{\bar{\epsilon}}_p^n, \theta^{n+1}) = \left[A + b\left(\bar{\epsilon}_p^n\right)^{n'}\right] f(\theta^{n+1}) g(\dot{\bar{\epsilon}}_p^n)$
(6) Compute direction vector and plastic multiplier:
    if $f\left(\tau'^{\,trial}_{\alpha\alpha}, \bar{\epsilon}_p^n\right) > 0$ then
        Direction vector: $\upsilon_\alpha^{n+1} = \frac{\tau'^{\text{trial}}_{\alpha\alpha}}{\left[\frac{2}{3}\sum_{\beta=1}^3 \left(\tau'^{\text{trial}}_{\beta\beta}\right)^2\right]^{1/2}}$
        Plastic multiplier: $\Delta\gamma$ (See Newton-Raphson algorithm 3)
    else
        $\upsilon_\alpha^{n+1} = \Delta\gamma = 0$
    end
(7) Update deviatoric Kirchoff stresss tensor:
    $\boldsymbol{\tau}'^{n+1} = \tau'^{n+1}_{\alpha\alpha} \boldsymbol{n}^{n+1} \otimes \boldsymbol{n}^{n+1}$;    $\tau'^{n+1}_{\alpha\alpha} = \tau'^{\text{trial}}_{\alpha\alpha} - 2\mu\Delta_\gamma \upsilon_\alpha^{n+1}$
(8) Evaluate first Piola Kirchoff stress tensor:
    $\boldsymbol{P}^{n+1} = \boldsymbol{\tau}'^{n+1} \left[\boldsymbol{F}^{-T}\right]^{n+1} + p^{n+1} \boldsymbol{H}^{n+1}$
(9) Update elastic left Cauchy strain tensor:
    $\boldsymbol{b}_e^{n+1} = \sum_{\alpha=1}^3 \left(\lambda_{e,\alpha}^{n+1}\right)^2 (\boldsymbol{n}_\alpha^{n+1} \otimes \boldsymbol{n}_\alpha^{n+1})$;    $\ln \lambda_{e,\alpha}^{n+1} = \ln \lambda_{e,\alpha}^{\text{trial}} - \Delta_\gamma \upsilon_\alpha^{n+1}$
(10) Compute plastic right Cauchy Green tensor:
    $\left[\boldsymbol{C}_p^{-1}\right]^{n+1} = [\boldsymbol{F}^{-1}]^{n+1} \boldsymbol{b}_e^{n+1} \left[\boldsymbol{F}^{-T}\right]^{n+1}$
(11) Update plastic strain: $\bar{\epsilon}_p^{n+1} = \bar{\epsilon}_p^n + \Delta\gamma$
```

chapter serves mainly to derive means of obtaining the temperature update, as well as accounting for the effects of a change in temperature over the deformation and vice-versa. The classic Johnson-Cook hardening law was implemented expanding the range of possible applications of the framework. It is worth noticing however that some authors have pointed out limitations of this model, such as dependency on the calibration strategy utilised to obtain its parameters [80] and lack of a coupling between strain rate and deformation temperature [81].

# Part III

# Smooth Particle Hydrodynamics Algorithm

# Chapter 4

# Smooth Particle Hydrodynamics

## 4.1 Introduction

In this chapter the fundamental aspects of the Smooth Particle Hydrodynamics (SPH) method are presented. The corrected SPH method is reviewed, followed by a discussion regarding the computation of the kernel function and its gradient. Four different descriptions of anisotropic compact supports are proposed. The chapter ends with some elementary test cases performed in order to assess the accuracy of the approximation. For a comprehensive view of meshless methods, one can refer to [1, 2]. Regarding the SPH itself, the works by Monaghan [12], Swegle et al. [13] and Vignjevic et al. [14] are particularly recommended.

## 4.2 Generalities of SPH

The foundation of SPH is interpolation theory. When applied to the context of continuum mechanics, the conservation laws in the form of differential equations are transformed into integral equations through the use of a kernel estimate of the field variables. Consider $\boldsymbol{y}$ as a vector function of the three-dimensional position vector $\boldsymbol{X}$, which lies in the material configuration, and the extension of the sifting property of the Dirac delta function [82] to the context of the present work

$$\boldsymbol{y}\left(\boldsymbol{X}\right) = \int_{\Omega_V} \boldsymbol{y}\left(\boldsymbol{X}'\right) \delta\left(\boldsymbol{X} - \boldsymbol{X}'\right) dV, \tag{4.1}$$

with $\boldsymbol{y}$ known at position $\boldsymbol{X}'$.

If the Dirac delta function is replaced by a kernel function $W\left(\boldsymbol{X} - \boldsymbol{X}', h\right)$ which has a compact support defined as a function of a smoothing parameter, the so-called smoothing length $h$, such that

$$W\left(\boldsymbol{X} - \boldsymbol{X}', h\right) = 0 \qquad \text{for} \qquad \left|\boldsymbol{X} - \boldsymbol{X}'\right| \geq 2h, \tag{4.2}$$

that is normalised,

$$\int_{\Omega_V} W\left(\boldsymbol{X} - \boldsymbol{X}', h\right) dV = 1, \tag{4.3}$$

and reduces to the Dirac delta function when $h$ approaches zero,

$$\lim_{h\to 0} W\left(\boldsymbol{X}-\boldsymbol{X}',h\right)=\delta\left(\boldsymbol{X}-\boldsymbol{X}'\right), \tag{4.4}$$

the result is the kernel estimate expressed as

$$\hat{\boldsymbol{y}}\left(\boldsymbol{X}\right)=\int_{\Omega_V}\boldsymbol{y}\left(\boldsymbol{X}'\right)W\left(\boldsymbol{X}-\boldsymbol{X}',h\right)dV. \tag{4.5}$$

Note that $\hat{\boldsymbol{y}}\left(\boldsymbol{X}\right)\approx\boldsymbol{y}\left(\boldsymbol{X}\right)$. The approximation will depend only on the values at positions within the sub-domain where the kernel is non-zero, this is imposed by condition 4.2. Condition 4.3 arises from consistency, although it does not guarantee consistency in a discrete level.

If $\boldsymbol{y}$ is known at $N$ discrete points (particles) spatially distributed over the domain and if each particle $i$ has an associated volume $V_i=\frac{m_i}{\rho_{0,i}}$, where $m_i$ is the particle mass, then an approximation to the kernel estimate evaluated at a position $\boldsymbol{X}_a$, that is coincident with the position of a particle $a$ (the target particle), is

$$\hat{\boldsymbol{y}}\left(\boldsymbol{X}_a\right)\approx\sum_{i=1}^{N}V_i\boldsymbol{y}_iW\left(\boldsymbol{X}_a-\boldsymbol{X}_i,h_i\right), \tag{4.6}$$

with $\boldsymbol{y}_i$ being the value of $\boldsymbol{y}$ stored at particle $i$ and $h_i$ the smoothing length of particle $i$. Note that in equation 4.6 the particle position $\boldsymbol{X}_a$ is also used as the quadrature point.

**Remark 5** *Note that for adaptive schemes in Smooth Particle Hydrodynamics, i.e., for SPH implementations where $h$ is not constant and uniform throughout the domain, neighbour smoothing presents a dualism [83]. If a field is to be smoothed at the position of particle "a", it can be done either by:*

- *Taking into account the contribution of particle "i" evaluated using the value of $h_i$ (from particle "i"), in what is called a "scatter" process, or*
- *Taking into account the contribution of particle "i" evaluated using the value of $h_a$ (from particle "a"), in what is called a "gather" process.*

*In the present work a "scatter" process is always employed, that is, the contribution of the neighbouring particle is evaluated using the smoothing length that belongs to the neighbouring particle itself.*

From 4.6 the gradient of $\hat{\boldsymbol{y}}\left(\boldsymbol{X}_a\right)$ can be computed (see the identity A.40a in Appendix A)

$$\boldsymbol{\nabla}_{\boldsymbol{X}}\hat{\boldsymbol{y}}\left(\boldsymbol{X}_a\right)\approx\sum_{i=1}^{N}V_i(\boldsymbol{y}_i-\boldsymbol{y}_a)\otimes\boldsymbol{\nabla}_{\boldsymbol{X}}W\left(\boldsymbol{X}_a-\boldsymbol{X}_i,h_i\right), \tag{4.7}$$

with the term $-\boldsymbol{y}_a$ introduced artificially in order to ensure that equation 4.7 vanishes for a constant vector field. Note that aiming at computational efficiency, the summation over particles can be performed as

$$\hat{\boldsymbol{y}}\left(\boldsymbol{X}_a\right) \approx \sum_{b \in \Lambda_a^b} V_b \boldsymbol{y}_b W\left(\boldsymbol{X}_a - \boldsymbol{X}_b, h_b\right), \tag{4.8}$$

$$\boldsymbol{\nabla}_{\boldsymbol{X}} \hat{\boldsymbol{y}}\left(\boldsymbol{X}_a\right) \approx \sum_{b \in \Lambda_a^b} V_b (\boldsymbol{y}_b - \boldsymbol{y}_a) \otimes \boldsymbol{\nabla}_{\boldsymbol{X}} W\left(\boldsymbol{X}_a - \boldsymbol{X}_b, h_b\right), \tag{4.9}$$

where $\Lambda_a^b$ represents the set of neighbouring particles $b$ belonging to the domain of influence of the target particle $a$. See figure 4.1 for an illustration of $\Lambda_a^b$ and refer to section 4.4 for a broader discussion regarding its definition.

In the above equations the kernel is expressed in terms of the set of variables $\{\boldsymbol{r}_{ab}, h_b\}$, with $\boldsymbol{r}_{ab} = \boldsymbol{X}_a - \boldsymbol{X}_b$. In order to improve readability of equations, the following simplified notation is employed from now on

$$W_{ba}^{\boldsymbol{X}} := W\left(\boldsymbol{r}_{ab}, h_b\right) = W\left(\boldsymbol{X}_a - \boldsymbol{X}_b, h_b\right), \tag{4.10}$$

and

$$\boldsymbol{\nabla}_{\boldsymbol{X}} W_{ba}^{\boldsymbol{X}} := \boldsymbol{\nabla}_{\boldsymbol{X}} W\left(\boldsymbol{r}_{ab}, h_b\right) = \boldsymbol{\nabla}_{\boldsymbol{X}} W\left(\boldsymbol{X}_a - \boldsymbol{X}_b, h_b\right). \tag{4.11}$$

To clarify, observe that $W_{ba}^{\boldsymbol{X}}$ is the kernel function belonging to particle $b$ evaluated at the quadrature point coincident with the position of particle $a$, expressed in terms of $\{\boldsymbol{X}_a - \boldsymbol{X}_b, h_b\}$. The kernel function $W$ employed in this work will be explicitly defined in the following sections.

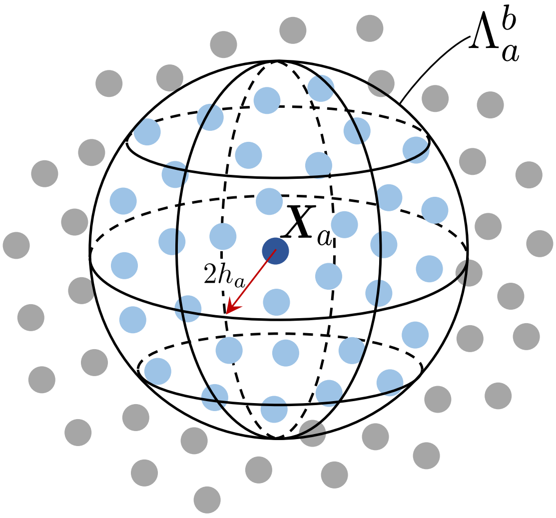

Figure 4.1: Domain of influence of the target particle $a$.

## 4.3 Corrected SPH

To ensure invariance with respect to rigid body motions, the following condition has to be satisfied by the gradient of the kernel function [29]

$$\sum_{b \in \Lambda_a^b} V_b \left(\boldsymbol{X}_b - \boldsymbol{X}_a\right) \otimes \boldsymbol{\nabla}_{\boldsymbol{X}} W_{ba}^{\boldsymbol{X}} = \boldsymbol{I}. \tag{4.12}$$

A gradient correction is performed with the introduction of a gradient correction operator $\boldsymbol{\mathcal{C}}_*[\bullet]$, or more specifically, with the introduction of the correction matrix $\boldsymbol{L}_a$, as follows

$$\tilde{\boldsymbol{\nabla}}_{\boldsymbol{X}} W_{ba}^{\boldsymbol{X}} = \boldsymbol{\mathcal{C}}_*[\boldsymbol{\nabla}_{\boldsymbol{X}} W_{ba}^{\boldsymbol{X}}] = \boldsymbol{L}_a \boldsymbol{\nabla}_{\boldsymbol{X}} W_{ba}^{\boldsymbol{X}}. \tag{4.13}$$

Enforcing that 4.12 is satisfied by the corrected kernel gradient allows $\boldsymbol{L}_a$ to be evaluated explicitly as [29]

$$\boldsymbol{L}_a = \left( \sum_{b \in \Lambda_a^b} V_b \boldsymbol{\nabla}_{\boldsymbol{X}} W_{ba}^{\boldsymbol{X}} \otimes (\boldsymbol{X}_b - \boldsymbol{X}_a) \right)^{-1}. \tag{4.14}$$

Since the SPH method does not fulfil the Kronecker-Delta property, in order to obtain the physical value of quantities at the material point occupied by a particle, the values stored at the particles must be interpolated using the kernel function. Note that the shape functions in SPH do not pass through the data, i.e. they are not true interpolants, but only “approximants”, as in the nomenclature proposed in [2]. To ensure the exact satisfaction of both constant and linear completeness, the operator $\mathcal{C}_*[\bullet]$ is introduced [29]

$$\tilde{W}_{ba}^{\boldsymbol{X}} = \mathcal{C}_*[W_{ba}^{\boldsymbol{X}}] = \alpha_a \left[1 + \boldsymbol{\beta}_a \cdot (\boldsymbol{X}_a - \boldsymbol{X}_b)\right] W_{ba}^{\boldsymbol{X}}, \tag{4.15}$$

where the parameters $\boldsymbol{\beta}_a$ and $\alpha_a$ can be evaluated by imposing the consistency conditions $\sum_{b \in \Lambda_a^b} V_b \tilde{W}_{ba}^{\boldsymbol{X}} = 1$ and $\sum_{b \in \Lambda_a^b} V_b (\boldsymbol{X}_a - \boldsymbol{X}_b) \tilde{W}_{ba}^{\boldsymbol{X}} = \boldsymbol{0}$, as follows

$$\boldsymbol{\beta}_a = \left[ \sum_{b \in \Lambda_a^b} V_b (\boldsymbol{X}_a - \boldsymbol{X}_b) \otimes (\boldsymbol{X}_a - \boldsymbol{X}_b) W_{ba}^{\boldsymbol{X}} \right]^{-1} \sum_{b \in \Lambda_a^b} V_b (\boldsymbol{X}_b - \boldsymbol{X}_a) W_{ba}^{\boldsymbol{X}}, \tag{4.16}$$

and

$$\alpha_a = \left( \sum_{b \in \Lambda_a^b} V_b \left[1 + \boldsymbol{\beta}_a \cdot (\boldsymbol{X}_a - \boldsymbol{X}_b)\right] W_{ba}^{\boldsymbol{X}} \right)^{-1}. \tag{4.17}$$

Observe that the notation used in this section employs variables defined in the initial configuration, such as $\boldsymbol{X}_\alpha$ and $V_\alpha$, with $\alpha = a, b$. However, the correction procedure is performed in the same manner in updated configurations.

## 4.4 Kernel function and smoothing length

Among the many different kernel functions available in the literature, the commonly used quadratic smoothing function [84] and the cubic spline [12] were chosen for this work due to their low computational cost, combined to the fact that the present formulation employs corrected kernels over small compact supports (few neighbouring particles available for the approximation) without degrading the solution. Higher order kernels, such as the 5th-order Wendland kernel [85, 86] are known to lead to improved behaviour in fluids simulations, since its Fourier space contains no zero crossing points. However, these were not explored in the present formulation.

In a Total Lagrangian Formulation the 3D quadratic kernel function of a particle $b$, evaluated at the target position $a$, is expressed as

$$W^{\boldsymbol{X}}_{\mathrm{q}_{ba}} = \begin{cases} \frac{5}{4\pi h_b^3}\left[\frac{3}{4}\left(\frac{1}{4}\xi^2 - \xi + 1\right)\right], & \text{for} \quad 0 \leq \xi < 2, \\ 0, & \text{for} \quad \xi \geq 2, \end{cases} \tag{4.18}$$

where

$$\xi = \frac{\|\boldsymbol{X}_a - \boldsymbol{X}_b\|}{h_b}. \tag{4.19}$$

The smoothing length $h_b$ featuring in the above equations is illustrated for particle $b$ in the material configuration in figure 4.2, and is defined as

$$h_b = f_h \max_{j \in \Lambda_b^j} \left(\|\boldsymbol{X}_j - \boldsymbol{X}_b\|\right), \tag{4.20}$$

where $\Lambda_b^j$ represents the set of neighbouring particles $j$ belonging to the domain of influence of particle $b$, and $f_h$ is a coefficient used to scale the size of the compact support.

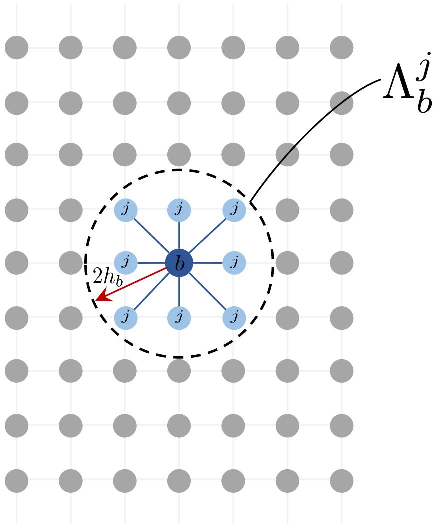

Figure 4.2: 2D view of the smoothing length in the material configuration.

From equations 4.18, the gradient of the quadratic kernel function can be computed as

$$\boldsymbol{\nabla}_{\boldsymbol{X}} W^{\boldsymbol{X}}_{\mathrm{q}_{ba}} = \begin{cases} \frac{5}{4\pi h_b^4}\left[\frac{3}{4}\left(\frac{1}{2}\xi - 1\right)\right]\left(\frac{\boldsymbol{X}_a - \boldsymbol{X}_b}{\|\boldsymbol{X}_a - \boldsymbol{X}_b\|}\right), & \text{for} \quad 0 \leq \xi < 2, \\ \boldsymbol{0}, & \text{for} \quad \xi \geq 2. \end{cases} \tag{4.21}$$

The 3D cubic spline, on the other hand, is expressed as:

$$W^{\boldsymbol{X}}_{\mathrm{c}_{ba}} = \begin{cases} \frac{1}{\pi h_b^3}\left[1 + \frac{3}{4}\xi^3 - \frac{3}{2}\xi^2\right], & \text{for} \quad 0 \leq \xi \leq 1, \\ \frac{1}{\pi h_b^3}\left[\frac{1}{4}\left(2 - \xi\right)^3\right], & \text{for} \quad 1 < \xi < 2, \\ 0, & \text{for} \quad \xi \geq 2. \end{cases} \tag{4.22}$$

From equations 4.22, the gradient of the cubic spline kernel function can be computed as

$$\boldsymbol{\nabla}_{\boldsymbol{X}} W^{\boldsymbol{X}}_{c_{ba}} = \begin{cases} \frac{1}{\pi h_b^4}\left[\frac{9}{4}\xi^2 - 3\xi\right]\left(\frac{\boldsymbol{X}_a - \boldsymbol{X}_b}{\|\boldsymbol{X}_a - \boldsymbol{X}_b\|}\right), & \text{for} \quad 0 \leq \xi \leq 1, \\ \frac{1}{\pi h_b^4}\left[-\frac{3}{4}(2-\xi)^2\right]\left(\frac{\boldsymbol{X}_a - \boldsymbol{X}_b}{\|\boldsymbol{X}_a - \boldsymbol{X}_b\|}\right), & \text{for} \quad 1 < \xi < 2, \\ \boldsymbol{0}, & \text{for} \quad \xi \geq 2. \end{cases} \tag{4.23}$$

A 2D representation of both kernel functions and their derivatives is shown in figures 4.3a and 4.3b, respectively.

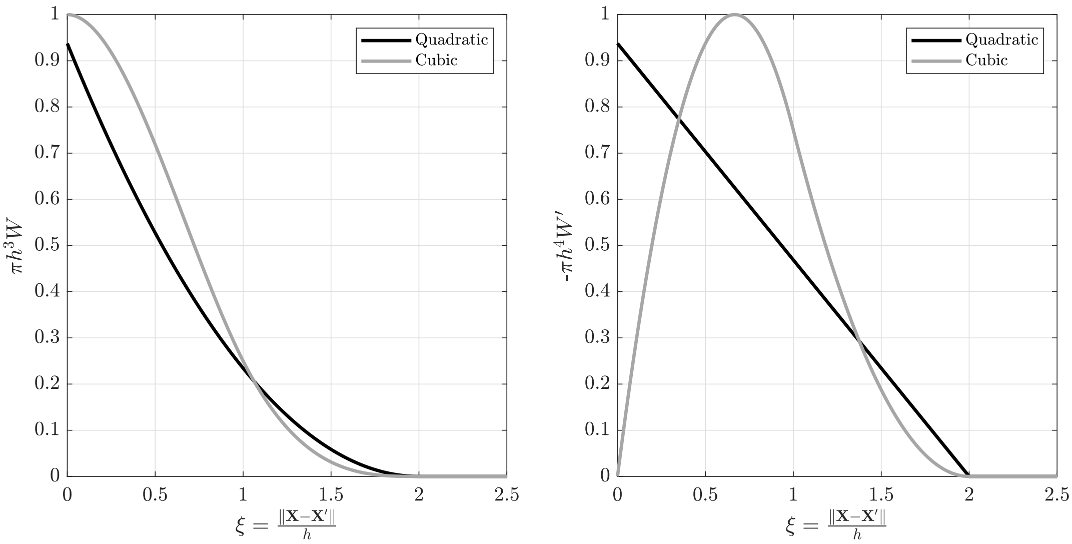

(a) (b)

Figure 4.3: (a) Smoothing functions. (b) Smoothing functions derivatives.

In the current work, in order to avoid performing time consuming searches for new neighbouring particles in the updated configurations (standard in classic Updated Lagrangian Formulation), an alternative approach is to employ anisotropic kernel functions and keep the initial list of neighbours constant throughout the simulation. In this case, unnecessary (if no topological changes take place) new searches are avoided. Notice however, that in the case of fracture, where a new boundary is formed, updating the list of neighbouring particles in the region surrounding the cracked particle is necessary. Moreover, since we aim at applications involving large deformations, standard updated isotropic (spherical) kernels would not be optimal (see e.g. [87]). Due to the possible presence of strong anisotropic changes in volume, and consequently in the particle spacing, the use of anisotropic kernels is better suited. An illustration of an anisotropic compact support is given in figure 4.4.

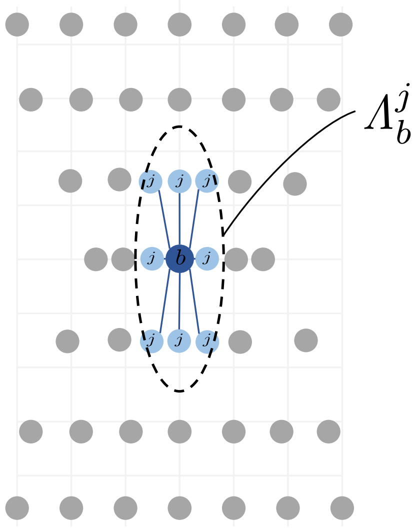

Figure 4.4: 2D view of an anisotropic compact support in the updated configuration.

Anisotropic kernel functions and their gradient evaluations can be obtained via adaptation of the general concepts of push forward and pull back operations. Namely, in what follows, $\phi_*[\bullet]$ refers to the push-forward operation of a kernel function and $\boldsymbol{\phi}_*[\bullet]$ refers to the push-forward operation of the gradient of a kernel function. Therefore, we can define

$$W_{ba}^{\boldsymbol{\chi}} = \phi_*[W_{ba}^{\boldsymbol{X}}] = J_{\boldsymbol{\chi},b}^{-1} W_{ba}^{\boldsymbol{X}}, \tag{4.24}$$

and

$$\boldsymbol{\nabla}_{\boldsymbol{\chi}} W_{ba}^{\boldsymbol{\chi}} = \boldsymbol{\phi}_*[\boldsymbol{\nabla}_{\boldsymbol{X}} W_{ba}^{\boldsymbol{X}}] = J_{\boldsymbol{\chi},b}^{-1} \boldsymbol{F}_{\boldsymbol{\chi},a}^{-T} \boldsymbol{\nabla}_{\boldsymbol{X}} W_{ba}^{\boldsymbol{X}}. \tag{4.25}$$

The push-forward operation of the gradient of a kernel function differs from the classic push-forward operation commonly seen in textbooks [88] due to the fact that a transformation of volume ($J_{\boldsymbol{\chi},b}^{-1}$) is also present in the operation (see remark 6 in chapter 5). Notice that the above evaluations for the reference kernel function and the associated gradient still require geometrical information attached to the material domain. In order to ensure that the kernel function depends solely on the information at the updated domain, one viable option is to approximate the material vector $\boldsymbol{r}_{ab} = \boldsymbol{X}_a - \boldsymbol{X}_b$ as the pull back equivalent of its updated counterpart $\boldsymbol{r}_{\boldsymbol{\chi},ab} = \boldsymbol{\chi}_a - \boldsymbol{\chi}_b$, that is

$$\boldsymbol{r}_{ab} = \boldsymbol{X}_a - \boldsymbol{X}_b \approx \boldsymbol{\phi}_*^{-1}[\boldsymbol{r}_{\boldsymbol{\chi},ab}] = \boldsymbol{F}_{\boldsymbol{\chi},ab}^{-1}(\boldsymbol{\chi}_a - \boldsymbol{\chi}_b) = \hat{\boldsymbol{r}}_{\boldsymbol{\chi},ab}, \tag{4.26}$$

where the average (second order) approximation $\boldsymbol{F}_{\boldsymbol{\chi},ab} = \frac{1}{2}(\boldsymbol{F}_{\boldsymbol{\chi},a} + \boldsymbol{F}_{\boldsymbol{\chi},b})$, and $\boldsymbol{\phi}_*^{-1}[\bullet]$ is the standard continuum mechanics pull-back operation applied to a vector.

Following such approach, the definition of $\xi$ given in equation 4.19 needs to be replaced by $\hat{\xi}$, which is defined as

$$\hat{\xi} = \frac{\|\boldsymbol{F}_{\boldsymbol{\chi},ab}^{-1}(\boldsymbol{\chi}_a - \boldsymbol{\chi}_b)\|}{\hat{h}_b}, \tag{4.27}$$

and the smoothing length $h_b$ is redefined as $\hat{h}_b$ in terms of the pulled-back vector as

$$\hat{h}_b = f_h \max_{j\in\hat{\Lambda}_b^j} \left( \boldsymbol{F}^{-1}_{\boldsymbol{\chi},bj} \left( \|\boldsymbol{\chi}_j - \boldsymbol{\chi}_b\| \right) \right) , \tag{4.28}$$

where $\hat{\Lambda}_b^j$ represents the set of neighbouring particles $j$ belonging to the domain of influence of particle $b$ in the pulled-back configuration, and $\boldsymbol{F}_{\boldsymbol{\chi},bj} = \frac{1}{2} \left( \boldsymbol{F}_{\boldsymbol{\chi},b} + \boldsymbol{F}_{\boldsymbol{\chi},j} \right)$.

The SPH mixed-based formulation presented in this work is applicable even when coarse particle distributions are used, i.e. even for the cases when few particles are located within the domain of influence, a good resolution can still be obtained for the approximation. Therefore, aiming at the best compromise between computational cost and accuracy, the general procedure employed herein consists of considering only the first layer of immediate neighbours, this can be easily achieved using a standard finite element pre-processor, from which the nodes will be taken as particles. Once the immediate neighbours (connected nodes) are known, the distance between a particle and each of its immediate neighbours can be measured, the largest distance is used to define the smoothing length together with the factor $f_h$. Notice that in this approach, if $f_h = 0.5$, the contribution of the most distant particle would be null, which leads to a poor approximation in practical simulations involving only one layer of neighbours. Therefore, $f_h$ needs to be specified so that all particles in the first layer of immediate neighbours provide meaningful contributions to the approximation.

To conclude this section, it is still left for discussion the combination of anisotropic kernel functions and SPH kernel and gradient corrections. In this work, four different options for obtaining updated kernel functions and their corresponding gradient evaluations are explored. Notice that in the right hand side of the following equations the arguments of the kernel functions are explicitly written in parenthesis. For the last two options, the arguments of the smoothing function are also explicitly written to make it clear that these functions rely on measures taken from the updated configuration.

- **Option#1**. Both kernel function and its gradient are first corrected (ensuring zeroth- and first-order completeness) in the material domain and then are pushed forward to the reference domain. Mathematically, these are expressed as

$$\tilde{W}^{\boldsymbol{\chi}}_{ba} = \phi_* \left[ \mathcal{C}_* \left[ W(\boldsymbol{r}_{ab}, h_b) \right] \right] = J^{-1}_{\boldsymbol{\chi},b} \mathcal{C}_* \left[ W(\boldsymbol{r}_{ab}, h_b) \right] , \tag{4.29a}$$

$$\tilde{\boldsymbol{\nabla}}_{\boldsymbol{\chi}} W^{\boldsymbol{\chi}}_{ba} = \boldsymbol{\phi}_* \left[ \boldsymbol{\mathcal{C}}_* \left[ \boldsymbol{\nabla}_{\boldsymbol{X}} W(\boldsymbol{r}_{ab}, h_b) \right] \right] = J^{-1}_{\boldsymbol{\chi},b} \boldsymbol{F}^{-T}_{\boldsymbol{\chi},a} \boldsymbol{\mathcal{C}}_* \left[ \boldsymbol{\nabla}_{\boldsymbol{X}} W(\boldsymbol{r}_{ab}, h_b) \right] . \tag{4.29b}$$

- **Option#2**. On the contrary, this particular option first pushes forward the material kernel function and its gradient to the reference domain, followed by the application of appropriate corrections at updated domain, that is

$$\tilde{W}^{\boldsymbol{\chi}}_{ba} = \mathcal{C}_* \left[ \phi_* \left[ W(\boldsymbol{r}_{ab}, h_b) \right] \right] = \mathcal{C}_* \left[ J^{-1}_{\boldsymbol{\chi},b} W(\boldsymbol{r}_{ab}, h_b) \right] , \tag{4.30a}$$

$$\tilde{\boldsymbol{\nabla}}_{\boldsymbol{\chi}} W^{\boldsymbol{\chi}}_{ba} = \boldsymbol{\mathcal{C}}_* \left[ \boldsymbol{\phi}_* \left[ \boldsymbol{\nabla}_{\boldsymbol{X}} W(\boldsymbol{r}_{ab}, h_b) \right] \right] = \boldsymbol{\mathcal{C}}_* \left[ J^{-1}_{\boldsymbol{\chi},b} \boldsymbol{F}^{-T}_{\boldsymbol{\chi},a} \boldsymbol{\nabla}_{\boldsymbol{X}} W(\boldsymbol{r}_{ab}, h_b) \right] . \tag{4.30b}$$

- **Option#3**. As an alternative to option#2, we can re-write the material kernel function (in terms of the reference geometrical information) via the pull back equivalent of the reference vector to yield

$$\begin{aligned} \tilde{W}_{ba}^{\mathcal{X}} &= \mathcal{C}_* \left[\phi_* \left[\hat{W}(\boldsymbol{\phi}_*^{-1}[\boldsymbol{r}_{\mathcal{X},ab}], \hat{h}_b(\boldsymbol{\phi}_*^{-1}[\boldsymbol{r}_{\mathcal{X},ab}]))\right]\right] \qquad (4.31a)\\ &= \mathcal{C}_* \left[J_{\mathcal{X},b}^{-1} \hat{W}(\hat{\boldsymbol{r}}_{ab}, \hat{h}_b)\right], \\ \tilde{\boldsymbol{\nabla}}_{\mathcal{X}} W_{ba}^{\mathcal{X}} &= \boldsymbol{\mathcal{C}}_* \left[\boldsymbol{\phi}_* \left[\boldsymbol{\nabla}_{\boldsymbol{X}} \hat{W}(\boldsymbol{\phi}_*^{-1}[\boldsymbol{r}_{\mathcal{X},ab}], \hat{h}_b \left(\boldsymbol{\phi}_*^{-1}[\boldsymbol{r}_{\mathcal{X},ab}]\right))\right]\right] \qquad (4.31b)\\ &= \boldsymbol{\mathcal{C}}_* \left[J_{\mathcal{X},b}^{-1} \boldsymbol{F}_{\mathcal{X},a}^{-T} \boldsymbol{\nabla}_{\boldsymbol{X}} \hat{W}(\hat{\boldsymbol{r}}_{ab}, \hat{h}_b)\right]. \end{aligned}$$

- **Option#4**. Alternatively, we can re-define the push-forward operation of the gradient operator using the average of the deformation mapping between pairwise interacting particles, which would be consistent with a derivation of the gradient starting from the kernel function and making use of the chain rule, that is $\boldsymbol{\phi}_* \left[\boldsymbol{\nabla}_{\boldsymbol{X}} W(\boldsymbol{r}_{ab}, h_b)\right] = J_{\mathcal{X},b}^{-1} \boldsymbol{F}_{\mathcal{X},ab}^{-T} \boldsymbol{\nabla}_{\boldsymbol{X}} W(\boldsymbol{r}_{ab}, h_b)$. Doing this will eventually yield

$$\begin{aligned} \tilde{W}_{ba}^{\mathcal{X}} &= \mathcal{C}_* \left[\phi_* \left[\hat{W}(\boldsymbol{\phi}_*^{-1}[\boldsymbol{r}_{\mathcal{X},ab}], \hat{h}_b(\boldsymbol{\phi}_*^{-1}[\boldsymbol{r}_{\mathcal{X},ab}]))\right]\right] \qquad (4.32a)\\ &= \mathcal{C}_* \left[J_{\mathcal{X},b}^{-1} \hat{W}(\hat{\boldsymbol{r}}_{ab}, \hat{h}_b)\right], \\ \tilde{\boldsymbol{\nabla}}_{\mathcal{X}} W_{ba}^{\mathcal{X}} &= \boldsymbol{\mathcal{C}}_* \left[\boldsymbol{\phi}_* \left[\boldsymbol{\nabla}_{\boldsymbol{X}} \hat{W}(\boldsymbol{\phi}_*^{-1}[\boldsymbol{r}_{\mathcal{X},ab}], \hat{h}_b \left(\boldsymbol{\phi}_*^{-1}[\boldsymbol{r}_{\mathcal{X},ab}]\right))\right]\right] \qquad (4.32b)\\ &= \boldsymbol{\mathcal{C}}_* \left[J_{\mathcal{X},b}^{-1} \boldsymbol{F}_{\mathcal{X},ab}^{-T} \boldsymbol{\nabla}_{\boldsymbol{X}} \hat{W}(\hat{\boldsymbol{r}}_{ab}, \hat{h}_b)\right]. \end{aligned}$$

For the numerical examples examined in this work, the robustness and accuracy of the overall algorithm would not be adversely affected regardless of which option is used for SPH kernel approximation. However, it is extremely informative to explore these various possibilities and provide the user with several options, in order to choose the most convenient one from the point of view of their computational implementation. It is worth pointing out that, for problems accompanied with large topological changes (such as material separation in dynamic fracture), it is instructive to use **Option#3** and **Option#4** where the computations of kernel function and its gradient are carried out at (post-fractured) updated configuration. This is in contrast to **Option#1** and **Option#2** where the computations are at (pre-fractured) material configuration without considering separation process, hence not suitable for scenarios involving severe topological changes.

## 4.5 Approximation test cases

In order to assess the accuracy of the approximations proposed in the previous sections, a simple test case is now performed. The initial model consists of a cube with dimensions 1 x 1 x 1. Initially, six model refinements considering 3, 5, 9, 17, 33 and 45 particles evenly spaced in each positive direction were studied. Tributary volume is defined for each particle. Only one layer of immediate neighbours is considered, and therefore a central particle has 27 neighbours including itself, while a corner particle has 8 neighbours including itself.

The kernels and gradients in this work are corrected up to first degree. Therefore, the first verification is to check the ability to approximate constant and linear fields exactly. Regardless of the smoothing function or option chosen for the computation of kernels and gradients, constant and linear fields are approximated exactly for all model refinements studied. In figure 4.5a the interpolated values of the constant scalar field $\mathrm{v} = 1$ are plotted at the middle section ($Z = 0.5$) of the cube, considering 5 particles in each direction. The resulting gradient is evidently null due to the term $-\boldsymbol{y}_a$ added to equation 4.7. In figure 4.5b the approximated values of the linear scalar field $\mathrm{v} = X + Y + Z$ are plotted at the middle section ($Z = 0.5$) of the cube. The approximated gradient computed at every particle is $\boldsymbol{\nabla}\mathrm{v} = [1, 1, 1]^T$ for this case.

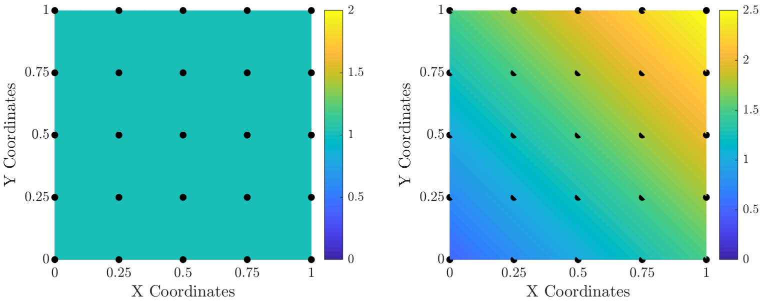

(a) (b)

Figure 4.5: (a) Approximation of a constant scalar field. (b) Approximation of a linear scalar field.

If the domain is stretched in order to obtain a cuboid 1 x 10 x 1, with the corresponding deformation gradient assumed to be $\boldsymbol{F} = 10\boldsymbol{I}$ and the volume map $J = 10$, the exact solution is obtained for all options, just as in the non-stretched domain. This is observed for the model with 5 particles in each direction in figures 4.6a and 4.6b, results are plotted at the middle section ($Z = 0.5$) of the cuboid. As in the 1 x 1 x 1 cube, the gradient computed at every particle is null for the constant field and $\nabla\mathrm{v} = [1, 1, 1]^T$ for the linear field.

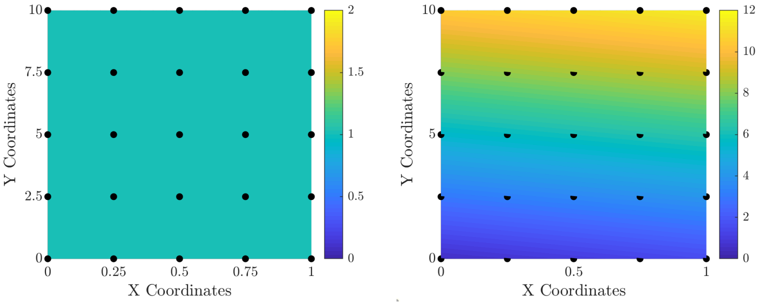

(a) (b)

Figure 4.6: (a) Approximation of a constant scalar field in a stretched domain. (b) Approximation of a linear scalar field in a stretched domain.

The tests performed up to now showed that the corrections applied to the kernel and to its gradient ensure that constant and linear fields are approximated exactly. Let us now observe the behaviour of the approximation for a quadratic scalar field $\mathrm{v} = X^2 + Y^2 + Z^2$. The stretched domain (cuboid 1 x 10 x 1) is considered again. In figures 4.7, 4.8 and 4.9 the convergence of the approximated function, as well as the components $\frac{\partial \mathrm{v}}{\partial X}$ and $\frac{\partial \mathrm{v}}{\partial Y}$ of the approximated gradient, are plotted for the selected positions $[0.5, 5, 0.5]^T$, $[1, 5, 0.5]^T$, $[0.5, 10, 0.5]^T$ and $[1, 10, 0.5]^T$. The convergence rate for the same quantities is shown as an $L_2$ norm error plotted against the particle spacing in figures 4.10a and 4.10b. For such simple test case, no difference in results were observed when employing the different kernel options presented in this work.

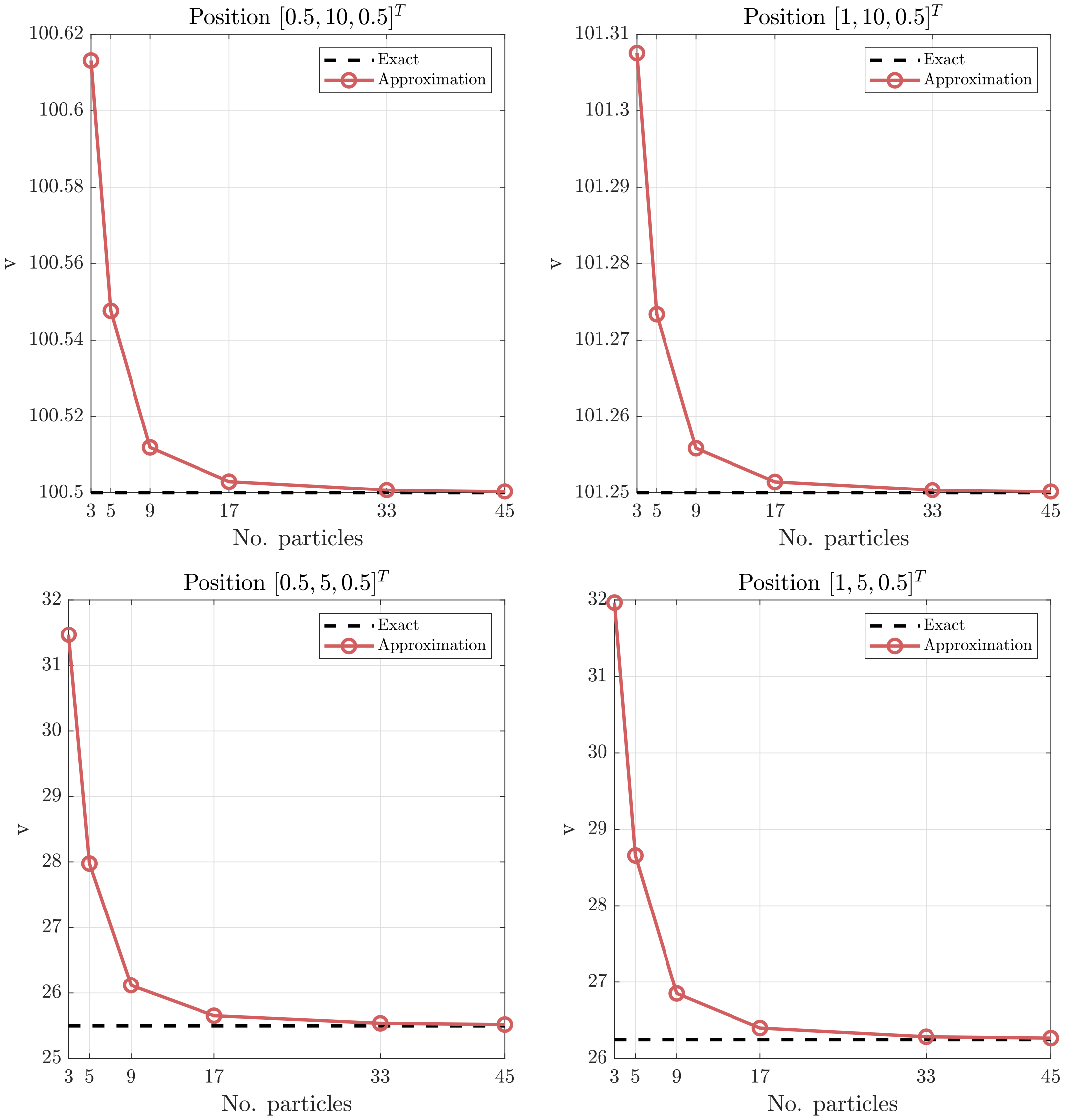

Figure 4.7: Convergence of approximated function $v$ computed at selected points.

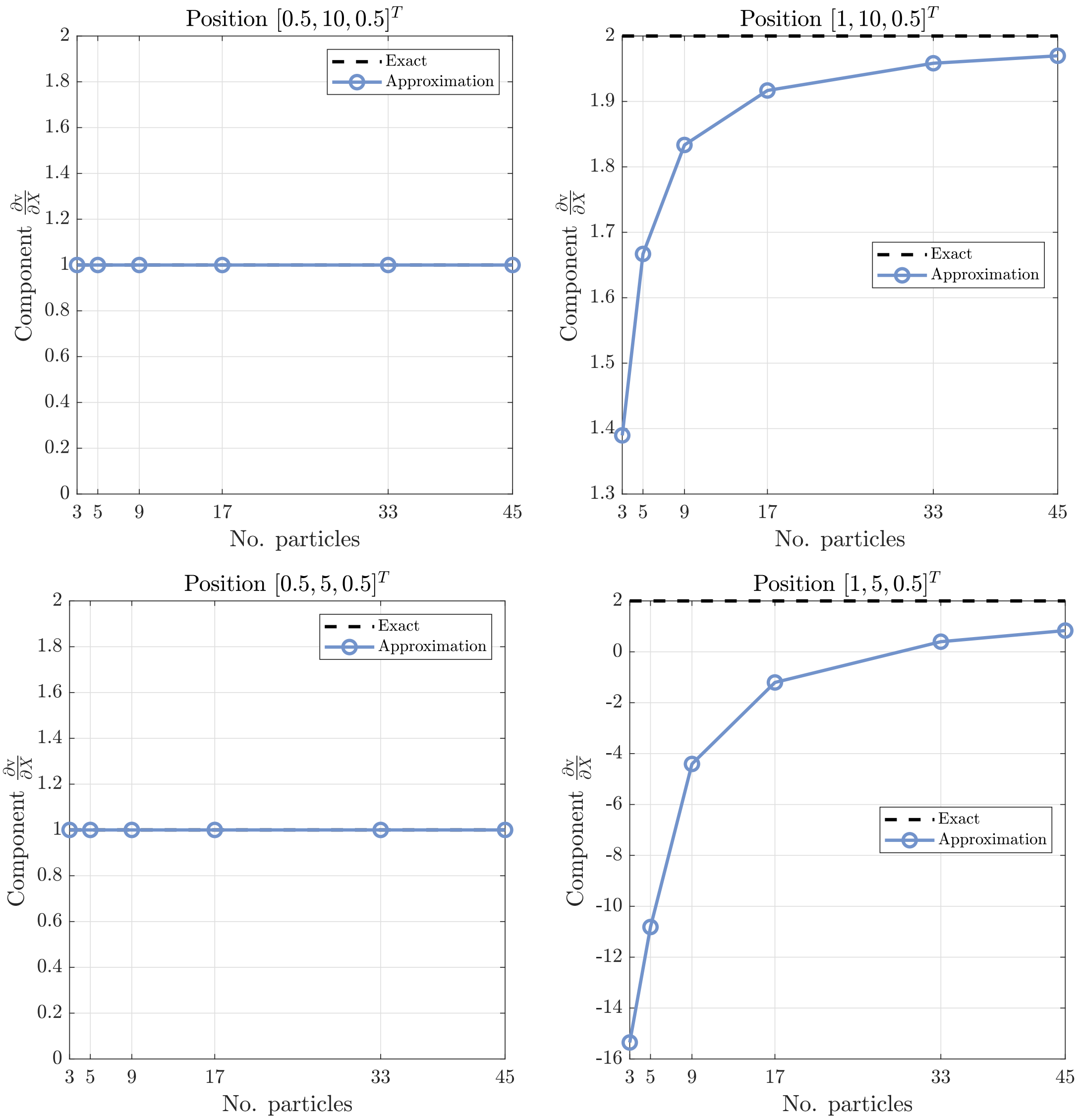

Figure 4.8: Convergence of the component $\frac{\partial \mathrm{v}}{\partial X}$ of the approximated gradient.

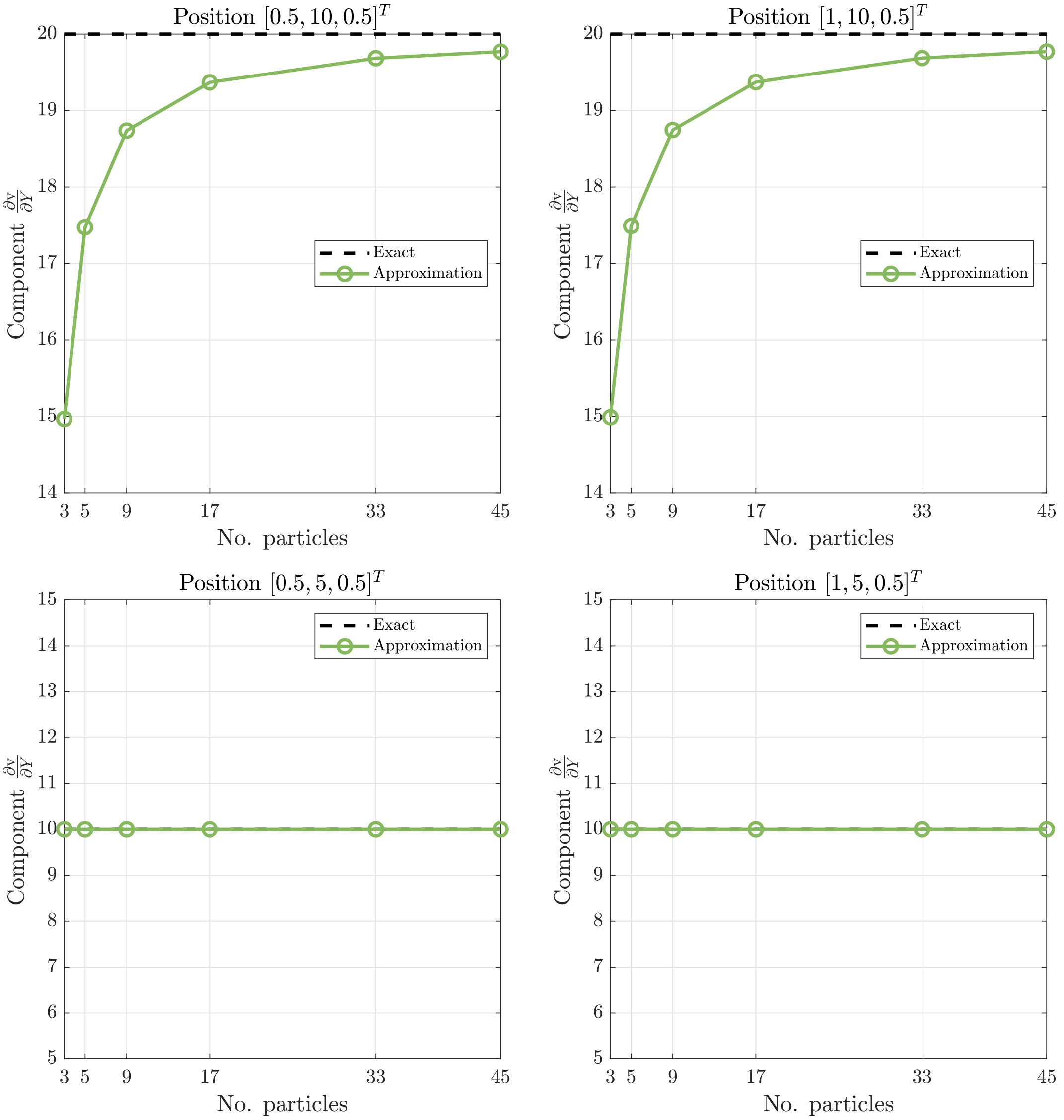

Figure 4.9: Convergence of the component $\frac{\partial \mathrm{v}}{\partial Y}$ of the approximated gradient.

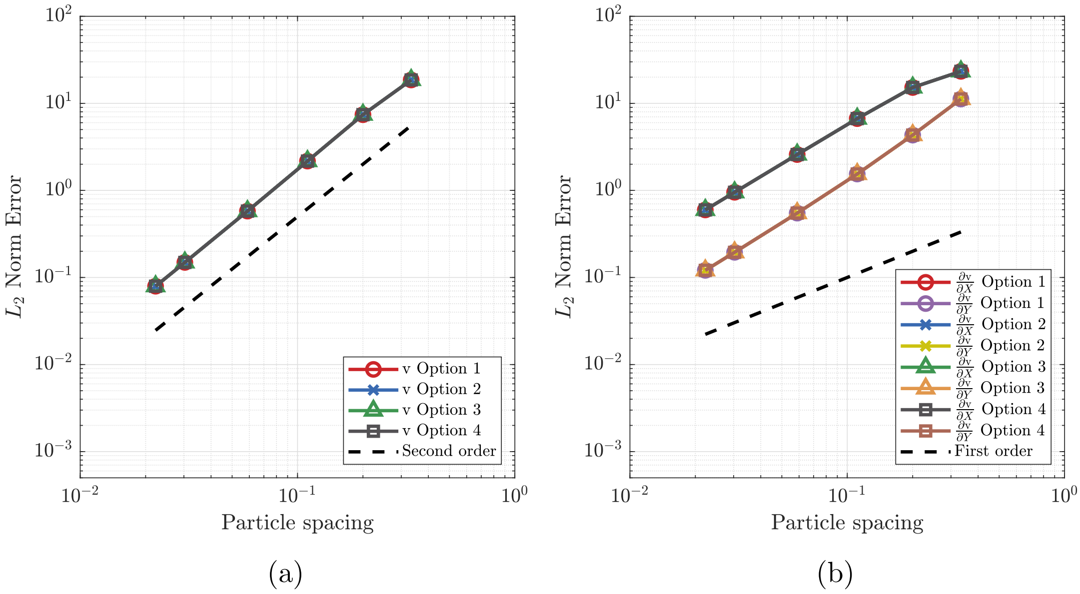

Figure 4.10: Convergence rate. a) Quadratic scalar field v. b) Components $\frac{\partial \mathrm{v}}{\partial X}$ and $\frac{\partial \mathrm{v}}{\partial Y}$ of the gradient of v.

## 4.6 Conclusion

This chapter reviewed the core concepts of the SPH method. The SPH approximation was presented departing from the sifting property of the Dirac delta function. The notation was defined and used with care to clarify the dualism of neighbour smoothing ("gather" vs. "scatter" processes). Remarkably, anisotropic types of compact support were developed to handle the strong anisotropic changes in the particle spacing observed in large deformation applications. Pull-back and push-forward operations of kernels and gradient of kernels were explored in combination with kernel and gradient corrections, leading to four robust anisotropic options.

# Chapter 5

# Stabilised updated reference Lagrangian SPH

## 5.1 Introduction

In this chapter the SPH framework, consisting of a stabilised updated reference Lagrangian set of equations, discretised using the SPH method, is fully developed. The chapter begins with the discretisation of the set of equations proposed in chapters 2 and 3. Afterwards, the Riemann-based stabilisation scheme is introduced, followed by the presentation of a linear reconstruction procedure and the time integration algorithm. The chapter ends with an algorithmic representation of the proposed framework.

## 5.2 Discrete equations

The set of total Lagrangian equations in 2.1-2.4 was discretised within the SPH formalism in [27], the equations are reproduced here to ease the understanding of this section.

$$V_a \frac{d\boldsymbol{p}_a}{dt} = \sum_{b\in\Lambda_a^b} \boldsymbol{T}_{ab} + V_a\boldsymbol{b}_a + A_a\boldsymbol{t}_a, \tag{5.1}$$

$$V_a \frac{d\boldsymbol{F}_a}{dt} = \sum_{b\in\Lambda_a^b} \frac{1}{2}(\boldsymbol{v}_b - \boldsymbol{v}_a) \otimes \boldsymbol{C}_{ba}^{\boldsymbol{X}}, \tag{5.2}$$

$$V_a \frac{d\boldsymbol{H}_a}{dt} = \boldsymbol{F}_a \boldsymbol{\times} \left( \sum_{b\in\Lambda_a^b} \frac{1}{2}(\boldsymbol{v}_b - \boldsymbol{v}_a) \otimes \boldsymbol{C}_{ba}^{\boldsymbol{X}} \right), \tag{5.3}$$

$$V_a \frac{dJ_a}{dt} = \boldsymbol{H}_a \colon \left( \sum_{b\in\Lambda_a^b} \frac{1}{2}(\boldsymbol{v}_b - \boldsymbol{v}_a) \otimes \boldsymbol{C}_{ba}^{\boldsymbol{X}} \right), \tag{5.4}$$

$$\begin{aligned} V_a \frac{dE_a}{dt} &= \sum_{b\in\Lambda_a^b} \frac{1}{2} \left[ \left(\boldsymbol{P}_a \boldsymbol{C}_{ba}^{\boldsymbol{X}}\right) \cdot \boldsymbol{v}_b - \left(\boldsymbol{P}_b \boldsymbol{C}_{ab}^{\boldsymbol{X}}\right) \cdot \boldsymbol{v}_a \right] \\ &\quad - \sum_{b\in\Lambda_a^b} \frac{1}{2} \left[ \left( \frac{\boldsymbol{Q}_a}{\theta_a} \cdot \boldsymbol{C}_{ba}^{\boldsymbol{X}} \right) \theta_b - \left( \frac{\boldsymbol{Q}_b}{\theta_b} \cdot \boldsymbol{C}_{ab}^{\boldsymbol{X}} \right) \theta_a \right] \\ &\quad + V_a \left( \boldsymbol{b}_a \cdot \boldsymbol{v}_a + s_{0,a} \right) + A_a \left( \boldsymbol{t}_a \cdot \boldsymbol{v}_a - Q_{B,a} \right). \end{aligned} \tag{5.5}$$

The pair-wise interacting force $\boldsymbol{T}_{ab}$ is given by

$$\boldsymbol{T}_{ab} = \frac{1}{2} \left( \boldsymbol{P}_a \boldsymbol{C}_{ba}^{\boldsymbol{X}} - \boldsymbol{P}_b \boldsymbol{C}_{ab}^{\boldsymbol{X}} \right), \tag{5.6}$$

with the (pseudo) area operators defined as

$$\boldsymbol{C}_{ba}^{\boldsymbol{X}} \coloneqq 2V_aV_b \tilde{\boldsymbol{\nabla}}_{\boldsymbol{X}} W_{ba}^{\boldsymbol{X}}, \qquad \boldsymbol{C}_{ab}^{\boldsymbol{X}} \coloneqq 2V_bV_a \tilde{\boldsymbol{\nabla}}_{\boldsymbol{X}} W_{ab}^{\boldsymbol{X}}. \tag{5.7}$$

Notice that the corrected pair-wise force expression 5.6 conserves linear momentum due to its anti-symmetry with respect to interchange of the particle indices $a$ and $b$.

As discussed in [27], the resulting spatially discretised system of equations suffers from severe numerical instabilities and requires some form of numerical dissipation. Using the same methodology, the set of updated reference Lagrangian equations described in 2.26-2.29 is now spatially discretised. The semi-discrete form of the first law of thermodynamics, written in terms of the total energy, completes the system of equations. Stabilisation terms, which will be developed later in this chapter, are added to the system now.

$$V_a^{\boldsymbol{\chi}} \frac{d\boldsymbol{p}_{\boldsymbol{\chi},a}}{dt} = \sum_{b\in\Lambda_a^b} \boldsymbol{T}_{ab}^{\boldsymbol{\chi}} + V_a^{\boldsymbol{\chi}} \boldsymbol{b}_{\boldsymbol{\chi},a} + A_a^{\boldsymbol{\chi}} \boldsymbol{t}_{\boldsymbol{\chi},a} + \sum_{b\in\Lambda_a^b} \boldsymbol{D}_{ab}^{\boldsymbol{p}_{\boldsymbol{\chi}}}, \tag{5.8}$$

$$V_a^{\boldsymbol{\chi}} \frac{d\boldsymbol{f}_a}{dt} = \sum_{b\in\Lambda_a^b} \frac{1}{2}(\boldsymbol{v}_b - \boldsymbol{v}_a) \otimes \boldsymbol{C}_{ba}^{\boldsymbol{\chi}}, \tag{5.9}$$

$$V_a^{\boldsymbol{\chi}} \frac{d\boldsymbol{h}_a}{dt} = \boldsymbol{f}_a \times \left( \sum_{b\in\Lambda_a^b} \frac{1}{2}(\boldsymbol{v}_b - \boldsymbol{v}_a) \otimes \boldsymbol{C}_{ba}^{\boldsymbol{\chi}} \right), \tag{5.10}$$

$$V_a^{\boldsymbol{\chi}} \frac{dj_a}{dt} = \boldsymbol{h}_a : \left( \sum_{b\in\Lambda_a^b} \frac{1}{2}(\boldsymbol{v}_b - \boldsymbol{v}_a) \otimes \boldsymbol{C}_{ba}^{\boldsymbol{\chi}} \right) + \sum_{b\in\Lambda_a^b} D_{ab}^{j}, \tag{5.11}$$

$$\begin{aligned} V_a^{\boldsymbol{\chi}} \frac{dE_{\boldsymbol{\chi},a}}{dt} &= \sum_{b\in\Lambda_a^b} \frac{1}{2} \left[ (\boldsymbol{\sigma}_{\boldsymbol{\chi},a} \boldsymbol{C}_{ba}^{\boldsymbol{\chi}}) \cdot \boldsymbol{v}_b - (\boldsymbol{\sigma}_{\boldsymbol{\chi},b} \boldsymbol{C}_{ab}^{\boldsymbol{\chi}}) \cdot \boldsymbol{v}_a \right] \\ &\quad - \sum_{b\in\Lambda_a^b} \frac{1}{2} \left[ \left( \frac{\boldsymbol{Q}_{\boldsymbol{\chi},a}}{\theta_a} \cdot \boldsymbol{C}_{ba}^{\boldsymbol{\chi}} \right) \theta_b - \left( \frac{\boldsymbol{Q}_{\boldsymbol{\chi},b}}{\theta_b} \cdot \boldsymbol{C}_{ab}^{\boldsymbol{\chi}} \right) \theta_a \right] \\ &\quad + V_a^{\boldsymbol{\chi}} \left( \boldsymbol{b}_{\boldsymbol{\chi},a} \cdot \boldsymbol{v}_a + s_{\boldsymbol{\chi},a} \right) + A_a^{\boldsymbol{\chi}} \left( \boldsymbol{t}_{\boldsymbol{\chi},a} \cdot \boldsymbol{v}_a - Q_{B,a} \right). \end{aligned} \tag{5.12}$$

In these equations, $V_a^{\boldsymbol{\chi}}$ and $A_a^{\boldsymbol{\chi}}$ are the volume and the area stored at the target particle $a$ in configuration $\Omega_{V\boldsymbol{\chi}}$, $\boldsymbol{v}_a = \frac{\boldsymbol{p}_{\boldsymbol{\chi},a}}{\rho_{\boldsymbol{\chi},a}}$ and $\boldsymbol{v}_b = \frac{\boldsymbol{p}_{\boldsymbol{\chi},b}}{\rho_{\boldsymbol{\chi},b}}$ are the velocities stored at particles $a$ and $b$, respectively. As before, $\boldsymbol{b}_{\boldsymbol{\chi},a}$ and $\boldsymbol{t}_{\boldsymbol{\chi},a}$ are body forces and surface tractions, $s_{\boldsymbol{\chi},a}$ represents a possible heat source and $Q_{B,a}$ represents a boundary heat flux. Note that in order to ensure the discrete satisfaction of the involutions presented in the continuum context, numerical dissipation is added only to equations 5.8 and 5.11. The development of these stabilisation terms is presented in section 5.3.

The pair-wise interacting force $\boldsymbol{T}_{ab}^{\boldsymbol{\chi}}$ is given by

$$\boldsymbol{T}_{ab}^{\boldsymbol{\chi}} = \frac{1}{2} \left( \boldsymbol{\sigma}_{\boldsymbol{\chi},a} \boldsymbol{C}_{ba}^{\boldsymbol{\chi}} - \boldsymbol{\sigma}_{\boldsymbol{\chi},b} \boldsymbol{C}_{ab}^{\boldsymbol{\chi}} \right), \tag{5.13}$$

with the (pseudo) area operators defined as

$$\boldsymbol{C}_{ba}^{\boldsymbol{\chi}} := 2 V_a^{\boldsymbol{\chi}} V_b^{\boldsymbol{\chi}} \tilde{\boldsymbol{\nabla}}_{\boldsymbol{\chi}} W_{ba}^{\boldsymbol{\chi}}, \qquad \boldsymbol{C}_{ab}^{\boldsymbol{\chi}} := 2 V_b^{\boldsymbol{\chi}} V_a^{\boldsymbol{\chi}} \tilde{\boldsymbol{\nabla}}_{\boldsymbol{\chi}} W_{ab}^{\boldsymbol{\chi}}. \tag{5.14}$$

The average of the (pseudo) area operators are defined as

$$\boldsymbol{C}_{ab}^{\boldsymbol{\chi}^{\text{Ave}}} := \frac{1}{2} \left( \boldsymbol{C}_{ba}^{\boldsymbol{\chi}} - \boldsymbol{C}_{ab}^{\boldsymbol{\chi}} \right), \qquad \boldsymbol{c}_{ab}^{\text{Ave}} := \frac{1}{2} \left( \boldsymbol{h}_a \boldsymbol{C}_{ba}^{\boldsymbol{\chi}} - \boldsymbol{h}_b \boldsymbol{C}_{ab}^{\boldsymbol{\chi}} \right). \tag{5.15}$$

The heat flux vector is evaluated at particle $a$ as

$$\boldsymbol{Q}_{\boldsymbol{\chi},a} = -\boldsymbol{K}_{\boldsymbol{\chi},a} \tilde{\boldsymbol{\nabla}}_{\boldsymbol{\chi}} \theta_a, \qquad \boldsymbol{K}_{\boldsymbol{\chi},a} = j_a^{-1} k \boldsymbol{h}_a^T \boldsymbol{h}_a, \tag{5.16}$$

with $k$ being the thermal conductivity of the material and the gradient $\tilde{\boldsymbol{\nabla}}_{\boldsymbol{\chi}} \theta_a$ obtained through a kernel approximation as $\tilde{\boldsymbol{\nabla}}_{\boldsymbol{\chi}} \theta_a = \sum_{b\in\Lambda_a^b} V_b^{\boldsymbol{\chi}} \left( \theta_b - \theta_a \right) \tilde{\boldsymbol{\nabla}}_{\boldsymbol{\chi}} W_{ba}^{\boldsymbol{\chi}}$. An analogous definition holds for $\boldsymbol{Q}_{\boldsymbol{\chi},b}$.

**Remark 6** *In order to obtain a relationship between the gradient evaluation of kernel functions defined in different configurations, we can start rewriting equation 5.9 as*

$$J_{\boldsymbol{\chi},a} V_a \frac{d\boldsymbol{f}_a}{dt} \boldsymbol{F}_{\boldsymbol{\chi},a} = \left( \sum_{b \in \Lambda_a^b} \frac{1}{2} (\boldsymbol{v}_b - \boldsymbol{v}_a) \otimes \boldsymbol{C}^{\boldsymbol{\chi}}_{ba} \right) \boldsymbol{F}_{\boldsymbol{\chi},a}, \tag{5.17}$$

*and then*

$$V_a \frac{d\boldsymbol{F}_a}{dt} = \left( \sum_{b \in \Lambda_a^b} \frac{1}{2} (\boldsymbol{v}_b - \boldsymbol{v}_a) \otimes \boldsymbol{C}^{\boldsymbol{\chi}}_{ba} \right) J^{-1}_{\boldsymbol{\chi},a} \boldsymbol{F}_{\boldsymbol{\chi},a} \tag{5.18a}$$

$$= \sum_{b \in \Lambda_a^b} \frac{1}{2} (\boldsymbol{v}_b - \boldsymbol{v}_a) \otimes J^{-1}_{\boldsymbol{\chi},a} \boldsymbol{F}^T_{\boldsymbol{\chi},a} \boldsymbol{C}^{\boldsymbol{\chi}}_{ba}. \tag{5.18b}$$

*Therefore, comparison of equations 5.18b and 5.2 leads to (Nanson's rule)*

$$\boldsymbol{C}^{\boldsymbol{\chi}}_{ba} = J_{\boldsymbol{\chi},a} \boldsymbol{F}^{-T}_{\boldsymbol{\chi},a} \boldsymbol{C}^{\boldsymbol{X}}_{ba}, \tag{5.19}$$

*which can be further expanded using the definitions from equations 5.7 and 5.14*

$$2 V^{\boldsymbol{\chi}}_a V^{\boldsymbol{\chi}}_b \tilde{\boldsymbol{\nabla}}_{\boldsymbol{\chi}} W^{\boldsymbol{\chi}}_{ba} = J_{\boldsymbol{\chi},a} \boldsymbol{F}^{-T}_{\boldsymbol{\chi},a} 2 V_a V_b \tilde{\boldsymbol{\nabla}}_{\boldsymbol{X}} W^{\boldsymbol{X}}_{ba}, \tag{5.20}$$

*which can be simplified as*

$$V^{\boldsymbol{\chi}}_b \tilde{\boldsymbol{\nabla}}_{\boldsymbol{\chi}} W^{\boldsymbol{\chi}}_{ba} = \boldsymbol{F}^{-T}_{\boldsymbol{\chi},a} V_b \tilde{\boldsymbol{\nabla}}_{\boldsymbol{X}} W^{\boldsymbol{X}}_{ba}, \tag{5.21}$$

*finally resulting in*

$$\tilde{\boldsymbol{\nabla}}_{\boldsymbol{\chi}} W^{\boldsymbol{\chi}}_{ba} = J^{-1}_{\boldsymbol{\chi},b} \boldsymbol{F}^{-T}_{\boldsymbol{\chi},a} \tilde{\boldsymbol{\nabla}}_{\boldsymbol{X}} W^{\boldsymbol{X}}_{ba}. \tag{5.22}$$

**Remark 7** *Note that in an isothermal context the total energy equation (5.12) becomes redundant. However, it is still meaningful for post-processing purposes. The evolution of the total energy itself can be monitored. Even further, the numerical dissipation added to the system can be obtained as the difference between the solved total energy and the summation of kinetic and internal energies.*

## 5.3 Riemann-based upwinding stabilisation

By taking advantage of the structure of the mixed-based set of equations 2.26-2.29, numerical stabilisation is added via a characteristic-based Riemann solver, introduced to the context of SPH in [27, 89–92]. The procedure to obtain consistent and locally conservative stabilisation terms starts by multiplying the semi-discrete equations by their dual energy conjugate variables. In a TLF context the work conjugates are $[\boldsymbol{v}_a, \boldsymbol{\Sigma}^a_{\boldsymbol{F}}, \boldsymbol{\Sigma}^a_{\boldsymbol{H}}, \Sigma^a_J]$, with $\boldsymbol{v}_a = \rho_0^{-1} \boldsymbol{p}_a$ and $\boldsymbol{\Sigma}^a_{\boldsymbol{F}}$, $\boldsymbol{\Sigma}^a_{\boldsymbol{H}}$ and $\Sigma^a_J$ defined in equation 2.32 (see also [27]). For the present updated reference Lagrangian formulation however, work conjugates are $\left[\boldsymbol{v}_a, \boldsymbol{\Sigma}^a_{\boldsymbol{f}}, \boldsymbol{\Sigma}^a_{\boldsymbol{h}}, \Sigma^a_j\right]$, with $\boldsymbol{v}_a = \rho^{-1}_{\boldsymbol{\chi},a} \boldsymbol{p}_{\boldsymbol{\chi},a}$ and $\boldsymbol{\Sigma}^a_{\boldsymbol{f}}$, $\boldsymbol{\Sigma}^a_{\boldsymbol{h}}$ and $\Sigma^a_j$ defined in equation 2.36. Consider

$$\frac{dE}{dt} = \sum_a V_a^{\mathcal{X}} \boldsymbol{v}_a \cdot \frac{d\boldsymbol{p}_{\mathcal{X},a}}{dt} + \sum_a V_a^{\mathcal{X}} \left[ \boldsymbol{\Sigma}_{\boldsymbol{f}}^a : \frac{d\boldsymbol{f}_a}{dt} + \boldsymbol{\Sigma}_{\boldsymbol{h}}^a : \frac{d\boldsymbol{h}_a}{dt} + \Sigma_j^a \frac{dj_a}{dt} \right], \tag{5.23}$$

where $E$ represents the total energy.

The first term on the right hand side of equation 5.23, summed over all particles, gives the time rate of the kinetic energy within the system, while the second summation results in the power of the internal forces. Physically, equation 5.23 represents the rate of the total energy, which is null within a closed system in exact continuum mechanics. However, due to the approximations introduced by time and space discretisation present in numerical methods, it happens that it may result less or, in the worst scenario, greater than zero. Thus, the need of adding numerical dissipation to the solution becomes evident.

Substituting 5.10 and 5.11 in equation 5.23, and using the properties of the tensor cross product gives

$$\begin{aligned} \frac{dE}{dt} =& \sum_a V_a^{\mathcal{X}} \boldsymbol{v}_a \cdot \frac{d\boldsymbol{p}_{\mathcal{X},a}}{dt} + \sum_a V_a^{\mathcal{X}} \left[ \left( \boldsymbol{\Sigma}_{\boldsymbol{f}}^a + \boldsymbol{\Sigma}_{\boldsymbol{h}}^a \boldsymbol{\times} \boldsymbol{f}_a + \Sigma_j^a \boldsymbol{h}_a \right) : \frac{d\boldsymbol{f}_a}{dt} \right] \\ &+ \sum_a \sum_{b \in \Lambda_a^b} \Sigma_j^a D_{ab}^j. \end{aligned} \tag{5.24}$$

Equation 5.24 can be rewritten noticing that

$$\left( \boldsymbol{\Sigma}_{\boldsymbol{f}}^a + \boldsymbol{\Sigma}_{\boldsymbol{h}}^a \boldsymbol{\times} \boldsymbol{f}_a + \Sigma_j^a \boldsymbol{h}_a \right) = \boldsymbol{\sigma}_{\mathcal{X},a}, \tag{5.25}$$

therefore

$$\frac{dE}{dt} = \sum_a V_a^{\mathcal{X}} \left[ \boldsymbol{v}_a \cdot \frac{d\boldsymbol{p}_{\mathcal{X},a}}{dt} + \boldsymbol{\sigma}_{\mathcal{X},a} : \frac{d\boldsymbol{f}_a}{dt} \right] + \sum_a \sum_{b \in \Lambda_a^b} \Sigma_j^a D_{ab}^j. \tag{5.26}$$

Substituting 5.8 and 5.9 in equation 5.26, after some algebraic manipulation involving the use of the properties of the double contraction, gives

$$\begin{aligned} \frac{dE}{dt} =& \sum_a \sum_{b \in \Lambda_a^b} \frac{1}{2} \left[ (\boldsymbol{\sigma}_{\mathcal{X},a} \boldsymbol{C}_{ba}^{\mathcal{X}}) \cdot \boldsymbol{v}_b - (\boldsymbol{\sigma}_{\mathcal{X},b} \boldsymbol{C}_{ab}^{\mathcal{X}}) \cdot \boldsymbol{v}_a \right] + \dot{\Pi}_{\text{ext}} \\ &+ \sum_a \sum_{b \in \Lambda_a^b} \left[ \boldsymbol{v}_a \cdot \boldsymbol{D}_{ab}^{\boldsymbol{p}_{\mathcal{X}}} + \Sigma_j^a D_{ab}^j \right], \end{aligned} \tag{5.27}$$

where the power of external forces was grouped as

$$\dot{\Pi}_{\text{ext}} = \sum_a \left( V_a^{\mathcal{X}} \boldsymbol{v}_a \cdot \boldsymbol{b}_{\mathcal{X},a} + A_a^{\mathcal{X}} \boldsymbol{v}_a \cdot \boldsymbol{t}_{\mathcal{X},a} \right). \tag{5.28}$$

The nested summation carried out over particles implies that the first summation term of 5.27 vanishes as a result of its anti-symmetric nature, resulting in

$$\frac{dE}{dt} - \dot{\Pi}_{\text{ext}} = \sum_a \sum_{b \in \Lambda_a^b} \left[ \boldsymbol{v}_a \cdot \boldsymbol{D}_{ab}^{\boldsymbol{p}_{\mathcal{X}}} + \Sigma_j^a D_{ab}^j \right]. \tag{5.29}$$

Rearranging the above expression, and noticing that the nested particle summation can be alternatively represented as a summation over edges by connecting neighbouring particles $a$ and $b$ (within a given support), equation 5.29 now becomes

$$\frac{dE}{dt} - \dot{\Pi}_{\text{ext}} = - \sum_{\substack{\text{edges} \\ a \leftrightarrow b}} \left[ (\boldsymbol{v}_b - \boldsymbol{v}_a) \cdot \boldsymbol{D}_{ab}^{\boldsymbol{p}_{\boldsymbol{\chi}}} + \left( \Sigma_j^b - \Sigma_j^a \right) D_{ab}^j \right]. \tag{5.30}$$

To guarantee non-negative (numerical) entropy production for every edge, which in this case is to ensure the time rate of total energy 5.30 $\leq 0$, appropriate numerical stabilisation can be introduced by defining $\left[ \boldsymbol{D}_{ab}^{\boldsymbol{p}_{\boldsymbol{\chi}}}, D_{ab}^j \right]$ as

$$\boldsymbol{D}_{ab}^{\boldsymbol{p}_{\boldsymbol{\chi}}} := \boldsymbol{S}_{ab}^{\boldsymbol{p}_{\boldsymbol{\chi}}} \left( \boldsymbol{v}_b - \boldsymbol{v}_a \right), \tag{5.31}$$

and

$$D_{ab}^j := S_{ab}^j \left( \Sigma_j^b - \Sigma_j^a \right). \tag{5.32}$$

The positive definite stabilisation tensor $\boldsymbol{S}_{ab}^{\boldsymbol{p}_{\boldsymbol{\chi}}}$ and the scalar $S_{ab}^j$ are expressed in terms of the physical pressure and shear wave speeds $c_{p,ab}^{\text{Ave}} = \frac{1}{2} \left( c_{p,a} + c_{p,b} \right)$ and $c_{s,ab}^{\text{Ave}} = \frac{1}{2} \left( c_{s,a} + c_{s,b} \right)$ as

$$\boldsymbol{S}_{ab}^{\boldsymbol{p}} = \frac{\rho_{\boldsymbol{\chi},ab}^{\text{Ave}} \| \boldsymbol{C}_{ab}^{\boldsymbol{\chi}^{\text{Ave}}} \|}{2} \left[ c_{p,ab}^{\text{Ave}} \boldsymbol{n}_{ab} \otimes \boldsymbol{n}_{ab} + c_{s,ab}^{\text{Ave}} \left( \boldsymbol{I} - \boldsymbol{n}_{ab} \otimes \boldsymbol{n}_{ab} \right) \right], \tag{5.33}$$

with $\boldsymbol{n}_{ab} = \frac{\boldsymbol{x}_b - \boldsymbol{x}_a}{\| \boldsymbol{x}_b - \boldsymbol{x}_a \|}$, and

$$S_{ab}^j = \frac{\boldsymbol{c}_{ab}^{\text{Ave}} \cdot \boldsymbol{c}_{ab}^{\text{Ave}}}{2 \rho_{\boldsymbol{\chi},ab}^{\text{Ave}} c_{p,ab}^{\text{Ave}} \| \boldsymbol{C}_{ab}^{\boldsymbol{\chi}^{\text{Ave}}} \|}. \tag{5.34}$$

The average density that features in equations 5.33 and 5.34 is computed as $\rho_{\boldsymbol{\chi},ab}^{\text{Ave}} = \frac{1}{2} \left( \rho_{\boldsymbol{\chi},a} + \rho_{\boldsymbol{\chi},b} \right)$.

**Remark 8** *In order to guarantee second order accuracy in space, a linear reconstruction procedure is employed for the evaluation of the neighbouring states of the Riemann values. Following the approach adopted in [27], for any individual component* $\mathcal{U}_{\boldsymbol{\chi}}$ *of a variable, the linear reconstructed value at any position* $\boldsymbol{\chi}$ *is in the form of*

$$\mathcal{U}_{\boldsymbol{\chi}} \left( \boldsymbol{\chi} \right) = \mathcal{U}_{\boldsymbol{\chi}}^a + \boldsymbol{\mathcal{G}}_a \cdot \left( \boldsymbol{\chi} - \boldsymbol{\chi}_a \right). \tag{5.35}$$

*In the present work a kernel estimate is employed in order to obtain the particle gradient operator, and therefore* $\boldsymbol{\mathcal{G}}_a$ *is computed as*

$$\boldsymbol{\mathcal{G}}_a = \sum_{b \in \Lambda_a^b} V_b^{\boldsymbol{\chi}} \left( \mathcal{U}_{\boldsymbol{\chi}}^b - \mathcal{U}_{\boldsymbol{\chi}}^a \right) \tilde{\boldsymbol{\nabla}}_{\boldsymbol{\chi}} W_{ba}^{\boldsymbol{\chi}}. \tag{5.36}$$

*Note that in [27], the particle gradient operator* $\boldsymbol{\mathcal{G}}_a$ *was computed as*

$$\boldsymbol{\mathcal{G}}_a = \left( \sum_{b \in \Lambda_a^b} \boldsymbol{\mathcal{N}}_{ab} \otimes \boldsymbol{\mathcal{N}}_{ab} \right)^{-1} \sum_{b \in \Lambda_a^b} \left( \frac{\mathcal{U}_{\boldsymbol{\chi}}^b - \mathcal{U}_{\boldsymbol{\chi}}^a}{\| \boldsymbol{\chi}_b - \boldsymbol{\chi}_a \|} \right) \boldsymbol{\mathcal{N}}_{ab}, \tag{5.37}$$

*with* $\boldsymbol{\mathcal{N}}_{ab} = \frac{\boldsymbol{\chi}_b - \boldsymbol{\chi}_a}{\|\boldsymbol{\chi}_b - \boldsymbol{\chi}_a\|}$.

*Notice that equations (5.35)-(5.37) do not guarantee that overshoot is avoided in the linear reconstruction process. To overcome this, limiters can be easily implemented e.g. [91–93].*

## 5.4 Time discretisation

The mixed-based system $[\boldsymbol{p}_{\boldsymbol{\chi}}, \boldsymbol{f}, \boldsymbol{h}, j]$ is rather large, it will only be suitable to employ an explicit type of time integrator. In this work, the three-stages Runge-Kutta scheme from [94] is employed. This is described by the following time update equations from time step $t^n$ to $t^{n+1}$

$$\boldsymbol{\mathcal{U}}_{\boldsymbol{\chi}}^{a^{\star}} = \boldsymbol{\mathcal{U}}_{\boldsymbol{\chi}}^{a^n} + \Delta_t \dot{\boldsymbol{\mathcal{U}}}_{\boldsymbol{\chi}}^{a^n}, \tag{5.38a}$$

$$\boldsymbol{\mathcal{U}}_{\boldsymbol{\chi}}^{a^{\star\star}} = \frac{3}{4}\boldsymbol{\mathcal{U}}_{\boldsymbol{\chi}}^{a^n} + \frac{1}{4}\left(\boldsymbol{\mathcal{U}}_{\boldsymbol{\chi}}^{a^{\star}} + \Delta_t \dot{\boldsymbol{\mathcal{U}}}_{\boldsymbol{\chi}}^{a^{\star}}\right), \tag{5.38b}$$

$$\boldsymbol{\mathcal{U}}_{\boldsymbol{\chi}}^{a^{n+1}} = \frac{1}{3}\boldsymbol{\mathcal{U}}_{\boldsymbol{\chi}}^{a^n} + \frac{2}{3}\left(\boldsymbol{\mathcal{U}}_{\boldsymbol{\chi}}^{a^{\star\star}} + \Delta_t \dot{\boldsymbol{\mathcal{U}}}_{\boldsymbol{\chi}}^{a^{\star\star}}\right). \tag{5.38c}$$

Note that in previous works [25–27], the two-stages scheme from [94] was employed

$$\boldsymbol{\mathcal{U}}_{\boldsymbol{\chi}}^{a^{\star}} = \boldsymbol{\mathcal{U}}_{\boldsymbol{\chi}}^{a^n} + \frac{\Delta_t}{2} \dot{\boldsymbol{\mathcal{U}}}_{\boldsymbol{\chi}}^{a^n}, \tag{5.39a}$$

$$\boldsymbol{\mathcal{U}}_{\boldsymbol{\chi}}^{a^{n+1}} = \boldsymbol{\mathcal{U}}_{\boldsymbol{\chi}}^{a^{\star}} + \frac{\Delta_t}{2} \dot{\boldsymbol{\mathcal{U}}}_{\boldsymbol{\chi}}^{a^{\star}}. \tag{5.39b}$$

Following [25–27], the geometry is also updated through the above algorithm. The result is a time integration procedure in which the unknowns $\boldsymbol{\mathcal{U}}_{\boldsymbol{\chi}} = (\boldsymbol{p}_{\boldsymbol{\chi}}, \boldsymbol{f}, \boldsymbol{h}, j)^T$ are updated along with the geometry $\boldsymbol{x}$ through equations 5.38 or 5.39. Morover, the maximum time step $\Delta_t := t^{n+1} - t^n$ is governed by a standard Courant–Friedrichs–Lewy (CFL) condition given as

$$\Delta_t = \alpha_{CFL} \min\left(\frac{\|\boldsymbol{x}_a - \boldsymbol{x}_b\|}{c_p^{ab}}\right), \tag{5.40}$$

where $\alpha_{CFL}$ is the CFL stability number and $c_p^{ab}$ is a nonlinear $p$-wave speed.

Note that for the formulation presented in this work, the characteristic particle spacing is computed with respect to the current configuration. Regarding the computation of pressure and shear wave speeds, the standard linear speeds are computed in the initial configuration as

$$\bar{c}_p = \sqrt{\frac{\lambda + 2\mu}{\rho_0}}, \qquad \bar{c}_s = \sqrt{\frac{\mu}{\rho_0}}, \tag{5.41}$$

with the shear modulus $\mu$ and the Lamé first parameter $\lambda$ given in terms of the Young's modulus $E$ and Poisson's ratio $\nu$ as $\mu = \frac{E}{2(1+\nu)}$ and $\lambda = \frac{E\nu}{(1+\nu)(1-2\nu)}$, respectively. Then, based on the derivations presented in [46], a nonlinear approximation is obtained dividing the linear wave speeds (5.41) by the average of the minimum stretch of particles $a$ and $b$, that is

$$c_p^{ab} = \frac{\bar{c}_p}{\lambda_{ab}}, \qquad c_s^{ab} = \frac{\bar{c}_s}{\lambda_{ab}}, \tag{5.42}$$

where $\lambda_{ab} = \frac{1}{2}\left(\lambda_a + \lambda_b\right)$, with $\lambda_a$ and $\lambda_b$ being the minimum stretch of particles $a$ and $b$, obtained in the spectral decomposition of the right Cauchy-Green tensor.

## 5.5 Conservation of angular momentum

The resulting SPH algorithm does not exactly fulfil conservation of angular momentum, since the strain measures $\{\boldsymbol{f}, \boldsymbol{h}, j\}$ are no longer exclusively obtained from the current geometry. Although deviation from strict conservation is minimal, a monolithic discrete angular momentum projection algorithm is presented, following the work of [25, 95]. In the numerical experiments, it was observed that activation of this algorithm is not strictly necessary unless “machine accurate” strict angular momentum conservation is sought. Specifically, the local internal nodal force $\boldsymbol{T}_a^{\boldsymbol{\mathfrak{X}}}$ is suitably modified (in a least-square sense) in order to preserve the global angular momentum, whilst still ensuring the global conservation of linear momentum.

Adapting the procedure presented in [95] to the Runge Kutta time integrator considered herein, sufficient conditions for the global preservation of the discrete linear and angular momentum within a time step are explicitly enforced at each of the three stages described as

$$\sum_a V_a^{\boldsymbol{\mathfrak{X}}} \boldsymbol{T}_a^{\boldsymbol{\mathfrak{X}},\alpha} = \boldsymbol{0}; \qquad \sum_a V_a^{\boldsymbol{\mathfrak{X}}} \boldsymbol{\mathfrak{X}}_a^{\alpha} \times \boldsymbol{T}_a^{\boldsymbol{\mathfrak{X}},\alpha} = \boldsymbol{0}, \tag{5.43}$$

where

$$\boldsymbol{\mathfrak{X}}_a^{\alpha} = \begin{cases} \boldsymbol{x}_a^n - \Delta t \boldsymbol{v}_a^n; & \alpha = n \\ \boldsymbol{x}_a^n + \frac{\Delta t}{6}\left(\boldsymbol{v}_a^{\star} - \boldsymbol{v}_a^n\right); & \alpha = \star \\ \boldsymbol{x}_a^n + \frac{\Delta t}{6}\left(\boldsymbol{v}_a^n + \boldsymbol{v}_a^{\star} + 4\boldsymbol{v}_a^{\star\star}\right); & \alpha = \star\star \end{cases} . \tag{5.44}$$

A least-square minimisation procedure is used to obtain a modified set of internal nodal forces $\hat{\boldsymbol{T}}_a^{\boldsymbol{\mathfrak{X}}}$ that satisfy the above conditions. This can be achieved by computing the minimum of the following functional (ignoring time arguments for brevity)

$$\begin{aligned} \Pi(\hat{\boldsymbol{T}}_a^{\boldsymbol{\mathfrak{X}}}, \boldsymbol{\lambda}_{\text{ang}}, \boldsymbol{\lambda}_{\text{lin}}) &= \frac{1}{2}\sum_a V_a^{\boldsymbol{\mathfrak{X}}} (\hat{\boldsymbol{T}}_a^{\boldsymbol{\mathfrak{X}}} - \boldsymbol{T}_a^{\boldsymbol{\mathfrak{X}}}) \cdot (\hat{\boldsymbol{T}}_a^{\boldsymbol{\mathfrak{X}}} - \boldsymbol{T}_a^{\boldsymbol{\mathfrak{X}}}) \\ &\quad - \boldsymbol{\lambda}_{\text{ang}} \cdot \left(\sum_a V_a^{\boldsymbol{\mathfrak{X}}} \boldsymbol{\mathfrak{X}}_a \times \hat{\boldsymbol{T}}_a^{\boldsymbol{\mathfrak{X}}}\right) - \boldsymbol{\lambda}_{\text{lin}} \cdot \left(\sum_a V_a^{\boldsymbol{\mathfrak{X}}} \hat{\boldsymbol{T}}_a^{\boldsymbol{\mathfrak{X}}}\right). \end{aligned} \tag{5.45}$$

After some simple algebra, a modified set of internal nodal forces $\hat{\boldsymbol{T}}_a$ is in the form of

$$\hat{\boldsymbol{T}}_a^{\boldsymbol{\mathfrak{X}}} = \boldsymbol{T}_a^{\boldsymbol{\mathfrak{X}}} + \boldsymbol{\lambda}_{\text{ang}} \times \boldsymbol{\mathfrak{X}}_a + \boldsymbol{\lambda}_{\text{lin}}, \tag{5.46}$$

where the Lagrange multipliers $\{\boldsymbol{\lambda}_{\text{ang}}, \boldsymbol{\lambda}_{\text{lin}}\}$ are the solution of the following system of equations

$$\begin{bmatrix} \sum_a V_a^{\boldsymbol{\mathcal{X}}} \left[(\boldsymbol{\mathcal{X}}_a \cdot \boldsymbol{\mathcal{X}}_a)\boldsymbol{I} - \boldsymbol{\mathcal{X}}_a \otimes \boldsymbol{\mathcal{X}}_a\right] & \sum_a V_a^{\boldsymbol{\mathcal{X}}} \hat{\boldsymbol{\mathcal{X}}}_a \\ \sum_a V_a^{\boldsymbol{\mathcal{X}}} \hat{\boldsymbol{\mathcal{X}}}_a & -\sum_a V_a^{\boldsymbol{\mathcal{X}}} \end{bmatrix} \begin{bmatrix} \boldsymbol{\lambda}_{\text{ang}} \\ \boldsymbol{\lambda}_{\text{lin}} \end{bmatrix} = \begin{bmatrix} -\sum_a V_a^{\boldsymbol{\mathcal{X}}} \boldsymbol{\mathcal{X}}_a \times \boldsymbol{T}_a^{\boldsymbol{\mathcal{X}}} \\ \sum_a V_a^{\boldsymbol{\mathcal{X}}} \boldsymbol{T}_a^{\boldsymbol{\mathcal{X}}} \end{bmatrix}, \tag{5.47}$$

with the indicial notation $\left[\hat{\boldsymbol{\mathcal{X}}}_a\right]_{ik} = \mathcal{E}_{ijk} \left[\boldsymbol{\mathcal{X}}_a\right]_j$. Refer to Appendix D for a more detailed development of these expressions.

## 5.6 Complete algorithm

**Algorithm 5:** Stabilised updated Lagrangian SPH

```
Input  : initial geometry $\boldsymbol{X}_a$ and initial states of $\boldsymbol{p}_{\boldsymbol{\chi},a}$, $\boldsymbol{f}_a$, $\boldsymbol{h}_a$ $j_a$
Output: current geometry $\boldsymbol{x}_a$, particle velocity $\boldsymbol{v}_a$ and current states of $\boldsymbol{F}_a$, $\boldsymbol{H}_a$ and $J_a$

(1) INITIALISE $\boldsymbol{F}_{\boldsymbol{\chi},a} = \boldsymbol{H}_{\boldsymbol{\chi},a} = \boldsymbol{I}$, $J_{\boldsymbol{\chi},a} = 1$ and $\boldsymbol{x}_a = \boldsymbol{\chi}_a = \boldsymbol{X}_a$
(2) FIND neighbouring particles within a given support size $(\Lambda_a^b)$
(3) COMPUTE corrected kernel and gradient approximations at $\boldsymbol{X}_a$: $\tilde{W}_{ba}^{\boldsymbol{X}}$ and $\tilde{\boldsymbol{\nabla}}_{\boldsymbol{X}} W_{ba}^{\boldsymbol{X}}$
for Time $t_0$ to Time $t$ do
    if update at this step = TRUE then
        (4) COMPUTE the velocity as $\boldsymbol{v}_a = \frac{J_{\boldsymbol{\chi},a}\boldsymbol{p}_{\boldsymbol{\chi},a}}{\rho_0}$
        (5) ASSIGN $\boldsymbol{F}_{\boldsymbol{\chi},a} \leftarrow \boldsymbol{f}_a \boldsymbol{F}_{\boldsymbol{\chi},a}$, $\boldsymbol{H}_{\boldsymbol{\chi},a} \leftarrow \boldsymbol{h}_a \boldsymbol{H}_{\boldsymbol{\chi},a}$, $J_{\boldsymbol{\chi},a} \leftarrow j_a J_{\boldsymbol{\chi},a}$ and $\boldsymbol{\chi}_a \leftarrow \boldsymbol{x}_a$
        (6) UPDATE the linear momentum $\boldsymbol{p}_{\boldsymbol{\chi},a} = J_{\boldsymbol{\chi},a}^{-1} \rho_0 \boldsymbol{v}_a$ and all other relevant variables
        (7) REINITIALISE $\boldsymbol{f}_a$, $\boldsymbol{h}_a$, $j_a$
        (8) COMPUTE corrected kernel and gradient approximations at $\boldsymbol{\chi}_a$: $\tilde{W}_{ba}^{\boldsymbol{\chi}}$ and $\tilde{\boldsymbol{\nabla}}_{\boldsymbol{\chi}} W_{ba}^{\boldsymbol{\chi}}$
    end
    (9) EVALUATE $p$ and $s$-wave speeds: $c_p$, $c_s$
    (10) COMPUTE time increment: $\Delta t$
    for Runge-Kutta time integrator = 1 to 3 do
        (11) COMPUTE slope of linear reconstruction procedure
        (12) COMPUTE right-hand-side of the mixed-based system:
               $\dot{\boldsymbol{p}}_{\boldsymbol{\chi},a}$, $\dot{\boldsymbol{f}}_a$, $\dot{\boldsymbol{h}}_a$ and $\dot{j}_a$
        (13) ENSURE conservation of angular momentum
        (14) COMPUTE smoothed velocities using the corrected kernel
        (15) EVOLVE $\boldsymbol{p}_{\boldsymbol{\chi},a}$, $\boldsymbol{f}_a$, $\boldsymbol{h}_a$ $j_a$ and $\boldsymbol{x}_a$
        (16) COMPUTE $\boldsymbol{\sigma}_{\boldsymbol{\chi},a}$
    end
    (17) COMPUTE smoothed variables using the corrected kernel
    (18) EXPORT results for this time step
    (19) ADVANCE in time
end
```

Note that, in practice, the use of the proposed updated reference Lagrangian formulation allows one to retrieve the standard Total Lagrangian Formulation. For this purpose, the conditional statement in algorithm 5 should evaluate as “FALSE” always, i.e., the reference domain is kept constant throughout the simulation and therefore, the corrected kernel and gradient approximations are computed only once. On the other hand, if the conditional statement is evaluated as “TRUE” at every time step, a truly Updated Lagrangian Formulation is retrieved and the corrections for the kernel and gradient are performed for every time step, which can be computationally costly. One advantage of having an updated reference Lagrangian formulation is that the updating of the reference configuration can be chosen to be performed only when it is convenient, possibly reducing the need of computing corrected kernel and gradient approximations.

In algorithm 5, only one search for neighbouring particles is performed over the initial geometry, in step (2). However, when dealing with cases in which particle split and separation are present, such as fracture and fragmentation, a new search may be necessary right before recomputing the corrected kernel and gradient.

The algorithm and the concept of updating the initial geometry only at some specified time steps are illustrated in figure 5.1. The proposed Updated Reference Lagrangian algorithm comprises a series of multiplicative incremental configurations as illustrated in the figure. For instance, from time $t_n$ to $t_{2n}$, the complete deformation gradient at time $t_{2n}$, namely $\boldsymbol{F}_{2n}$, is evaluated via the previously computed deformation gradient $\boldsymbol{F}_n$ (now being stored and assigned as a deformation gradient at intermediate configuration $\Omega_v(t_n)$) and a series of incremental deformation gradients $\{\boldsymbol{f}_{\Delta_1}, \boldsymbol{f}_{\Delta_2}, \dots, \boldsymbol{f}_{\Delta_n}\}$ between the reference configuration $\Omega_v(t_n)$ and the new configuration $\Omega_v(t_{2n})$.

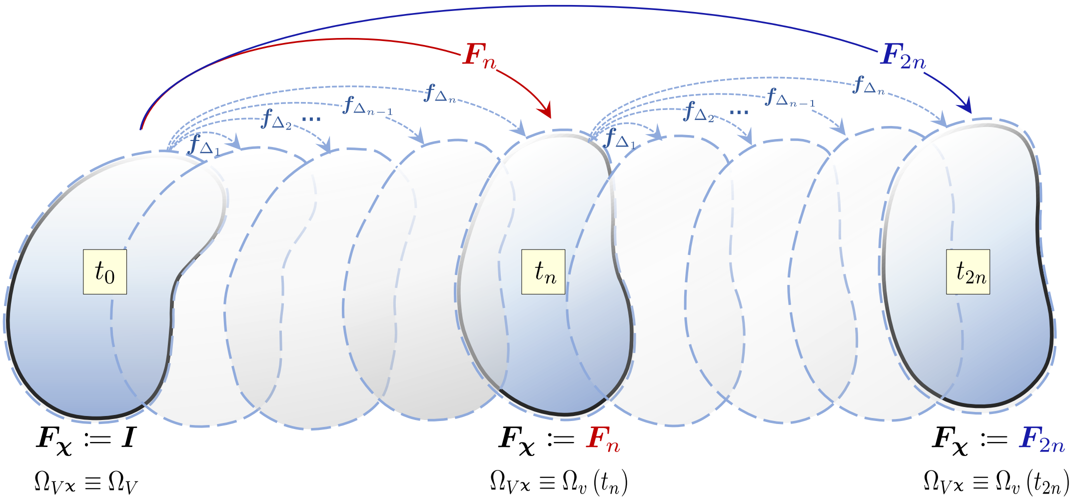

Figure 5.1: Updated reference Lagrangian scheme. At times $t_n$ and $t_{2n}$ an update is performed. Not only $\boldsymbol{F}_{\boldsymbol{\chi}}$, but also the other deformation variables ($\boldsymbol{H}_{\boldsymbol{\chi}}$ and $J_{\boldsymbol{\chi}}$) are updated. The particle positions are updated using the current positions, i.e., $\boldsymbol{\chi} \leftarrow \boldsymbol{x}$. The incremental deformation variables ($\boldsymbol{f}$, $\boldsymbol{h}$ and $j$) are re-initialised. Corrected kernels and gradients are re-computed at times $t_n$ and $t_{2n}$ using the updated domain.

## 5.7 Conclusion

This chapter applied the SPH discretisation technique to the set of conservation laws, including the total energy equation. The chapter serves to develop, describe and illustrate all numerical ingredients required by the computational framework. A consistent Riemann-based stabilisation scheme was fully developed without resorting to any artificial parameter. Second-order accuracy in space and time were ensured via a linear reconstruction procedure and the use of a three stages Runge-Kutta time integrator, respectively. A nonlinear approximation of pressure and shear wave speeds, required to compute stable time increments as well as physically-based stabilisation terms, was also discussed. Finally, an angular momentum preserving algorithm compatible with the proposed time integrator was developed.

# Chapter 6

# Isothermal numerical examples

## 6.1 Introduction

This chapter is intended to exploit the capabilities of the framework through several numerical examples in an isothermal context. Challenging test cases are analysed comprising a variety of geometries and constitutive models.

## 6.2 Isothermal elasticity

### 6.2.1 Convergence

As presented in references [25–27], this example shows a cube of unit side length (see Figure 6.1) with symmetric boundary conditions (i.e. roller supports) at faces $X = 0$, $Y = 0$ and $Z = 0$ and skew-symmetric boundary conditions (i.e. restricted tangential displacement) at faces $X = 1$, $Y = 1$ and $Z = 1$. The objective of this example is to assess the spatial convergence behaviour of the proposed formulation.

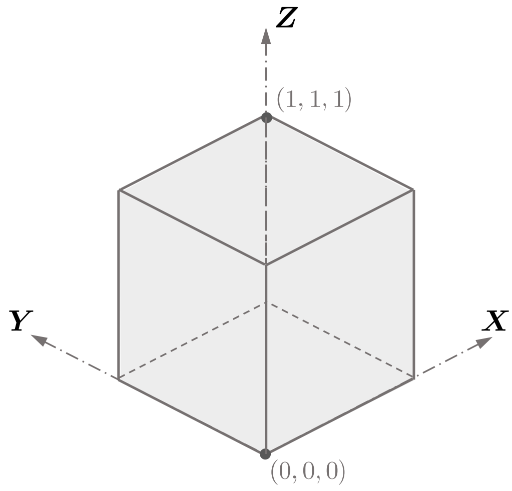

Figure 6.1: Convergence cube.

For small deformations, the problem has a closed-form displacement field of the form

$$\boldsymbol{u}\left(\boldsymbol{X},t\right)=U_0\cos\left(\frac{\sqrt{3}}{2}\bar{c}_p\pi t\right)\begin{bmatrix}A\sin\left(\frac{\pi X_1}{2}\right)\cos\left(\frac{\pi X_2}{2}\right)\cos\left(\frac{\pi X_3}{2}\right)\\ B\cos\left(\frac{\pi X_1}{2}\right)\sin\left(\frac{\pi X_2}{2}\right)\cos\left(\frac{\pi X_3}{2}\right)\\ C\cos\left(\frac{\pi X_1}{2}\right)\cos\left(\frac{\pi X_2}{2}\right)\sin\left(\frac{\pi X_3}{2}\right)\end{bmatrix},\quad \bar{c}_p=\sqrt{\frac{\lambda+2\mu}{\rho_0}}. \tag{6.1}$$

The simulation is carried out assuming $A=B=C=1$, $U_0=5\times10^{-4}$m and initial density $\rho_0=1100\frac{\text{kg}}{\text{m}^3}$, Young's modulus $E=1.7\times10^7\frac{\text{N}}{\text{m}^2}$ and Poisson's ratio $\nu=0.3$ were adopted as the material parameters for a nearly incompressible neo-Hookean constitutive model. A fixed $\alpha_{CFL}=0.9$ was used for the simulations.

The problem is initialised with a given deformation gradient $\boldsymbol{F}(\boldsymbol{X},0)=\boldsymbol{I}+\boldsymbol{\nabla}_{\boldsymbol{X}}\boldsymbol{u}$ where the terms $\boldsymbol{\nabla}_{\boldsymbol{X}}\boldsymbol{u}$ are evaluated from the above expression 6.1. The convergence analysis is carried out by measuring $L_2$ norm errors between the numerical and analytical solutions. Figure 6.2 depicts the expected second order $L_2$ norm convergence pattern for both velocities and the components of the deformation gradient.

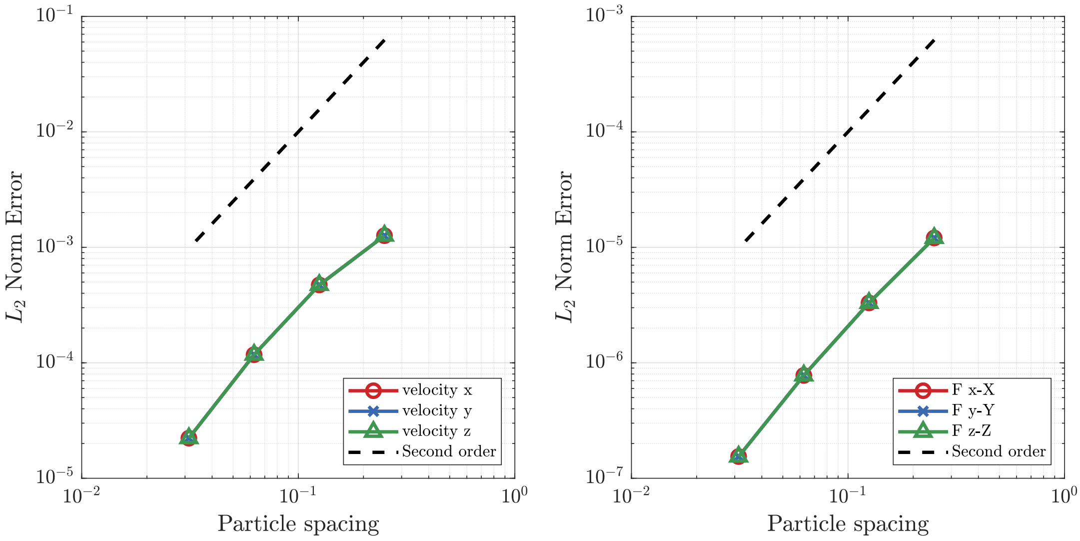

(a) (b)

Figure 6.2: (a) Velocities. (b) Deformation gradient.

### 6.2.2 Square cross-section column

As a first general example, a column with square cross-section 1m x 1m and 6m long is subjected to three different dynamic loading cases: bending, tensile and twisting, as illustrated in figure 6.3. A uniform distribution of (5 x 5 x 25) particles was employed for the three cases. Additional refined models were also studied: (7 x 7 x 35), (9 x 9 x 49) and (17 x 17 x 97) particles. For this specific example, the total volume was equally distributed between the particles. Note that the minimum number of neighbours that a particle can have is 8 (the corner particles), while the maximum number (a central particle) is 27, including itself. Initial density $\rho_0=1100\frac{\text{kg}}{\text{m}^3}$, Young's modulus $E=1.7\times10^7\frac{\text{N}}{\text{m}^2}$ and Poisson's ratio $\nu=0.3$

were adopted as the material parameters for a nearly incompressible neo-Hookean constitutive model. A fixed $\alpha_{CFL} = 0.9$ was used for the simulations.

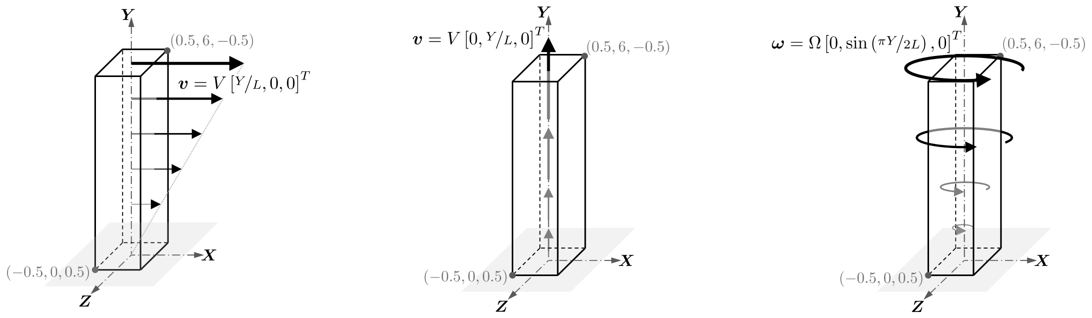

(a) (b) (c)

Figure 6.3: Column test cases. (a) Bending. (b) Tensile. (c) Twisting.

In what follows, results may be measured at specific locations of the column, in figure 6.4a these points are identified from $N_1$ to $N_{15}$. Moreover, for the twisting column, the twisting angle may be of interest. The time evolution of the angle $\theta$ illustrated in figure 6.4b will be plotted for different measurement points. Note that the initial angle of each point is measured from axis $\boldsymbol{X}$ in a counter-clockwise direction, meaning that position $N_{11}$, for example, has an initial angle $\theta = 225°$, position $N_{12}$ has an initial angle $\theta = 315°$, position $N_{13}$ has an initial angle $\theta = 45°$ and position $N_{14}$ has an initial angle $\theta = 135°$. The measurement of the angle $\theta$ is continuously accumulated along the simulation.

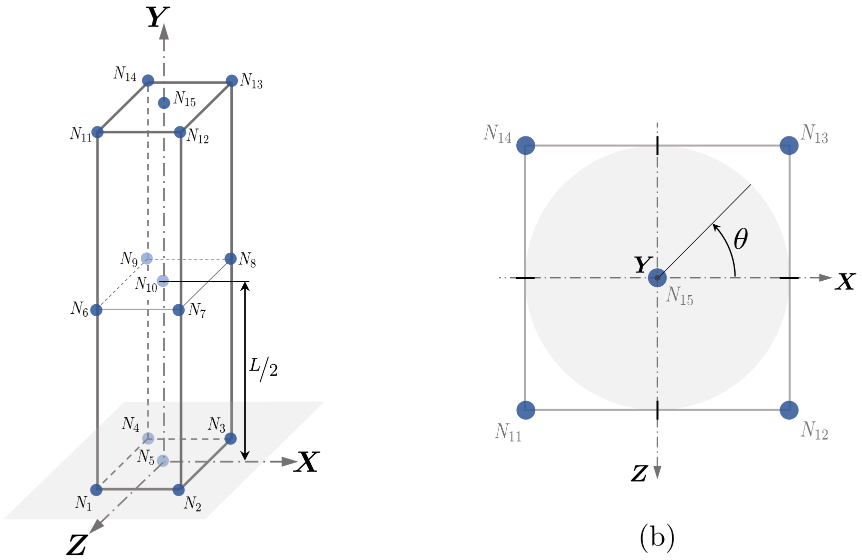

(a) (b)

Figure 6.4: (a) Identification of measurement points in the column. (b) Twisting angle.

### Bending column

The bending column case is illustrated in Figure 6.3a. This example simulates a column travelling with an initial speed, which is suddenly fixed at its base. An initial velocity $\boldsymbol{v}$ was defined as $\boldsymbol{v} = V\left[{}^{Y}\!/_{L}, 0, 0\right]^T$, where $V = 10\frac{\mathrm{m}}{\mathrm{s}}$ and $L = 6\mathrm{m}$. No further loading is applied to the column and the only restriction applied to this model is at the bottom face (particles presenting coordinates $Y = 0$), which is constrained in all directions.

The main objective of this problem [24, 25, 96, 97] is to assess the applicability of the proposed algorithm by carrying out frequent updates of the reference configuration. Doing this with the classical SPH algorithm [24] would activate spurious mechanisms, and eventually lead to the breakdown of the scheme. For this reason, updates of the reference configuration are carried out at every time step. Obviously this is unnecessary but has been done on purpose to check if the algorithm would trigger possible instabilities. In this example, the anisotropic updated kernel and kernel gradient are obtained as a push-forward of the corrected material kernel and corrected material gradient (Option#1). A 3D quadratic smoothing function is employed with a factor $f_h = 0.6$ for all the simulations.

In figure 6.5, the pressure distribution is plotted at different instants of the simulation, for a Total Lagrangian Formulation and also for an updated reference Lagrangian formulation (ULF), with updates performed at every time step.

Evolution of internal, kinetic and total energies is shown for both TLF and ULF in figure 6.6a. In addition, in figure 6.6b the deviatoric and the volumetric components of the internal energy are plotted separated for both cases. Note that the numerical dissipation is not added to the total energy in figure 6.6a, and therefore the total energy of the system slightly decreases along the simulation. The evolution of total energy considering different model refinements is shown for both TLF and ULF in figures 6.7a and 6.7b, respectively. Uniform distributions of (5 x 5 x 25), (7 x 7 x 35), (9 x 9 x 49) and (17 x 17 x 97) particles were compared. The pressure distribution at time 0.450s is shown for the four models in figure 6.8 for an updated reference Lagrangian formulation, with updates performed at every time step. Since internal energy is initially zero for this example and no dissipation mechanisms are present, the exact total energy remains constant and equal in magnitude to the initial kinetic energy of the system. Therefore, the exact solution plotted in figures 6.7a and 6.7b is obtained by computing $\int_{\Omega_V} \frac{1}{2}\rho_0 \boldsymbol{v}\cdot\boldsymbol{v}\, dV$, with $\boldsymbol{v} = V\left[{}^{Y}\!/_{L}, 0, 0\right]^T$.

In figure 6.9a, the x and y coordinates of the particle located at position $N_{15}$ are tracked for both TLF and ULF for the coarse (5 x 5 x 25) model. In addition, the numerical dissipation in the same model is shown in figure 6.9b. The same results are shown for the most refined model (17 x 17 x 97) in figures 6.9c and 6.9d.

In the results identified as “ULF” the updates were performed at every time step. Even though this is not needed, performing this test ensures that the updates are not activating any spurious mechanisms. In figure 6.10a, for the model (5 x 5 x 25), the evolution of internal, kinetic and total energies is also shown for updates performed at every 30 time steps (ULF30), the results are compared to TLF. In figure 6.10b the total energies for models considering updates at every 3, 30 and 300 time steps are compared to TLF and to the exact solution.

The results presented up to now employed a 3D quadratic kernel function for the SPH approximation. An alternative option (3D cubic spline) is available within the proposed framework. In figure 6.11a, for the model (5 x 5 x 25), the evolution of

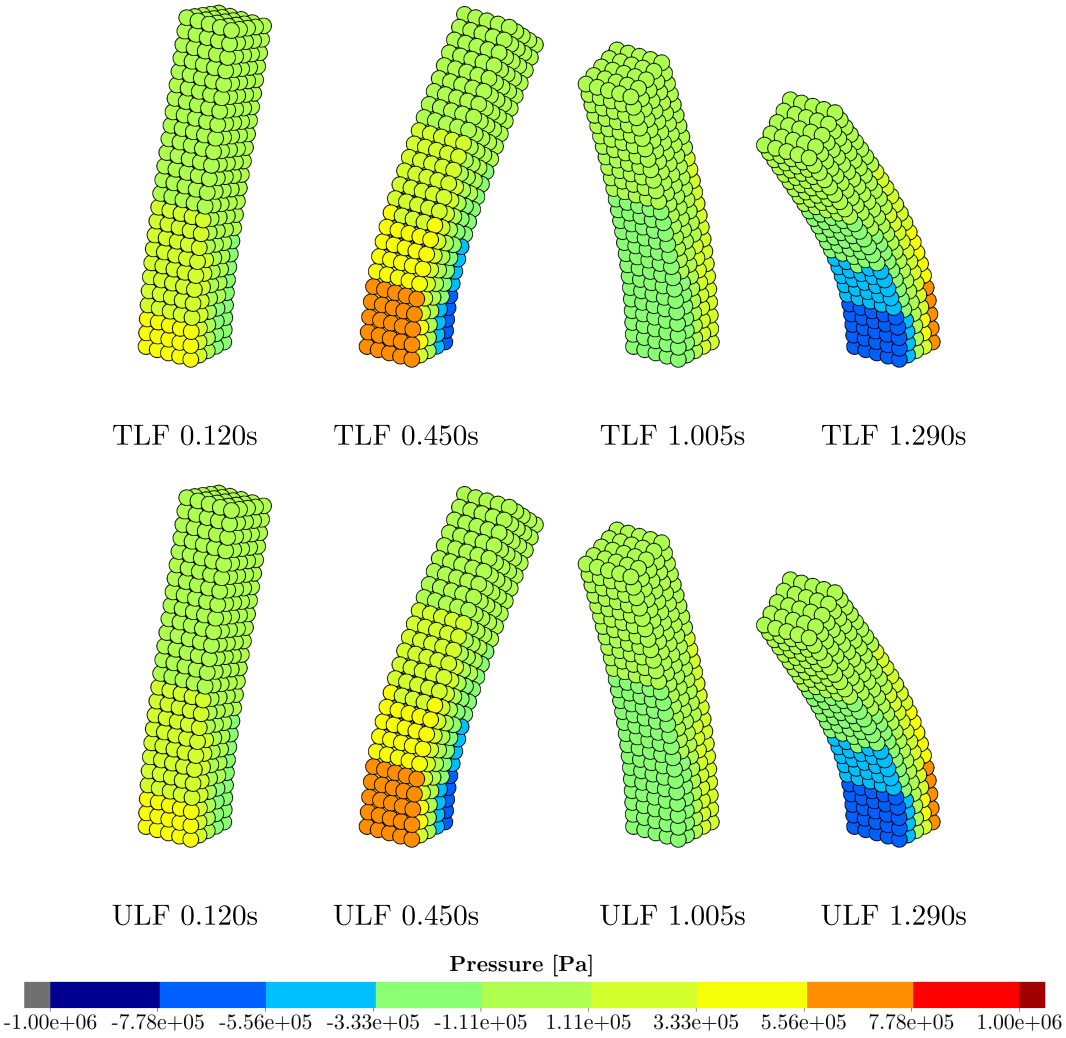
TLF 0.120s TLF 0.450s TLF 1.005s TLF 1.290s

ULF 0.120s ULF 0.450s ULF 1.005s ULF 1.290s

Figure 6.5: Bending column (5 x 5 x 25) pressure distribution.

internal, kinetic and total energies is shown comparing these two smoothing functions. In addition, in figure 6.11b the deviatoric and the volumetric components of the internal energy are plotted separated for both cases. Considering this alternative smoothing function, the evolution of total energy considering different model refinements is shown for both TLF and ULF in figures 6.12a and 6.12b, respectively. Uniform distributions of (5 x 5 x 25), (7 x 7 x 35), (9 x 9 x 49) and (17 x 17 x 97) particles were compared. The pressure distribution at time 0.450s is shown for the four models in figure 6.13 for an updated reference Lagrangian formulation, with updates performed at every time step.

As the conclusions of the bending column example, the proposed formulation was shown to be robust and did not activate any spurious mechanisms in this test case. The results for the simulations evolved based on updated reference configurations are as good as the ones based on the initial geometry (TLF). Remarkably, even with a small number of particles, the obtained result agrees very well with the Total Lagrangian result. No instabilities are observed. For completeness, the same problem was also simulated updating the reference configuration at every 3, 30 and 300 time steps. Exactly the same results were obtained. The consistency of

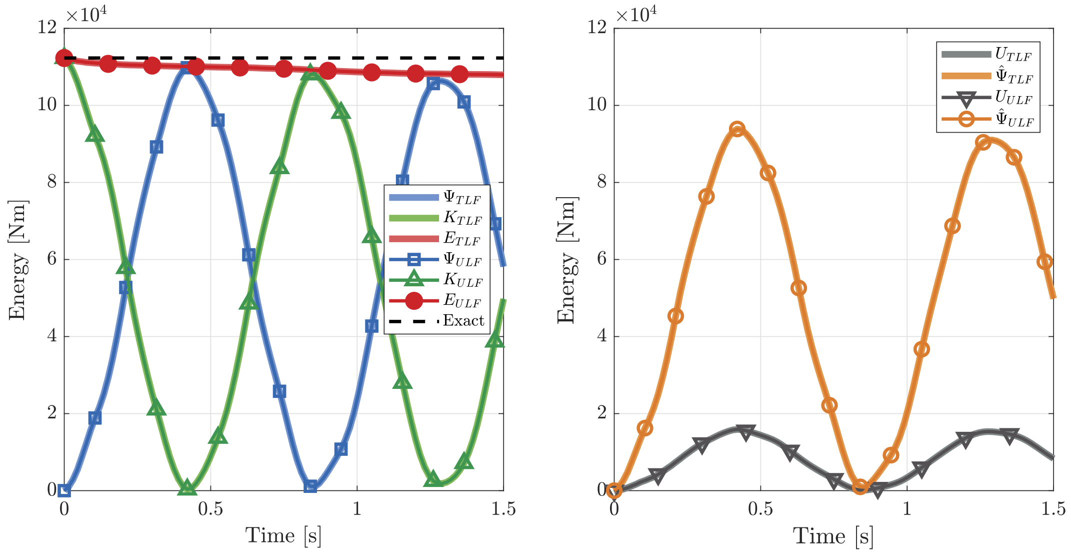

(a) (b)

Figure 6.6: (a) Evolution of kinetic ($K$), internal ($\Psi$) and total ($E$) energies for bending column (5 x 5 x 25). (b) Evolution of deviatoric ($\hat{\Psi}$) and volumetric ($U$) components of internal energy for bending column (5 x 5 x 25). Exact in this figure represents the total energy of the system in the hypothetical absence of numerical dissipation.

the stabilisation scheme proposed is also verified with the model refinement, less numerical dissipation is observed and the total energy of the system converges to the exact solution. The differences between results employing a 3D quadratic kernel function (with $f_h = 0.6$) or a 3D cubic spline kernel function (with $f_h = 0.8$) are negligible for this example.

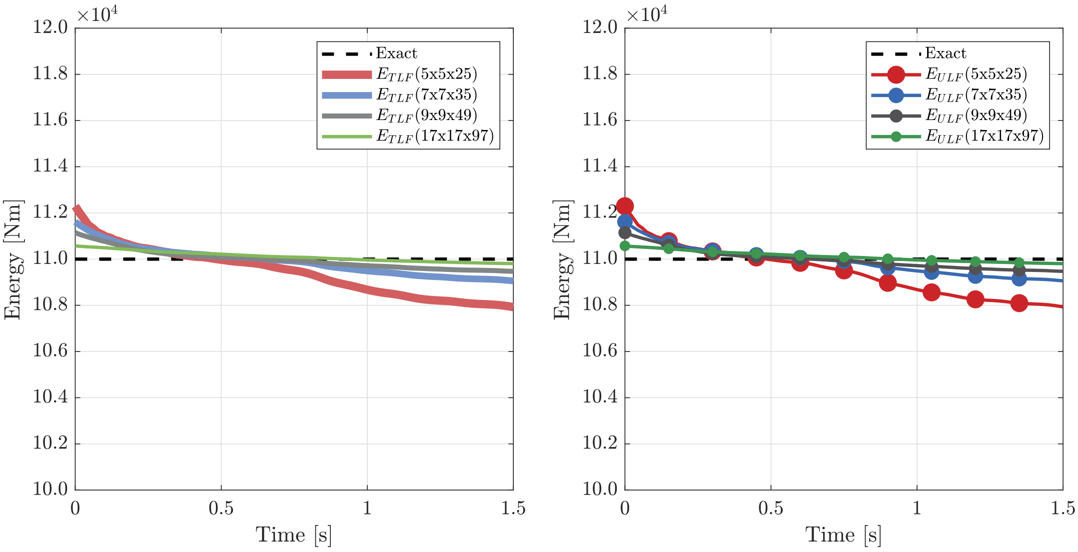

(a) (b)

Figure 6.7: Evolution of total energy ($E$) for different model refinements for the bending column. (a) Total Lagrangian Formulation. (b) Updated Lagrangian Formulation.

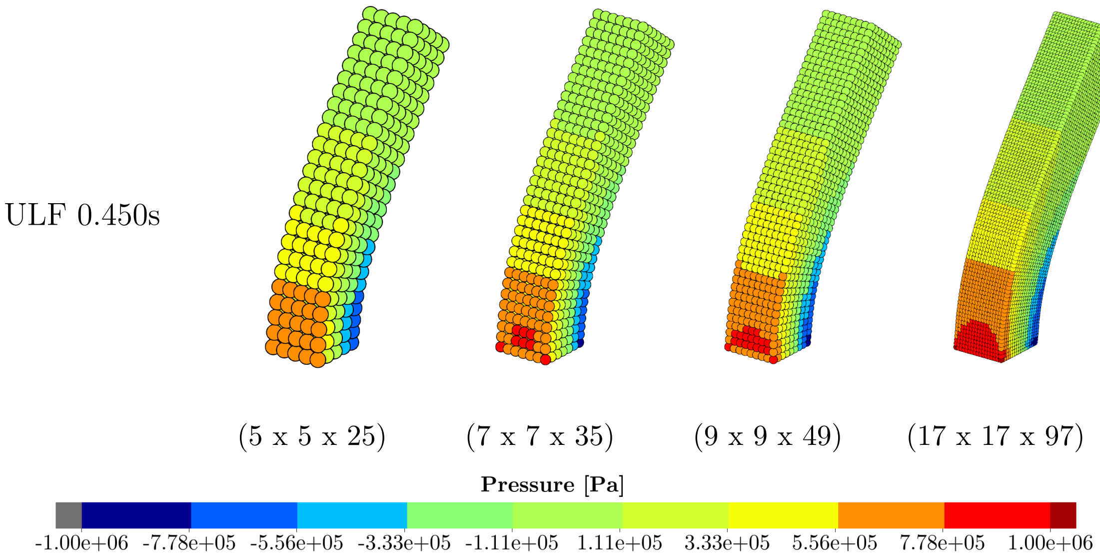

Figure 6.8: Bending column pressure distribution at time 0.450s, considering different model refinements in an updated reference Lagrangian formulation, with updates performed at every time step.

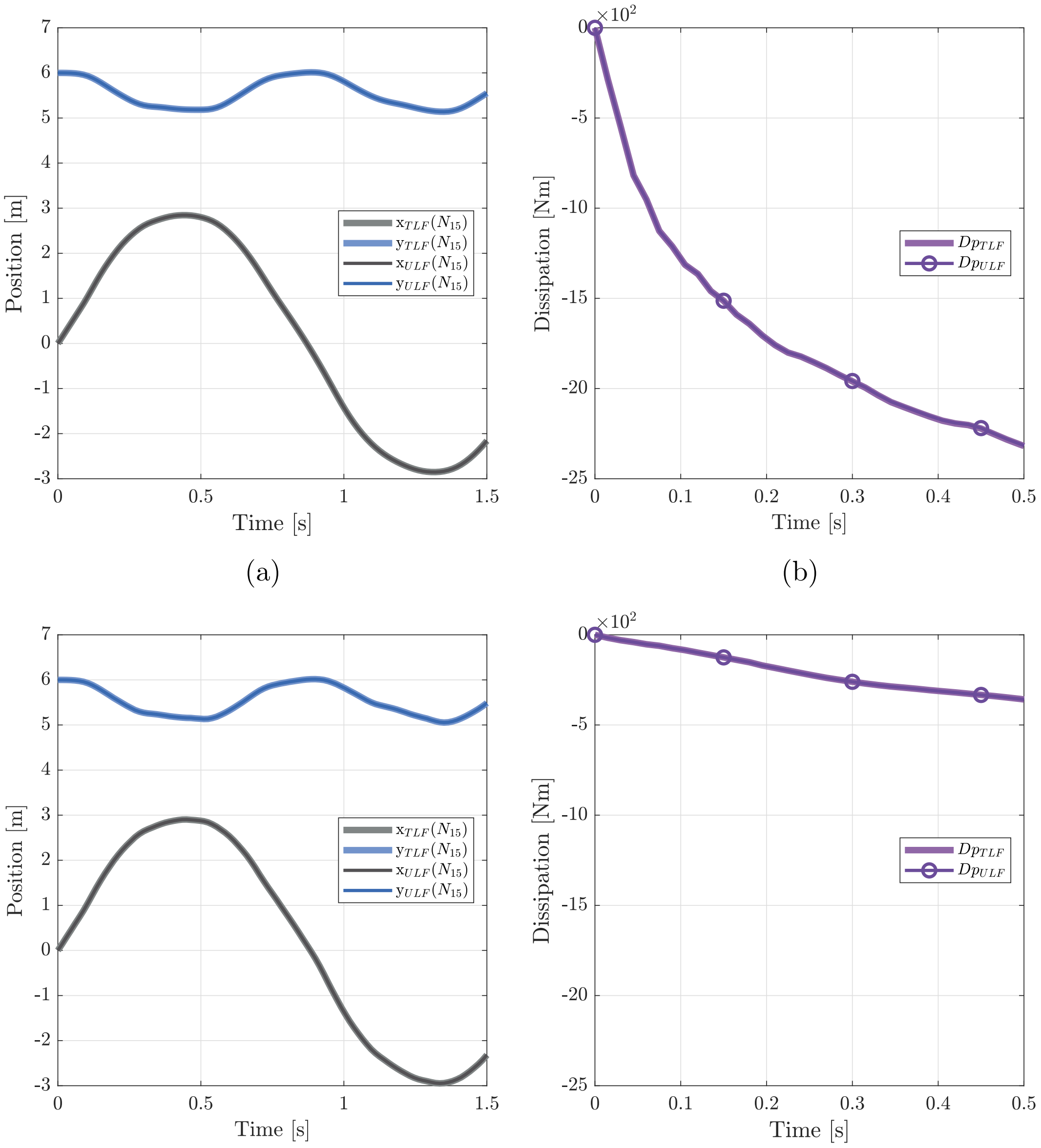

(a) (b)

(c) (d)

Figure 6.9: Evolution of x and y coordinates at position $N_{15}$ for the bending column (a) model (5 x 5 x 25) and (c) model (17 x 17 x 97). Numerical dissipation for the bending column (b) model (5 x 5 x 25) and (d) model (17 x 17 x 97).

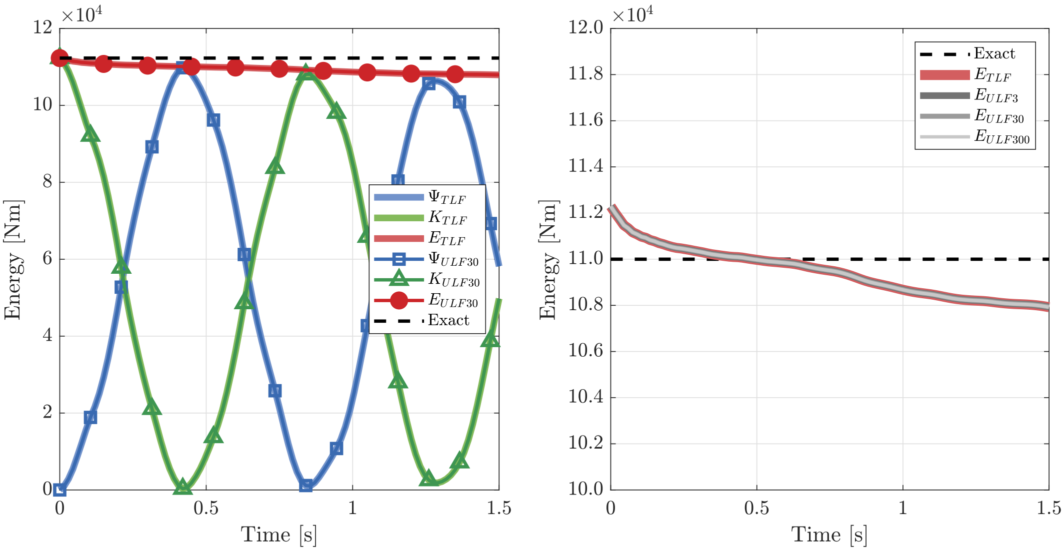

(a) (b)

Figure 6.10: (a) Evolution of kinetic ($K$), internal ($\Psi$) and total ($E$) energies for bending column (5 x 5 x 25) with updates at every 30 time steps. (b) Evolution of total energy ($E$) for bending column (5 x 5 x 25) with updates at every 3, 30 and 300 time steps.

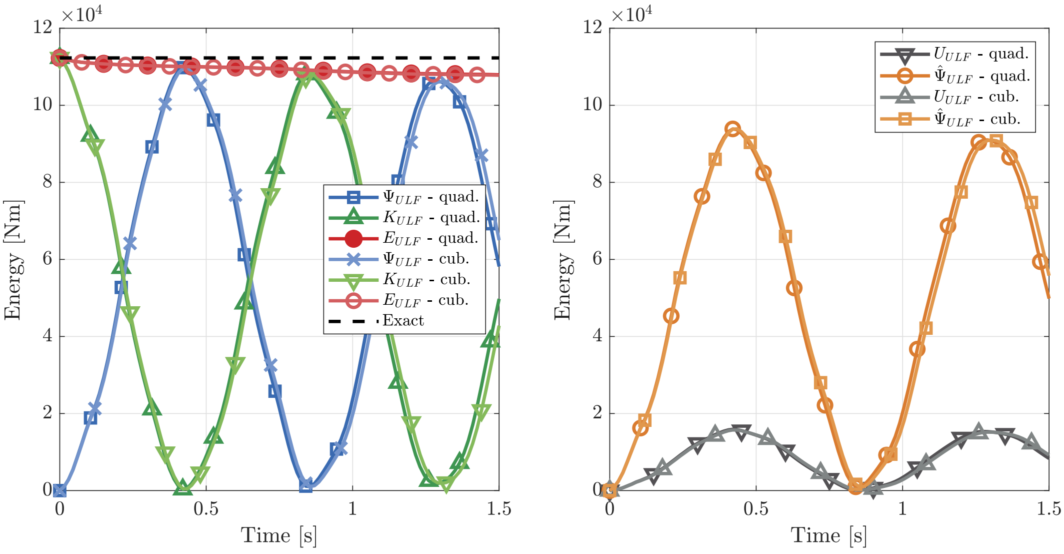

(a) (b)

Figure 6.11: Comparison between results employing the 3D quadratic and the 3D cubic spline kernel functions for bending column (5 x 5 x 25). (a) Evolution of kinetic ($K$), internal ($\Psi$) and total ($E$) energies. (b) Evolution of deviatoric ($\hat{\Psi}$) and volumetric ($U$) components of internal energy. Exact in this figure represents the total energy of the system in the hypothetical absence of numerical dissipation.

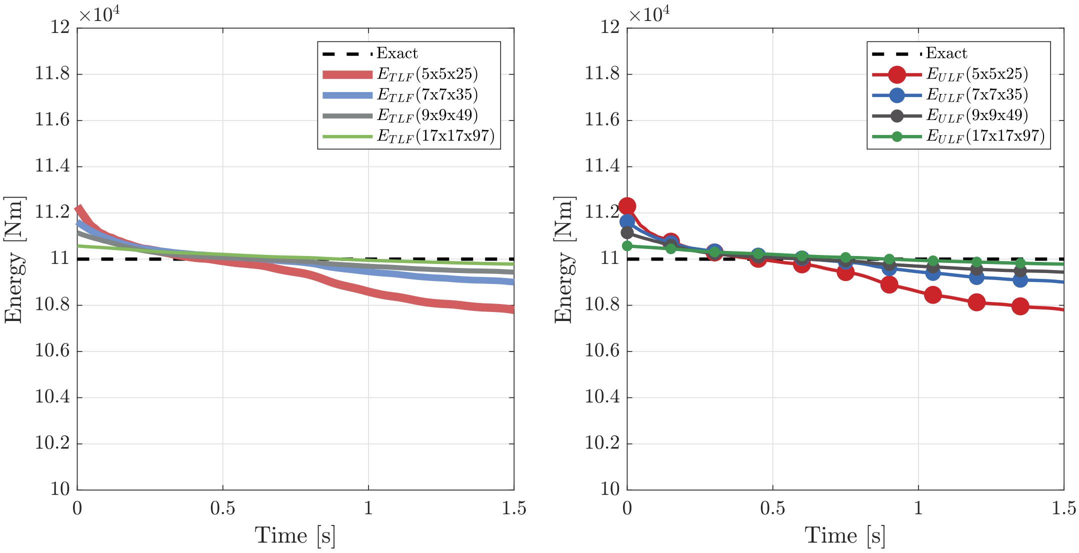

(a) (b)

Figure 6.12: Evolution of total energy ($E$) for different model refinements for the bending column employing a 3D cubic spline kernel function. (a) Total Lagrangian Formulation. (b) Updated Lagrangian Formulation.

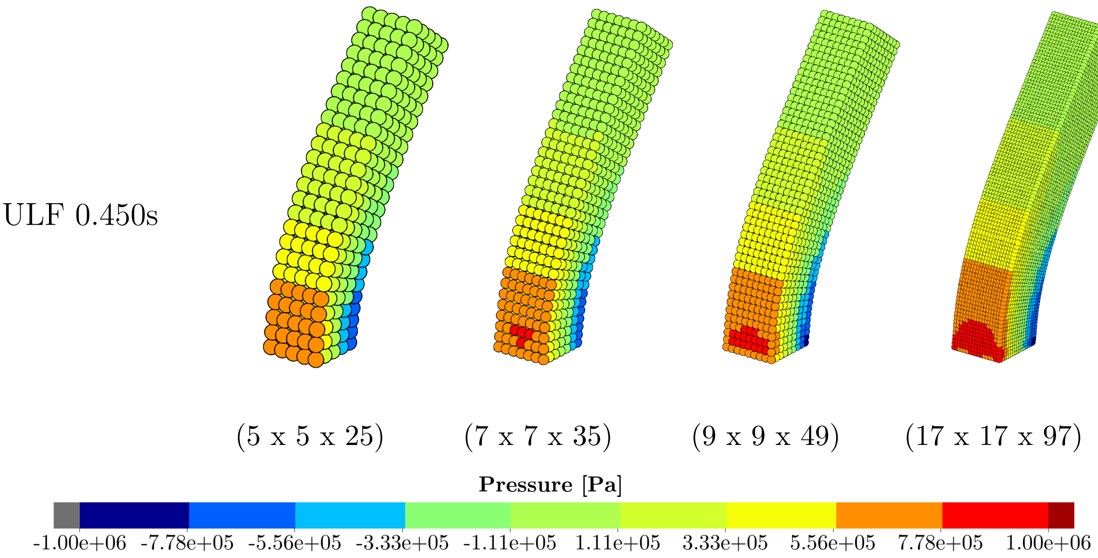

Figure 6.13: Bending column pressure distribution at time 0.450s, considering different model refinements in an updated reference Lagrangian formulation, with updates performed at every time step, employing a 3D cubic spline kernel function.

### Tensile column

The tensile column case is illustrated in Figure 6.3b. An initial velocity $\boldsymbol{v}$ was defined as $\boldsymbol{v} = V\,[0, {}^{Y}\!/_{L}, 0]^T$, where $V = 50\frac{\mathrm{m}}{\mathrm{s}}$ and $L = 6\mathrm{m}$. No further loading is applied to the column and the restrictions applied to this model are at the bottom face (particles presenting coordinates $Y = 0$), which is constrained in all directions and at all the lateral faces, which have the movement in the direction normal to the face restricted. This problem is specifically designed to check if the proposed method can circumvent spurious modes in stretching dominated problems.

In figure 6.14, the pressure distribution is plotted at different instants of the simulation, for a Total Lagrangian Formulation and also for an updated reference Lagrangian formulation, with updates performed at every time step.

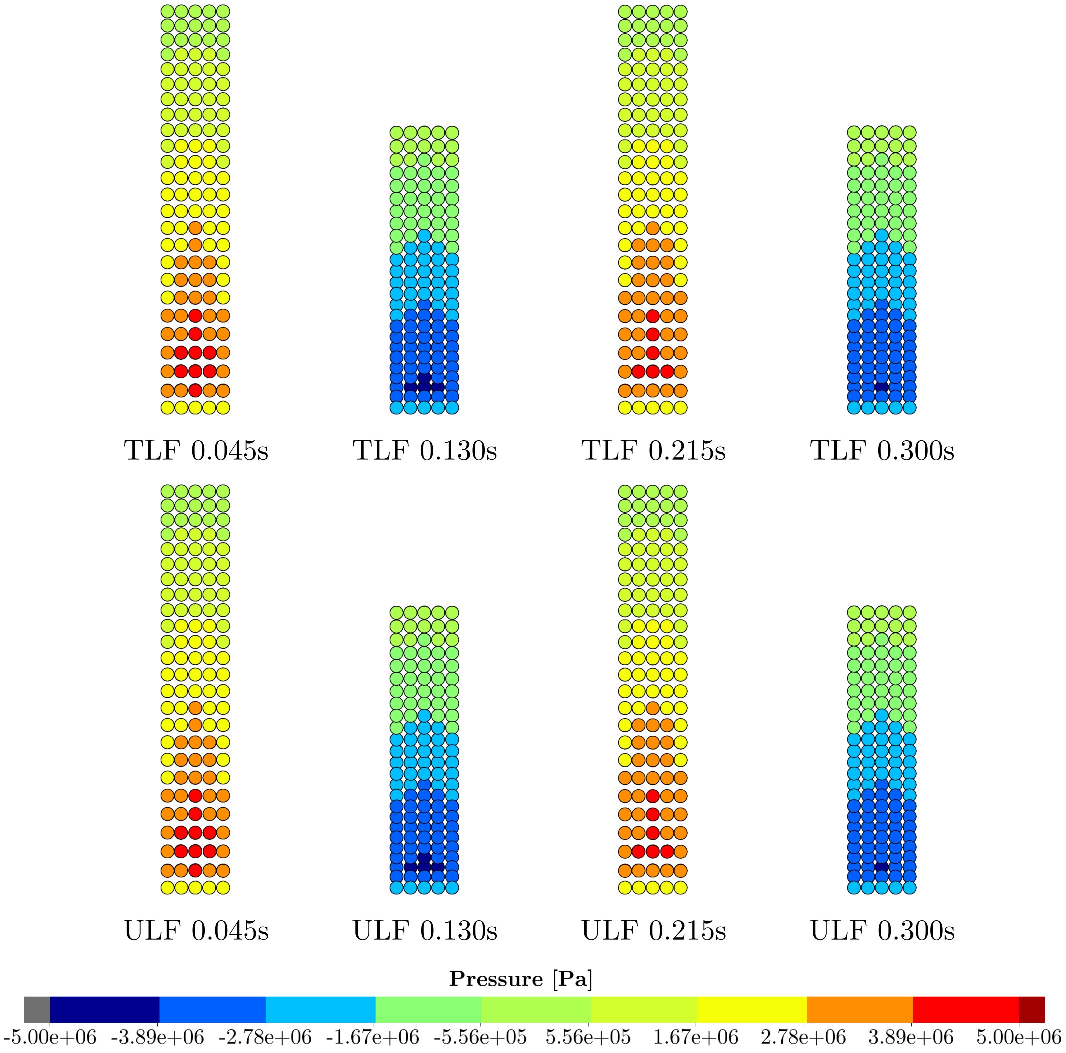
TLF 0.045s TLF 0.130s TLF 0.215s TLF 0.300s

ULF 0.045s ULF 0.130s ULF 0.215s ULF 0.300s

Figure 6.14: Tensile column (5 x 5 x 25) pressure distribution.

Evolution of internal, kinetic and total energies is shown for both TLF and ULF in figure 6.15a. In addition, in figure 6.15b the deviatoric and the volumetric components of the internal energy are plotted separated for both cases.

Notice that the numerical dissipation is not added to the total energy in figure 6.15a, and therefore the total energy of the system slightly decreases along the simulation. The evolution of total energy considering different model refinements

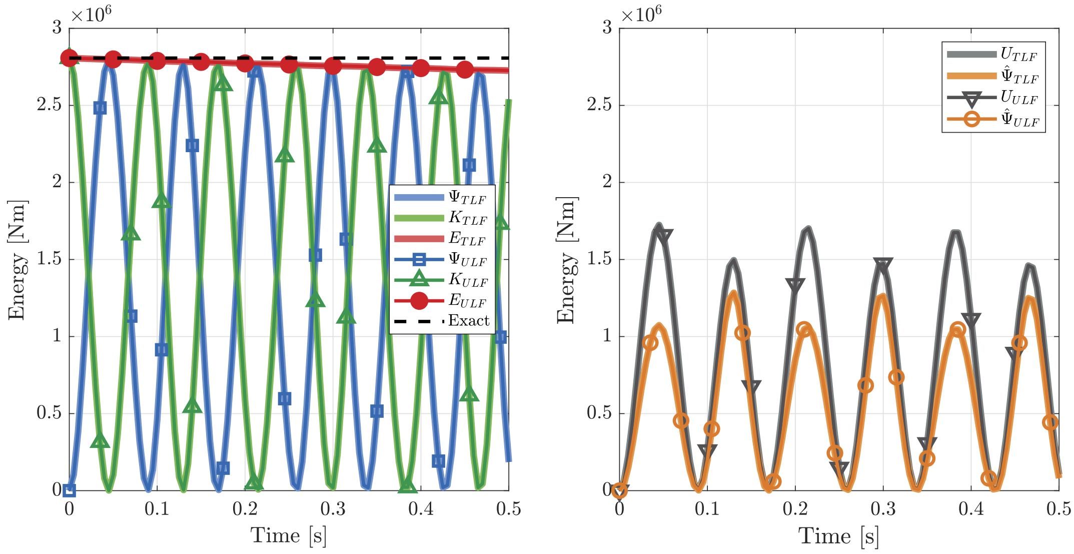

(a) (b)

Figure 6.15: (a) Evolution of kinetic ($K$), internal ($\Psi$) and total ($E$) energies for tensile column (5 x 5 x 25). (b) Evolution of deviatoric ($\hat{\Psi}$) and volumetric ($U$) components of internal energy for tensile column (5 x 5 x 25). Exact in this figure represents the total energy of the system in the hypothetical absence of numerical dissipation.

is shown for both TLF and ULF in figures 6.16a and 6.16b, respectively. Uniform distributions of (5 x 5 x 25), (7 x 7 x 35), (9 x 9 x 49) and (17 x 17 x 97) particles were compared. The pressure distribution at time 0.215s is shown for the four models in figure 6.17 for an updated reference Lagrangian formulation, with updates performed at every time step. Since internal energy is initially zero for this example and no dissipation mechanisms are present, the exact total energy remains constant and equal in magnitude to the initial kinetic energy of the system. Therefore, the exact solution plotted in figures 6.16a and 6.16b is obtained by computing $\int_{\Omega_V} \frac{1}{2}\rho_0 \boldsymbol{v}\cdot\boldsymbol{v}\, dV$, with $\boldsymbol{v} = V\,[0, {}^{Y}\!/_{L}, 0]^T$.

In figure 6.18a, the vertical position of the particle located at position $N_{15}$ is tracked for both TLF and ULF for the coarse (5 x 5 x 25) model. In addition, the numerical dissipation in the same model is shown in figure 6.18b. The same results are shown for the most refined model (17 x 17 x 97) in figures 6.18c and 6.18d.

The results presented up to now employed a 3D quadratic kernel function, with the updated kernel and gradient obtained as a push-forward of the corrected material kernel and corrected material gradient (Option#1). Due to the large stretches developed during the oscillation of the column, this problem is very sensitive to instabilities, and therefore, it is worth verifying the robustness of the alternative ways of obtaining the updated kernels and gradients proposed in chapter 4. Four different options were presented in section 4.4 and consist of:

- Option#1: Push-forward of corrected material kernel and gradient.
- Option#2: Push-forward of material kernel and gradient, corrections in the updated domain.

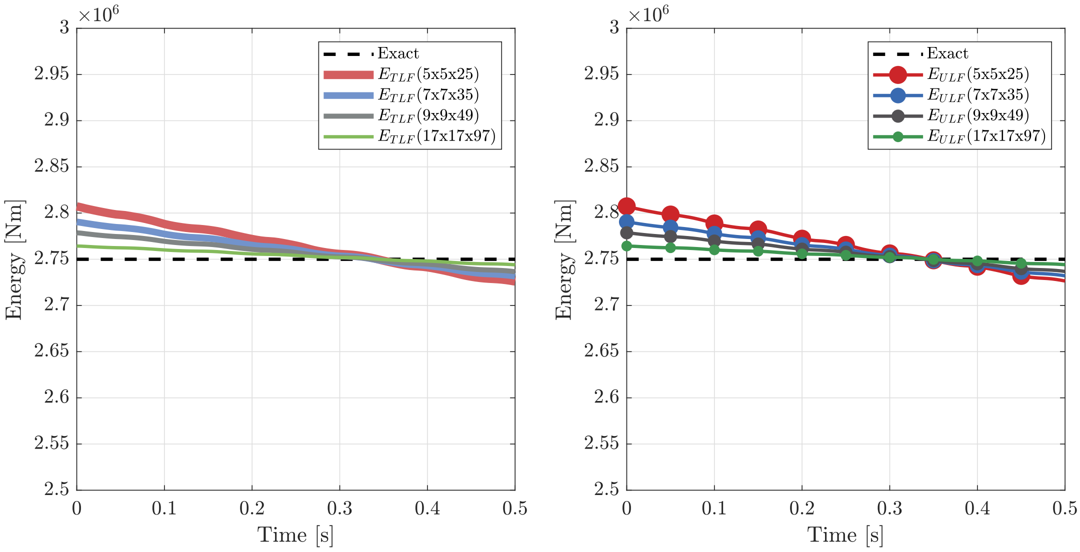

(a) (b)

Figure 6.16: Evolution of total energy ($E$) for different model refinements for the tensile column. (a) Total Lagrangian Formulation. (b) Updated Lagrangian Formulation.

- Option#3: Push-forward of kernel and gradient based on the pull-back of updated coordinates, corrections in the updated domain.
- Option#4: Similar to Option#3, but employing $\boldsymbol{F}_{\boldsymbol{\chi},ab} = \frac{1}{2}\left(\boldsymbol{F}_{\boldsymbol{\chi},a} + \boldsymbol{F}_{\boldsymbol{\chi},b}\right)$ for the push-forward operation.

In figure 6.19, the evolution of total energy considering different model refinements is shown for an updated reference Lagrangian formulation, with updates performed at every time step, considering the four different approaches of obtaining updated anisotropic kernels. A 3D cubic spline smoothing function is employed with a factor $f_h = 0.8$ for all the simulations. In figure 6.20 the pressure distribution at times 0.215s and 0.300s is shown for model (17 x 17 x 97) considering the four options. All four options yield extremely similar results in comparison to the Total Lagrangian result, almost undistinguishable. Regardless of which option is used, the total numerical dissipation of the algorithm is not significantly affected by the choice and is reduced when increasing the number of particles.

As the conclusions of the tensile column example, the proposed formulation was shown to be robust and did not activate any spurious mechanisms in this test case. The results for the simulations evolved based on updated reference configurations are as good as the ones based on the initial geometry (TLF). The coarse model studied (5 x 5 x 25) already provides satisfactory results and the solution improves with model refinement. The consistency of the stabilisation scheme proposed is also verified with the model refinement, less numerical dissipation is observed and the total energy of the system converges to the exact solution. The example was also used to test different options of obtaining updated anisotropic kernels and gradients. The four options are shown to perform equally well, with the differences in the results being minimal.

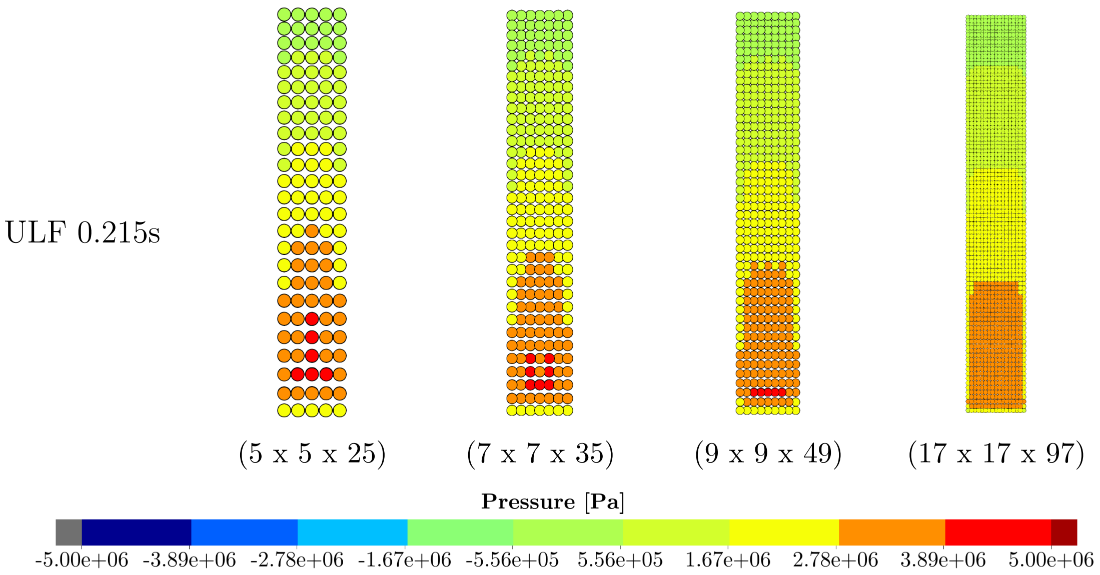

Figure 6.17: Tensile column pressure distribution at time 0.215s, considering different model refinements in an updated reference Lagrangian formulation, with updates performed at every time step.

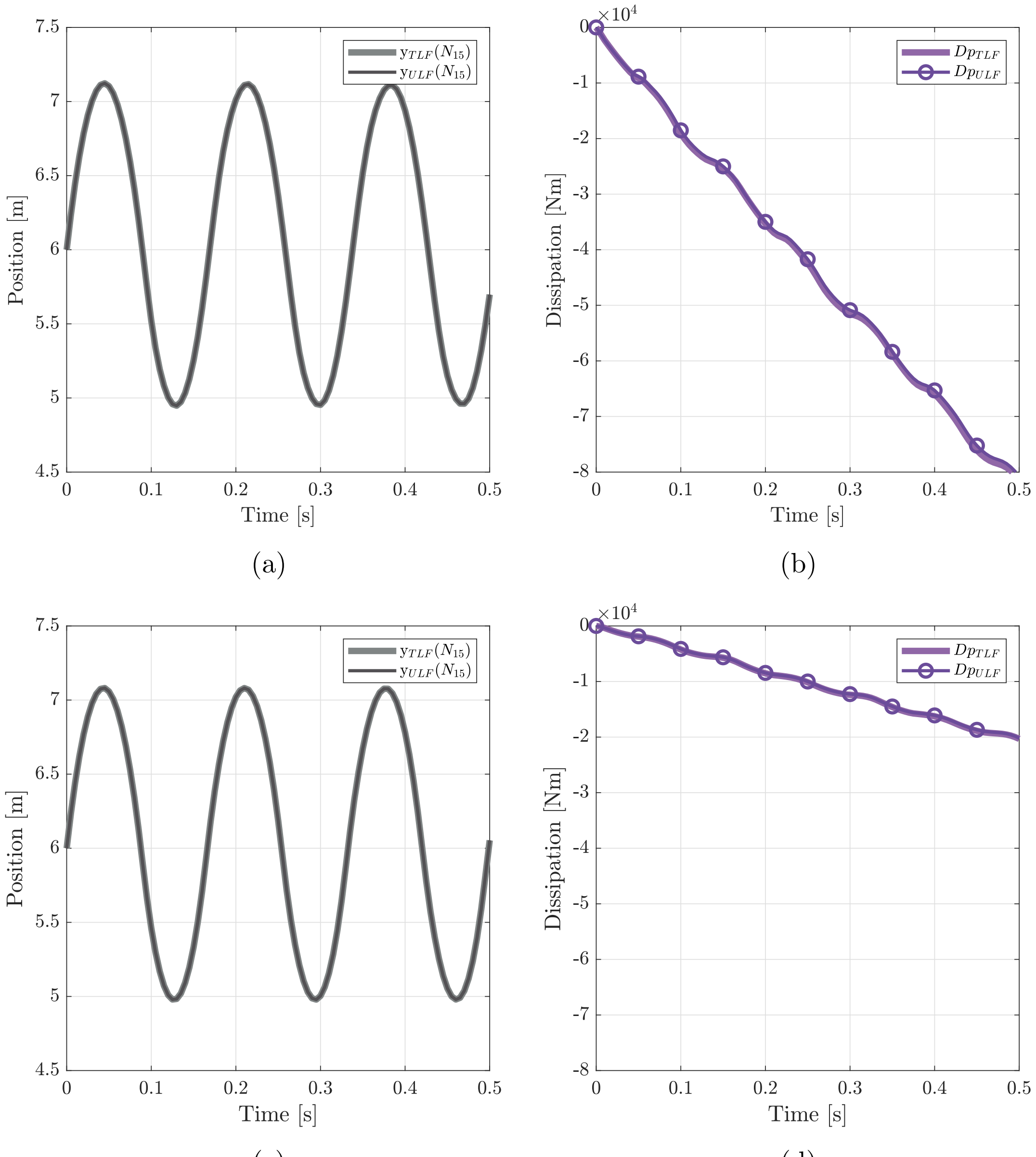

(a) (b)

(c) (d)

Figure 6.18: Evolution of y coordinate at position $N_{15}$ for the tensile column (a) model (5 x 5 x 25) and (c) model (17 x 17 x 97). Numerical dissipation for the tensile column (b) model (5 x 5 x 25) and (d) model (17 x 17 x 97).

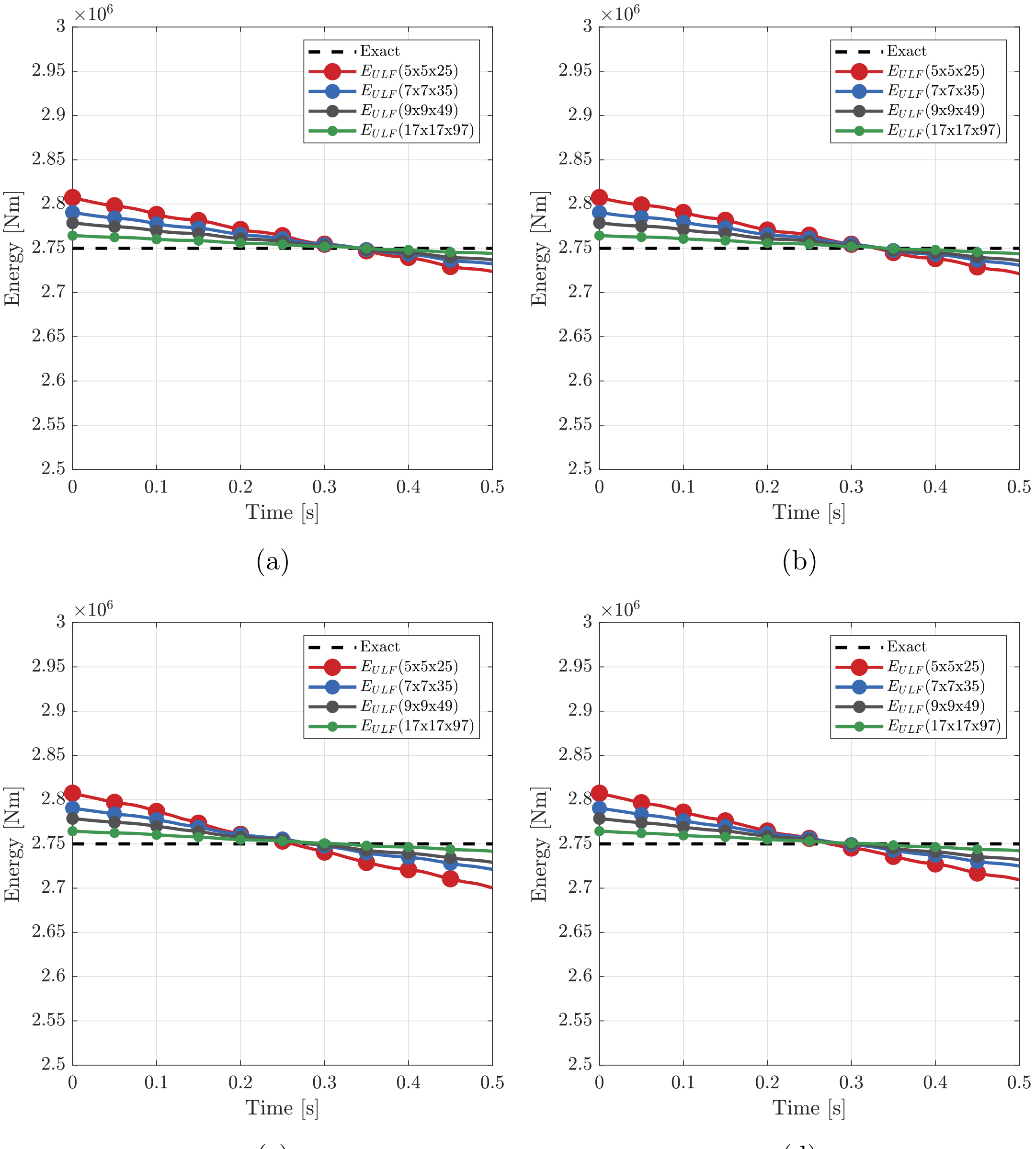

(a) (b)

(c) (d)

Figure 6.19: Evolution of total energy ($E$) for different model refinements for the tensile column considering different options of obtaining updated kernels in an updated reference Lagrangian formulation, with updates performed at every time step. (a) Option 1. (b) Option 2. (c) Option 3. (d) Option 4.

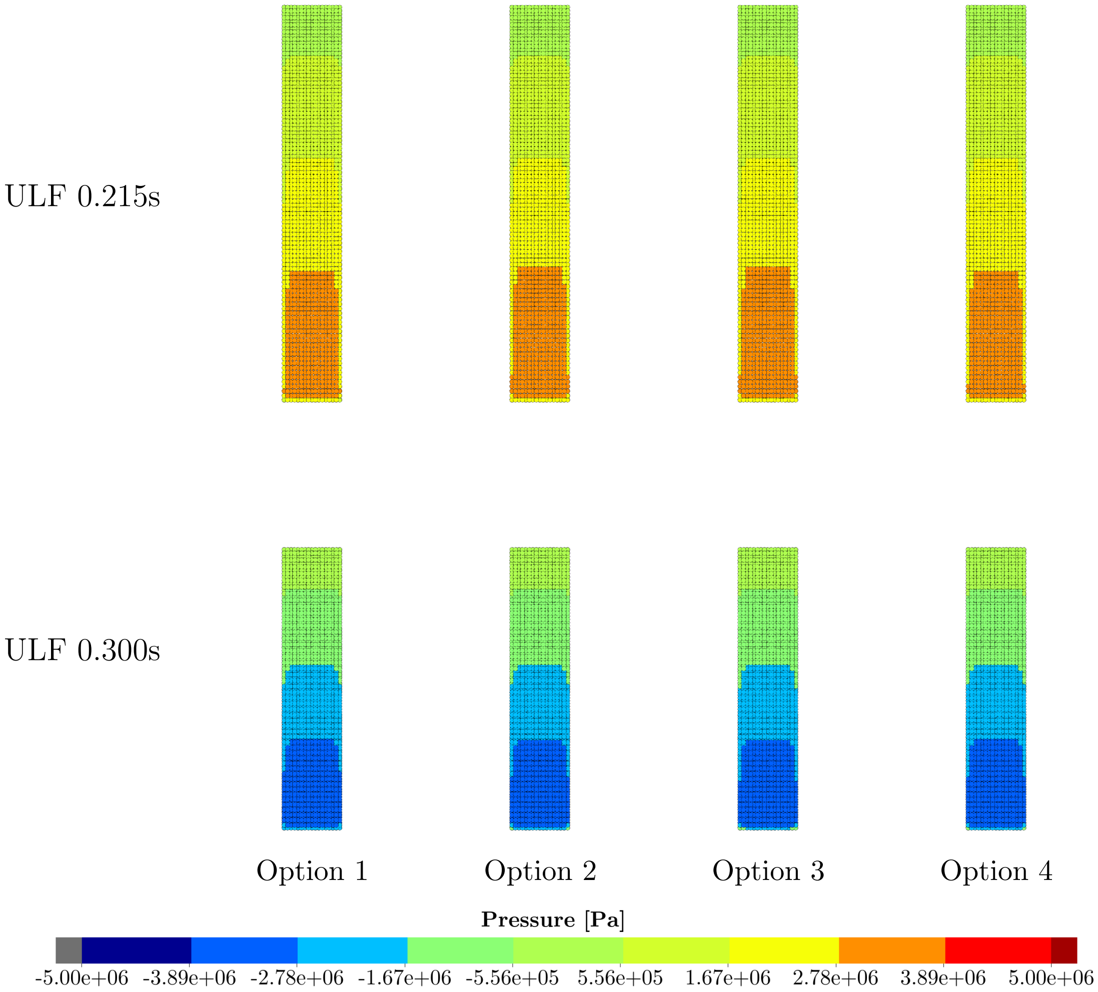

Figure 6.20: Tensile column pressure distribution for model (17 x 17 x 97) at times 0.215s and 0.300s, considering different options of obtaining updated kernels in an updated reference Lagrangian formulation, with updates performed at every time step.

### Twisting column

The twisting column case is illustrated in Figure 6.3c. This example simulates a column rotating around its longitudinal axis, which is suddenly fixed at its base. An initial angular velocity $\boldsymbol{\omega}$ was defined as $\boldsymbol{\omega} = \Omega\,[0, \sin({}^{\pi Y}/_{2L}), 0]^T$, where $\Omega = 105\frac{\text{rad}}{\text{s}}$ and $L = 6\text{m}$. No further loading is applied to the column and the only restriction applied to this model is at the bottom face (particles presenting coordinates $Y = 0$), which is constrained in all directions. The main objective of this well documented twisting example [25–27, 98] is to examine the robustness of the algorithm.

In this example, the anisotropic updated kernel and kernel gradient are obtained as a push-forward of the corrected material kernel and corrected material gradient (Option#1). A 3D quadratic smoothing function is employed with a factor $f_h = 0.6$ for all the simulations.

In figure 6.21, the pressure distribution is plotted at different instants of the simulation, for a Total Lagrangian Formulation and also for an updated reference Lagrangian formulation, with updates performed at every time step.

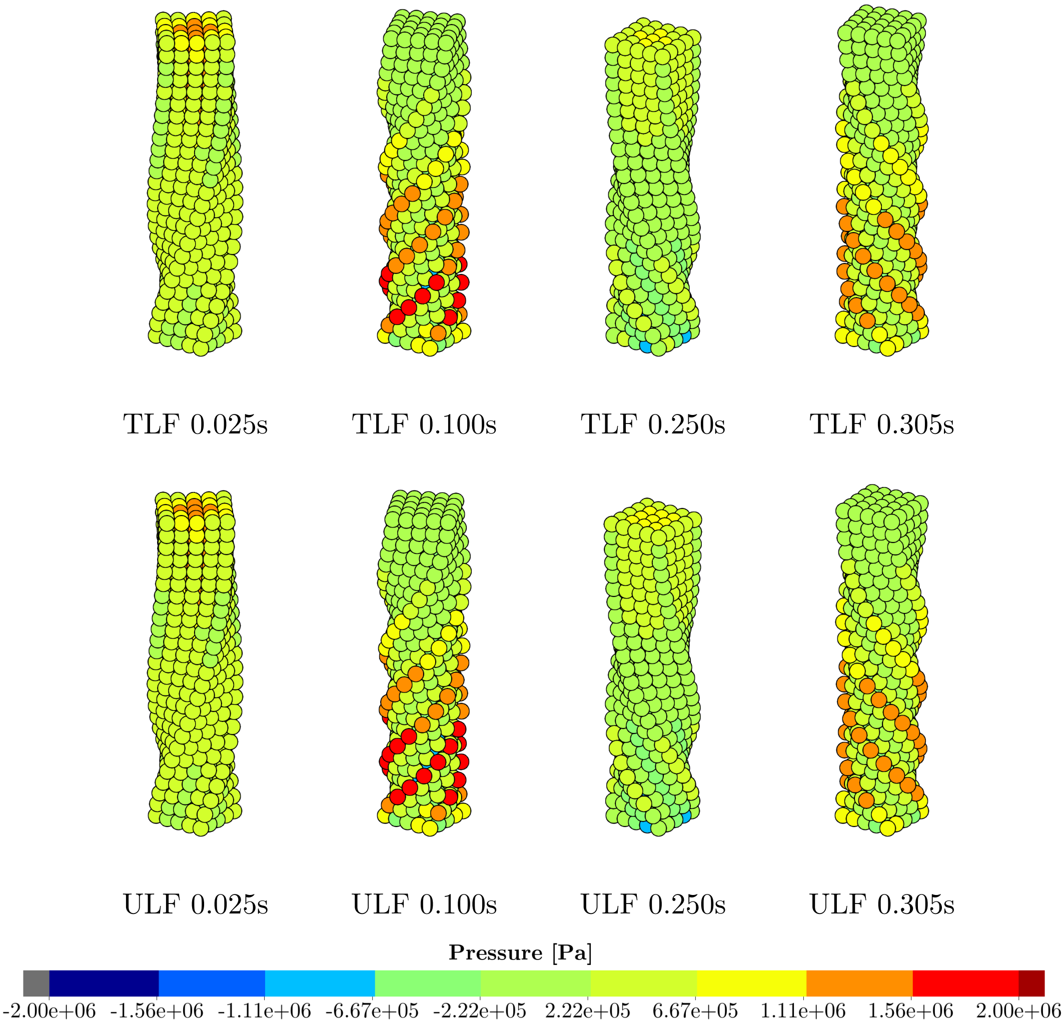
TLF 0.025s TLF 0.100s TLF 0.250s TLF 0.305s

ULF 0.025s ULF 0.100s ULF 0.250s ULF 0.305s

Figure 6.21: Twisting column (5 x 5 x 25) pressure distribution.

Evolution of internal, kinetic and total energies is shown for both TLF and ULF in figure 6.22a. In addition, in figure 6.22b the deviatoric and the volumetric components of the internal energy are plotted separated for both cases.

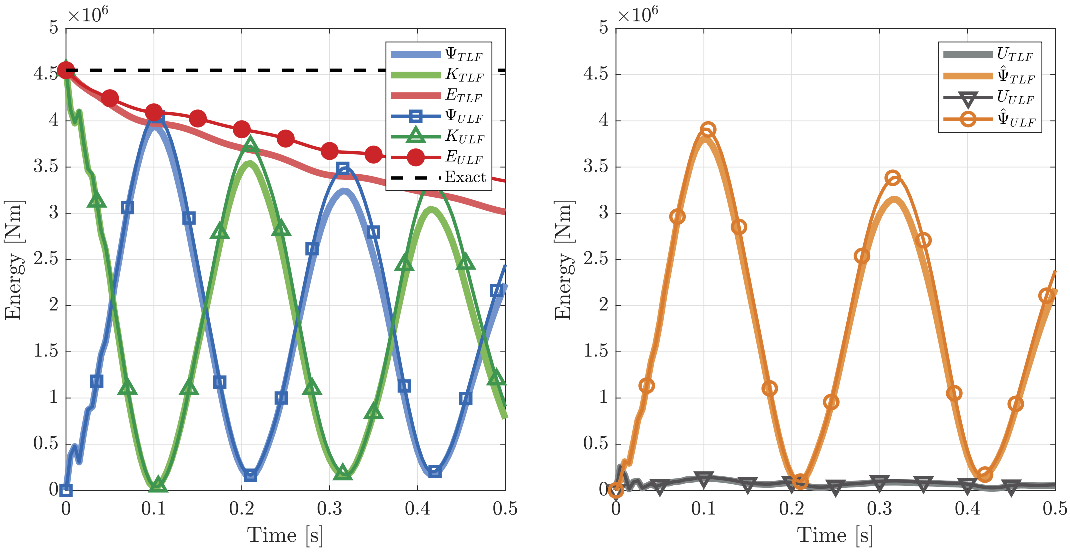

(a) (b)

Figure 6.22: (a) Evolution of kinetic ($K$), internal ($\Psi$) and total ($E$) energies for twisting column (5 x 5 x 25). (b) Evolution of deviatoric ($\hat{\Psi}$) and volumetric ($U$) components of internal energy for twisting column (5 x 5 x 25). Exact in this figure represents the total energy of the system in the hypothetical absence of numerical dissipation.

For such challenging example, the coarse model is over dissipative and the total energy of the system in figure 6.22a significantly decreases along the simulation. The energies of the system are plotted for the refined models in figures 6.23, 6.24 and 6.25. The evolution of total energy comparing the different model refinements is shown for both TLF and ULF in figures 6.26a and 6.26b, respectively. Since internal energy is initially zero for this example and no dissipation mechanisms are present, the exact total energy remains constant and equal in magnitude to the initial kinetic energy of the system. Therefore, the exact solution plotted in figures 6.26a and 6.26b is obtained by computing $\int_{\Omega_V} \frac{1}{2}\rho_0 \boldsymbol{v}\cdot\boldsymbol{v}\, dV$, with $\boldsymbol{v} = \boldsymbol{\omega} \times \boldsymbol{X}$, where $\boldsymbol{\omega} = \Omega\,[0, \sin\left({}^{\pi Y}\!/_{2L}\right), 0]^T$ and $\boldsymbol{X}$ is the vector position of material points.

Uniform distributions of (5 x 5 x 25), (7 x 7 x 35), (9 x 9 x 49) and (17 x 17 x 97) particles were compared. The pressure distribution at time 0.100s is shown for the four models in figure 6.27 for an updated reference Lagrangian formulation, with updates performed at every time step. For the most refined model, figure 6.28 shows the components of the first Piola-Kirchhoff stress tensor, comparing results of updated reference Lagrangian formulation, with updates performed at every time step, against total Lagrangian results.

In figure 6.29, the points $N_{11}$, $N_{12}$, $N_{13}$ and $N_{14}$ (see figure 6.4) are highlighted for the coarse (5 x 5 x 25) model at different instants of the simulation, for a Total Lagrangian Formulation and also for an updated reference Lagrangian formulation, with updates performed at every time step. Additionally, in the same figure the accumulated angle formed between the particle and the $X$ direction is plotted for the entire simulation. The same results are shown for the most refined model (17 x 17 x 97) in figure 6.30.

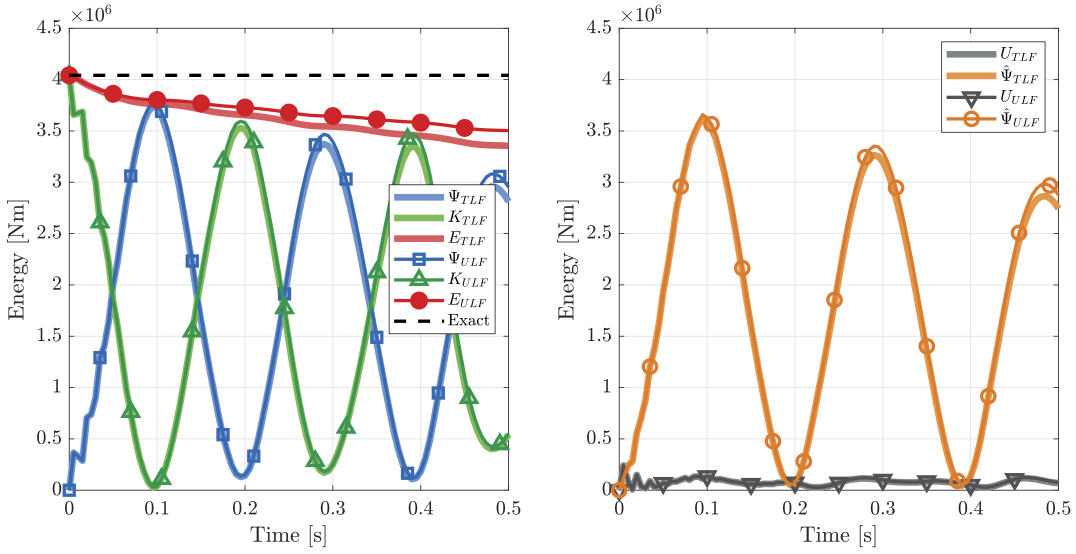

(a) (b)

Figure 6.23: (a) Evolution of kinetic ($K$), internal ($\Psi$) and total ($E$) energies for twisting column (7 x 7 x 35). (b) Evolution of deviatoric ($\hat{\Psi}$) and volumetric ($U$) components of internal energy for twisting column (7 x 7 x 35). Exact in this figure represents the total energy of the system in the hypothetical absence of numerical dissipation.

In order to explore the formulation even further, the Poisson's ratio is increased from 0.3 to 0.4995. In figure 6.31 the pressure distribution at time 0.100s is shown for the four model refinements for an updated reference Lagrangian formulation, with updates performed at every time step. The evolution of total energy comparing the four models is shown in figure 6.32a. In addition, in figure 6.32b, the evolution of the time increments for the four models are compared considering the Poisson's ratio $\nu = 0.3$ and $\nu = 0.4995$. As discussed in [27], this problem becomes significantly more challenging by increasing the initial angular velocity to $\Omega_0 = 200$ rads$^{-1}$ with a Poisson's ratio of $\nu = 0.4995$. This simulation was performed for the most refined model and the results are compared to the Total Lagrangian results in figure 6.33.

As the conclusions of the twisting column example, the proposed formulation was shown to be robust and did not activate any spurious mechanisms in this test case. The results for the simulations evolved based on updated reference configurations are as good as the ones based on the initial geometry (TLF). The coarse model studied (5 x 5 x 25) is over dissipative, but the solution quickly improves with model refinement. The consistency of the stabilisation scheme proposed is also verified with the model refinement, less numerical dissipation is observed and the total energy of the system converges to the exact solution. The example was also used to test the robustness of the formulation with respect to cases approaching incompressibility. The Poisson's ratio was increased to $\nu = 0.4995$ and no instabilities were observed.

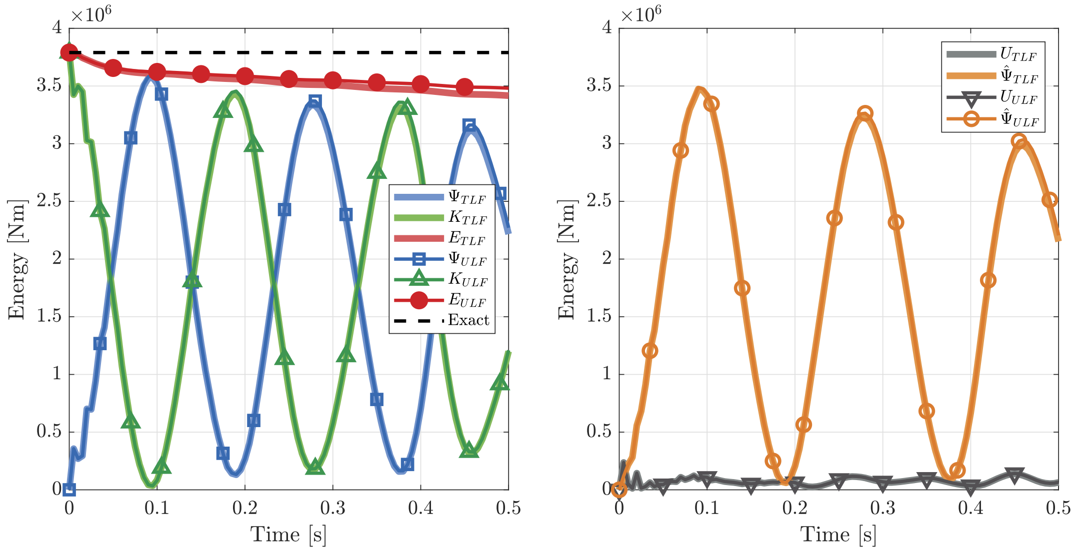

(a) (b)

Figure 6.24: (a) Evolution of kinetic ($K$), internal ($\Psi$) and total ($E$) energies for twisting column (9 x 9 x 49). (b) Evolution of deviatoric ($\hat{\Psi}$) and volumetric ($U$) components of internal energy for twisting column (9 x 9 x 49). Exact in this figure represents the total energy of the system in the hypothetical absence of numerical dissipation.

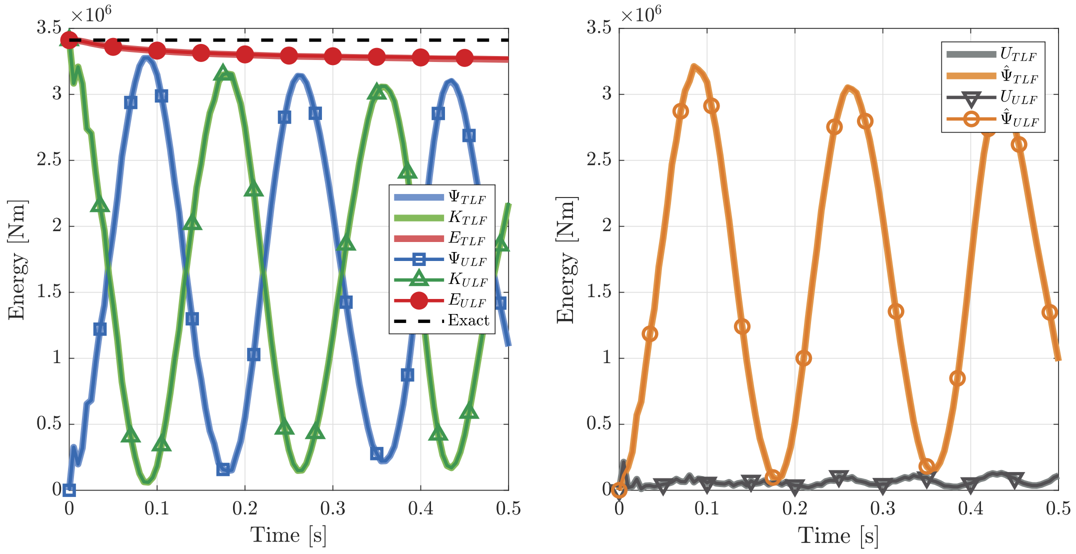

(a) (b)

Figure 6.25: (a) Evolution of kinetic ($K$), internal ($\Psi$) and total ($E$) energies for twisting column (17 x 17 x 97). (b) Evolution of deviatoric ($\hat{\Psi}$) and volumetric ($U$) components of internal energy for twisting column (17 x 17 x 97). Exact in this figure represents the total energy of the system in the hypothetical absence of numerical dissipation.

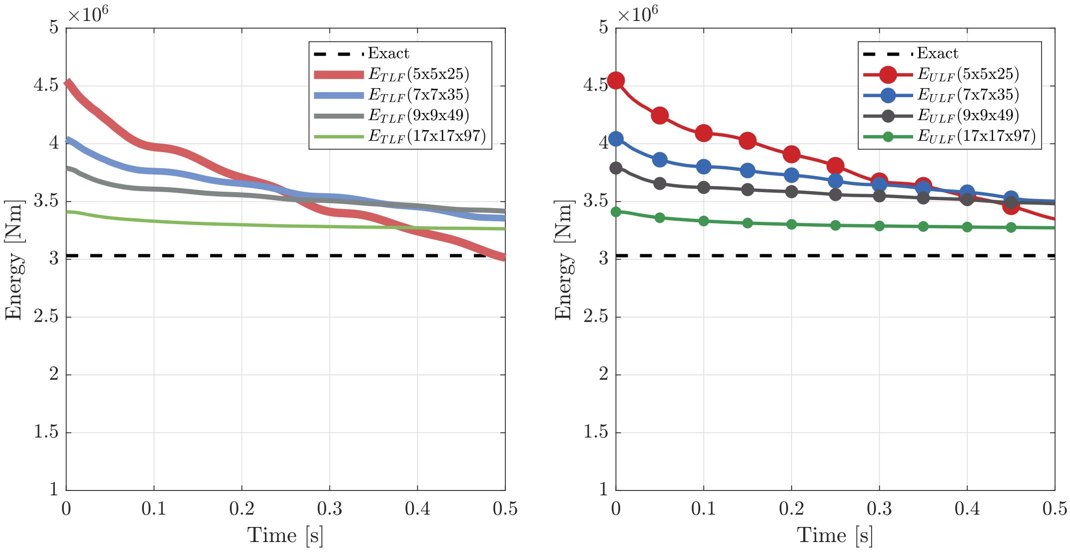

(a) (b)

Figure 6.26: Evolution of total energy ($E$) for different model refinements for the twisting column. (a) Total Lagrangian Formulation. (b) Updated Lagrangian Formulation.

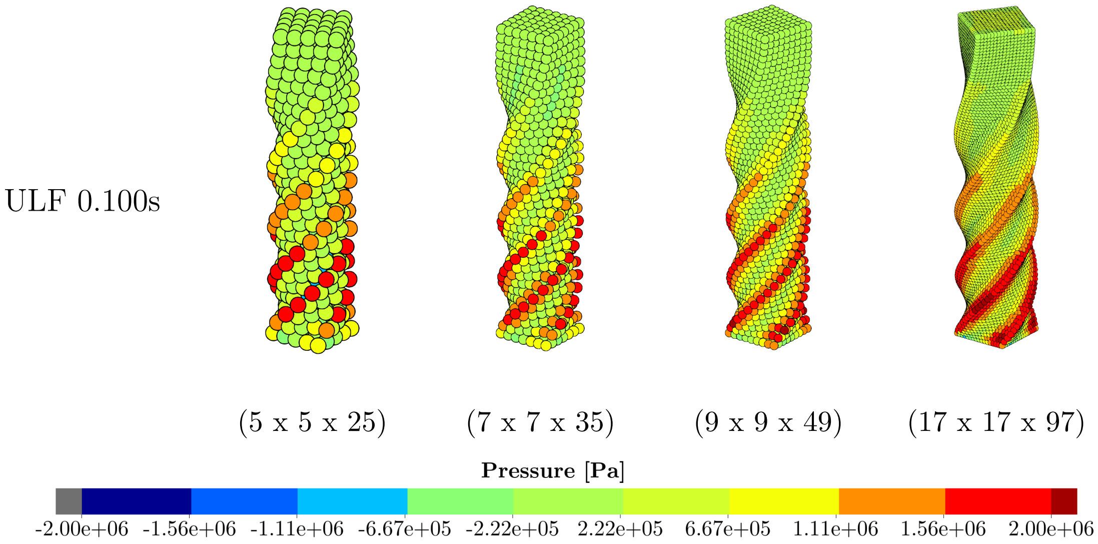

Figure 6.27: Twisting column pressure distribution at time 0.100s, considering different model refinements in an updated reference Lagrangian formulation, with updates performed at every time step.

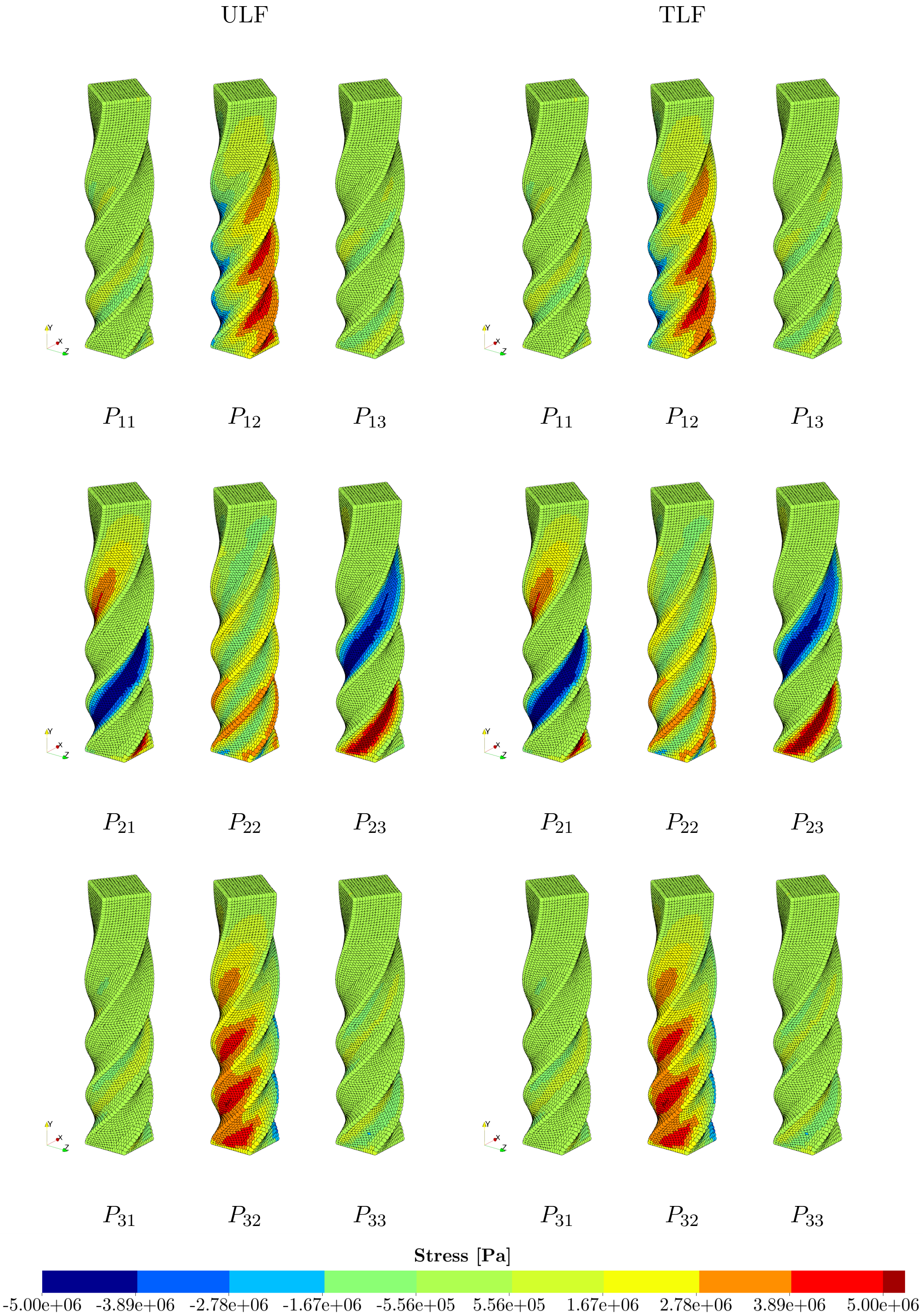

Figure 6.28: Twisting column (17 x 17 x 97) components of the first Piola-Kirchhoff stress tensor at time 0.100s. The nine figures on the left (first three columns) show the updated reference Lagrangian formulation, with updates performed at every time step. The remaining figures (three columns on the right side) show the TLF solution.

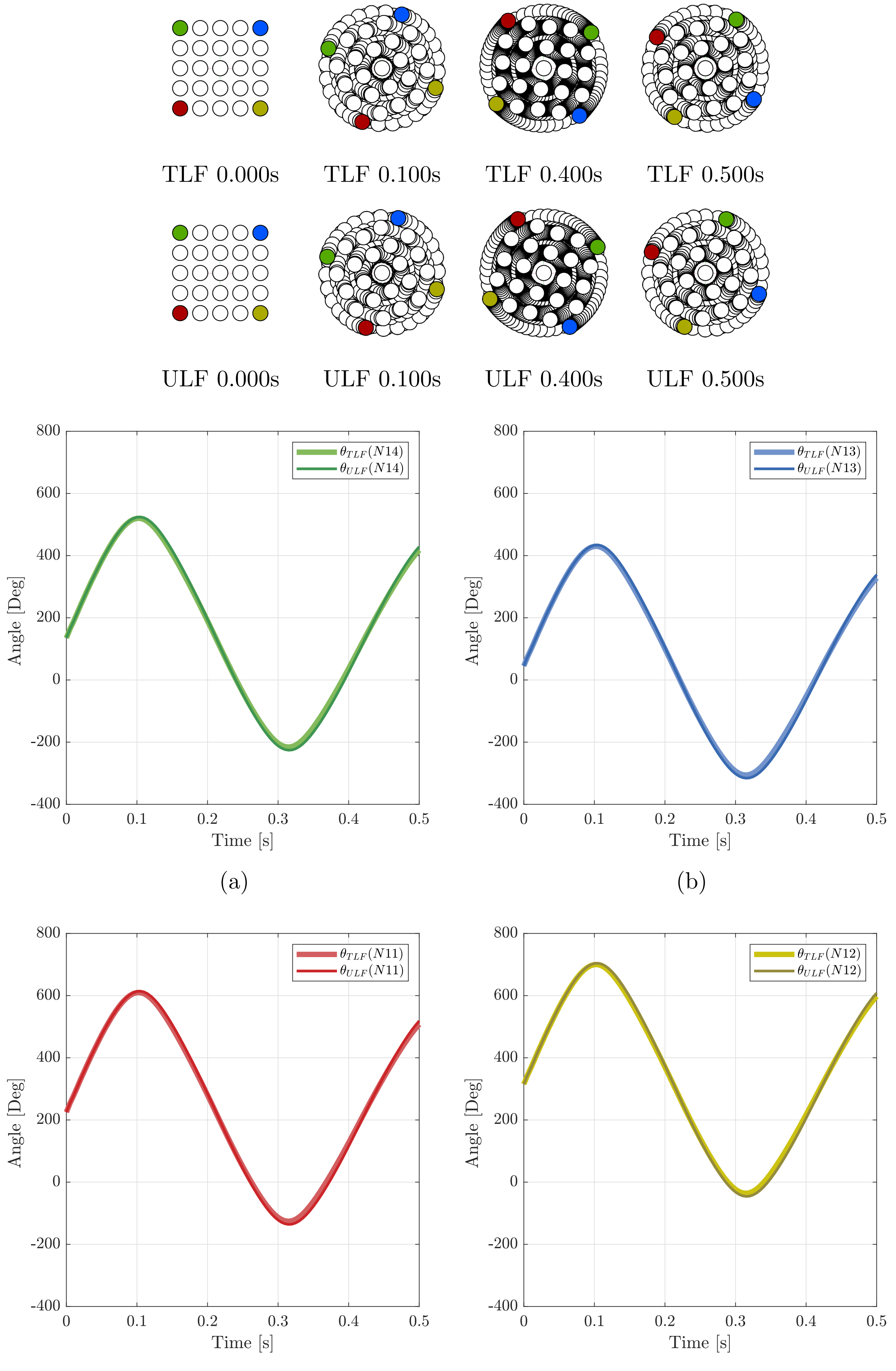

(a)

(b)

(c)

(d)

Figure 6.29: Evolution of twisting angle illustrated in figure 6.4 for twisting column (5 x 5 x 25). (a) Position $N_{14}$. (b) Position $N_{13}$. (c) Position $N_{11}$. (d) Position $N_{12}$.

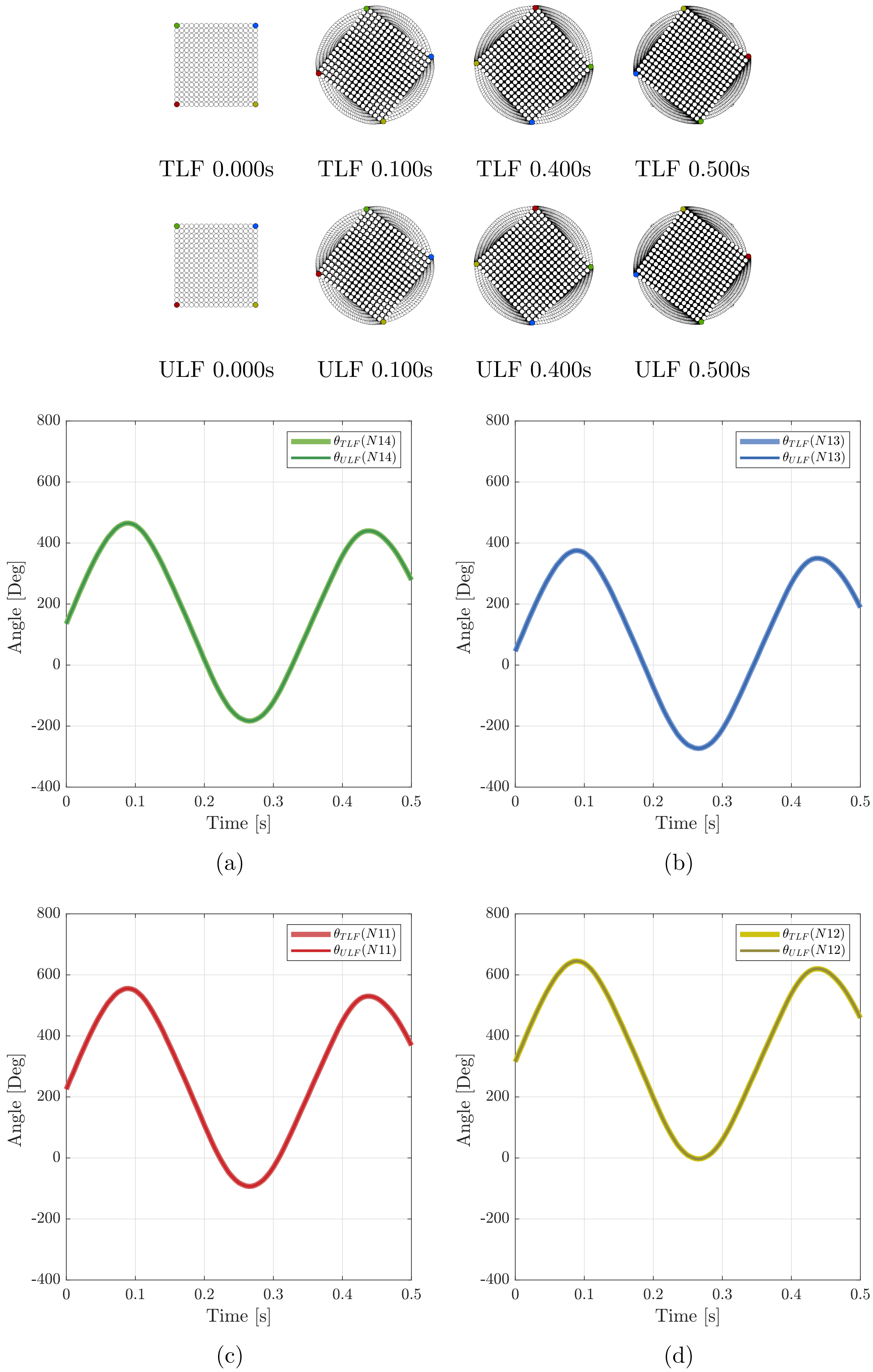

(a) (b) (c) (d)

Figure 6.30: Evolution of twisting angle illustrated in figure 6.4 for twisting column (17 x 17 x 97). (a) Position $N_{14}$. (b) Position $N_{13}$. (c) Position $N_{11}$. (d) Position $N_{12}$.

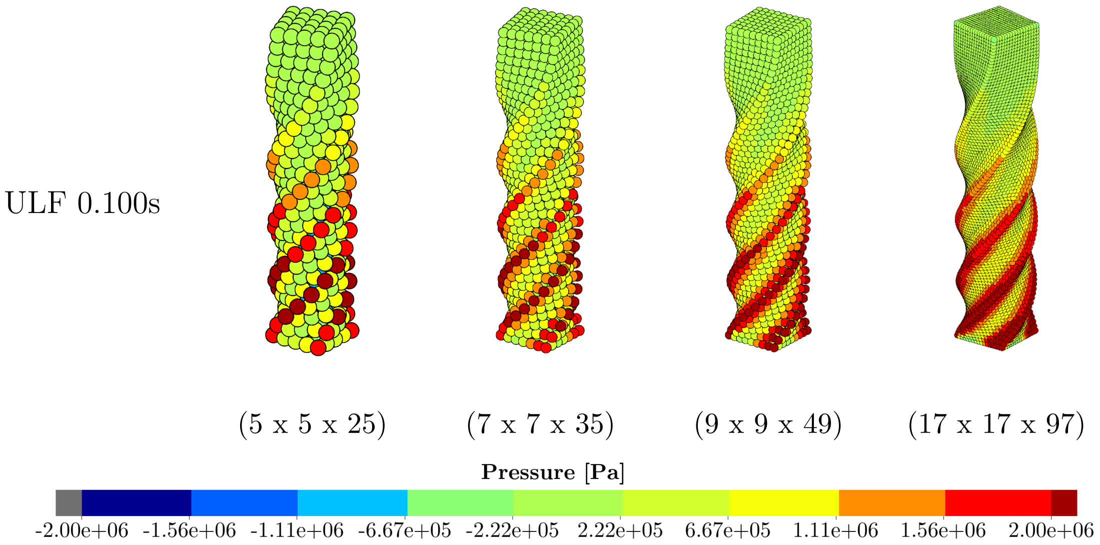

Figure 6.31: Twisting column pressure distribution at time 0.100s, considering Poisson's ratio $\nu = 0.4995$ in an updated reference Lagrangian formulation, with updates performed at every time step.

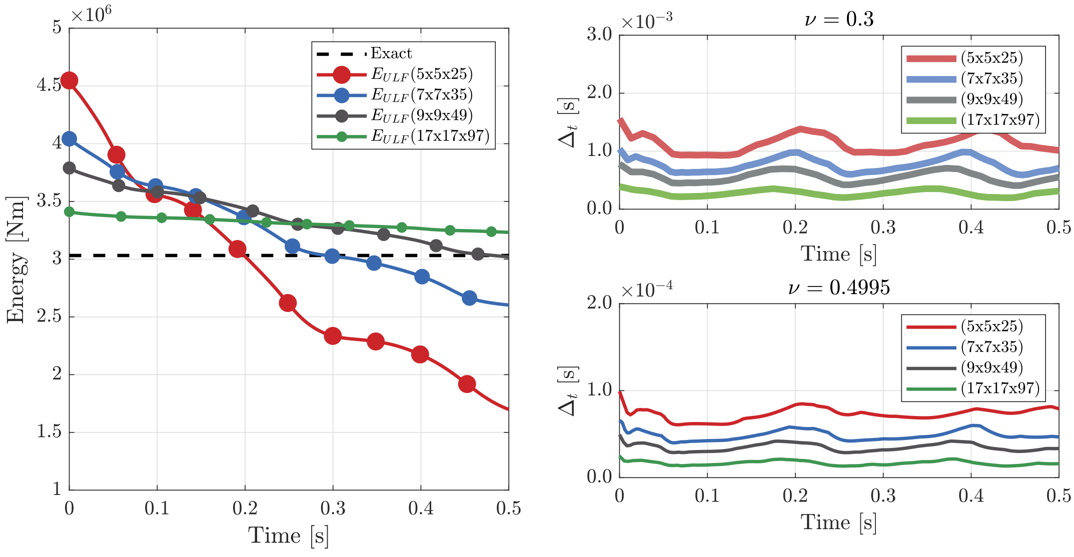

(a) (b)

Figure 6.32: (a) Evolution of total energy ($E$) for different model refinements for the twisting column considering a Poisson's ratio $\nu = 0.4995$ in an updated reference Lagrangian formulation, with updates performed at every time step. (b) Time step evolution considering Poisson's ratio $\nu = 0.3$ and $\nu = 0.4995$.

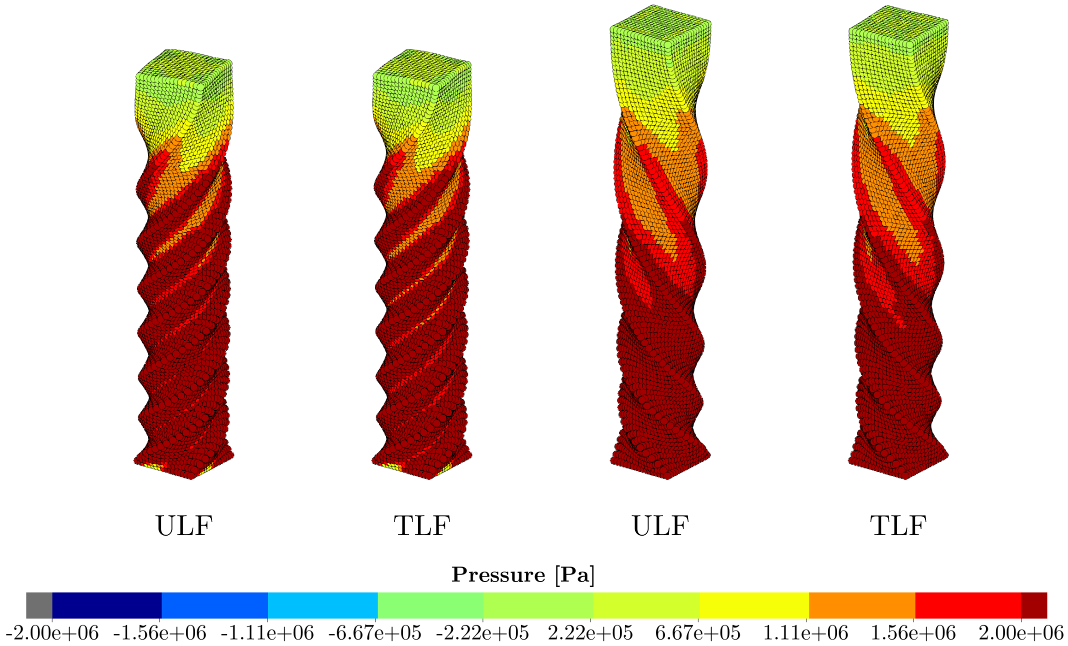

Figure 6.33: Twisting column with increased $\Omega_0 = 200$ rads$^{-1}$ and Poisson's ratio $\nu = 0.4995$. Pressure distribution at times $t = 0.1$ s and $t = 0.3$ s using model refinement (17 x 17 x 97). Comparison of the results obtained using an updated reference Lagrangian formulation, with updates performed at every time step and the Total Lagrangian SPH results.

### 6.2.3 Punch test

The punch test example was previously studied by many authors and the characteristics of the model developed in this work follows [24] and [99]. Due to the symmetry of the problem, only one quarter of the geometry is represented. An in-plane solution is obtained by restricting the movement of all particles in the $Z$ direction. The model consists of a rectangular block 0.03m x 0.01m. Initially, a uniform distribution of (25 x 9) particles was employed. A refined model was also studied considering (49 x 17) particles. Note that because of the three-dimensional nature of the formulation, two layers of particles are created along the thickness. The distance between particles in the $Z$ direction is chosen to be the same as that in $X$ and $Y$ directions. For this specific example, the total volume was equally distributed between the particles. Initial density $\rho_0 = 1000\frac{\text{kg}}{\text{m}^3}$, Young's modulus $E = 1.0 \times 10^6 \frac{\text{N}}{\text{m}^2}$ and Poisson's ratio $\nu = 0.4$ were adopted as the material parameters for a nearly incompressible neo-Hookean constitutive model. A constant velocity $V = -10\frac{\text{m}}{\text{s}}$, was imposed in the vertical $(Y)$ direction to one third of the top face, as illustrated in figure 6.34. A fixed $\alpha_{CFL} = 0.5$ was used for the simulations.

In this example, the anisotropic updated kernel and kernel gradient are obtained as a push-forward of the material kernel and material gradient, with corrections performed in the updated configuration (Option#2). A 3D cubic smoothing function is employed with a factor $f_h = 0.8$ for all the simulations.

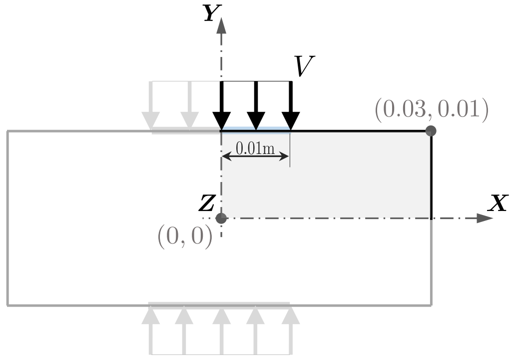

Figure 6.34: Punch test definition sketch.

In figures 6.35 and 6.36, the pressure distribution is plotted for models M1 and M2, respectively, at different instants of the simulation, for a Total Lagrangian Formulation and also for an updated reference Lagrangian formulation, with updates performed at every time step. Note that both simulations are taken to very large deformations, where the material is compressed up to 60%.

In figures 6.37 and 6.38, the $X$ and $Y$ components of the velocity are plotted for models M1 and M2 at the end of the simulation (0.0006s).

Evolution of internal, kinetic and total energies is shown for both models in TLF and ULF in figures 6.39a and 6.39c. In addition, the numerical dissipation for the

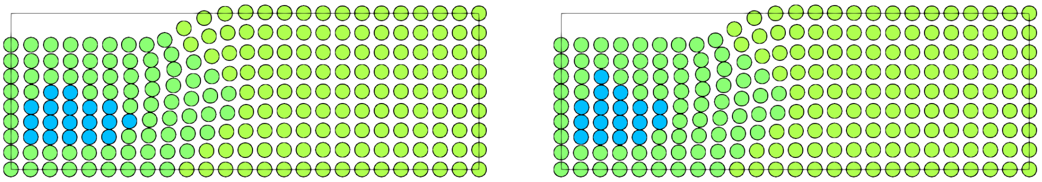

TLF 0.2ms ULF 0.2ms

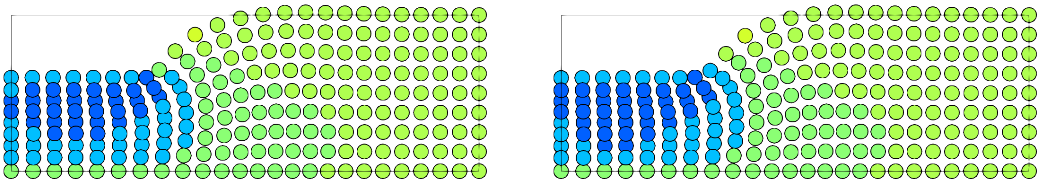

TLF 0.4ms ULF 0.4ms

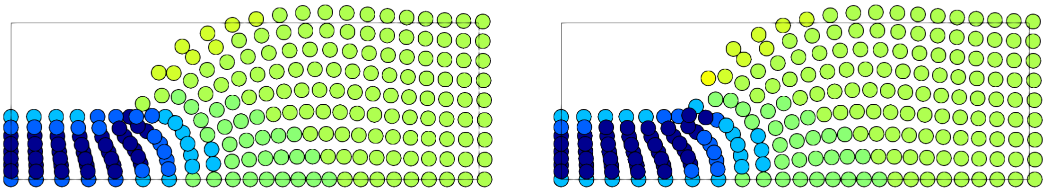

TLF 0.6ms ULF 0.6ms

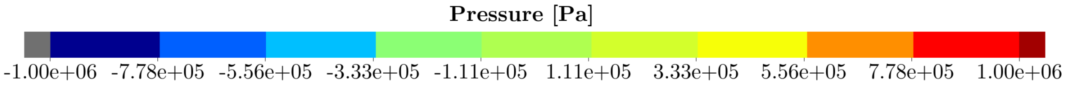

Figure 6.35: Punch test model M1 pressure distribution.

respective model is shown in figures 6.39b and 6.39d. Note that the energies were computed considering only the represented geometry, i.e., one quarter of the block.

The results presented up to now employed a 3D cubic spline kernel function, with the updated kernel and gradient obtained as a push-forward of the material kernel and material gradient, with corrections performed in the updated configuration (Option#2). The punch test example is highly compressed at the end of the simulation, which makes this problem very sensible to instabilities [24]. The robustness of the methodologies Option#3 and Option#4 of obtaining the updated kernels and gradients proposed in chapter 4 is also verified for this example. Evolution of internal, kinetic and total energies are shown for an updated reference Lagrangian formulation in figure 6.40a considering these two options. Updates are performed at every time step, and the updated kernel and gradient are obtained as a push-forward of kernel and gradient based on the pull-back of updated coordinates, corrections are performed in the updated domain (Option#3 and Option#4). In addition, the numerical dissipation for both models is shown in figure 6.40b and the pressure distribution at different instants of the simulation is shown in figure 6.41.

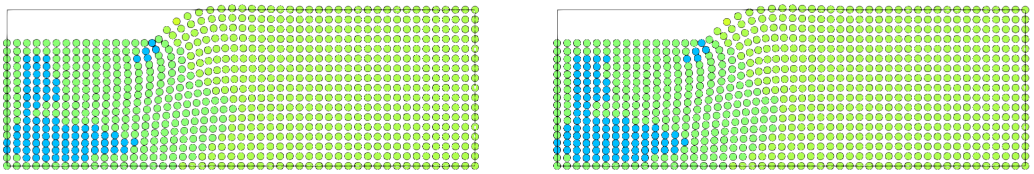

TLF 0.2ms ULF 0.2ms

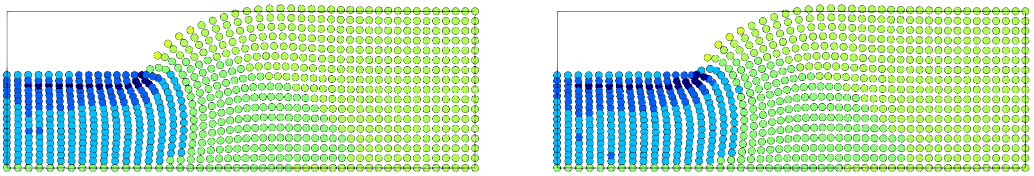

TLF 0.4ms ULF 0.4ms

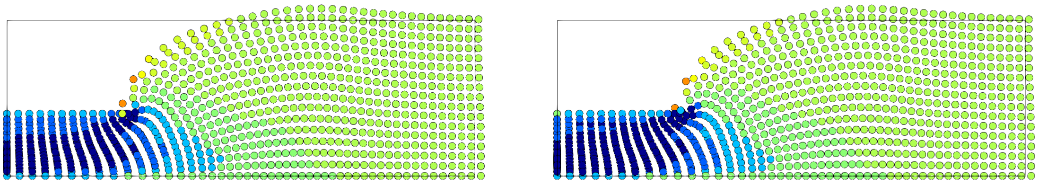

TLF 0.6ms ULF 0.6ms

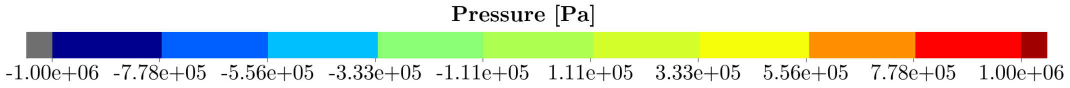

Figure 6.36: Punch test model M2 pressure distribution.

As the conclusions of the punch test example, the proposed formulation was shown to be robust and did not activate any spurious mechanisms in this test case. The results for the simulations evolved based on updated reference configurations are as good as the ones based on the initial geometry (TLF). The example was also used to test different options of obtaining updated anisotropic kernels and gradients. The options based on the updated coordinates (Option#3 and Option#4) are once again shown to work well, even for an extremely deformed domain. Regardless of which option is used, the total numerical dissipation of the algorithm is not significantly affected by the choice.

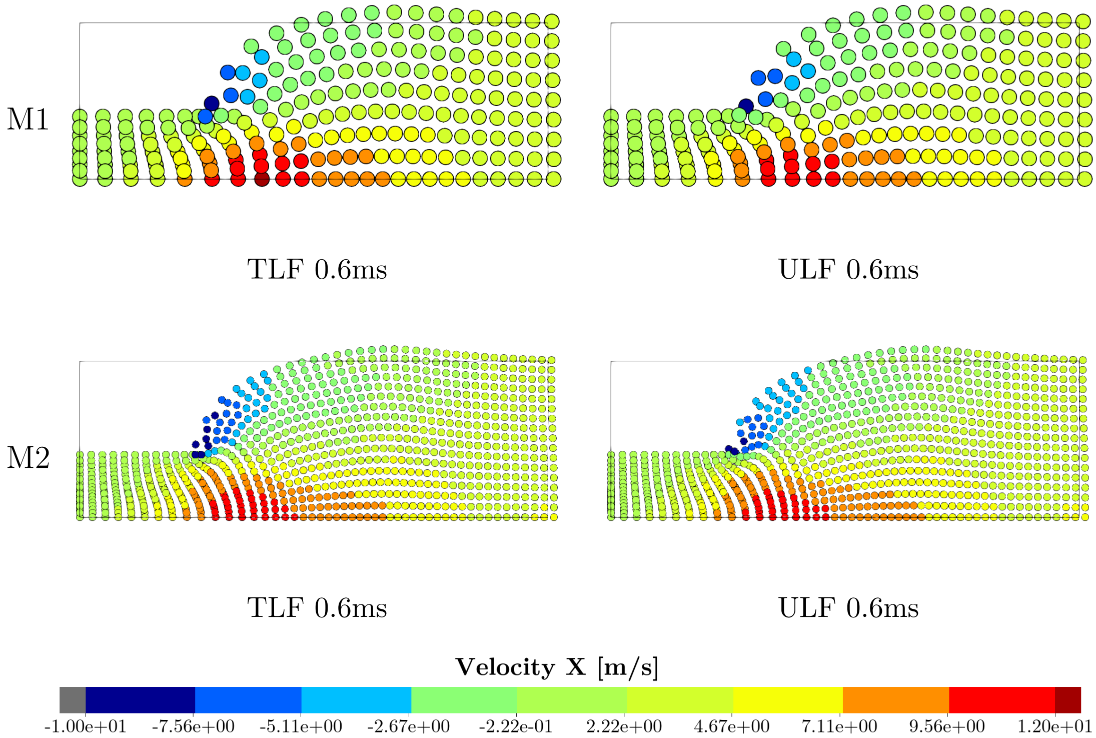

Figure 6.37: $X$ component of the velocity for the punch test models M1 and M2.

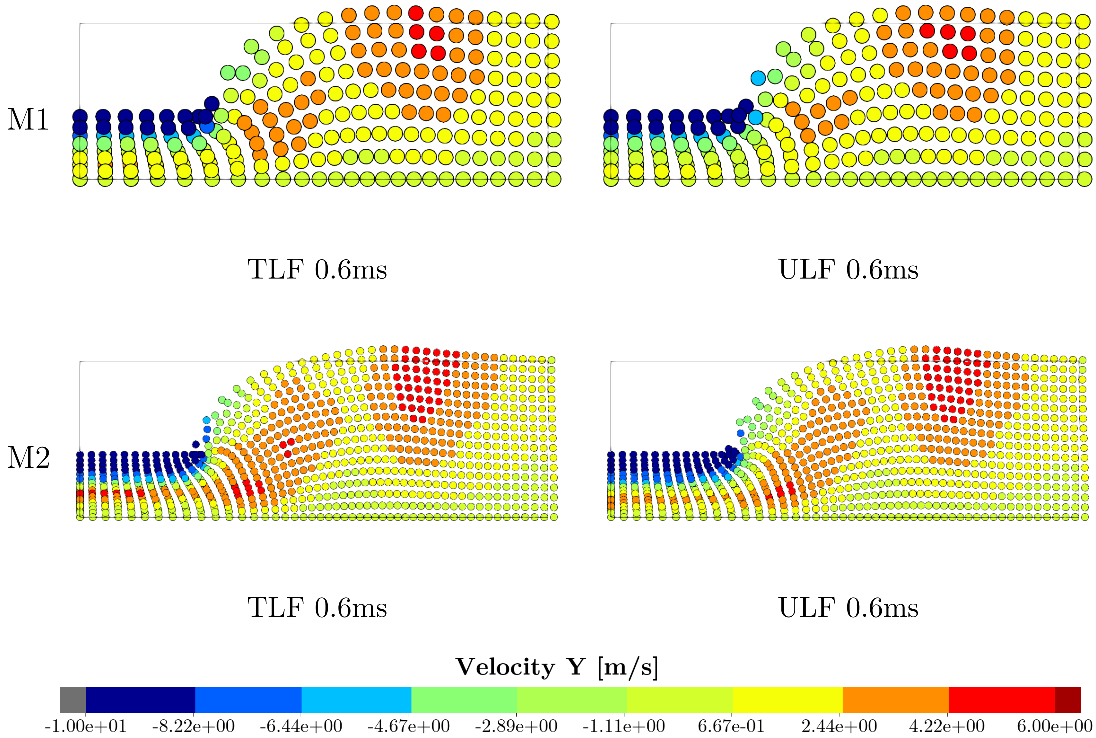

Figure 6.38: $Y$ component of the velocity for the punch test models M1 and M2.

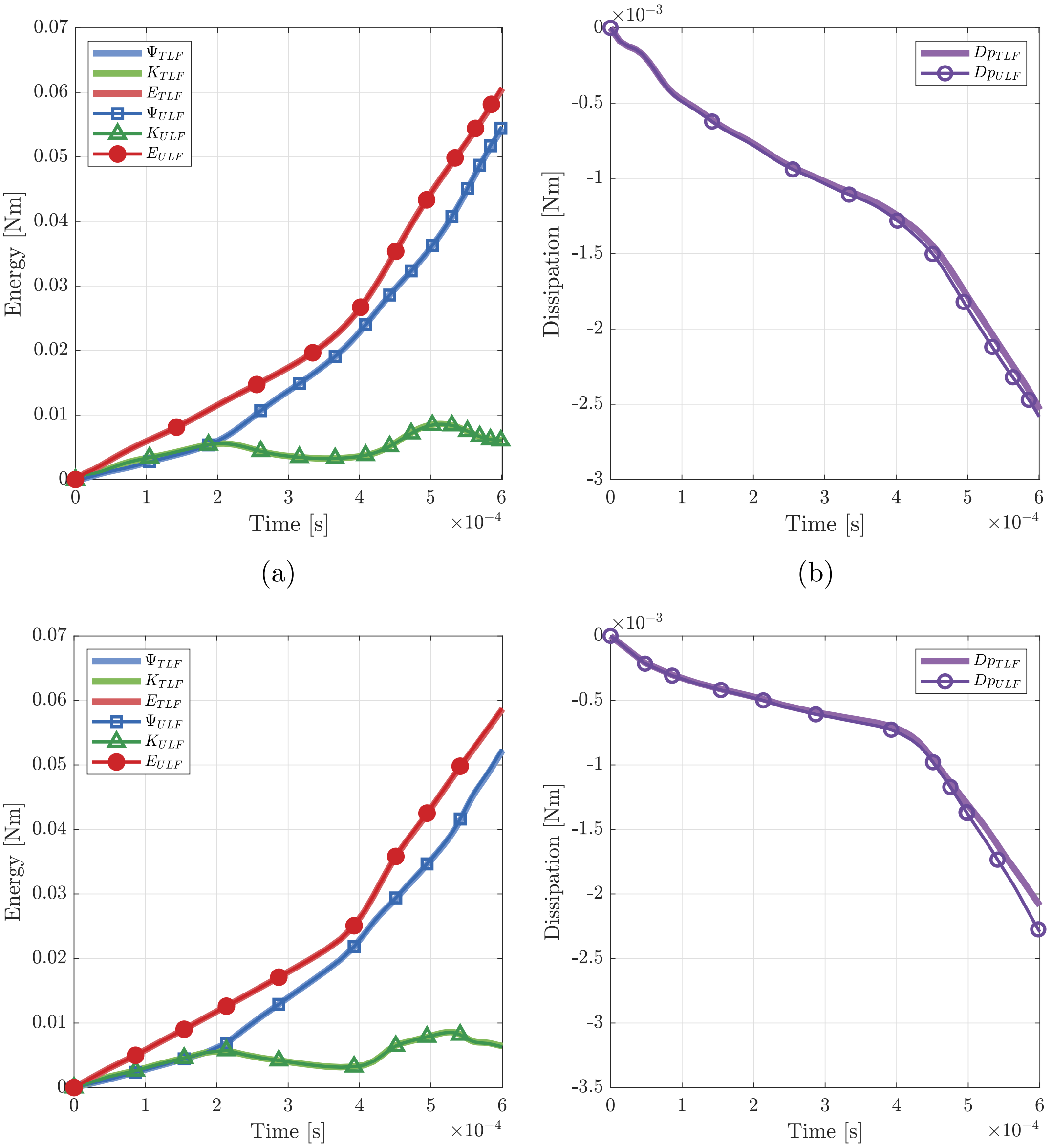

(a) (b)

(c) (d)

Figure 6.39: Evolution of kinetic ($K$), internal ($\Psi$) and total ($E$) energies for the punch test (a) model M1 and (c) model M2. Numerical dissipation for the punch test (b) model M1 and (d) model M2.

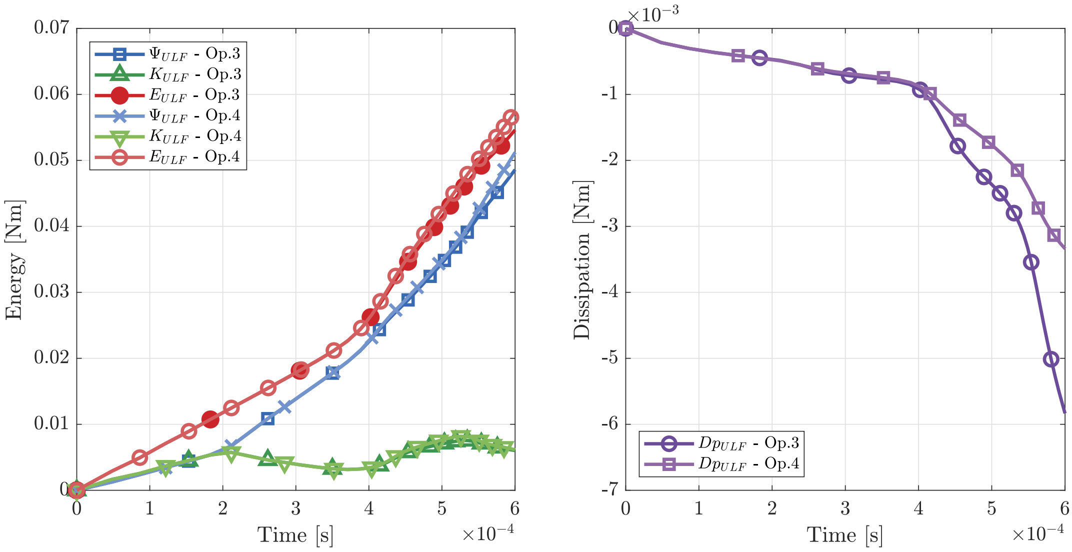

(a) (b)

Figure 6.40: (a) Evolution of kinetic ($K$), internal ($\Psi$) and total ($E$) energies for the punch test model M2, considering Option#3 and Option#4 for obtaining updated kernels and gradients. (b) Numerical dissipation for the punch test model M2.

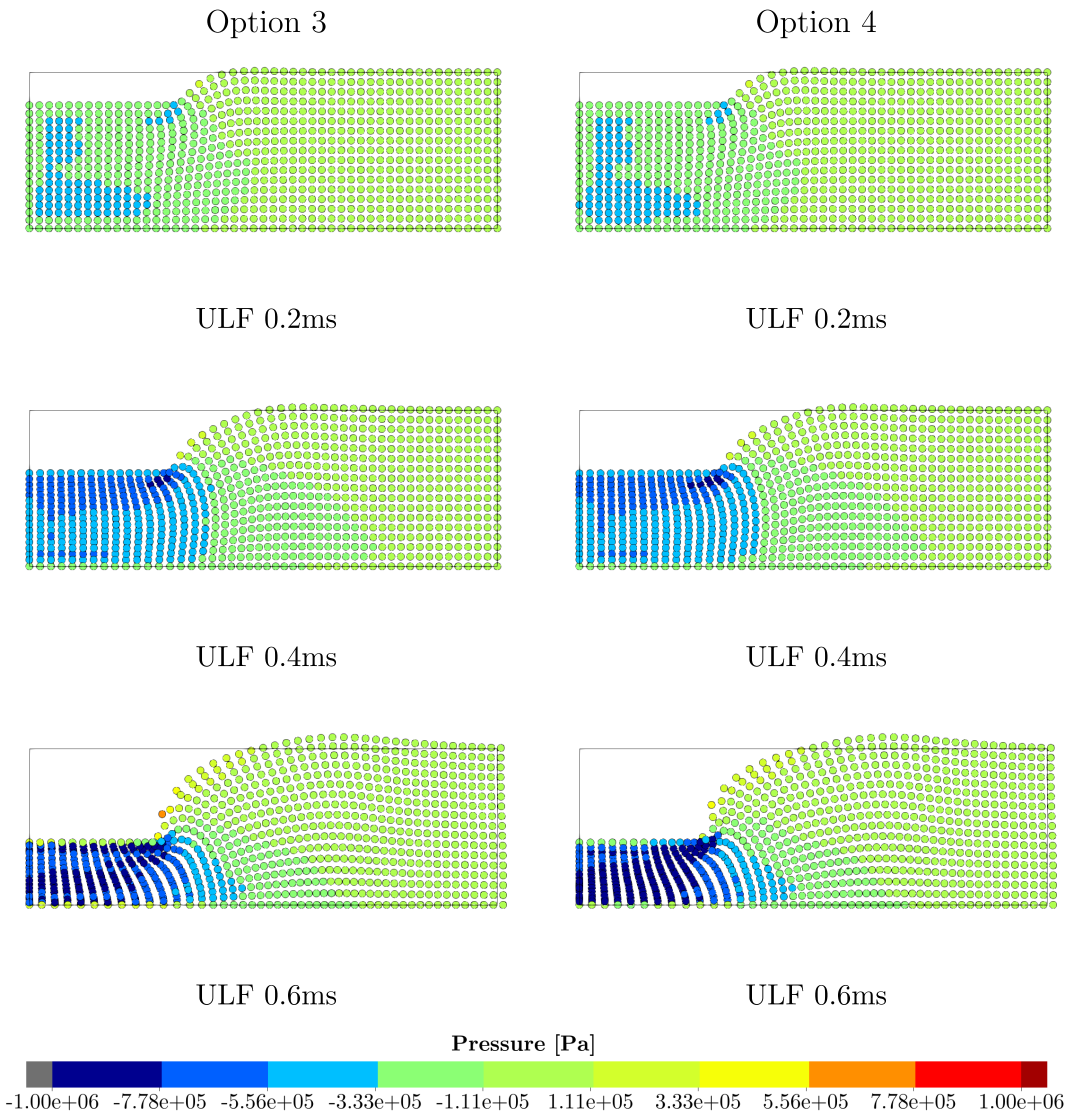

Figure 6.41: Punch test pressure distribution for model M2, considering Option#3 and Option#4 for obtaining updated kernels and gradients.

### 6.2.4 L-shaped block

This example was previously studied by many authors, e.g. [26, 76, 100–102]. The main objective of this classical benchmark problem is to examine the capability of preserving both the linear and angular momenta of a system. An L-shaped block with square cross-section 3m x 3m is subjected to an external torque induced by a pair of time-varying forces acting on two of its boundary faces, as illustrated in figure 6.42. The traction forces $\boldsymbol{F}_1(t)$ and $\boldsymbol{F}_2(t)$ are given in $\frac{\mathrm{N}}{\mathrm{m}^2}$ as

$$\boldsymbol{F}_1(t) = -\boldsymbol{F}_2(t) = \begin{bmatrix} 150 \\ 300 \\ 450 \end{bmatrix} f(t), \qquad f(t) = \begin{cases} t & 0 \leq t < 2.5\mathrm{s}, \\ 5 - t & 2.5 \leq t < 5\mathrm{s}, \\ 0 & t \geq 5\mathrm{s}. \end{cases} \tag{6.2}$$

A uniform distribution of particles was employed and a sequence of model refinements were analysed: models M1 to M3 with 828, 5445 and 13950 particles, respectively. For this specific example, a tributary volume distribution was employed. Initial density $\rho_0 = 1100\frac{\mathrm{kg}}{\mathrm{m}^3}$, Young's modulus $E = 50500\frac{\mathrm{N}}{\mathrm{m}^2}$ and Poisson's ratio $\nu = 0.3$ were adopted as the material parameters for a nearly incompressible neo-Hookean constitutive model. A fixed $\alpha_{CFL} = 0.9$ was used for the simulations.

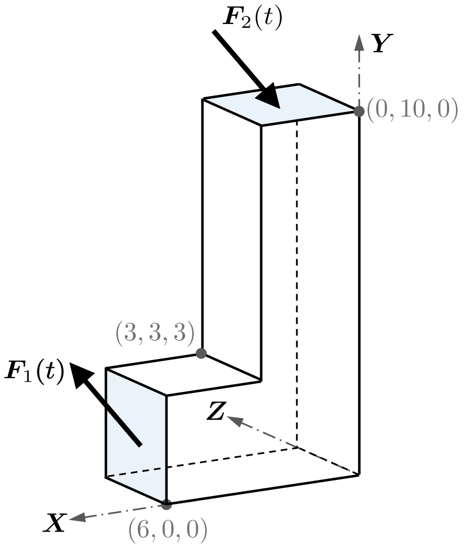

Figure 6.42: L-shaped block.

In this example, the anisotropic updated kernel and kernel gradient are obtained as a push-forward of the material kernel and material gradient, with corrections performed in the updated configuration (Option#2). A 3D quadratic smoothing function is employed with a factor $f_h = 0.6$ for all the simulations.

In figure 6.43 the pressure distribution for model M1 is plotted at different instants of the simulation, for a Total Lagrangian Formulation and also for an updated reference Lagrangian formulation, with updates performed at every time step. The same results are shown for model M3 in figure 6.44.

Evolution of internal, kinetic and total energies is shown for both TLF and ULF for models M1 and M3 in figures 6.45a and 6.45b, respectively. Moreover, for the

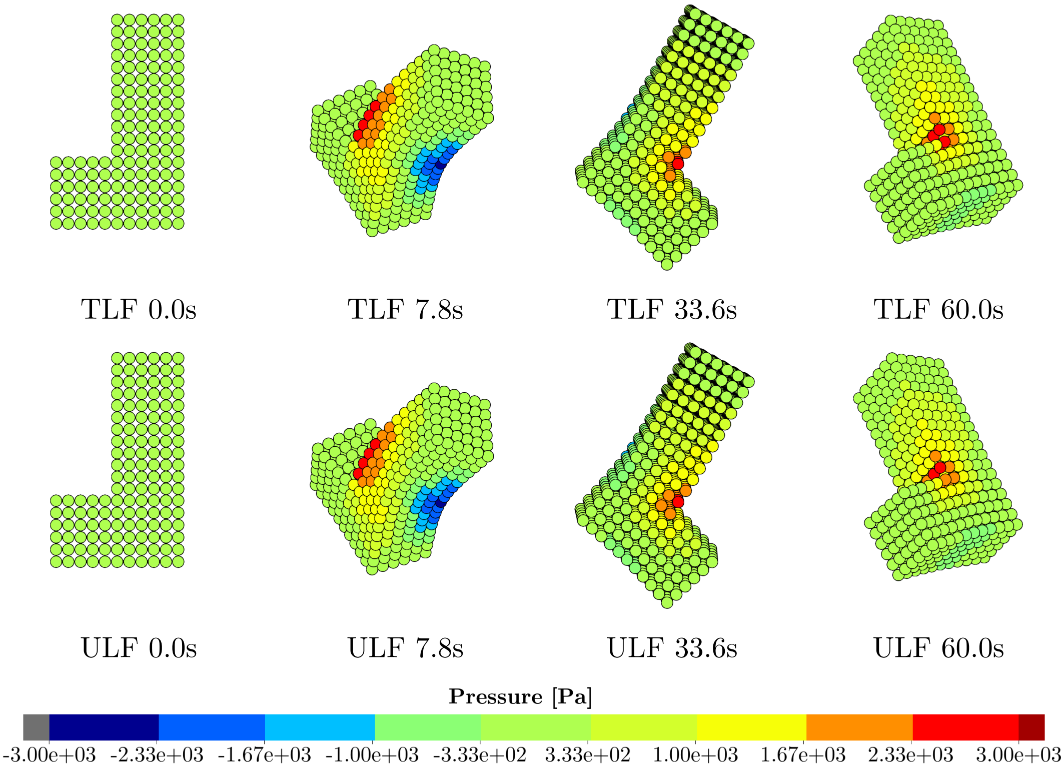

Figure 6.43: L-shaped block M1 pressure distribution.

ULF models M1 and M3, the evolution of global linear and angular momenta is plotted in figures 6.46a, 6.46b, 6.46c, 6.46d.

The evolution of total energy comparing the different model refinements is shown for ULF in figure 6.47a. In addition, the numerical dissipation for the corresponding model is shown in figure 6.47b. The pressure distribution at time 51.0s is also shown for the three models in figure 6.48 for an updated reference Lagrangian formulation, with updates performed at every time step.

As the conclusions of the L-shaped block example, the proposed formulation was shown to be robust and did not activate any spurious mechanisms in this test case. The results for the simulations evolved based on updated reference configurations are as good as the ones based on the initial geometry (TLF). The example demonstrates the ability of the proposed algorithm in preserving both the linear momentum and angular momentum of the system. Specifically, the total linear momentum is close to (and oscillates around) zero machine accuracy at all times, whereas the total angular momentum is conserved after the loading phase.

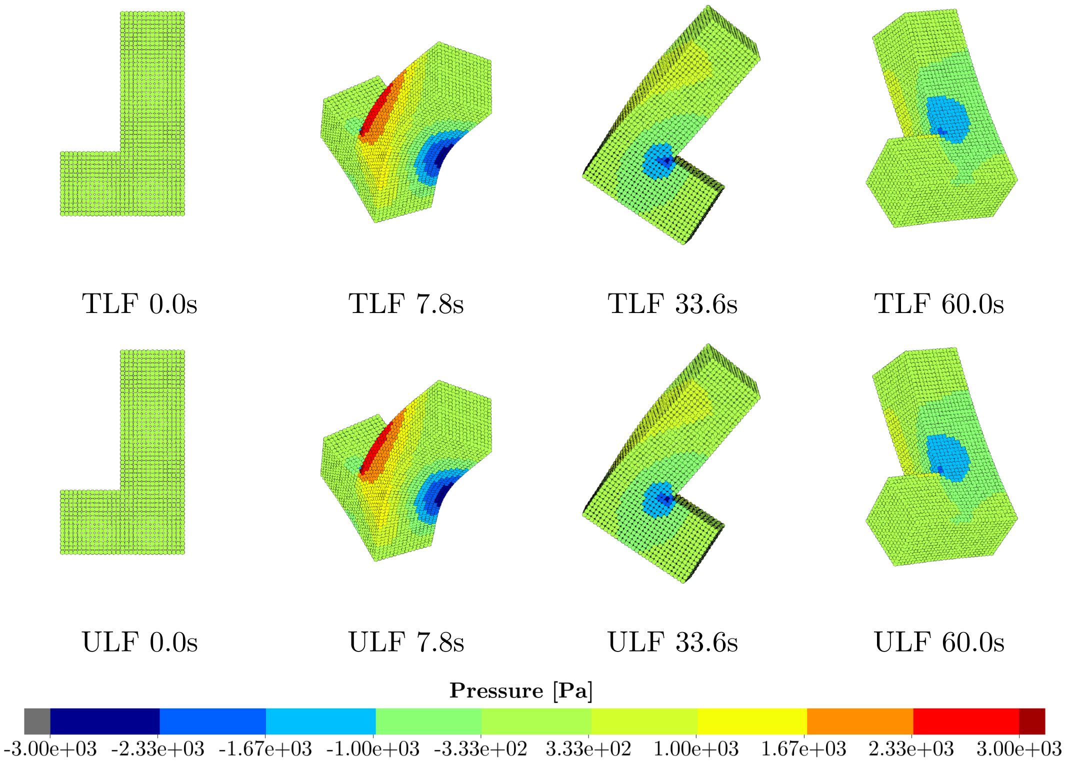

Figure 6.44: L-shaped block M3 pressure distribution.

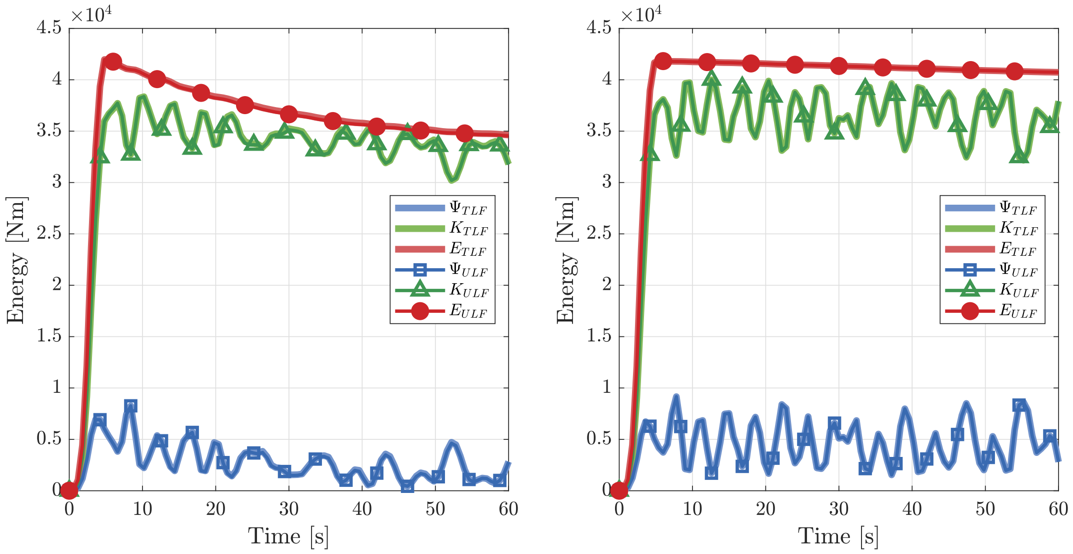

(a) (b)

Figure 6.45: Evolution of kinetic ($K$), internal ($\Psi$) and total ($E$) energies for the L-shaped block: (a) model M1. (b) model M3.

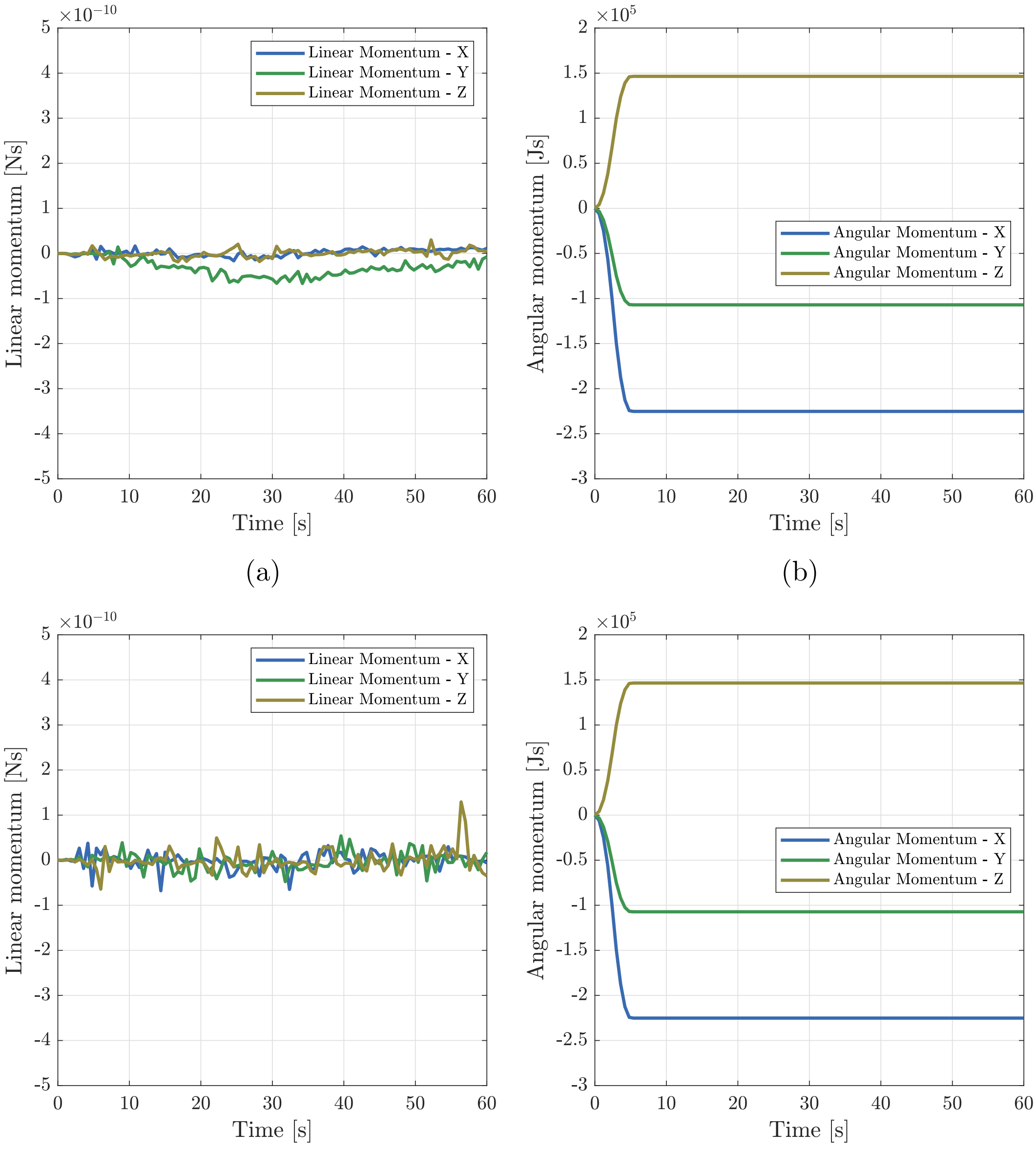

(a)

(b)

(c)

(d)

Figure 6.46: Evolution of the components of the global linear and angular momenta for the L-shaped block. (a) and (b) model M1. (c) and (d) model M3.

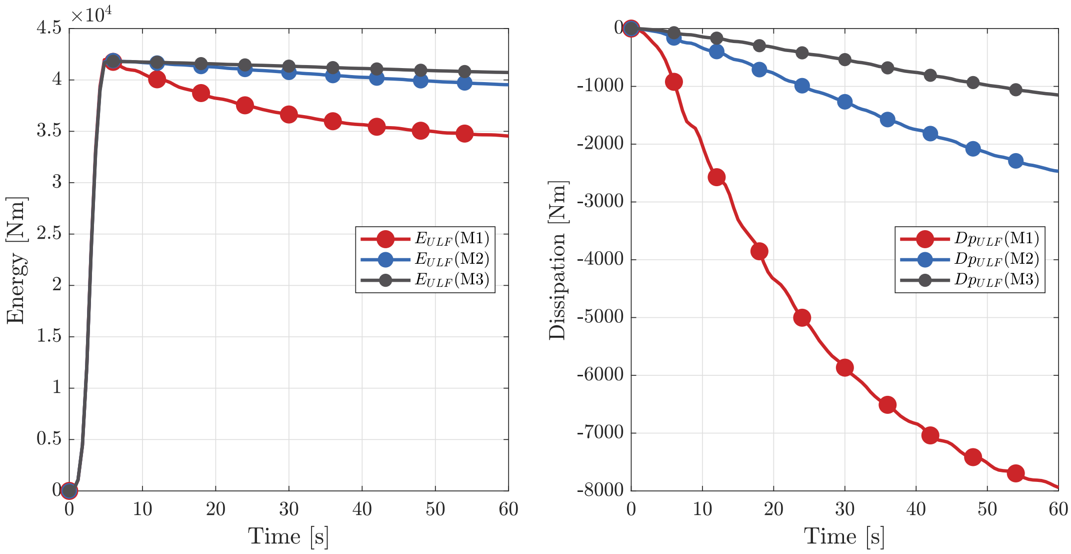

(a) (b)

Figure 6.47: (a) Evolution of total energy ($E$) for different model refinements of the L-shaped block. b) Numerical dissipation.

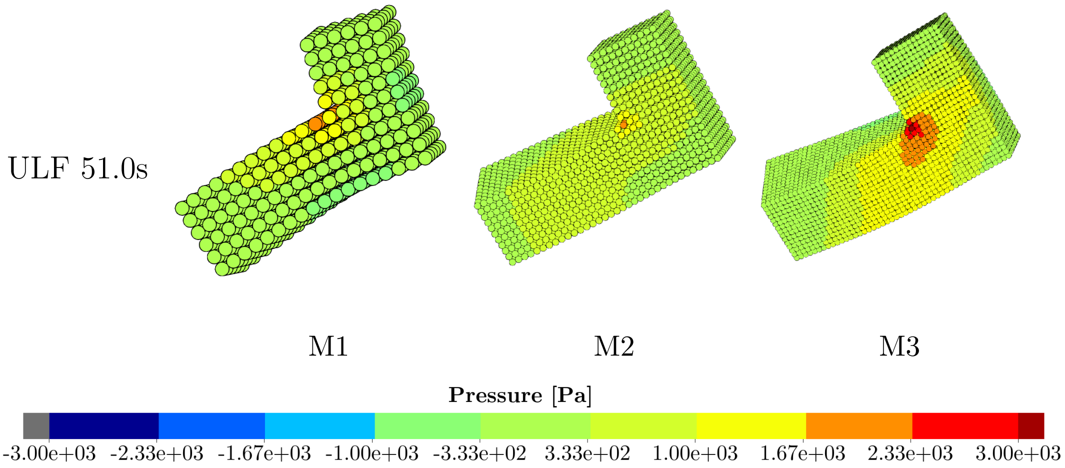

Figure 6.48: Pressure distribution at time 51.0s for the L-shaped block considering different model refinements in an updated reference Lagrangian formulation, with updates performed at every time step.

## 6.3 Isothermal plasticity

### 6.3.1 Impact bar

This example simulates the high speed impact of a cylindrical bar onto a rigid wall. The test is also described as the Taylor bar experiment. The characteristics of the model presented herein follows [103]. The same example was analysed by many other authors, including [27], where it was studied under a TLF-SPH framework. The model consists of a cylindrical bar of radius $R = 0.0032\text{m}$ and length $L = 0.0324\text{m}$, the main characteristics of the model are illustrated in figure 6.49. The properties of the Hencky-based von Mises plasticity model, with linear hardening (equation 2.52), are: initial density $\rho_0 = 8930\frac{\text{kg}}{\text{m}^3}$, Young's modulus $E = 117\times10^9\frac{\text{N}}{\text{m}^2}$, Poisson's ratio $\nu = 0.35$, yield stress, $\tau_y^0 = 400\times10^6\frac{\text{N}}{\text{m}^2}$ and linear hardening modulus $H = 100 \times 10^6\frac{\text{N}}{\text{m}^2}$. The frictionless contact between the bar and the rigid support is taken into account by restricting the movement of the bottom particles in the $Z$ direction. An initial velocity $\boldsymbol{v} = V\,[0,0,1]^T$, where $V = -227\frac{\text{m}}{\text{s}}$, was imposed for all particles in the model. The contact condition is active since the beginning of the simulation and a total time of $8.0 \times 10^{-5}$s was simulated with a fixed $\alpha_{CFL} = 0.9$.

In this example, the anisotropic updated kernel and kernel gradient are obtained as a push-forward of the corrected material kernel and corrected material gradient (Option#1). A 3D quadratic smoothing function is employed with a factor $f_h = 0.6$ for all the simulations.

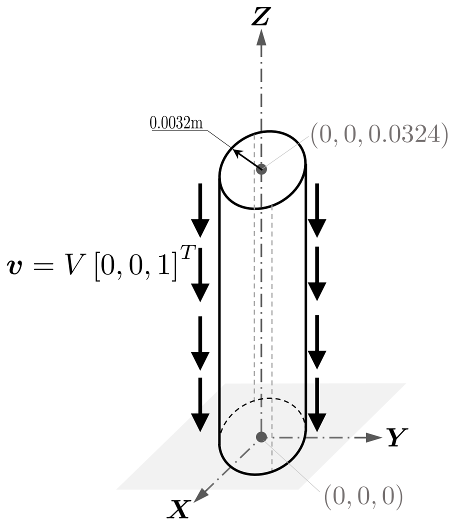

Figure 6.49: Impact bar.

Due to the symmetry of the problem, only one quarter of the geometry is represented. Initially, 1560 particles were used for the discretisation and approximately the same refinement is used for all regions of the bar. Refined models with 3744 and 7280 particles were also studied, the three different models are illustrated in figure 6.50. For this specific example, a tributary volume distribution was employed.

In figures 6.51, 6.52 and 6.53, the von Mises stress distribution and the equivalent plastic strain are plotted at different instants of the simulation, for a Total Lagrangian Formulation and also for an updated reference Lagrangian formulation, with updates performed at every time step, for the three models.

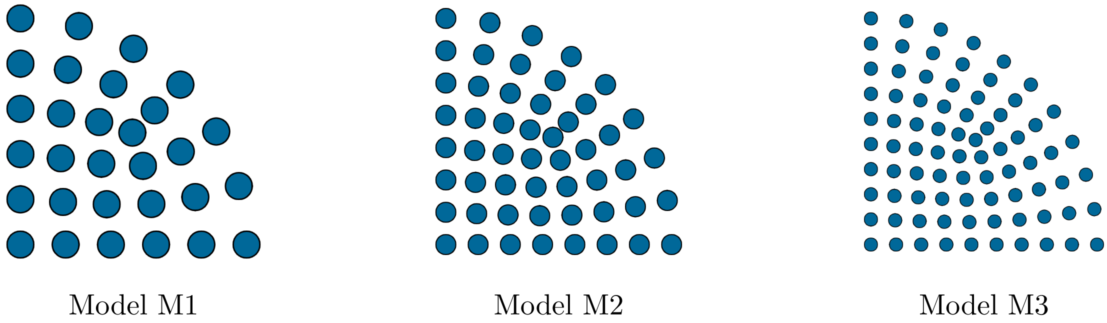

Figure 6.50: Impact bar particle distribution.

Evolution of internal, kinetic and total energies is shown for both TLF and ULF in figure 6.54a for model M1. In addition, the numerical dissipation in the same model is shown in figure 6.54b. The same results are shown for models M2 and M3 in figures 6.55 and 6.56. Note that the energies were computed considering only the represented geometry, i.e., one quarter of the cylinder. In terms of the energy plots, the kinetic energy of the system decreases upon impact. Such energy first transforms into elastic strain energy (prior to plasticity), followed by the addition of plastic dissipation (within the plastic regime). Moreover, given the nature of the proposed algorithm, a very small amount of the kinetic energy also converts to monotonic decreasing numerical dissipation during the deformation process.

In figure 6.57a, for the model M1, the pressure distribution is shown at the end of the simulation. Total Lagrangian results are presented on the left half of bar, while the updated Lagrangian solution is shown on the right side. In addition, figure 6.57b shows the evolution of the radius of the bar in the impact region as a function of the vertical top displacement, results are presented for total and updated formulations. Similar figures are presented for model M2 in 6.58a and 6.58b, and M3 in 6.59a and 6.59b.

Figure 6.60 shows the time evolution of the radius of the bar in the impact region for the three models. The final radius of the copper bar at time $t = 80$ $\mu$s predicted by the proposed algorithm is benchmarked against other published numerical results [27, 104]. As shown in Reference [104], the solutions obtained using the standard linear 4-noded tetrahedra (being widely used in commercial software) typically suffers from volumetric locking and pressure instabilities. The proposed meshfree method clearly circumvents these issues.

The results presented up to now were obtained employing a 3D quadratic kernel function. Additionally, the 3D cubic spline smoothing function is now tested with model M3, in both Total Lagrangian Formulation and updated reference Lagrangian formulation with updates performed at every time step. The pressure distribution is shown at the end of the simulation in figure 6.61a, total Lagrangian results are presented on the left half of bar, while the updated Lagrangian solution is shown on the right side. The evolution of the radius of the bar in the impact region as a function of the vertical top displacement is presented in figure 6.61b. For the same model, von Mises stresses and equivalent plastic strains are presented in figures 6.62a and 6.62b.

As the conclusions of the impact bar example, extremely high plastic strains develop at the crushed end of the bar and the proposed formulation was shown to

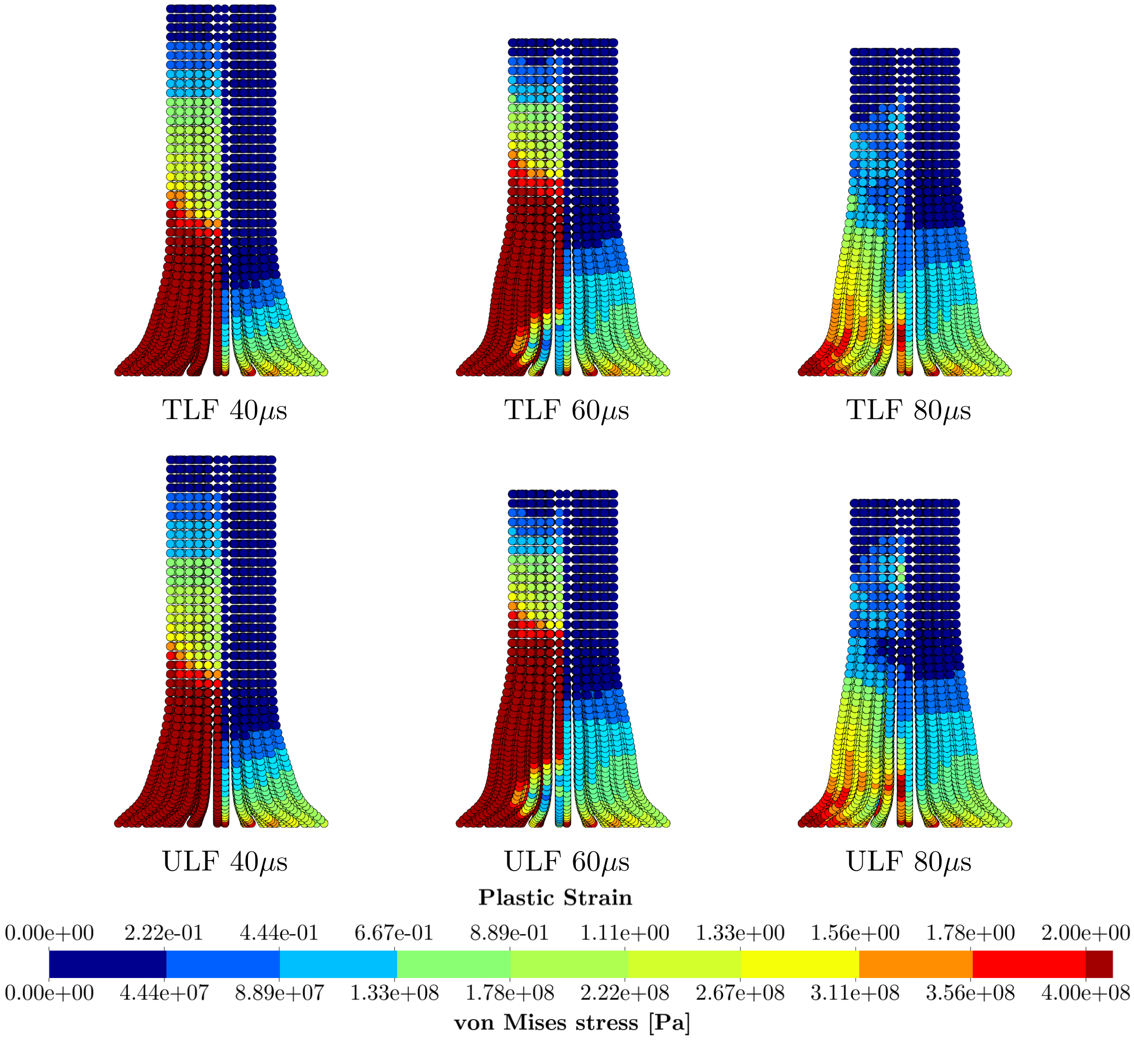

TLF 40$\mu$s TLF 60$\mu$s TLF 80$\mu$s

ULF 40$\mu$s ULF 60$\mu$s ULF 80$\mu$s

Figure 6.51: Impact bar model M1 von Mises stresses (left side) and equivalent plastic strain (right side).

be robust in such scenario. The results for the simulations evolved based on updated reference configurations are as good as the ones based on the initial geometry (TLF). Moreover, no expressive differences were observed if a 3D quadratic or a 3D cubic spline kernel function is employed, both smoothing functions performed equally well for this example. The results approach the values reported in the literature as the model is refined. The consistency of the stabilisation scheme proposed is also verified with the model refinement, less numerical dissipation is observed as the number of particles is increased.

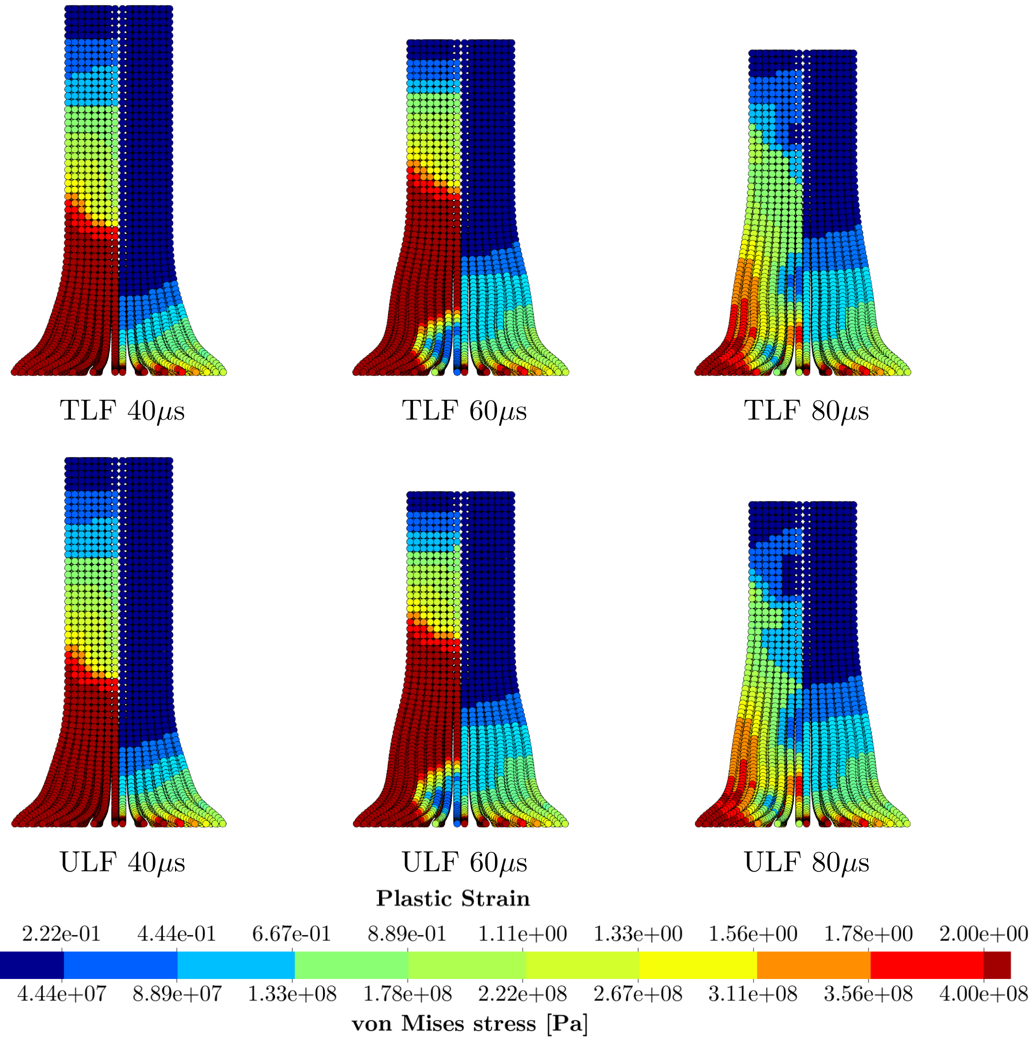

TLF 40$\mu$s TLF 60$\mu$s TLF 80$\mu$s

ULF 40$\mu$s ULF 60$\mu$s ULF 80$\mu$s

Figure 6.52: Impact bar model M2 von Mises stresses (left side) and equivalent plastic strain (right side).

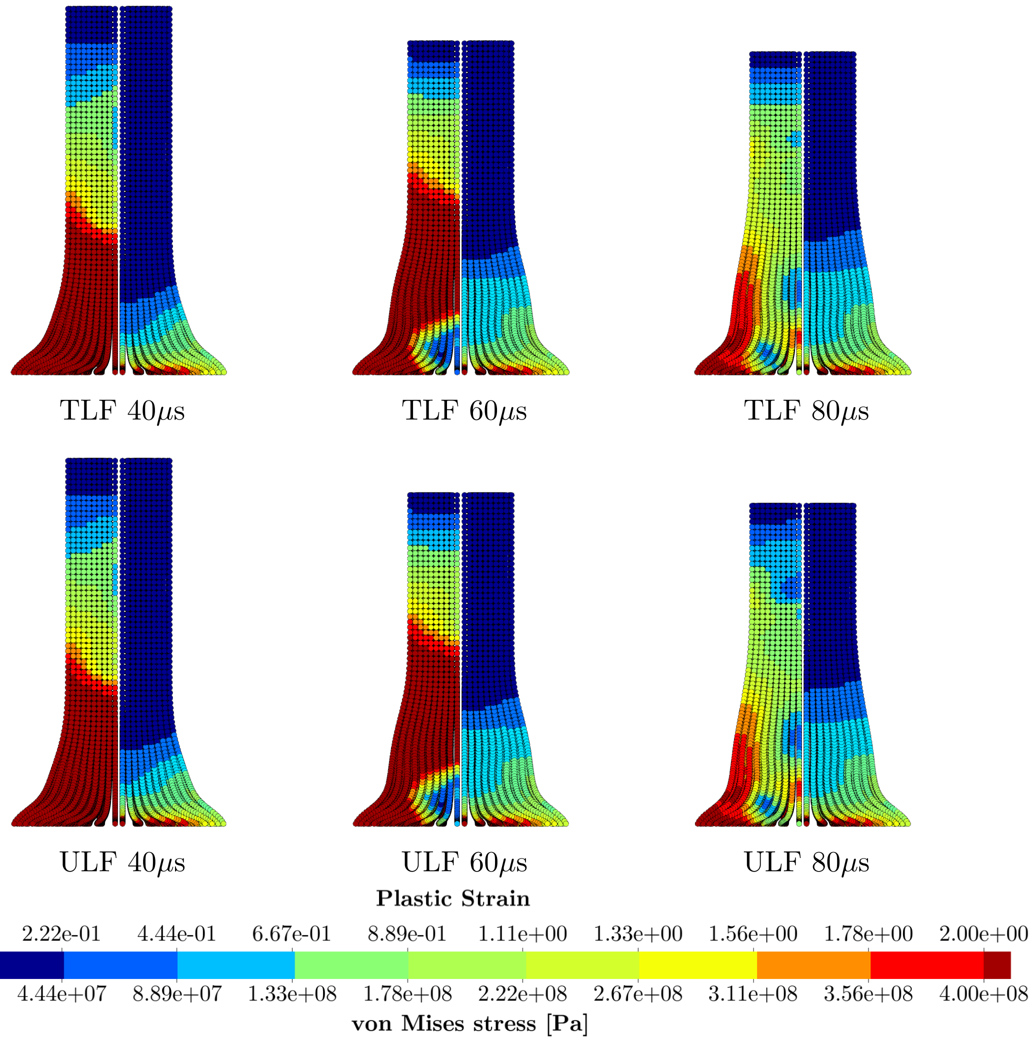
TLF 40$\mu$s TLF 60$\mu$s TLF 80$\mu$s

ULF 40$\mu$s ULF 60$\mu$s ULF 80$\mu$s

Figure 6.53: Impact bar model M3 von Mises stresses (left side) and equivalent plastic strain (right side).

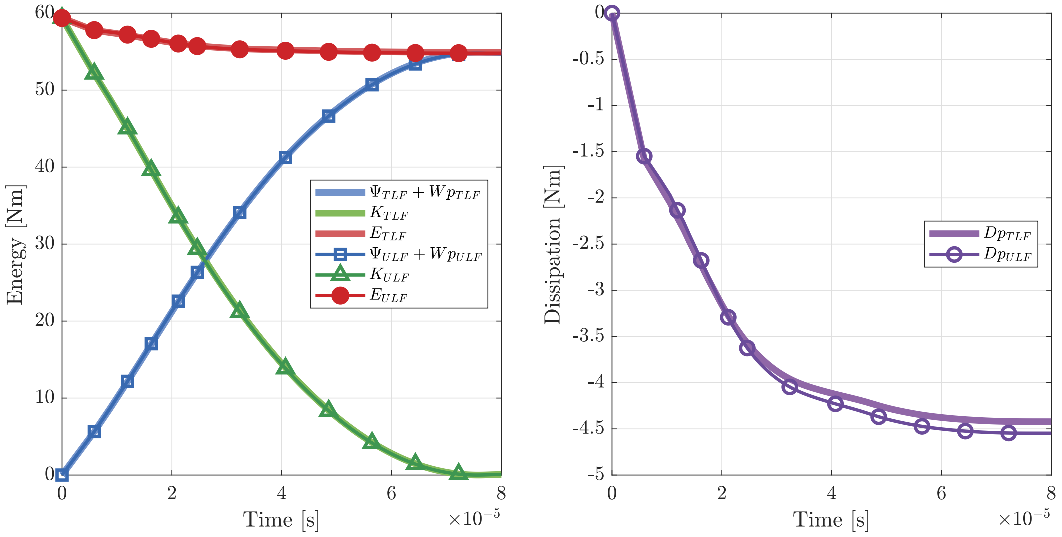

(a) (b)

Figure 6.54: (a) Evolution of kinetic ($K$), internal ($\Psi$) plus plastic dissipation ($Wp$) and total ($E$) energies for impact bar model M1. (b) Numerical dissipation for the model M1.

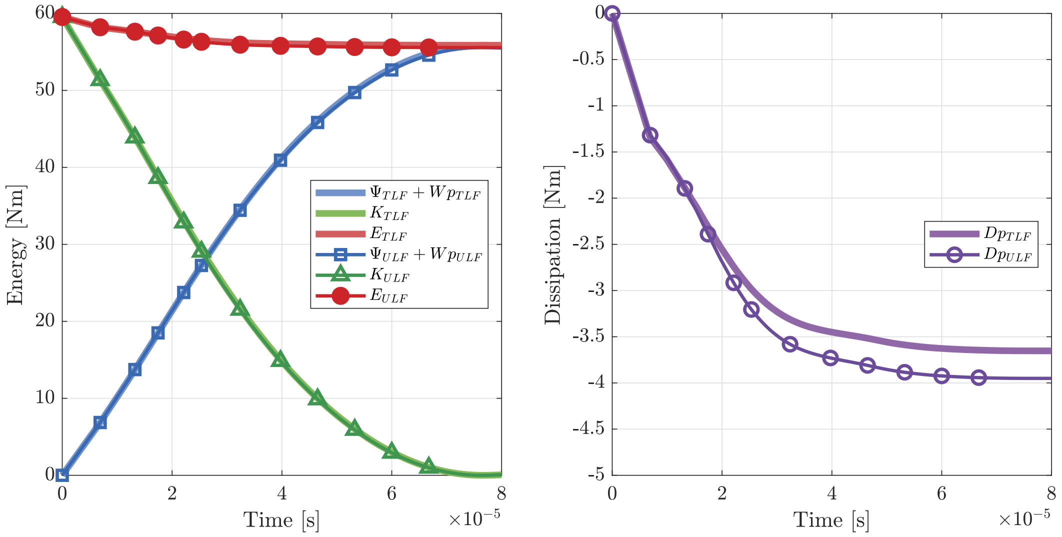

(a) (b)

Figure 6.55: (a) Evolution of kinetic ($K$), internal ($\Psi$) plus plastic dissipation ($Wp$) and total ($E$) energies for impact bar model M2. (b) Numerical dissipation for the model M2.

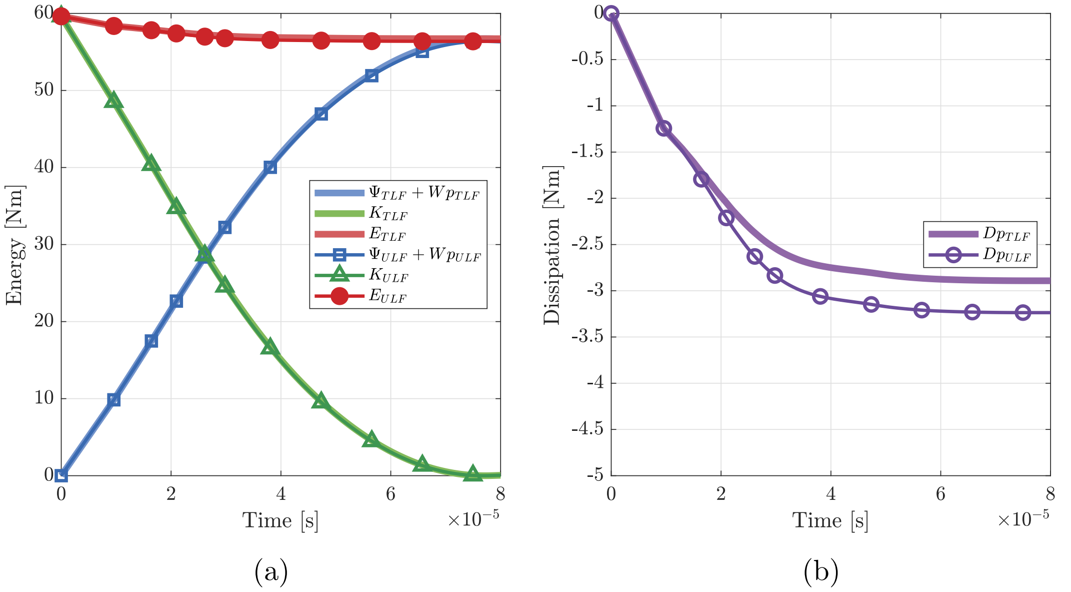

(a) (b)

Figure 6.56: (a) Evolution of kinetic ($K$), internal ($\Psi$) plus plastic dissipation ($Wp$) and total ($E$) energies for impact bar model M3. (b) Numerical dissipation for the model M3.

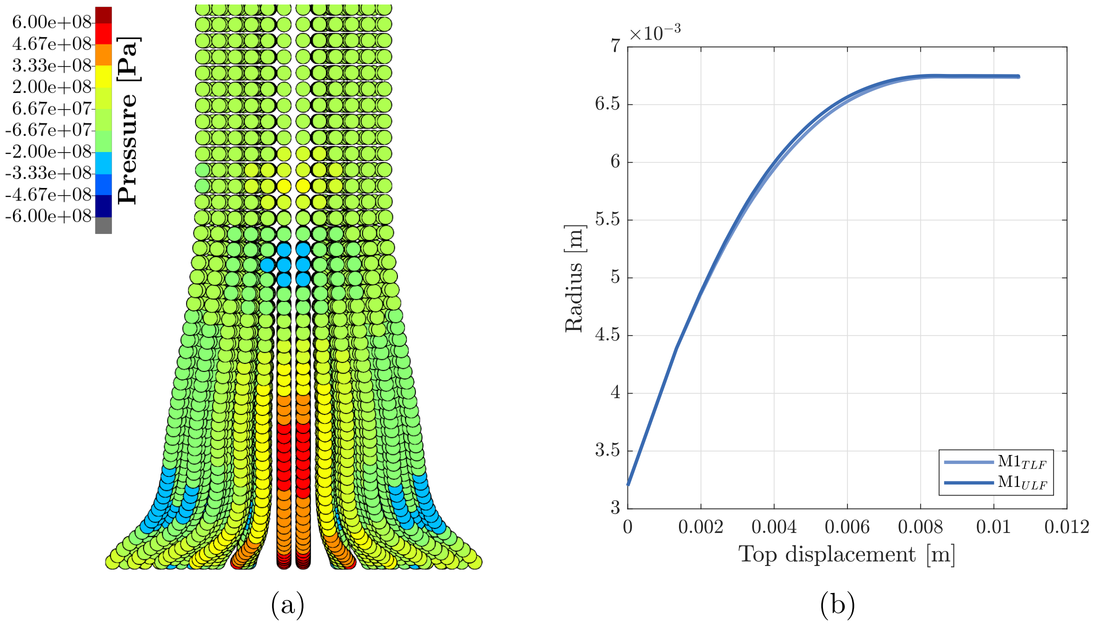

(a) (b)

Figure 6.57: (a) Pressure distribution after $8.0 \times 10^{-5}$s for the model M1: TLF on the left side and ULF on the right side. (b) Evolution of the radius of the bar measured at the impact interface as a function of the top displacement.

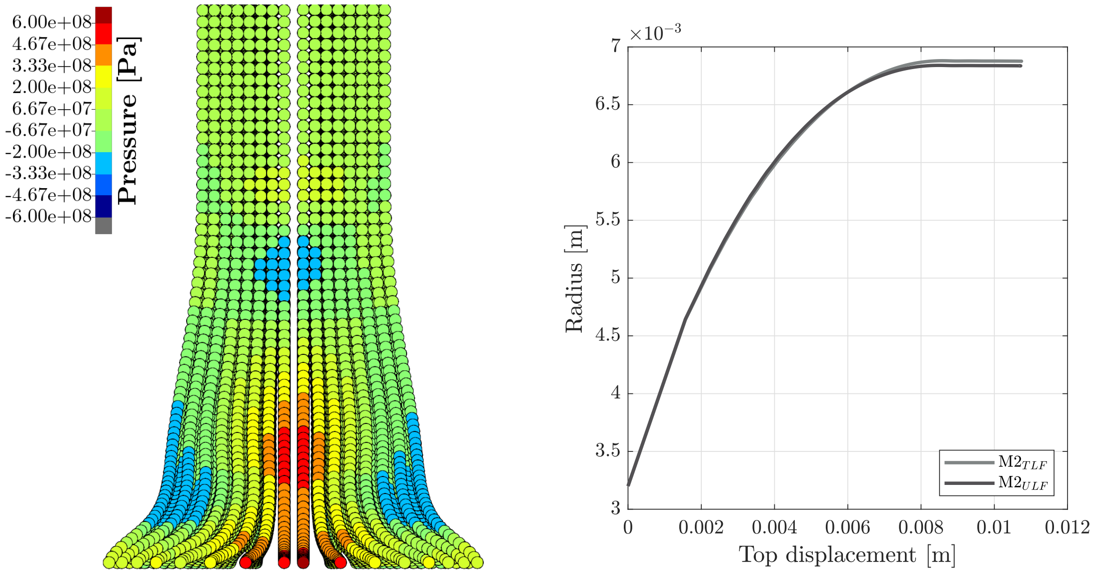

(a) (b)

Figure 6.58: (a) Pressure distribution after $8.0 \times 10^{-5}$s for the model M2: TLF on the left side and ULF on the right side. (b) Evolution of the radius of the bar measured at the impact interface as a function of the top displacement.

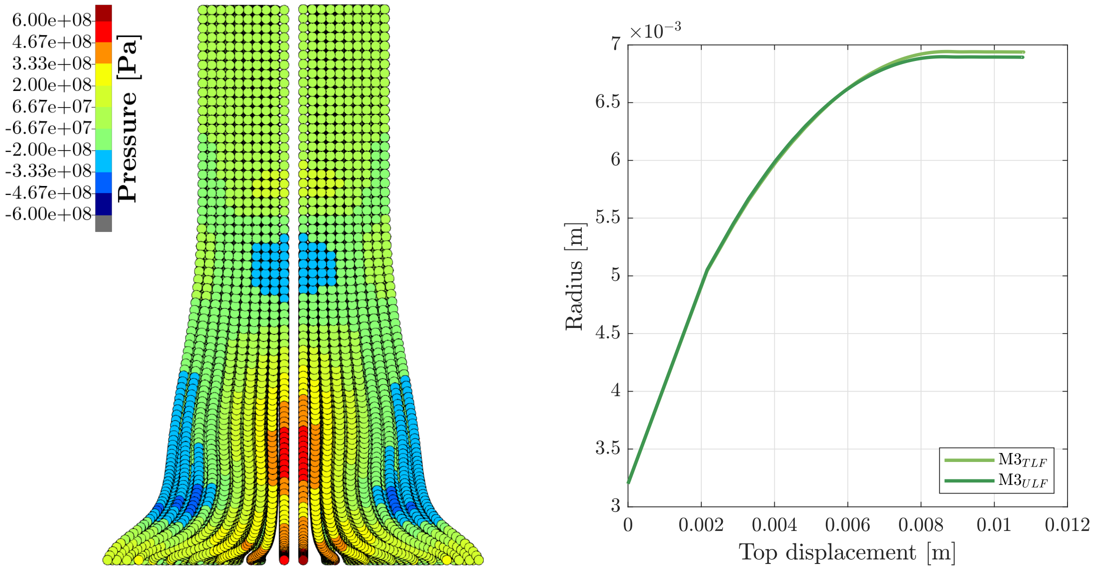

(a) (b)

Figure 6.59: (a) Pressure distribution after $8.0 \times 10^{-5}$s for the model M3: TLF on the left side and ULF on the right side. (b) Evolution of the radius of the bar measured at the impact interface as a function of the top displacement.

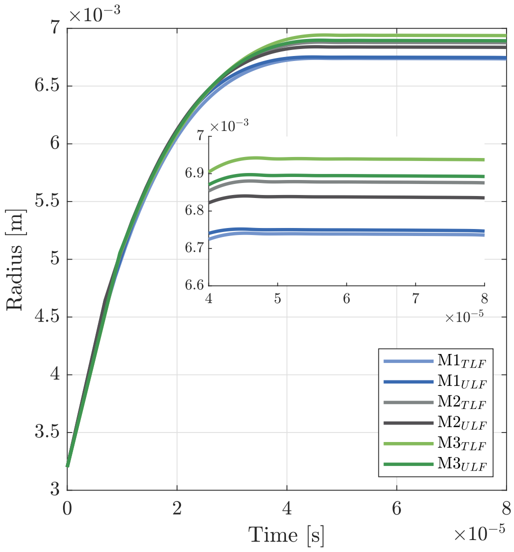

| Method | | Final radius (cm) |
|---|---|---|
| Standard 4-noded tetrahedra [104] | | 0.555 |
| Under-integrated 8-noded hexahedra [104] | | 0.695 |
| Average nodal pressure 4-noded tetrahedra [104] | | 0.699 |
| Upwind-SPH Total Lagrangian [27] | | 0.689 |
| **Updated reference Lagrangian SPH** | M1 | **0.675** |
| **Updated reference Lagrangian SPH** | M2 | **0.684** |
| **Updated reference Lagrangian SPH** | M3 | **0.689** |

Figure 6.60: Time evolution of the radius of the bar measured at the impact interface.

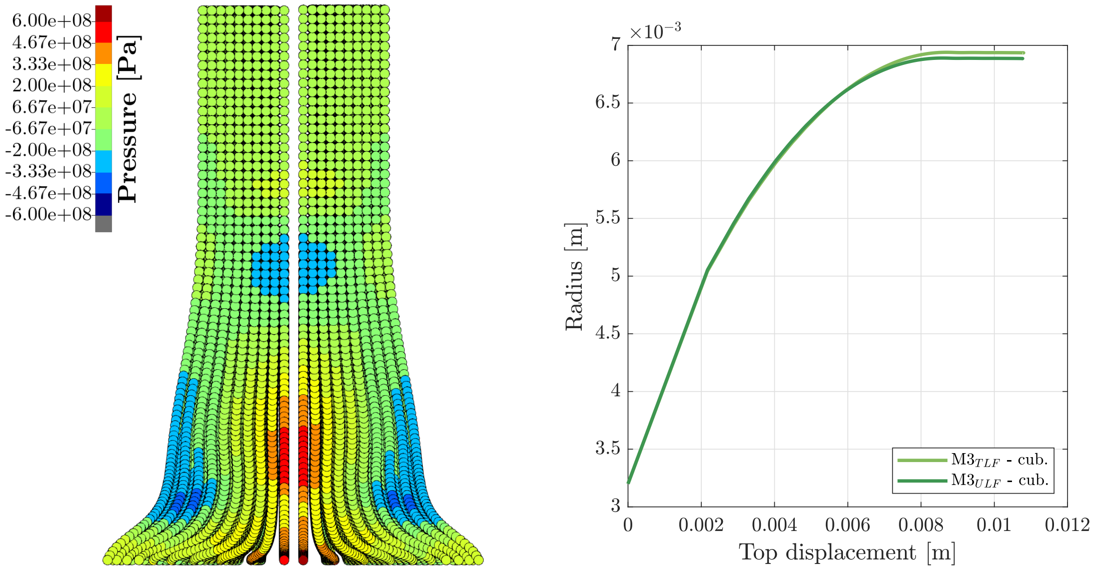

(a) (b)

Figure 6.61: (a) Pressure distribution after $8.0 \times 10^{-5}$s for the model M3 employing a 3D cubic spline kernel function: TLF on the left side and ULF on the right side. (b) Evolution of the radius of the bar measured at the impact interface as a function of the top displacement.

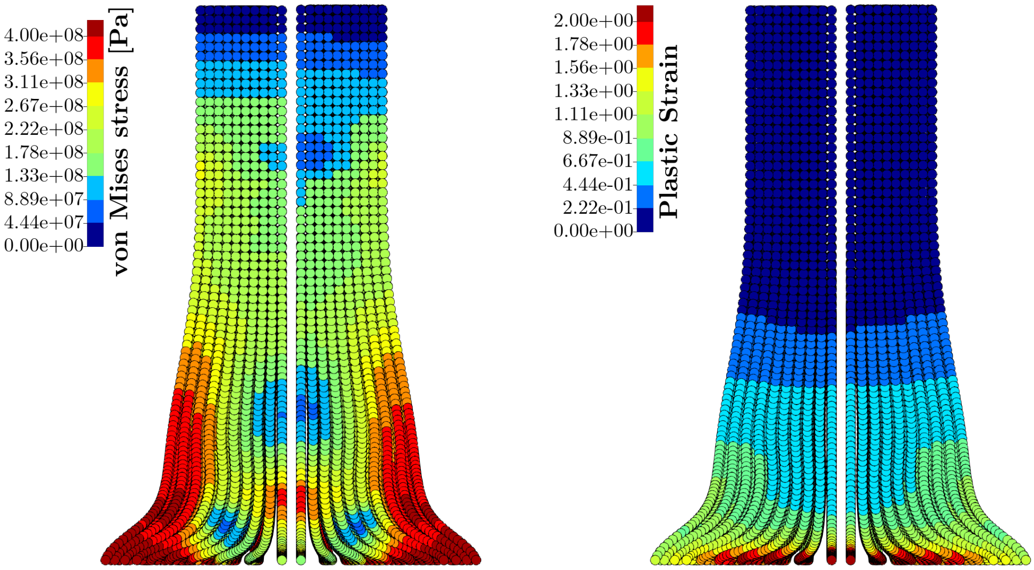

(a) (b)

Figure 6.62: Impact bar model M3 after $8.0 \times 10^{-5}$s employing a 3D cubic spline kernel function: (a) von Mises stresses, TLF on the left side and ULF on the right side. (b) Equivalent plastic strain, TLF on the left side and ULF on the right side.

### 6.3.2 Necking bar

This example illustrates the necking of a round tensile bar. The necking bar was previously studied by many authors, for example [105–109]. The model presented herein consists of a cylindrical bar of radius $R = 0.006413\text{m}$ and length $L = 0.053334\text{m}$, the main characteristics of the model are illustrated in figure 6.63. Notice in figure 6.63b that a geometric imperfection (1% of reduction in the radius) is introduced to induce necking in the central region of the bar. The model presents many possibilities for making use of symmetry conditions, in this work, only a slice of $\frac{\pi}{16}$rad of the upper half of the cylinder was modelled. Therefore, in addition to the conditions to provide an axisymmetric-like behaviour, a symmetry condition was also applied in the longitudinal direction. Two different refinements were studied, the particle distribution is non-uniform and the refinement is concentrated in the necking region. Model M1 contains 1428 particles, while model M2 consists of 5535 particles (see figure 6.64). For this specific example, a tributary volume distribution was used.

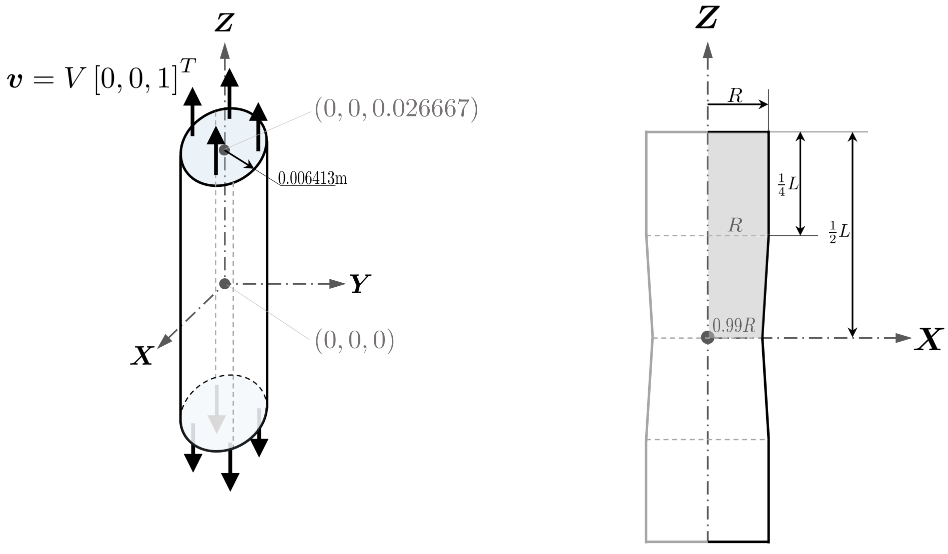

(a) (b)

Figure 6.63: (a) Necking bar overview. (b) Necking bar details.

The properties of the Hencky-based von Mises plasticity model, with nonlinear hardening (equation 2.63), are: initial density $\rho_0 = 7850\frac{\text{kg}}{\text{m}^3}$, Young's modulus $E = 206.9 \times 10^9\frac{\text{N}}{\text{m}^2}$, Poisson's ratio $\nu = 0.29$, yield stress $\tau_y^0 = 450 \times 10^6\frac{\text{N}}{\text{m}^2}$, residual yield stress $\tau_y^\infty = 715 \times 10^6\frac{\text{N}}{\text{m}^2}$, linear hardening modulus $H = 129.24 \times 10^6\frac{\text{N}}{\text{m}^2}$ and saturation exponent $\delta = 16.93$. A quasi-static approach is aimed and the top particles, i.e., particles with $Z$ coordinates equal $L/2$, are subjected to a velocity $\boldsymbol{v} = V\,[0,0,1]^T$, with $V$ varying as follows: $t_0 = 0\text{s}$, $V_0 = 0\frac{\text{m}}{\text{s}}$; $t_1 = 0.0007\text{s}$, $V_1 = 10\frac{\text{m}}{\text{s}}$ and $t_2 = 0.0014\text{s}$, $V_2 = 0\frac{\text{m}}{\text{s}}$. The resulting total elongation of the bar is 14mm (7mm observed in the half model). Note that the top particles are restricted in the radial direction.

In order to avoid non-smooth imposed velocities, the amplitude between any two consecutive data points $(t_i, V_i)$ and $(t_{i+1}, V_{i+1})$ is smoothed as:

$$V = V_i + (V_{i+1} - V_i)\,\xi^3\left(10 - 15\xi + 6\xi^2\right), \quad \text{for} \quad t_i \le t \le t_{i+1} \tag{6.3}$$

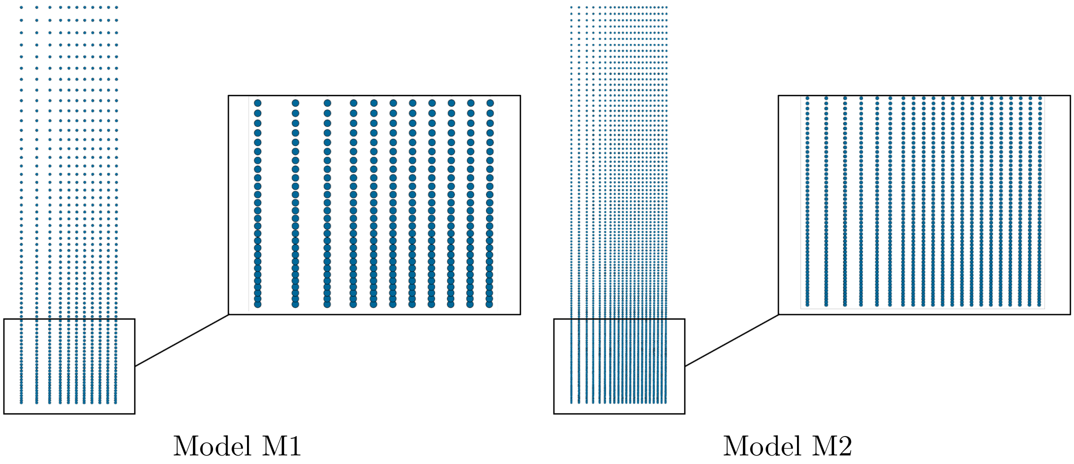

Figure 6.64: Necking bar particle distribution

with $\xi = \frac{t-t_i}{t_{i+1}-t_i}$. Graphical representation of this bell-shaped velocity profile (6.3) is depicted in Figure 6.65.

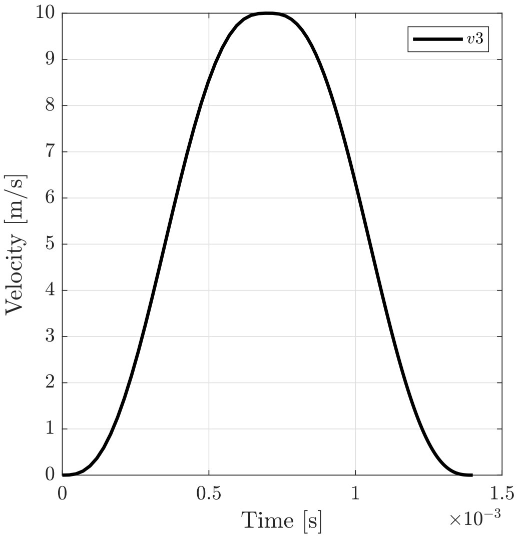

Figure 6.65: Applied bell-shaped velocity profile (Equation 6.3).

A fixed $\alpha_{CFL} = 0.9$ was used for the simulations.

In this example, the anisotropic updated kernel and kernel gradient are obtained as a push-forward of the corrected material kernel and corrected material gradient (Option#1). A 3D quadratic smoothing function is employed with a factor $f_h = 0.6$ for all the simulations.

In figures 6.66 and 6.67, the von Mises stress distribution and the equivalent plastic strain are plotted at different instants of the simulation, for a Total Lagrangian Formulation and also for an updated reference Lagrangian formulation, with updates performed at every time step, for the two models.

Figure 6.68 shows a sequence of deformed states of Model M2 of the necking bar and the evolution of the von Mises stresses for this model.

Evolution of internal, kinetic and total energies is shown for both TLF and ULF in figures 6.69a and 6.69c for models M1 and M2, respectively. In addition, the

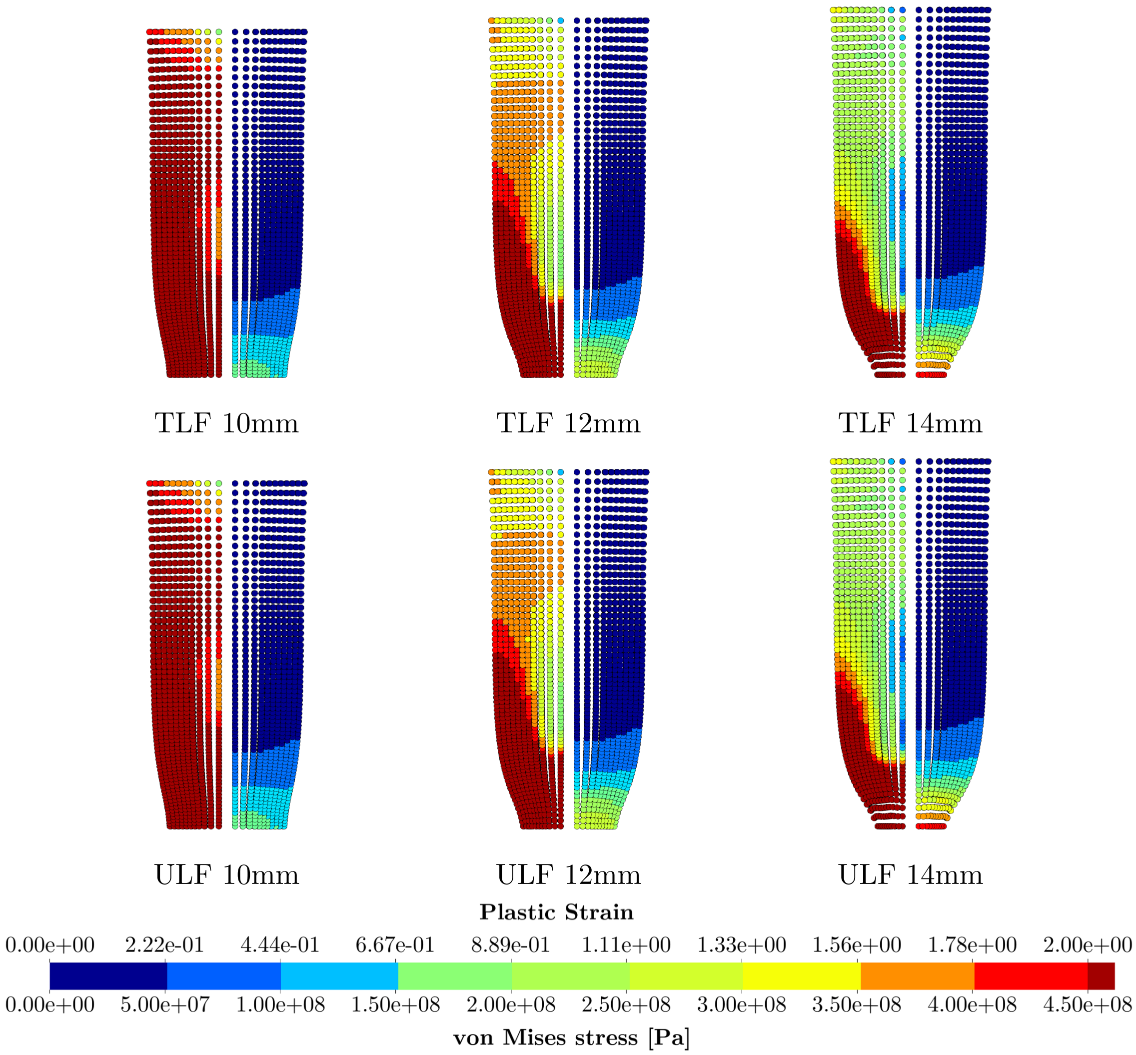
TLF 10mm TLF 12mm TLF 14mm

ULF 10mm ULF 12mm ULF 14mm

Figure 6.66: Necking bar model M1 von Mises stresses (left side) and equivalent plastic strain (right side).

numerical dissipation in the correponding model is shown in figures 6.69b and 6.69d. Note that the energies were computed considering only the represented geometry, i.e., a slice of $\frac{\pi}{16}$rad of the upper half of the cylinder.

In figure 6.70a, for the model M1, the pressure distribution is shown at the end of the simulation. Total Lagrangian results are presented on the left half of the bar, while the updated Lagrangian solution is shown on the right side. In addition, figure 6.70b shows the evolution of the radius of the bar in the necking region, as a function of the vertical top displacement, results are presented for total and updated formulations. Similar figures are presented for model M2 in 6.71a and 6.71b.

Figure 6.72 shows the ratio between current and initial radius of the bar in the necking region for the two models plotted as a function of the elongation. Experimental and numerical results published by other authors are plotted together for comparison.

In the results identified as "ULF" the updates were performed at every time step. Even though this is not needed, performing this test ensures that the updates are not activating any spurious mechanisms. In figure 6.73a, for the model M2, the von Mises stress distribution and the equivalent plastic strain are plotted at the

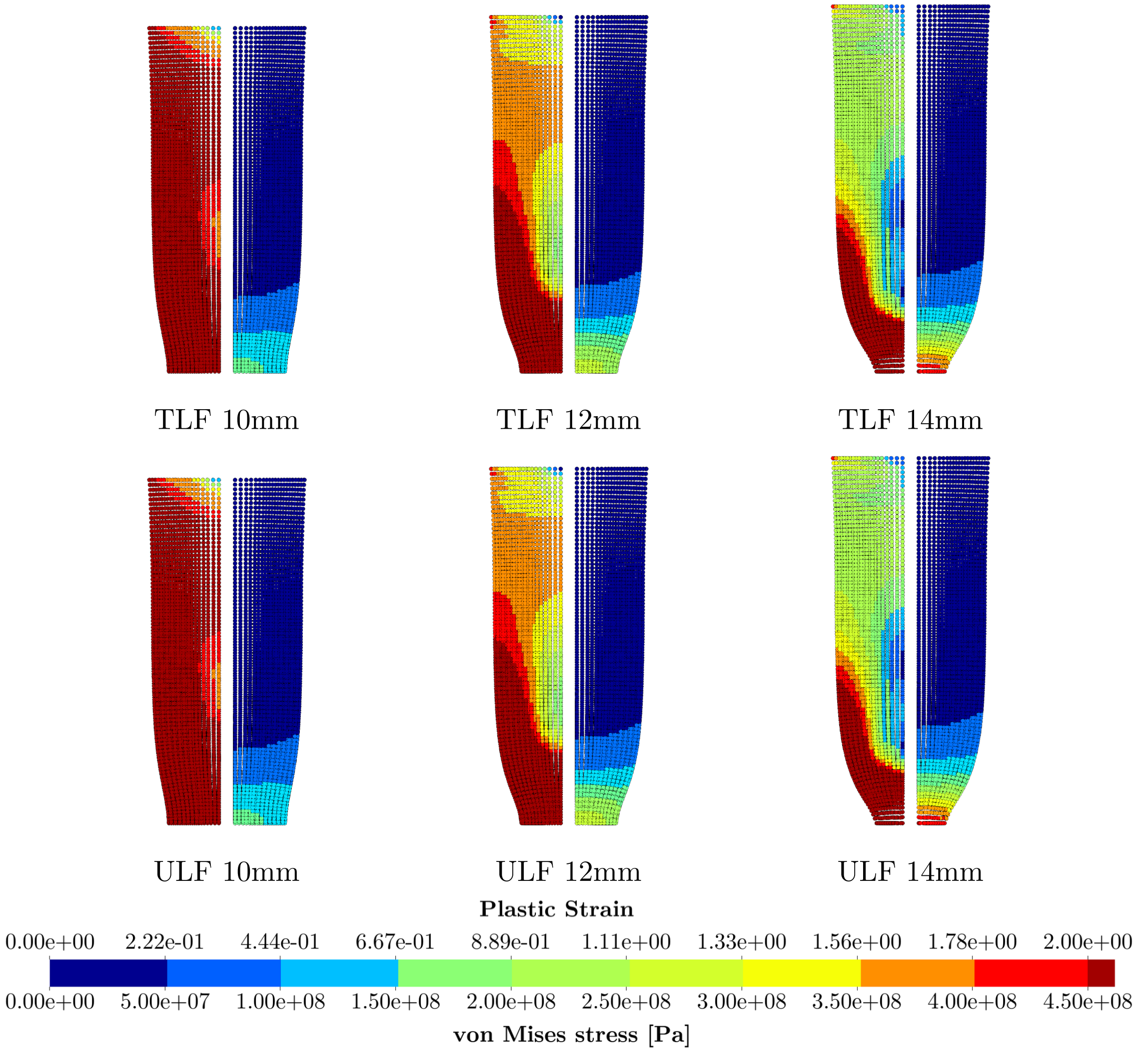

Figure 6.67: Necking bar model M2 von Mises stresses (left side) and equivalent plastic strain (right side).

end of the simulation, for an updated reference Lagrangian formulation, with only 10 updates performed along the simulation. The radius reduction in the necking section is shown in 6.73b.

The imperfection shown in figure 6.63b is a numerical artifice to trigger the necking in the central region of the bar and it can be introduced in many other different ways. An alternative to what was presented in figure 6.63b is, for example, to decrease the radius linearly from the top of the bar to the center, as detailed in figure 6.74a. Employing the same particle distribution as model M2, a new model M2b was also studied considering this alternative way of inducing the necking. The ratio between current and initial radius of the bar in the necking region for this model is plotted as a function of the elongation in figure 6.74b. Figures 6.75a and 6.75b show the von Mises stresses and the equivalent plastic strain for model M2b, Total lagrangian results are shown on the left half, while updated Lagrangian results are shown on the right.

As the conclusions of the necking bar example, extremely high plastic strains develop at the necking region and the proposed formulation was shown to be robust in such a scenario. The results for the simulations evolved based on updated reference configurations are as good as the ones based on the initial geometry (TLF). Moreover, the proposed formulation offers the flexibility of performing updates at every time step or only a few times along the simulation, without affecting the quality of the results. The results are in agreement with those reported in the literature and compare well with the experimental data. It was shown that different considerations can be assumed for the geometric description of the model, and the results are affected accordingly. The problem was solved in a quasi-static manner and presents a plastic-dominated response, therefore, since the stabilisation scheme is physically based, it plays a minimum role in the solution.

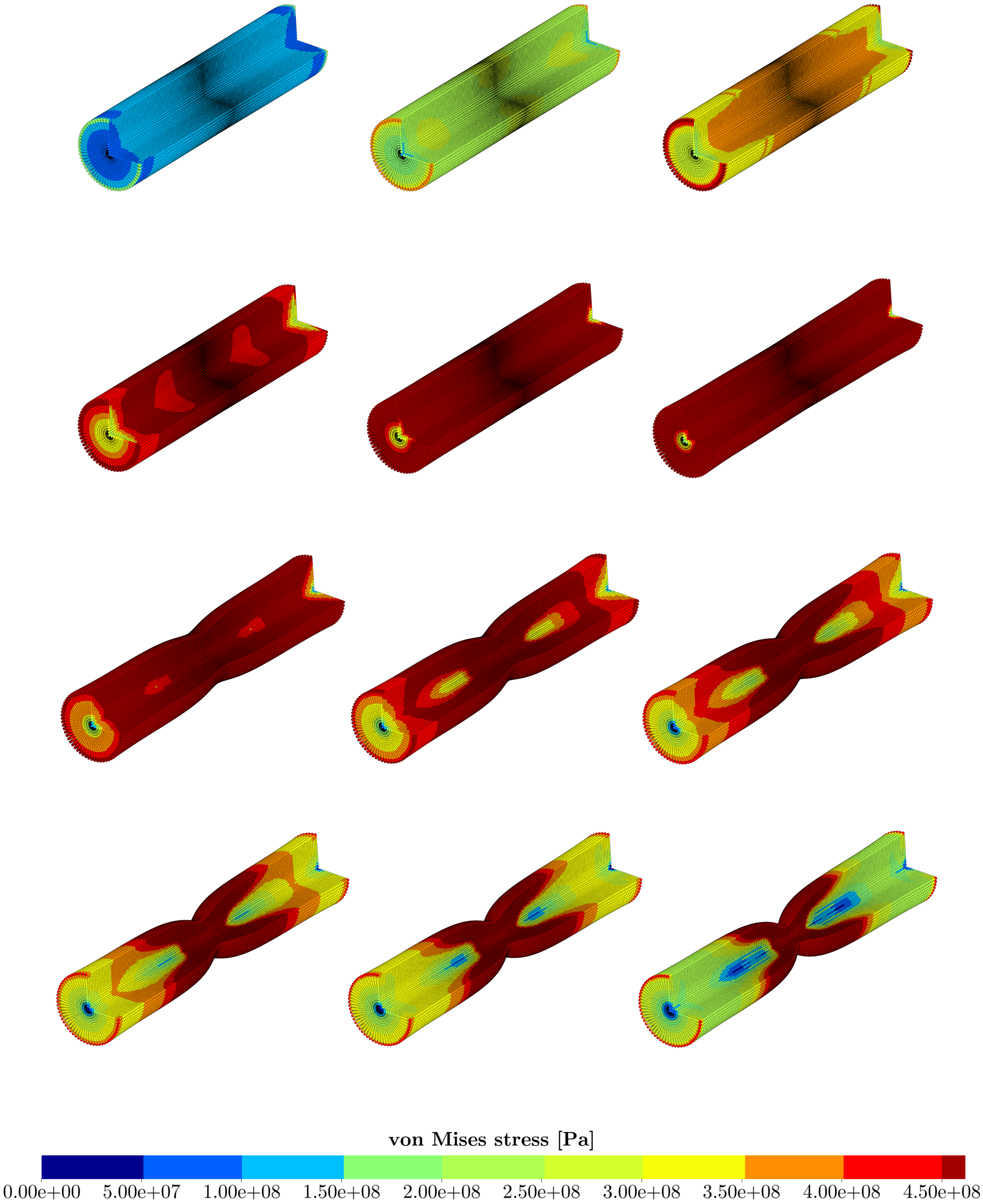

Figure 6.68: Necking bar model M2. A sequence of deformed states showing von Mises stress distribution when the total elongation of the bar is of {0.028, 0.054, 0.09, 0.124, 1.854, 5.864, 9.852, 10.956, 11.642, 12.342, 12.704, 14} mm (from left to right and top to bottom). Results obtained with updates performed at every time step.

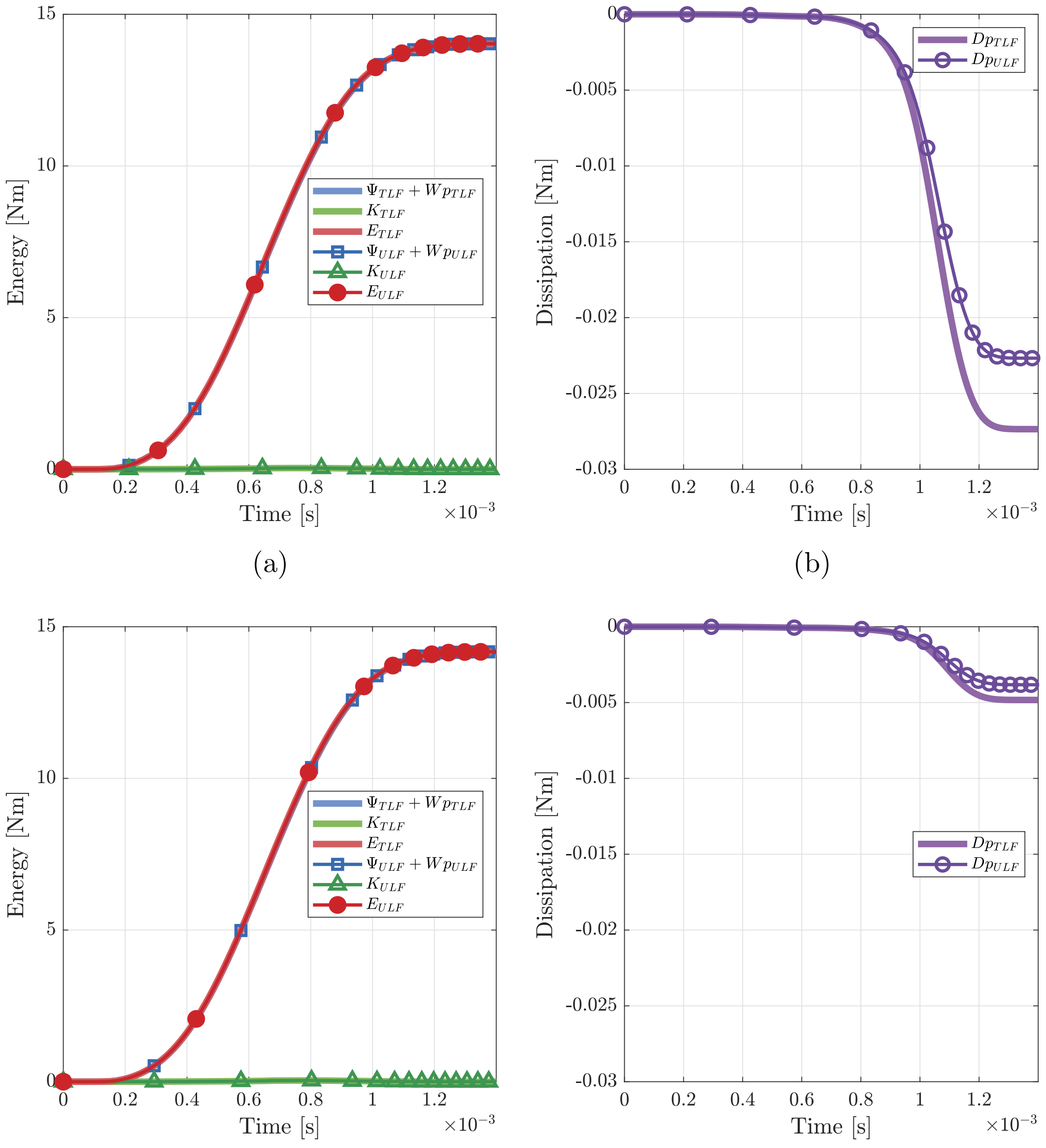

(a) (b)

(c) (d)

Figure 6.69: Evolution of kinetic ($K$), internal ($\Psi$) plus plastic dissipation ($Wp$) and total ($E$) energies for necking bar (a) model M1 and (c) model M2. Numerical dissipation for (b) model M1 and (d) model M2.

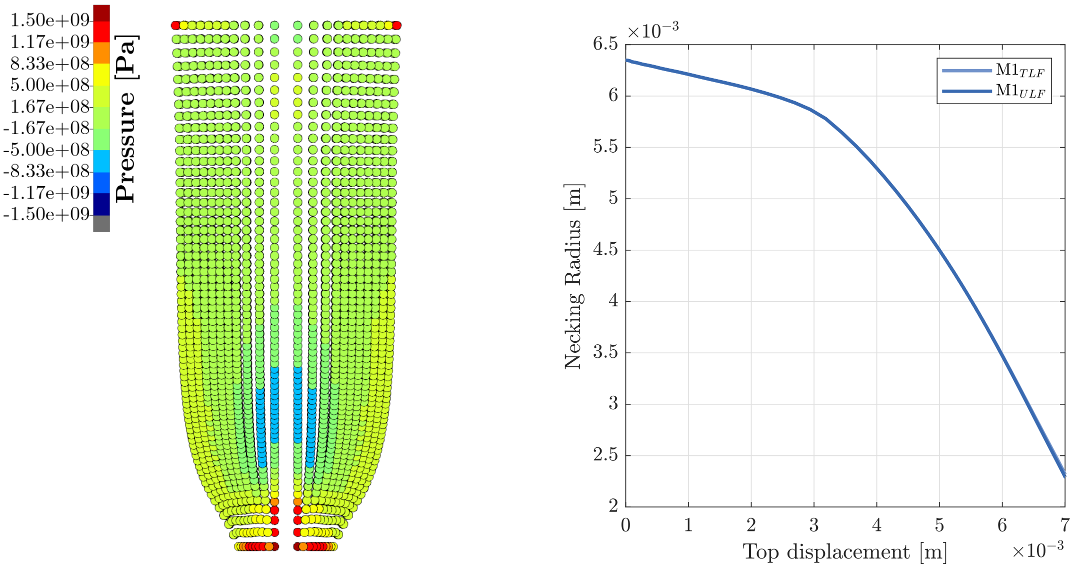

(a) (b)

Figure 6.70: (a) Pressure distribution for 14mm elongation for model M1: TLF on the left side and ULF on the right side. (b) Radius reduction in the necking section.

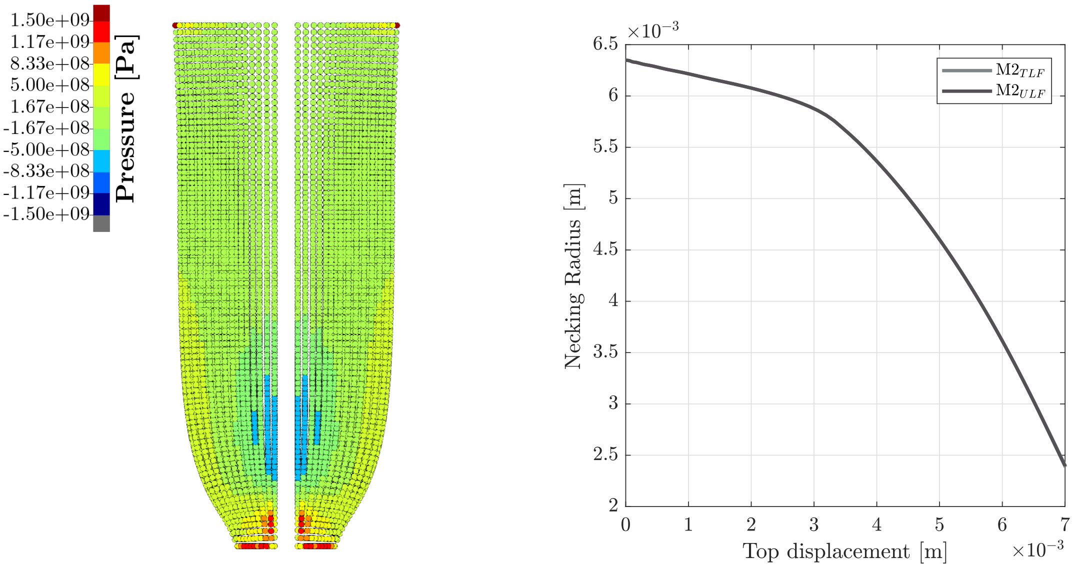

(a) (b)

Figure 6.71: (a) Pressure distribution for 14mm elongation for model M2: TLF on the left side and ULF on the right side. (b) Radius reduction in the necking section.

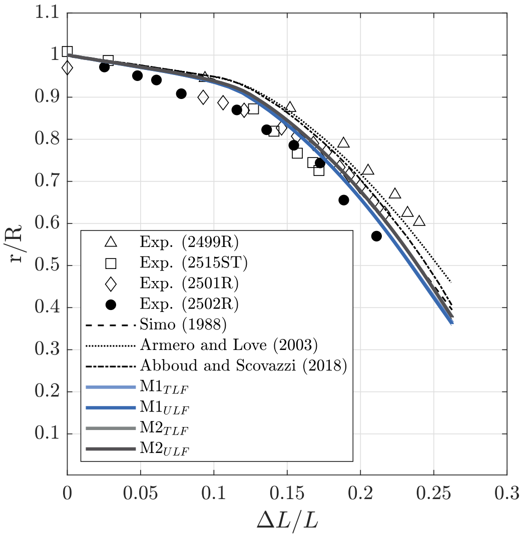

Figure 6.72: Radius reduction in the necking section (experimental results extracted from [105]).

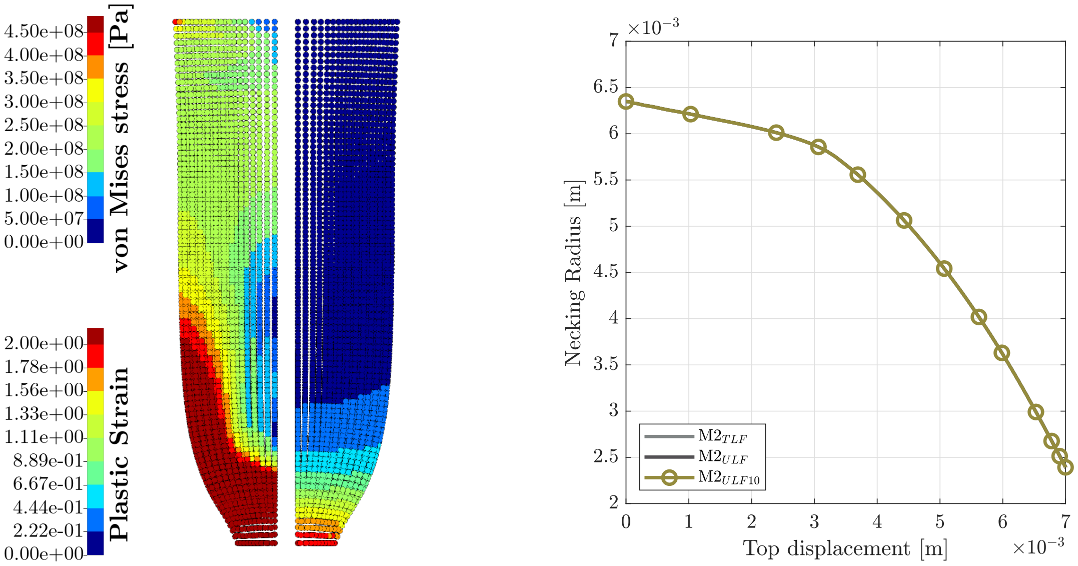

(a) (b)

Figure 6.73: (a) Necking bar model M2 considering only 10 updates along the simulation: von Mises stresses (left side) and equivalent plastic strain (right side). (b) Radius reduction in the necking section.

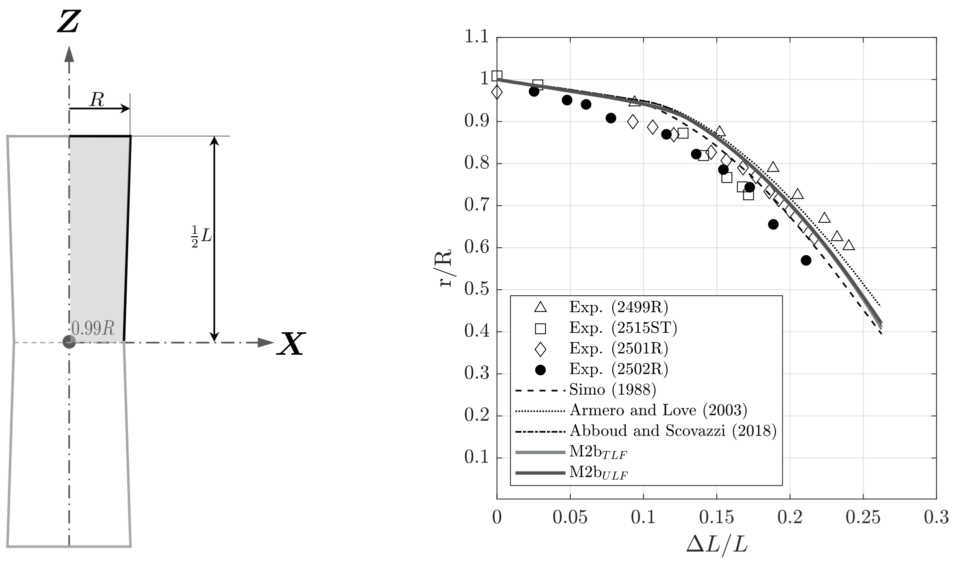

(a) (b)

Figure 6.74: (a) Alternative way of introducing the numerical imperfection: model M2b. (b) Radius reduction in the necking section considering model M2b.

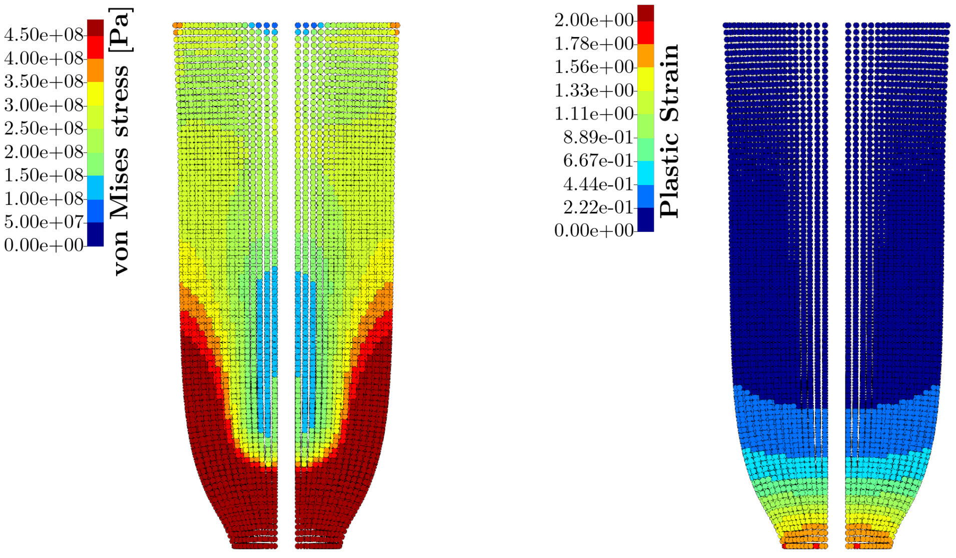

(a) (b)

Figure 6.75: Necking bar model M2b at 14mm elongation: (a) von Mises stresses, TLF on the left side and ULF on the right side. (b) Equivalent plastic strain, TLF on the left side and ULF on the right side.

### 6.3.3 Strain localisation

This example illustrates the occurrence of shear bands during the stretching of a rectangular bar. The example was previously studied by many authors, for example [110] and [111]. The model presented herein consists of a rectangular bar of width $W = 0.012826\text{m}$ and length $L = 0.053334\text{m}$, the main characteristics of the model are illustrated in figure 6.76. Notice in figure 6.76b that a geometric imperfection (1.8% of reduction in the width) is introduced to induce necking in the central region of the bar. Due to the symmetry of the problem, only one quarter of the geometry is represented. An in-plane solution is obtained by restricting the movement of all particles in the $Y$ direction. Note that because of the three-dimensional nature of the formulation, two layers of particles are created along the thickness. The distance between particles in the $Y$ direction is chosen to be proportional to that in the $X$ and $Z$ directions. Two model refinements were analysed: model M1 with 2310 particles, and model M2 with 8938 particles. The distribution is non-uniform with the refinement concentrated in the necking region, figure 6.77 shows both models. For this specific example, a tributary volume distribution was used.

The properties of the Hencky-based von Mises plasticity model, with nonlinear hardening (equation 2.63), are: initial density $\rho_0 = 7850\frac{\text{kg}}{\text{m}^3}$, Young's modulus $E = 206.9 \times 10^9 \frac{\text{N}}{\text{m}^2}$, Poisson's ratio $\nu = 0.29$, yield stress $\tau_y^0 = 450 \times 10^6 \frac{\text{N}}{\text{m}^2}$, residual yield stress $\tau_y^\infty = 715 \times 10^6 \frac{\text{N}}{\text{m}^2}$, linear softening modulus $H = -129.24 \times 10^5 \frac{\text{N}}{\text{m}^2}$ and saturation exponent $\delta = 16.93$. A quasi-static approach is aimed and the top particles, i.e., particles with $Z$ coordinates equal $L/2$ are subjected to a velocity in the vertical ($Z$) direction, as illustrated in figure 6.76. The magnitude $V$ varies as follows: $t_0 = 0\text{s}$, $V_0 = 0\frac{\text{m}}{\text{s}}$; $t_1 = 0.005\text{s}$, $V_1 = 1\frac{\text{m}}{\text{s}}$ and $t_2 = 0.010\text{s}$, $V_2 = 0\frac{\text{m}}{\text{s}}$. The resulting total elongation of the bar is 10mm (5mm observed in the half model). Note that the top particles are free in the horizontal direction.

In order to avoid non-smooth imposed velocities, the amplitude between any two consecutive data points $(t_i, V_i)$ and $(t_{i+1}, V_{i+1})$ is smoothed as:

$$V = V_i + (V_{i+1} - V_i)\,\xi^3\left(10 - 15\xi + 6\xi^2\right), \quad \text{for} \quad t_i \leq t \leq t_{i+1} \tag{6.4}$$

with $\xi = \frac{t - t_i}{t_{i+1} - t_i}$.

A fixed $\alpha_{CFL} = 0.9$ was used for the simulations.

In this example, the anisotropic updated kernel and kernel gradient are obtained as a push-forward of the material kernel and material gradient, with corrections performed in the updated configuration (Option#2). A 3D cubic smoothing function is employed with a factor $f_h = 0.8$ for all the simulations.

For this example, results are benchmarked against a finite elements simulation performed using Abaqus/Explicit. The set-up of the analysis as well as the geometric characteristics of the finite elements model are exactly the same as the ones used in SPH. The element type is an 8-nodes first-order, reduced integration brick (C3D8R).

In figure 6.78, the von Mises stress distribution and the equivalent plastic strain are plotted at different instants of the simulation, for a Total Lagrangian Formulation and also for an updated reference Lagrangian formulation, with updates performed at every time step. Similar results are shown for model M2 in figure 6.79. In addition, figure 6.80 shows a zoom of the necking region at the end of the simulation. Notice that the particles located at the center of the bar move very far from each other. However, the interaction between particles is never broken, i.e., the list of

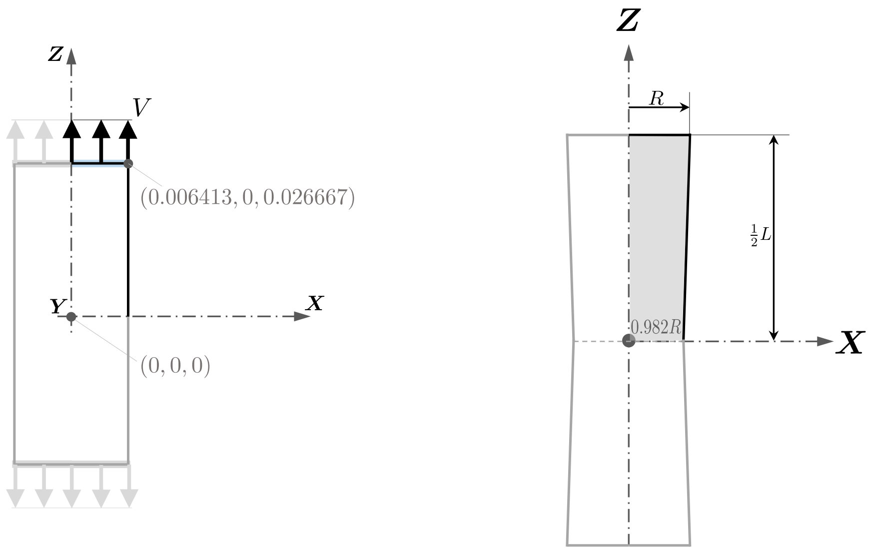

(a) (b)

Figure 6.76: (a) Localisation bar overview. (b) Localisation bar details.

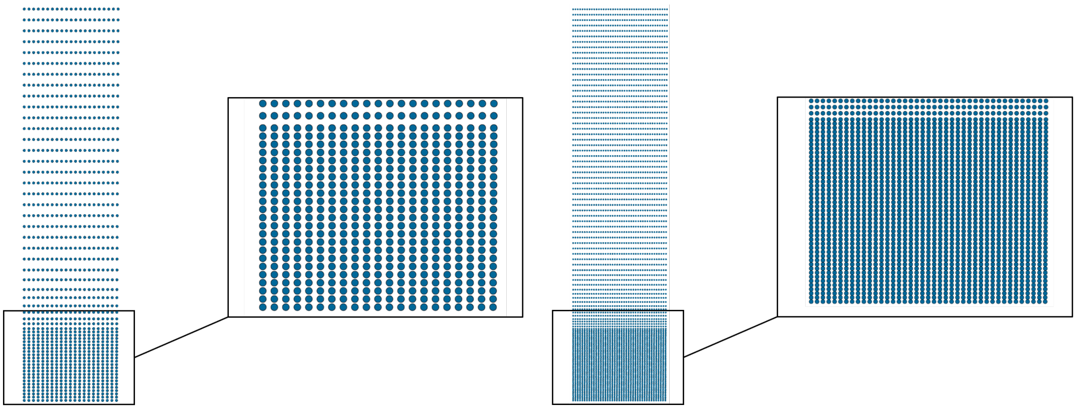

Model M1 Model M2

Figure 6.77: Localisation bar particle distribution.

neighbouring particles remains unchanged throughout the simulation. The accuracy of the results is not affected by this highly-distorted domain thanks to the use of corrected anisotropic kernels. The results obtained in the finite elements simulation are shown in figure 6.81 for comparison.

In figure 6.82a, the pressure distribution is shown for model M2 at the end of the simulation. Total Lagrangian results are presented on the left half of the bar, while the updated Lagrangian solution is shown on the right side. In addition, figure 6.82b shows the evolution of the width of the bar in the necking region, as a function of the vertical top displacement, results are presented for models M1 and M2 in total and updated formulations, and compared with Abaqus/Explicit results.

As the conclusions of the strain localisation example, high plastic strains and the formation of shear bands are observed in this example and the proposed formulation was shown to be robust in such scenarios. The results for the simulations evolved based on updated reference configurations are as good as the ones based on the initial geometry (TLF). The results are in agreement with those obtained using

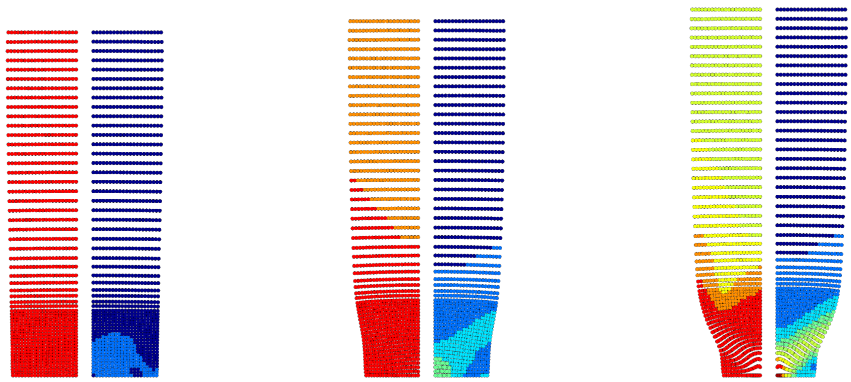

TLF 6mm TLF 8mm TLF 10mm

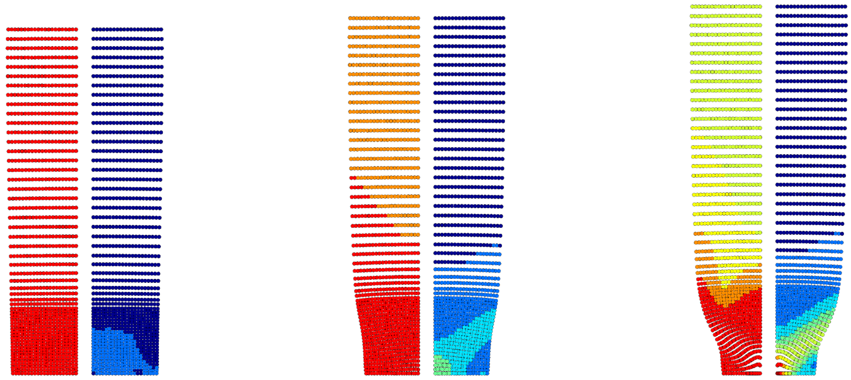

ULF 6mm ULF 8mm ULF 10mm

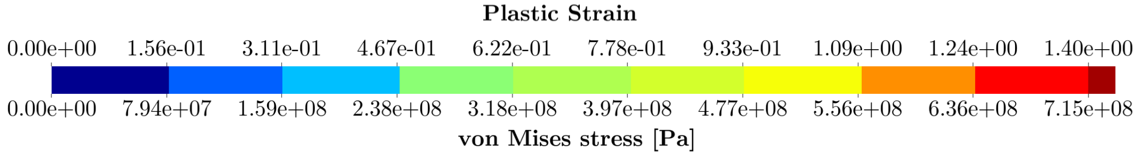

Figure 6.78: Strain localisation model M1 von Mises stresses (left side) and equivalent plastic strain (right side).

finite elements. The problem was solved in a quasi-static manner and also presents a plastic-dominated response, therefore, the stabilisation scheme plays a minimum role in the solution.

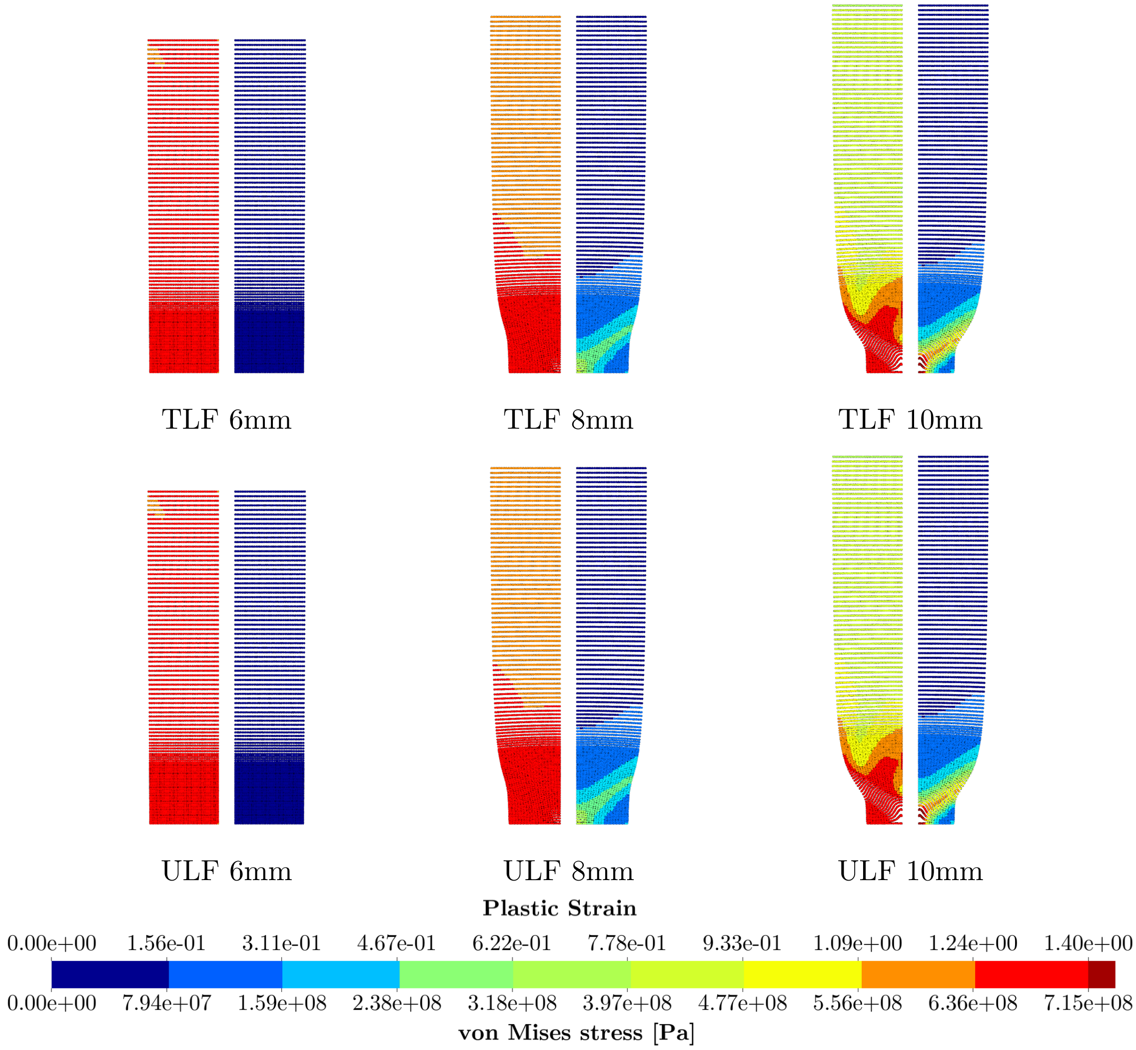
TLF 6mm TLF 8mm TLF 10mm

ULF 6mm ULF 8mm ULF 10mm

Figure 6.79: Strain localisation model M2 von Mises stresses (left side) and equivalent plastic strain (right side).

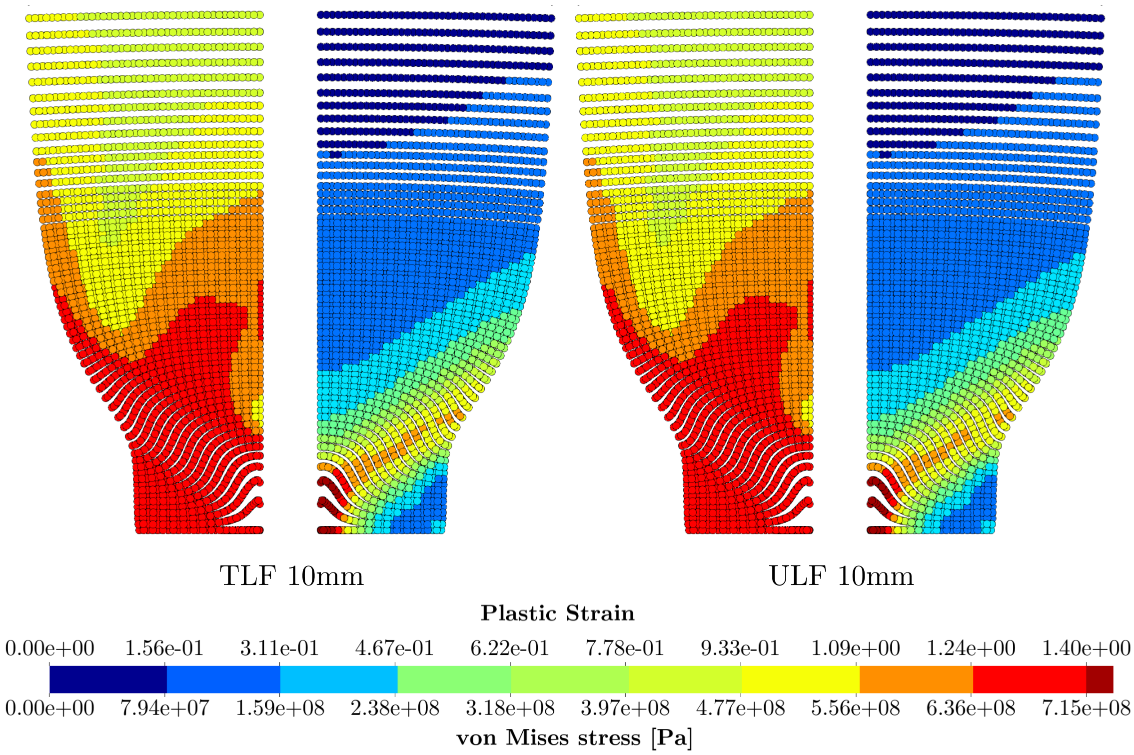

Figure 6.80: Strain localisation model M2 von Mises stresses (left side) and equivalent plastic strain (right side).

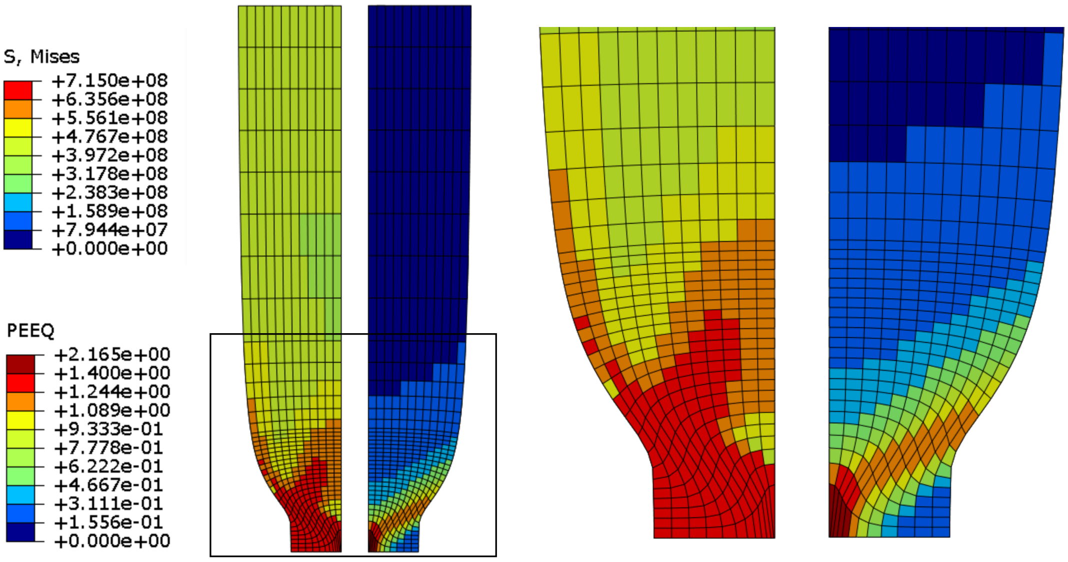

Figure 6.81: Strain localisation Abaqus/Explicit model von Mises stresses (left side) and equivalent plastic strain (right side) for 10mm displacement.

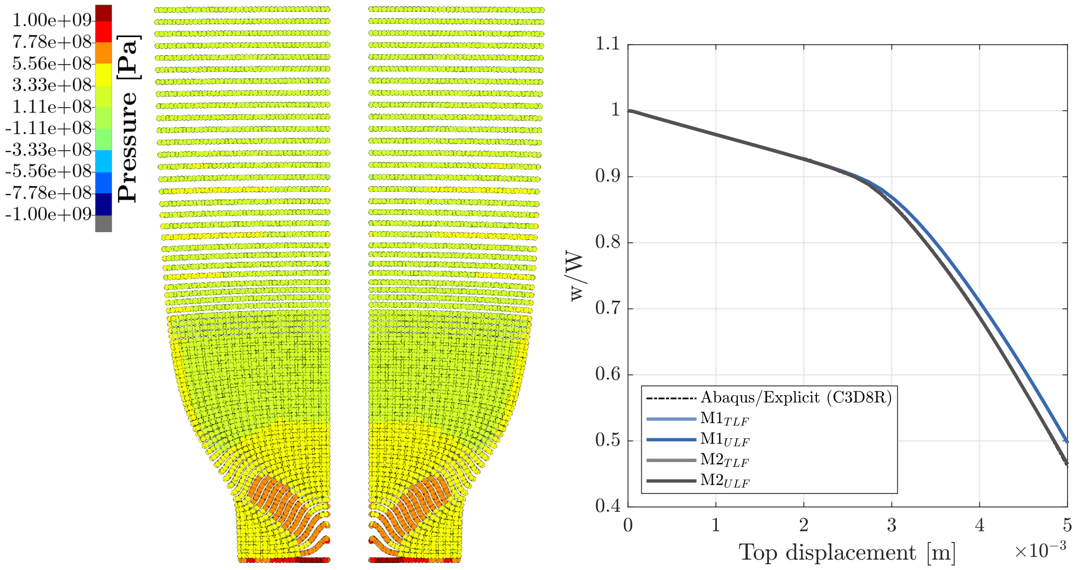

(a) (b)

Figure 6.82: (a) Pressure distribution for 10mm displacement: TLF on the left side and ULF on the right side. (b) Width reduction in the necking section.

# Chapter 7

# Thermo-mechanics numerical examples

## 7.1 Introduction

In this chapter, in continuation of the numerical examples presented so far, the potential of the formulation for applications in thermo-mechanics is explored in different test cases.

## 7.2 Thermal L-shaped block

This example was previously studied by many authors, e.g. [26, 76, 100–102], and the characteristics of the model developed in this work follows [102]. The main objective of this classical benchmark problem is to examine the capability of preserving both the linear and angular momenta of a system. An L-shaped block with square cross-section 3m x 3m is subjected to an external torque induced by a pair of time-varying forces acting on two of its boundary faces, as illustrated in figure 7.1. The traction forces $\boldsymbol{F}_1(t)$ and $\boldsymbol{F}_2(t)$ are given in $\frac{\mathrm{N}}{\mathrm{m}^2}$ as

$$\boldsymbol{F}_1(t) = -\boldsymbol{F}_2(t) = \begin{bmatrix} 150 \\ 300 \\ 450 \end{bmatrix} f(t), \qquad f(t) = \begin{cases} t & 0 \leq t < 2.5\mathrm{s}, \\ 5 - t & 2.5 \leq t < 5\mathrm{s}, \\ 0 & t \geq 5\mathrm{s}. \end{cases} \tag{7.1}$$

Moreover, the initial distribution of the temperature profile on the structure is not entirely homogeneous, and is given as

$$\theta|_{t=0} = \begin{cases} 300\mathrm{K} & Y = 10\mathrm{m}, \\ 250\mathrm{K} & X = 6\mathrm{m}, \\ \theta_R = 293.15\mathrm{K} & \text{elsewhere}. \end{cases} \tag{7.2}$$

A uniform distribution of particles was employed and a sequence of model refinements were analysed: models M1 to M4 with 828, 5445, 13950 and 39249 particles, respectively. For this specific example, a tributary volume distribution was employed. Initial density $\rho_0 = 1100\frac{\mathrm{kg}}{\mathrm{m}^3}$, Young's modulus $E = 50500\frac{\mathrm{N}}{\mathrm{m}^2}$, Poisson's ratio $\nu = 0.3$, specific heat capacity $C_v = 1\frac{\mathrm{J}}{\mathrm{kgK}}$, thermal conductivity $k = 10\frac{\mathrm{W}}{\mathrm{mK}}$ and thermal expansion coefficient $\alpha = 2.223 \times 10^{-4}\frac{1}{\mathrm{K}}$ were adopted as the material parameters for a nearly incompressible neo-Hookean constitutive model combined with a Mie-Grüneisen equation of state. The Mie-Grüneisen coefficients are $q = 1$ and $\Gamma_0 = 0.0255$. The material constants are given for a reference temperature $\theta_R = 293.15\mathrm{K}$. A fixed $\alpha_{CFL} = 0.9$ was used for the simulations.

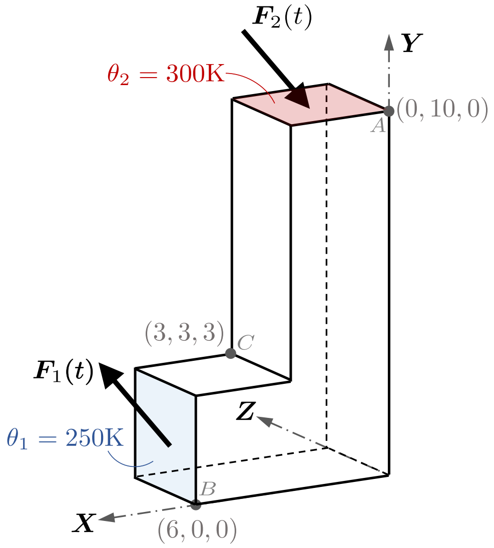

Figure 7.1: Thermal L-shaped block.

In this example, the anisotropic updated kernel and kernel gradient are obtained as a push-forward of the corrected material kernel and corrected material gradient (Option#1). A 3D quadratic smoothing function is employed with a factor $f_h = 0.6$ for all the simulations.

In figures 7.2 and 7.3, the pressure and the temperature distributions for model M1 are plotted at different instants of the simulation, for a Total Lagrangian Formulation and also for an updated reference Lagrangian formulation, with updates performed at every time step. The same results are shown for model M4 in figures 7.4 and 7.5.

Evolution of internal, kinetic, thermal and total energies is shown for both TLF and ULF for models M1 and M4 in figures 7.6a and 7.6b, respectively. Moreover, for the ULF models M1 and M4, the evolution of global linear and angular momenta is plotted in figures 7.7a, 7.7b, 7.7c, 7.7d.

For such challenging example, even though the coarse model captures the kinematics well, the total energy of the system, which is an unknown variable in the proposed thermal-stress formulation, is poorly approximated for the coarser models. This is due to the non-smooth nature of the initial temperature field (sudden change from 250K to 300K), which requires finer models. The evolution of total energy comparing the different model refinements is shown for ULF in figure 7.8a. In addition to models M1-M4, an extra model M5 with 93296 particles was included in the study. The pressure distribution at time 7.2s and the temperature distribution at time 16.8s are also shown for the five models in figure 7.9 for an updated reference Lagrangian formulation, with updates performed at every time step. As can be observed from these figures, even though the mechanical behaviour was well

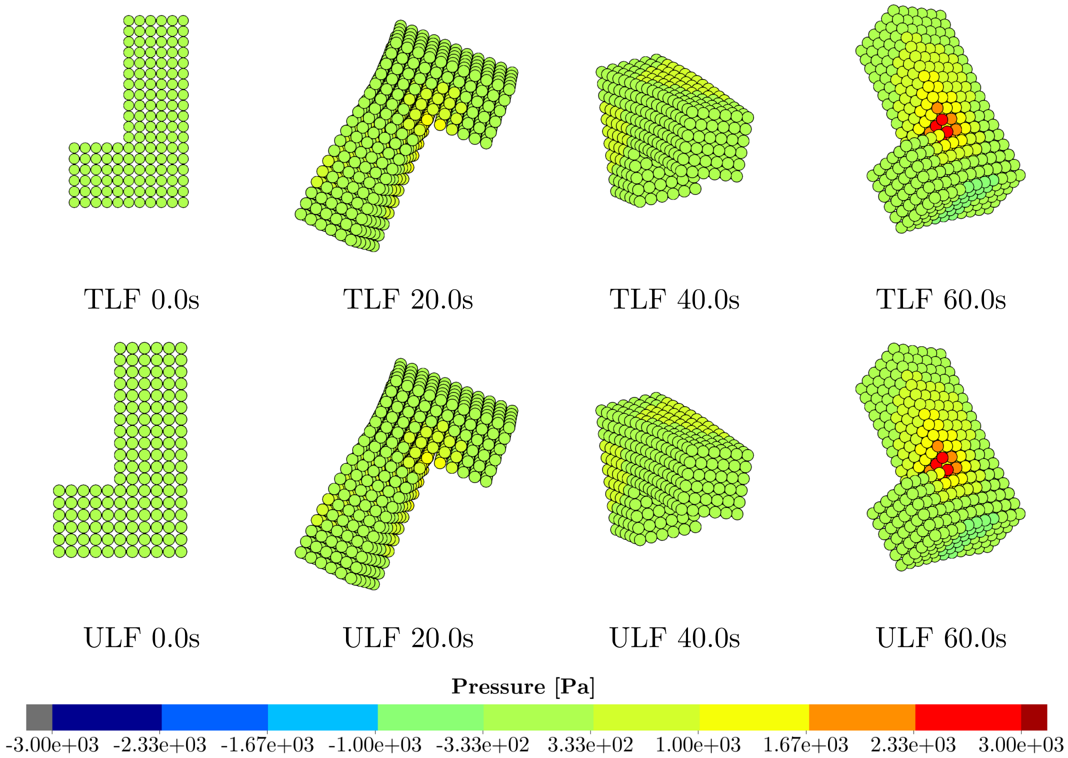

Figure 7.2: Thermal L-shaped block M1 pressure distribution.

represented for all model refinements, the temperature field requires finer models in order to provide the expected results. The evolution of the temperature measured at points $A = [0, 10, 0]^T$, $B = [6, 0, 0]^T$ and $C = [3, 3, 3]^T$ (see figure 7.1) is presented, for models M1, M3 and M5, in figure 7.8b for ULF.

As mentioned before, the convergence of the total energy for this example is affected by the non-smooth initial temperature field. For completeness, a variation of the L-shaped block example, where the temperature is initiated smoothly, was also performed. Models M1, M2 and M3 were analysed with the initial temperature increasing linearly from $\theta_1$ to $\theta_R$, and decreasing linearly from $\theta_2$ to $\theta_R$, as illustrated in figure 7.10a. The evolution of total energies considering this alternative initial condition are compared for different model refinements for ULF in figure 7.10b.

As the conclusions of the thermal L-shaped block example, the proposed formulation was shown to be robust and did not activate any spurious mechanisms in this test case. The results for the simulations evolved based on updated reference configurations are as good as the ones based on the initial geometry (TLF). The example demonstrates the ability of the proposed algorithm in preserving both the linear momentum and angular momentum of the system. Specifically, the total linear momentum is close to (and oscillates around) zero machine accuracy at all times, whereas the total angular momentum is conserved after the loading phase. Due to the non-smooth characteristics of the initial conditions, finer models are required in order to capture the thermal effects accurately, the results drastically improve with model refinement. Nevertheless, the kinematics of the problem is well computed even for the very first coarse model.

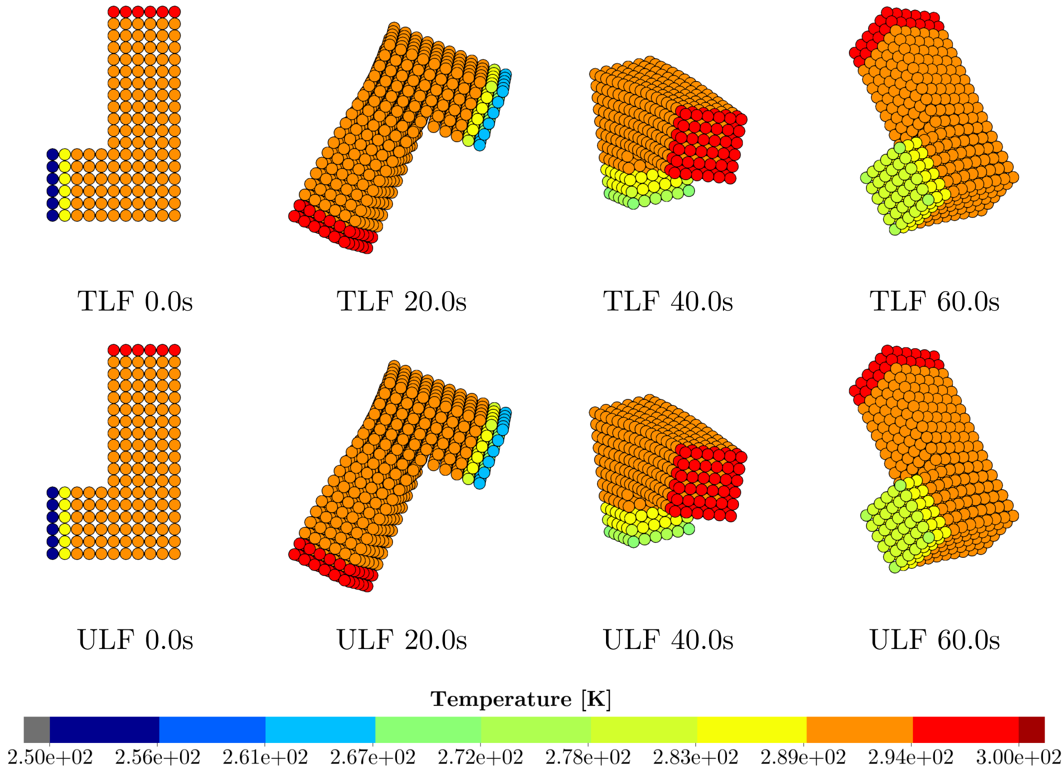

Figure 7.3: Thermal L-shaped block M1 temperature distribution.

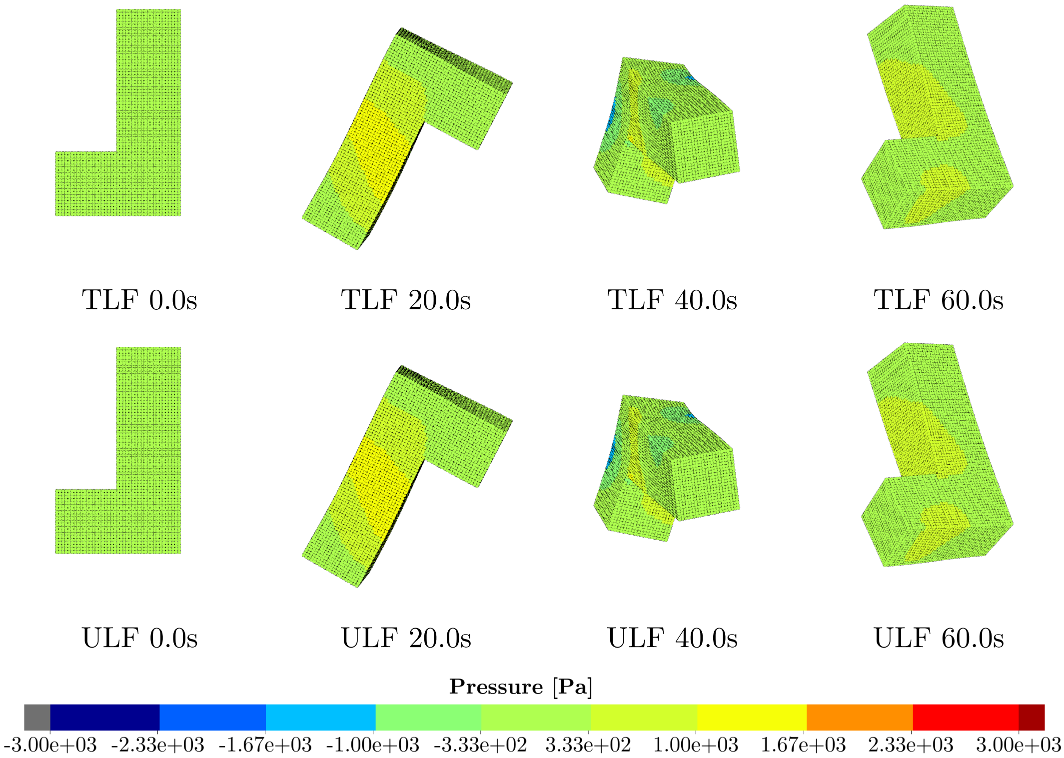

Figure 7.4: Thermal L-shaped block M4 pressure distribution.

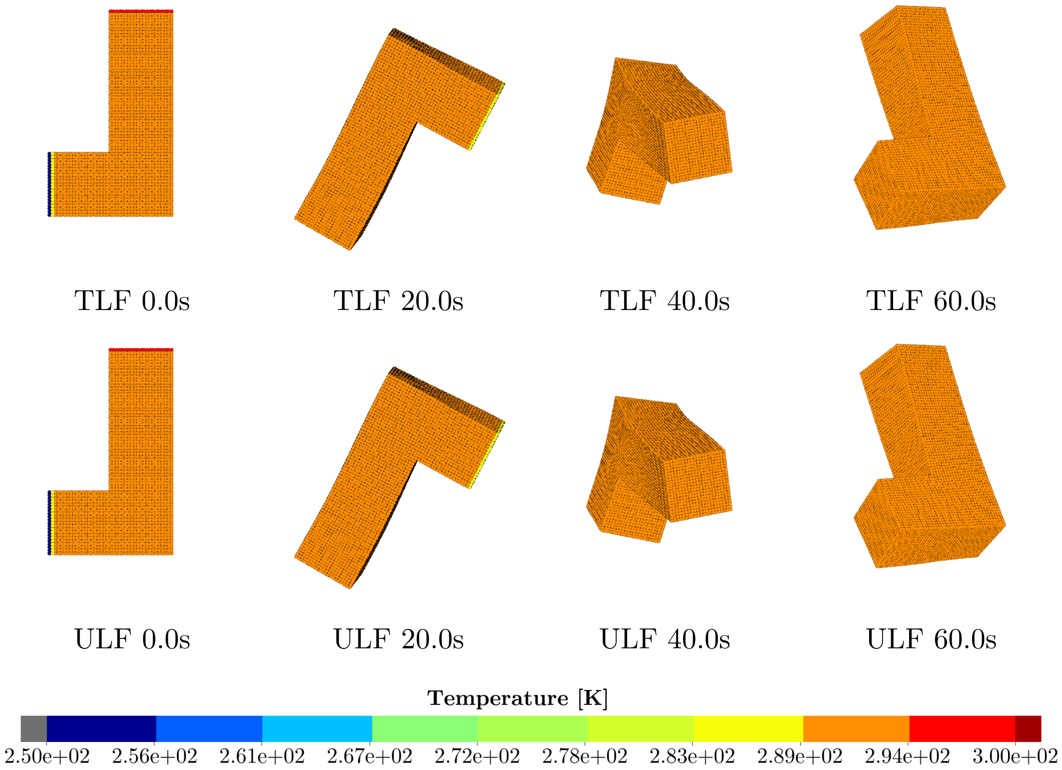

Figure 7.5: Thermal L-shaped block M4 temperature distribution.

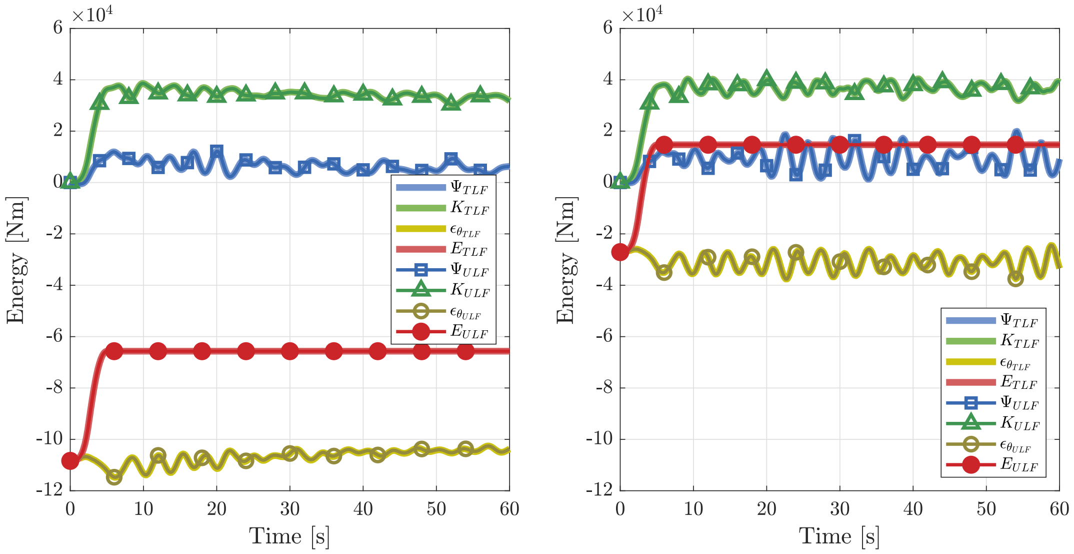

(a) (b)

Figure 7.6: Evolution of kinetic ($K$), internal ($\Psi$), thermal ($\epsilon_\theta$) and total ($E$) energies for the thermal L-shaped block: (a) model M1. (b) model M4.

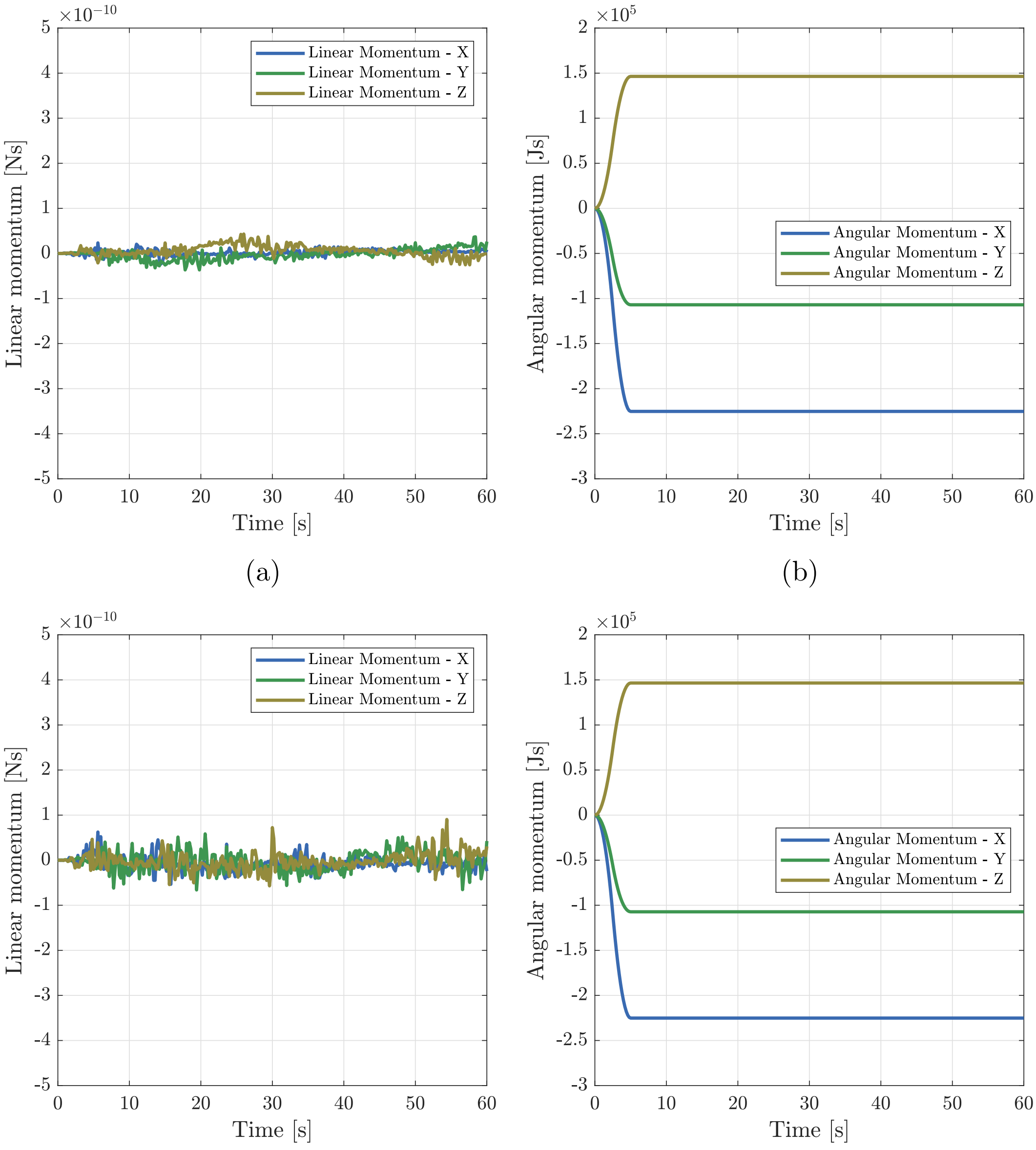

(a) (b)

(c) (d)

Figure 7.7: Evolution of the components of the global linear and angular momenta for the thermal L-shaped block: (a) and (b) model M1, (c) and (d) model M4.

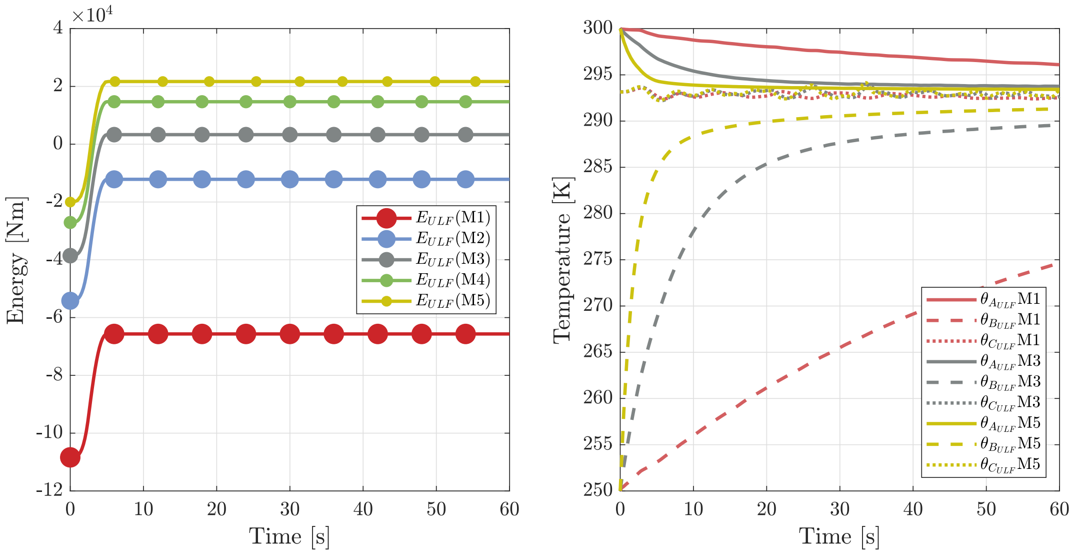

(a) (b)

Figure 7.8: (a) Evolution of total energy ($E$) for different model refinements for the thermal L-shaped block. (b) Evolution of temperature at points $A$, $B$ and $C$ for different model refinements for the thermal L-shaped block.

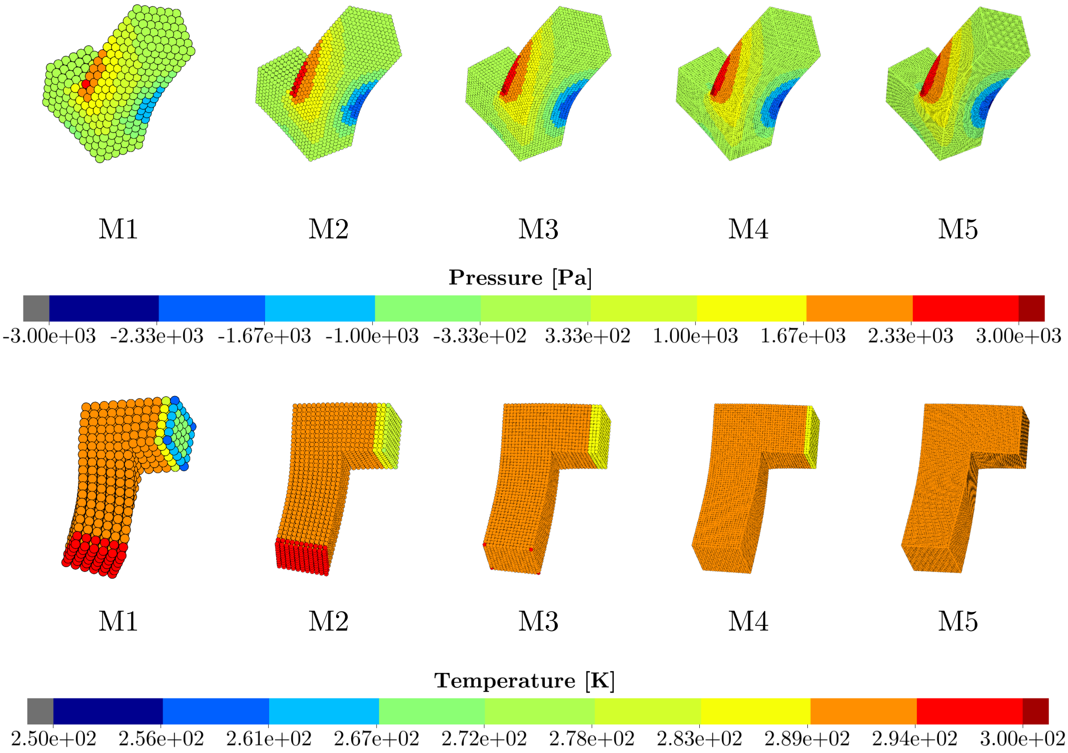

Figure 7.9: Thermal L-shaped block considering different model refinements in an updated reference Lagrangian formulation, with updates performed at every time step. First row shows the pressure distribution at time 7.2s, the second row shows the temperature distribution at time 16.8s.

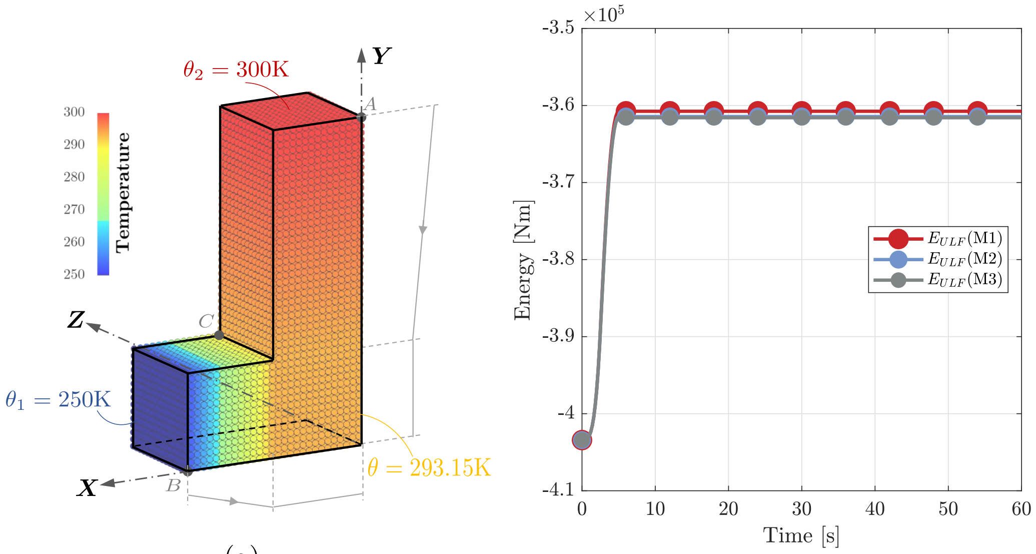

(a)

(b)

Figure 7.10: (a) Thermal L-shaped block with a linear varying initial temperature. (b) Evolution of total energy ($E$) for different model refinements for the thermal L-shaped block with a linear varying initial temperature profile.

## 7.3 Constrained punch block

This example was previously studied in an isothermal context in [74] and thermal effects were recently considered in [102]. The model consists of a block 1m x 1m x 0.5m, including nine holes with diameter equal to 0.2m each. The geometry is detailed in figure 7.11a. An initial velocity $\boldsymbol{v}$ was defined for one quarter of the model (all particles presenting $X \geq 0$ and $Y \geq 0$) as $\boldsymbol{v} = V\left[0, 0, {}^{Z}\!/_{H}\right]^{T}$, where $V = -5\frac{\mathrm{m}}{\mathrm{s}}$ and $H = 0.5$m, the initial velocity is illustrated in figure 7.11b. Moreover, the initial temperature is defined across the structure as $\theta = \theta_R + 10\left({}^{Z}\!/_{H}\right)$, as illustrated in figure 7.11c. No further loading is applied to the block and apart from the top surface ($Z = 0.5$), which is a free boundary, all the other boundaries have the movement in the direction normal to the face restricted.

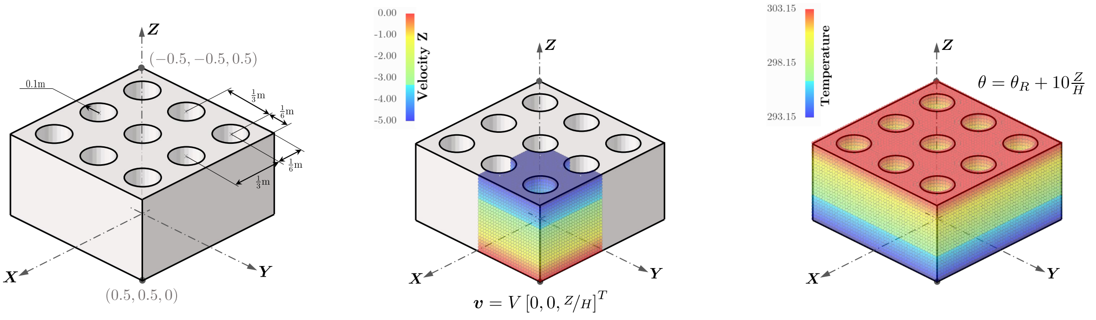

(a) (b) (c)

Figure 7.11: Constrained punch block. (a) Geometry. (b) Initial velocity profile. (c) Initial temperature distribution.

Initially, 22420 particles were used for the discretisation and approximately the same refinement is used for all regions of the block. Refined models with 49900 and 167536 particles were also studied, the three different models are illustrated in figure 7.12. For this specific example, a tributary volume distribution was employed.

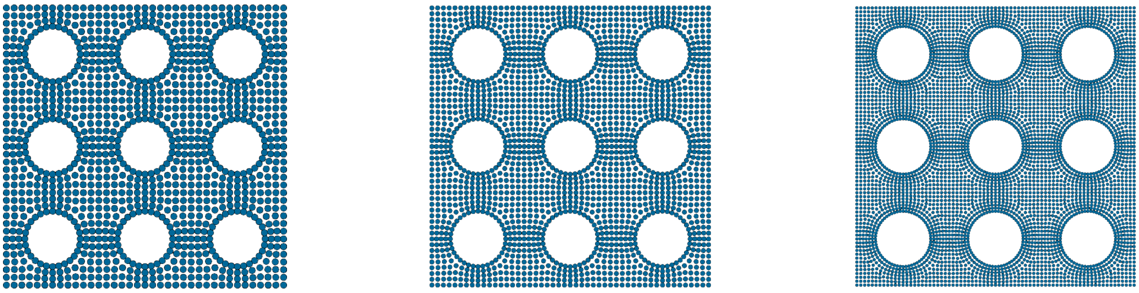

Model M1 Model M2 Model M3

Figure 7.12: Constrained punch block particle distribution.

Initial density $\rho_0 = 1000\frac{\mathrm{kg}}{\mathrm{m}^3}$, Young's modulus $E = 50500\frac{\mathrm{N}}{\mathrm{m}^2}$, Poisson's ratio $\nu = 0.3$, specific heat capacity $C_v = 1\frac{\mathrm{J}}{\mathrm{kgK}}$, thermal conductivity $k = 10\frac{\mathrm{W}}{\mathrm{mK}}$ and thermal expansion coefficient $\alpha = 2.223 \times 10^{-4}\frac{1}{\mathrm{K}}$ were adopted as the material parameters for a nearly incompressible neo-Hookean constitutive model combined with a Mie-Grüneisen equation of state. The Mie-Grüneisen coefficients are $q = 1$

and $\Gamma_0 = 0.0281$. The material constants are given for a reference temperature $\theta_R = 293.15\text{K}$. A fixed $\alpha_{CFL} = 0.9$ was used for the simulations.

In this example, the anisotropic updated kernel and kernel gradient are obtained as a push-forward of the corrected material kernel and corrected material gradient (Option#1). A 3D quadratic smoothing function is employed with a factor $f_h = 0.6$ for all the simulations.

In figures 7.13 and 7.14, the pressure and the temperature distributions for model M1 are plotted at different instants of the simulation, for a Total Lagrangian Formulation and also for an updated reference Lagrangian formulation, with updates performed at every time step. The same results are shown for model M3 in figures 7.15 and 7.16.

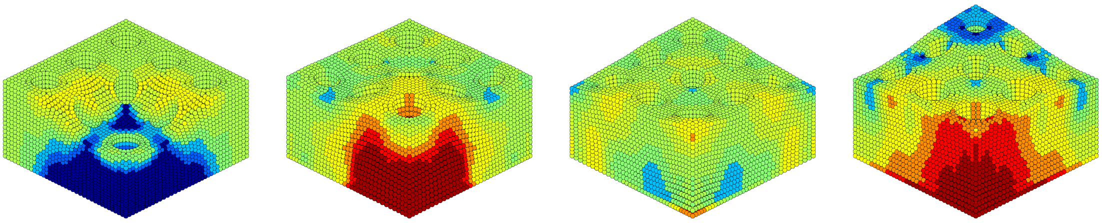

TLF 0.05s TLF 0.15s TLF 0.25s TLF 0.45s

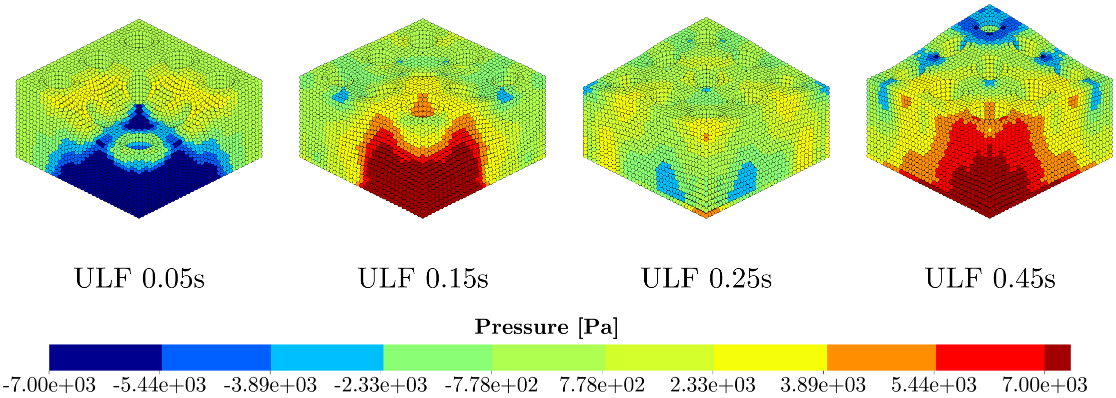

ULF 0.05s ULF 0.15s ULF 0.25s ULF 0.45s

Figure 7.13: Constrained punch block M1 pressure distribution.

Evolution of internal, kinetic, thermal and total energies is shown for both TLF and ULF for models M1 and M3 in figures 7.17a and 7.17b, respectively. A bottom view of the pressure and temperature distribution at time 0.12s is shown for the three models in figure 7.18 for an updated reference Lagrangian formulation, with updates performed at every time step.

The results presented up to now employed a 3D quadratic kernel function, with the updated kernel and gradient obtained as a push-forward of the corrected material kernel and corrected material gradient (Option#1). The four different approaches of obtaining updated anisotropic kernels are considered now. In figure 7.19, the evolution of total energy and global entropy for model M3 is shown considering the four options, updates are performed at every time step. In the same figure, the pressure and temperature distributions at time 0.45s are shown for the same models.

As the conclusions of the constrained punch block example, the proposed formulation was shown to be robust and did not activate any spurious mechanisms in this test case. The results for the simulations evolved based on updated reference

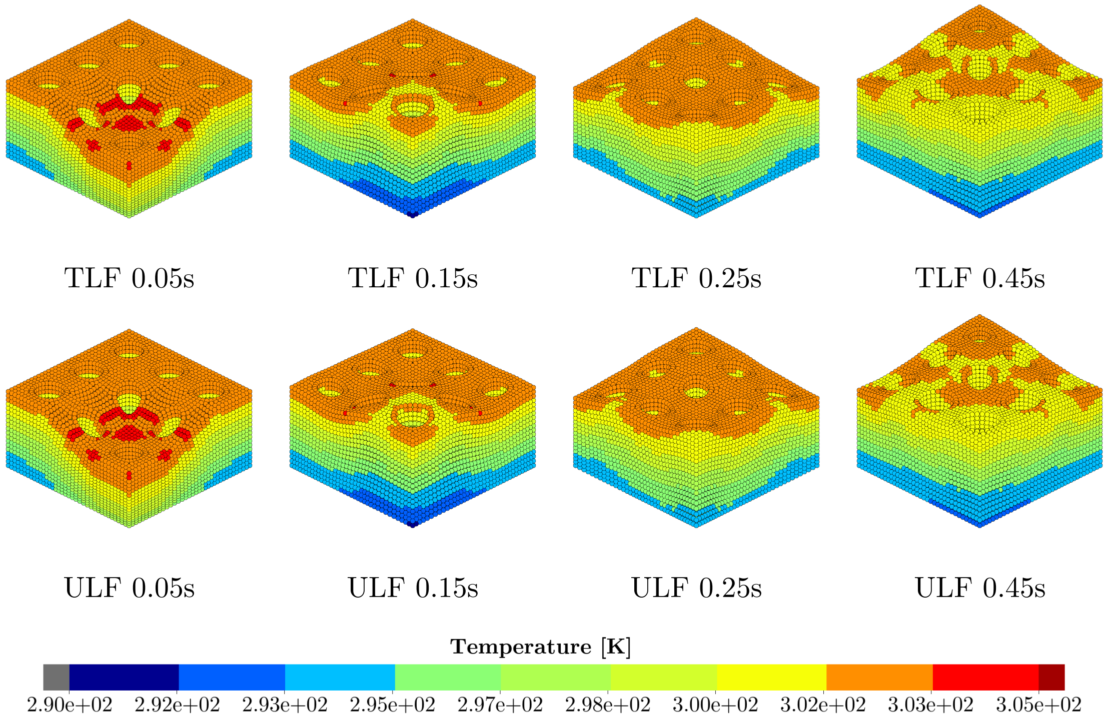

TLF 0.05s TLF 0.15s TLF 0.25s TLF 0.45s

ULF 0.05s ULF 0.15s ULF 0.25s ULF 0.45s

Figure 7.14: Constrained punch block M1 temperature distribution.

configurations are as good as the ones based on the initial geometry (TLF). The example demonstrates the ability of the proposed algorithm in dealing with more complex geometries involving a large number of particles and subjected to extreme deformations in a thermal-stress context. Moreover, the example was also used to compare different options of obtaining updated kernels and gradients, with all approaches performing equally well.

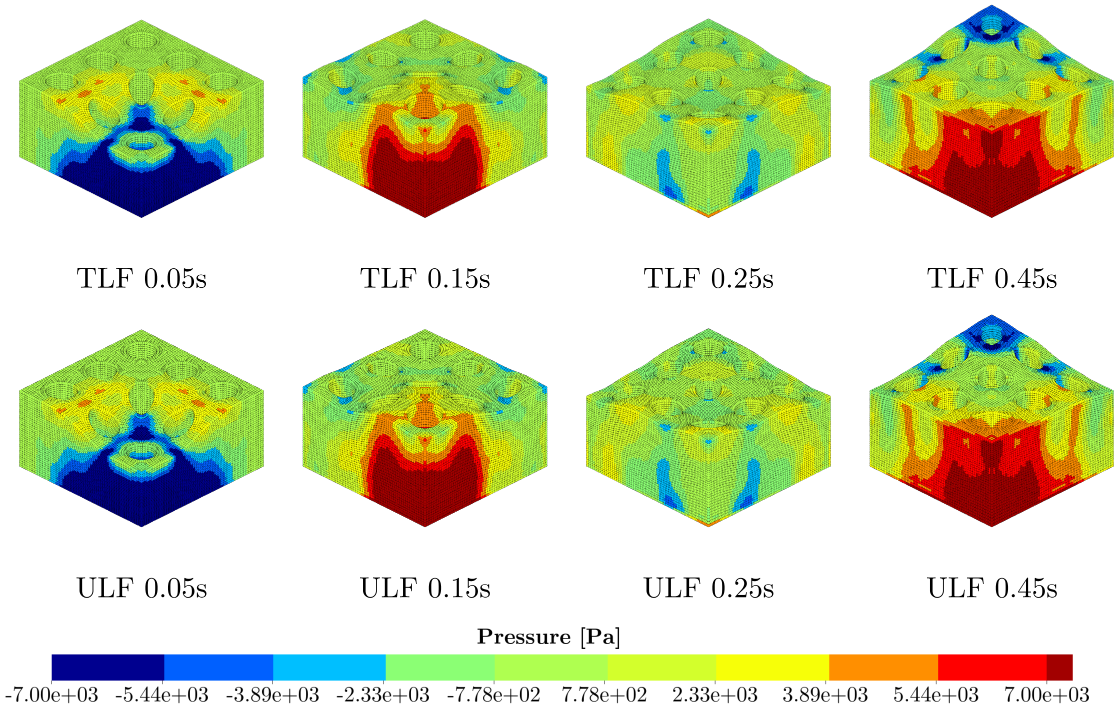

TLF 0.05s TLF 0.15s TLF 0.25s TLF 0.45s

ULF 0.05s ULF 0.15s ULF 0.25s ULF 0.45s

Figure 7.15: Constrained punch block M3 pressure distribution.

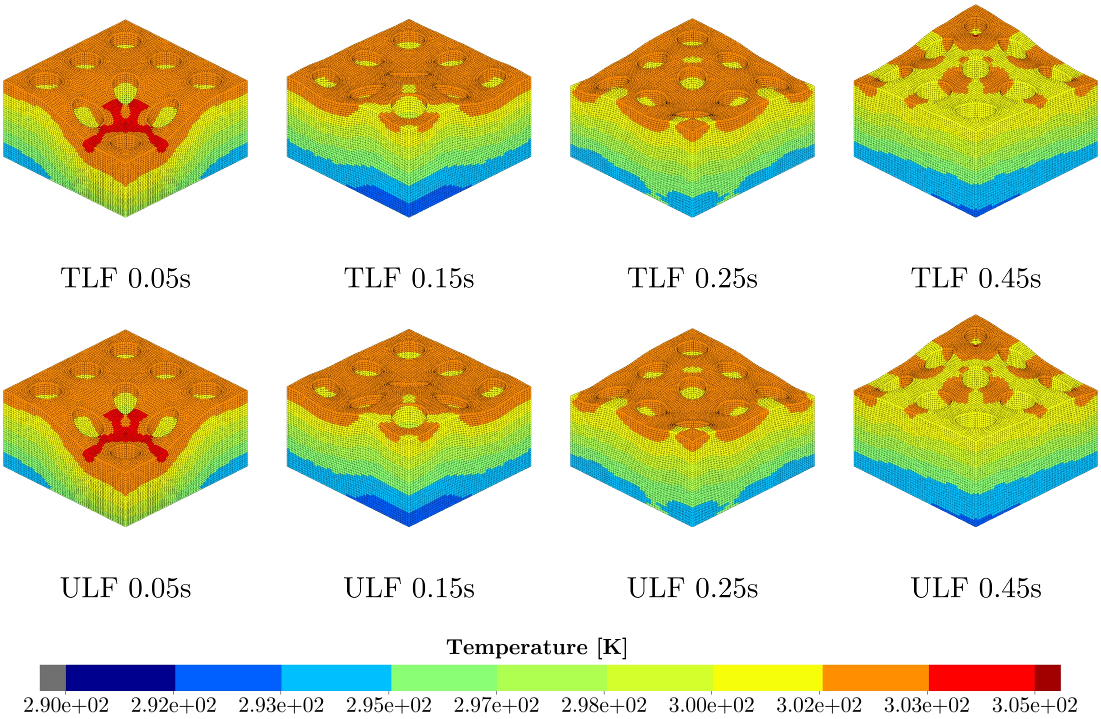

TLF 0.05s TLF 0.15s TLF 0.25s TLF 0.45s

ULF 0.05s ULF 0.15s ULF 0.25s ULF 0.45s

Figure 7.16: Constrained punch block M3 temperature distribution.

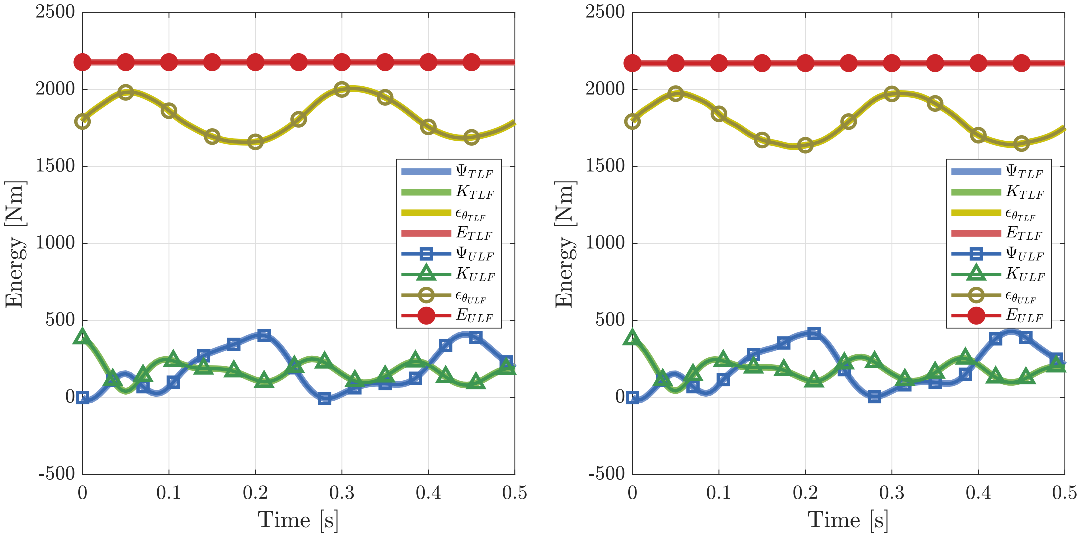

(a) (b)

Figure 7.17: Evolution of kinetic ($K$), internal ($\Psi$), thermal ($\epsilon_\theta$) and total ($E$) energies for the constrained punch block: (a) model M1. (b) model M3.

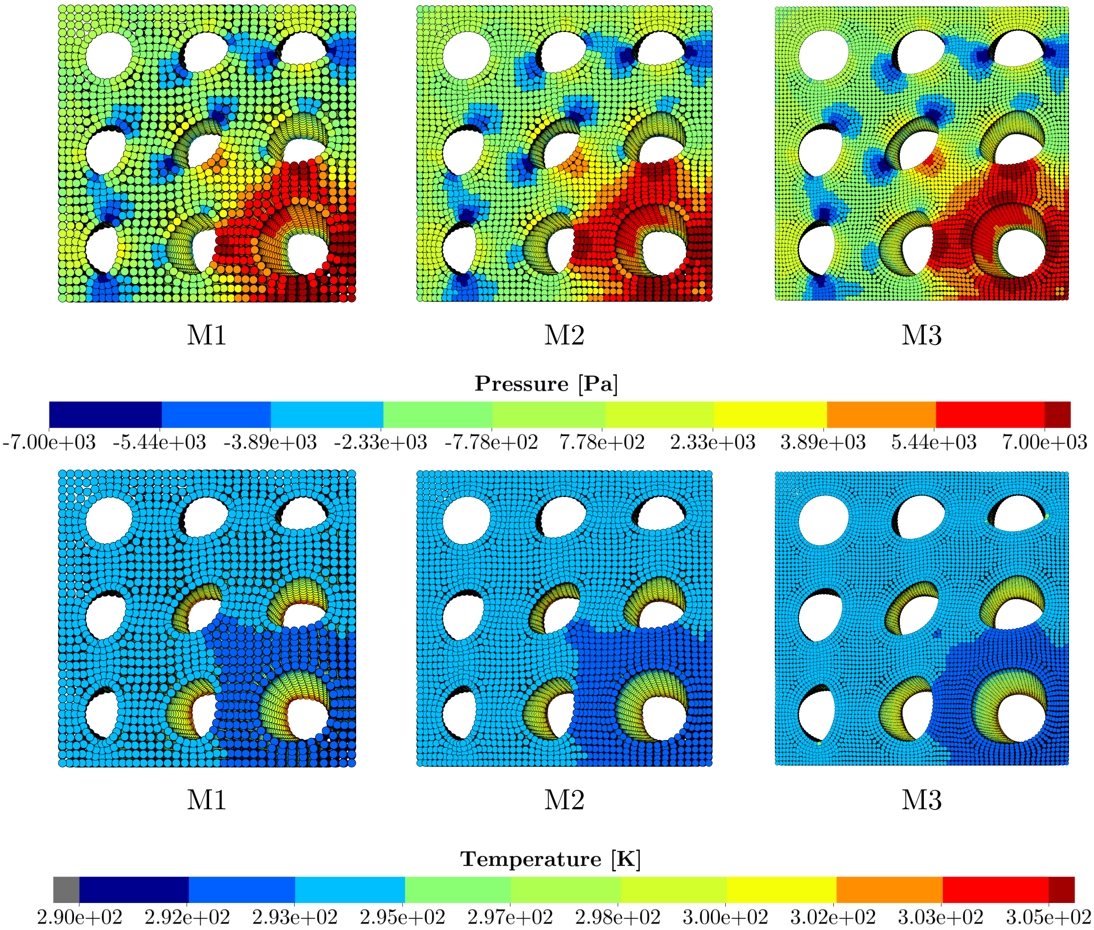

Figure 7.18: Constrained punch block (bottom view) considering different model refinements in an updated reference Lagrangian formulation, with updates performed at every time step. First row shows the pressure distribution at time 0.12s, the second row shows the temperature distribution at time 0.12s.

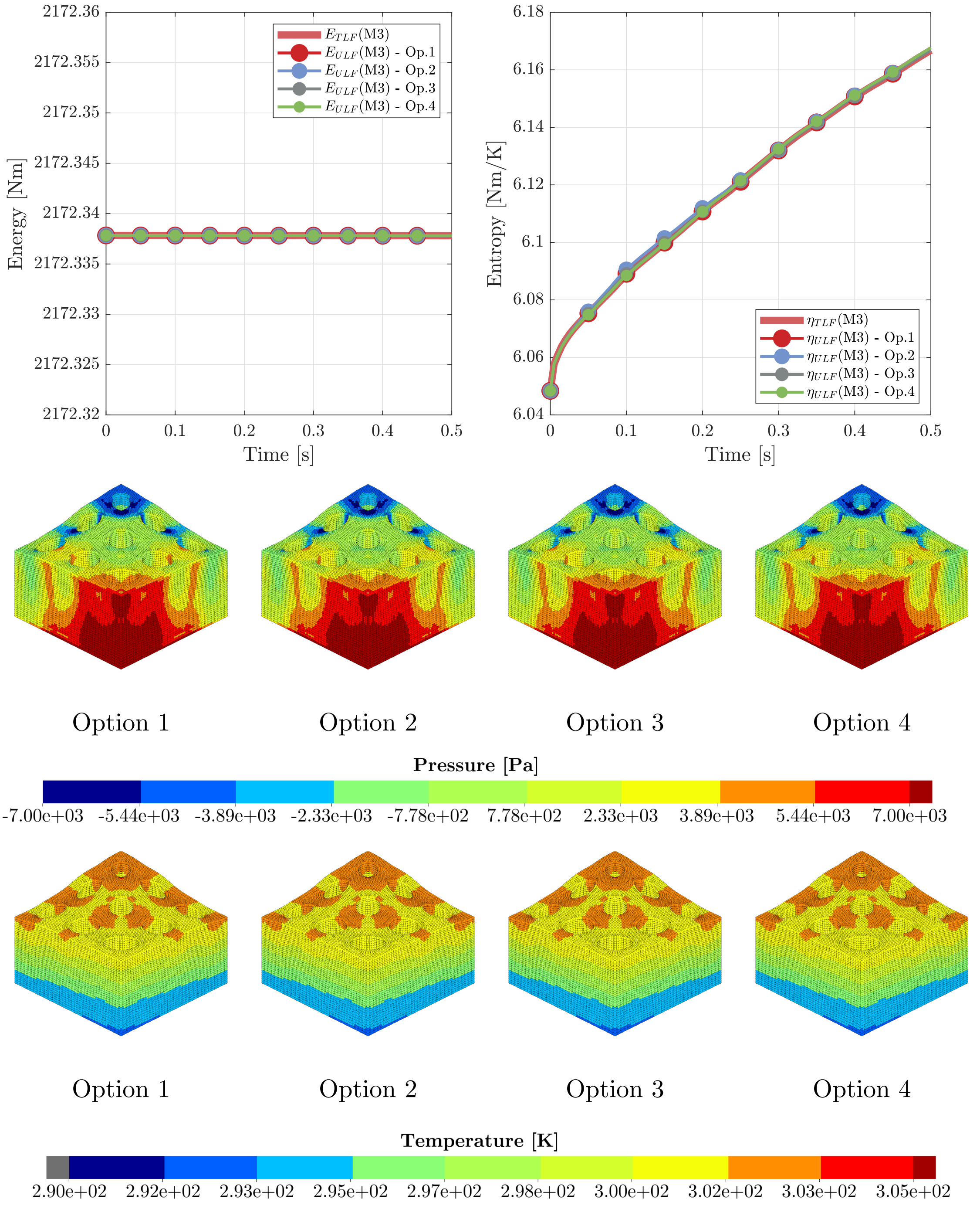

Figure 7.19: Constrained punch block M3 employing different options of obtaining updated kernels and gradients. The first row shows the evolution of total energy ($E$) and global entropy ($\eta$), second and third rows show the pressure and temperature distribution at time 0.45s.

## 7.4 Impact bar with adiabatic heating effects

The Taylor bar benchmark presented in example 6.3.1 is considered again, but now in an adiabatic thermal-stress analysis [112, 113]. Therefore, the mechanical deformation will cause heating, but the event is assumed to be so rapid that heat has no time to diffuse through the material (no conduction). The main characteristics of the model were presented in example 6.3.1, only model M3 with 7280 particles is considered now. In the present example a Hencky-based von Mises plasticity model, with rate-dependent Johnson-Cook hardening is used with the following properties taken from [78]: initial density $\rho_0 = 8960\frac{\text{kg}}{\text{m}^3}$, Young's modulus $E = 124 \times 10^9 \frac{\text{N}}{\text{m}^2}$, Poisson's ratio $\nu = 0.34$, yield stress $A = 90 \times 10^6 \frac{\text{N}}{\text{m}^2}$, hardening parameter $b = 292 \times 10^6 \frac{\text{N}}{\text{m}^2}$, hardening exponent $n' = 0.31$, strain rate coefficient $c = 0.025$, reference strain rate $\dot{\epsilon}_0 = 1\frac{1}{\text{s}}$, melting temperature $\theta_{\text{melt}} = 1356.15\text{K}$, transition temperature $\theta_{\text{transition}} = 298.15\text{K}$, temperature exponent $m = 1.09$ and specific heat capacity $C_v = 383\frac{\text{J}}{\text{kgK}}$. The temperature is initialized uniformly across the bar with $\theta = 298.15\text{K}$. The material constants are given for a reference temperature $\theta_R = 298.15\text{K}$. A fixed $\alpha_{CFL} = 0.9$ was used for the simulations.

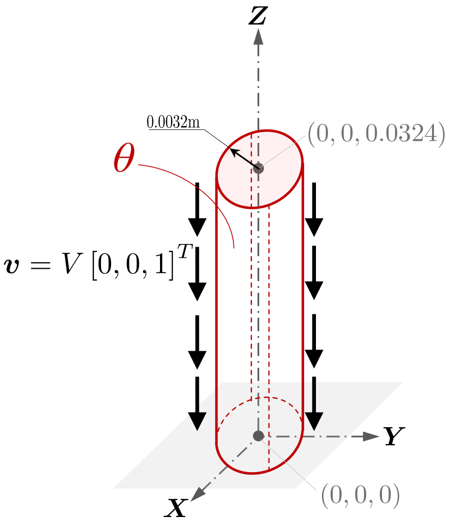

Figure 7.20: Thermal Impact bar.

In this example, the anisotropic updated kernel and kernel gradient are obtained as in Option#4. A 3D quadratic smoothing function is employed with a factor $f_h = 0.6$ for all the simulations.

Results are benchmarked against a finite elements simulation performed using Abaqus/Explicit. The set-up of the analysis as well as the geometric characteristics of the finite elements model are exactly the same as the ones used in SPH. The element type is an 8-nodes first-order, reduced integration brick (C3D8R).

In figure 7.21, the von Mises stress distribution and the equivalent plastic strain are plotted at different instants of the simulation, for a Total Lagrangian Formulation and also for an updated reference Lagrangian formulation, with updates performed at every time step.

Evolution of internal, kinetic and total energies is shown for both TLF and ULF in figure 7.22a. In addition, the numerical dissipation in the same model is shown in

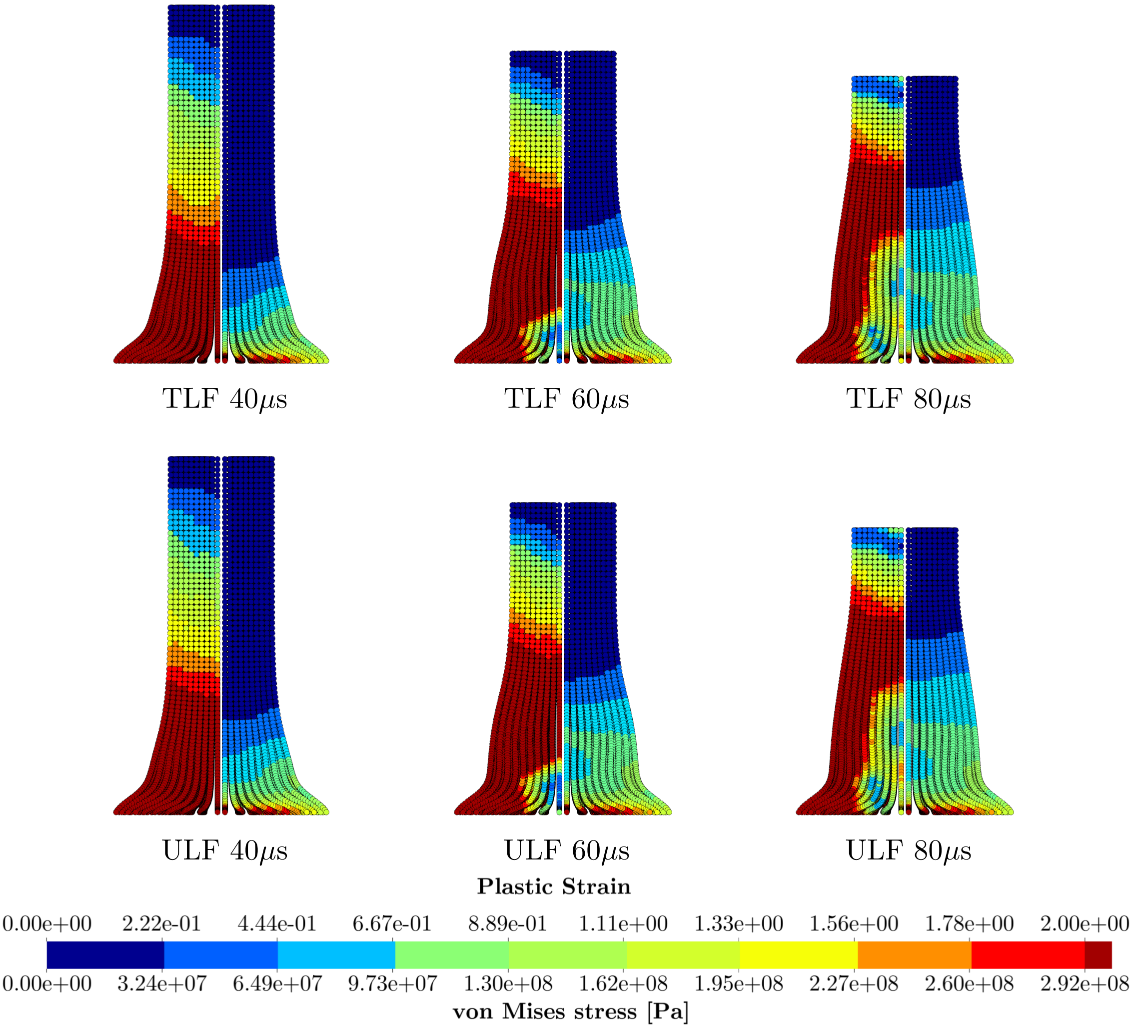
TLF 40$\mu$s TLF 60$\mu$s TLF 80$\mu$s

ULF 40$\mu$s ULF 60$\mu$s ULF 80$\mu$s

Figure 7.21: Impact bar model M3 including adiabatic heating effects von Mises stresses (left side) and equivalent plastic strain (right side).

figure 7.22b. Note that the energies were computed considering only the represented geometry, i.e., one quarter of the cylinder.

In figure 7.23a, the temperature distribution is shown at the end of the simulation. Updated Lagrangian results are presented on the left half of bar, while the reference solution using finite elements is shown on the right side. In addition, figure 7.23b shows the time evolution of the radius of the bar in the impact region, results are presented for total and updated formulations, considering different model refinements.

As a final test for this example, conduction of heat was allowed in a fully thermally-coupled analysis. In this case, the thermal expansion coefficient was taken from [78] as $\alpha = 0.00005\frac{1}{\mathrm{K}}$ and the thermal conductivity as $h = 386\frac{\mathrm{W}}{\mathrm{mK}}$. Figure 7.24a shows side-by-side the pressure distribution for the adiabatic simulation presented above and the thermally-coupled one. Figure 7.24b shows the temperature distribution for the same simulations. Model M3 was used in an updated reference Lagrangian formulation, with updates performed at every time step. Figures 7.25a and 7.25b show the comparison of the energies and the numerical dissipation between adiabatic and thermally-coupled models. The representativeness of these

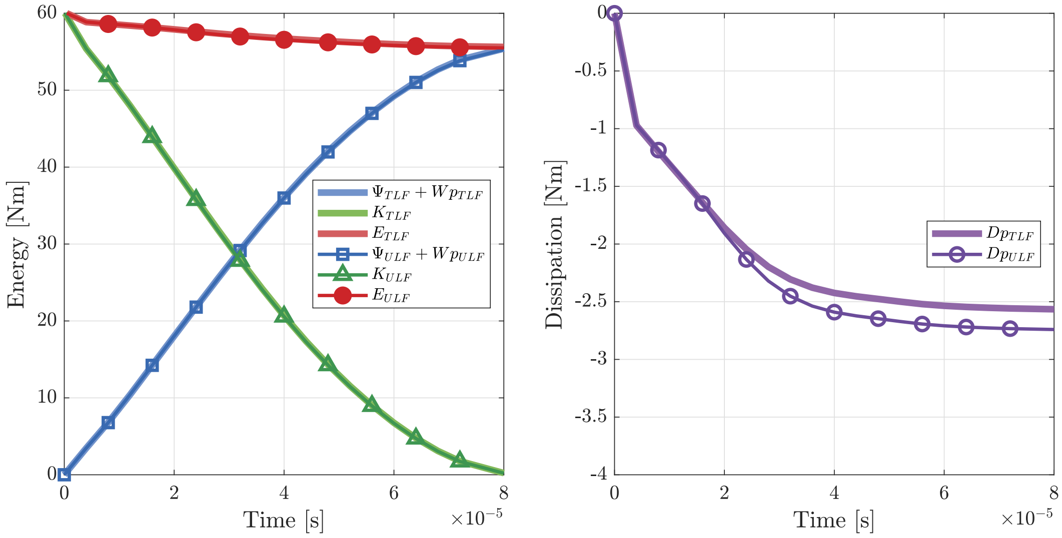

(a) (b)

Figure 7.22: (a) Evolution of kinetic ($K$), internal ($\Psi$) plus plastic dissipation ($Wp$) and total ($E$) energies for impact bar model M3 including adiabatic heating effects. (b) Numerical dissipation for the model M3.

results needs to be judged with care. Further investigations into this and other thermally-coupled elasto-plastic examples are under preparation and will appear in future author's publications.

As the conclusions of this example, the proposed formulation was shown to be applicable to scenarios where heating of the material caused by its deformation is important because of the temperature-dependent material properties. The temperature increase is calculated proportionally to the inelastic dissipation, in this study it appears in full as heat flux (alternatively only a fraction of it could have been used). Conduction of heat was not allowed in the main part of this study, i.e., it was assumed that the process happens so rapid that there is no time for the heat to propagate through the material. The results are comparable to the reference simulation performed employing finite elements. As a final test, heat conduction was allowed, the formulation did not face any particular issues in solving the fully-coupled problem. However, the results obtained for this last case are to be further investigated.

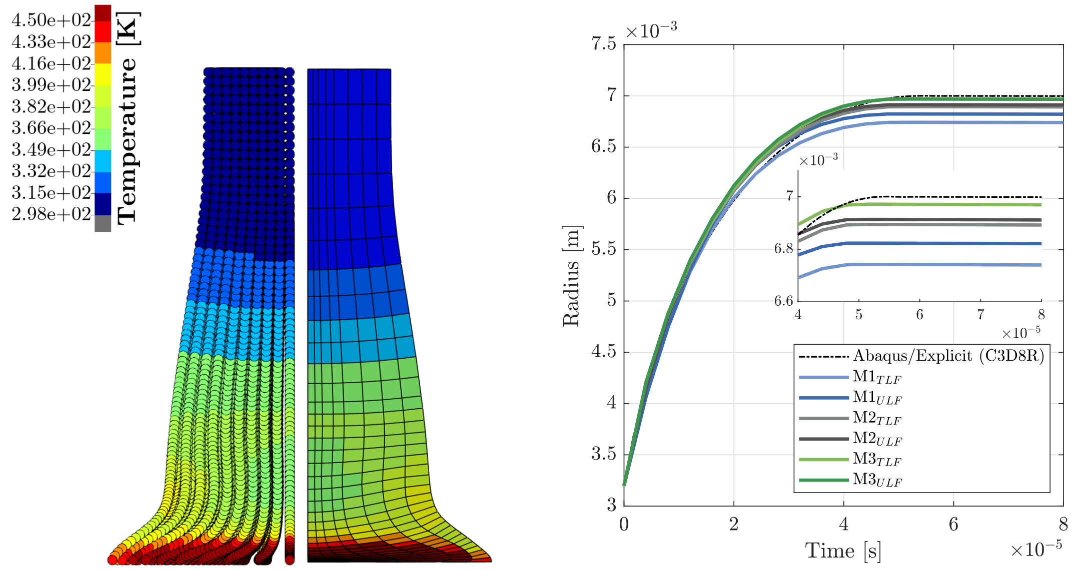

(a) (b)

Figure 7.23: Impact bar model M3 including adiabatic heating effects: (a) Temperature distribution at time $8.0 \times 10^{-5}$s. ULF-SPH results on the left, Abaqus/Explicit (FEM) on the right. (b) Time evolution of the radius of the bar measured at the impact interface.

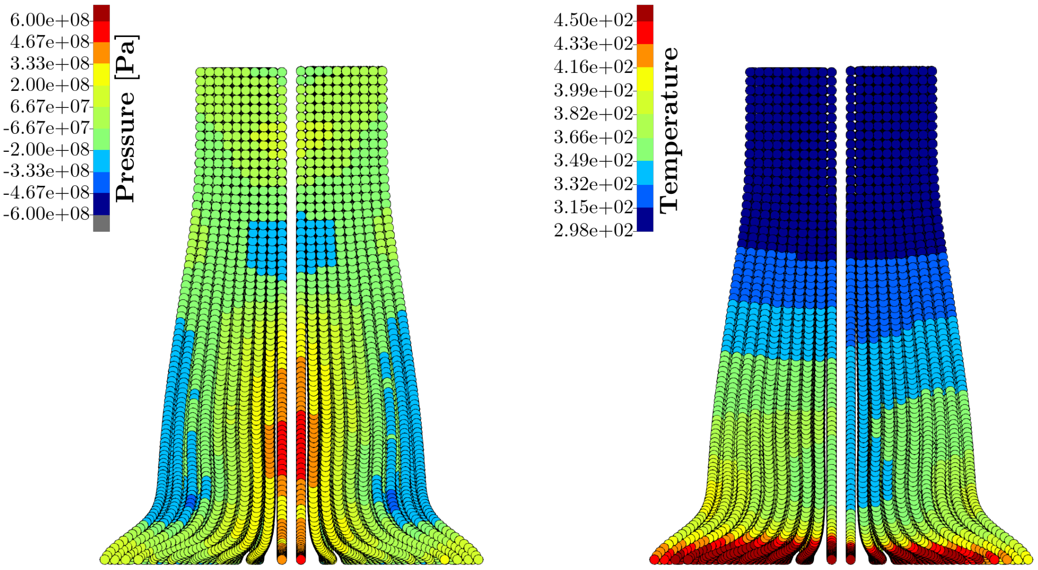

(a) (b)

Figure 7.24: Impact bar model M3 ULF-SPH after $8.0 \times 10^{-5}$s: (a) Pressure distribution, adiabatic heating effects on the left side and thermally-coupled on the right side. (b) Temperature distribution, adiabatic heating effects on the left side and thermally-coupled on the right side.

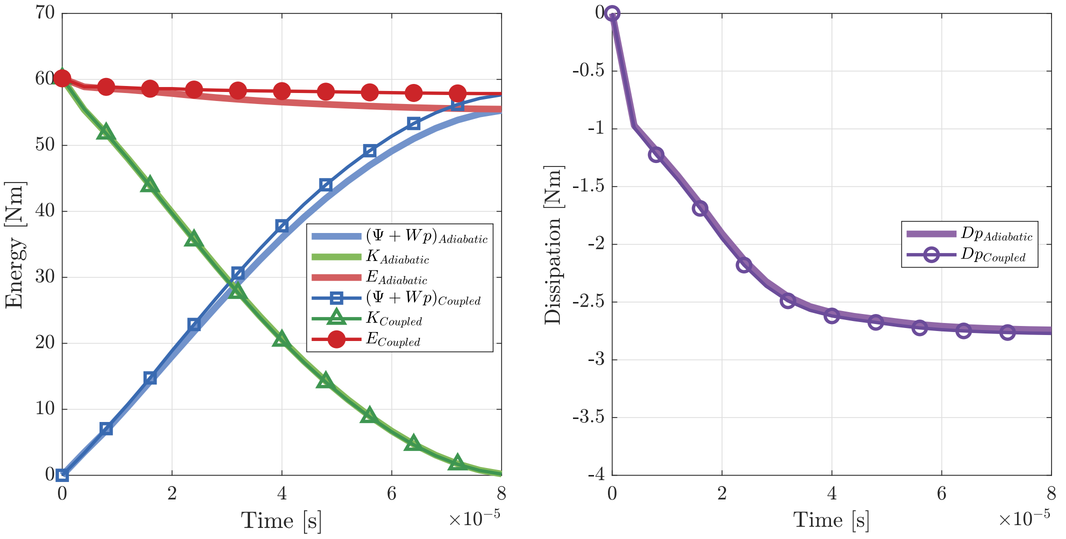

(a) (b)

Figure 7.25: Impact bar model M3 ULF-SPH including adiabatic heating effects vs. thermally-coupled.(a) Evolution of kinetic ($K$), internal ($\Psi$) plus plastic dissipation ($Wp$) and total ($E$) energies. (b) Numerical dissipation.

# Part IV

# Dynamic Fracture

# Chapter 8

# SPH method for dynamic fracture

## 8.1 Introduction

In this chapter the SPH framework developed in this work is extended to the context of dynamic fracture. The post-fracture velocities and deformation gradient are derived considering the satisfaction of conservation of linear momentum and energy. The development of a methodology to obtain the new domains of influence once fracture takes place is presented afterwards and is followed by the discussion of the failure criteria employed.

## 8.2 Discrete fracture mechanics

The first assumption made in the proposed methodology is that a continuous crack is represented as a set of contiguous cracked particles, as schematically illustrated in figure 8.1. The fracture phenomenon is treated locally at each particle.

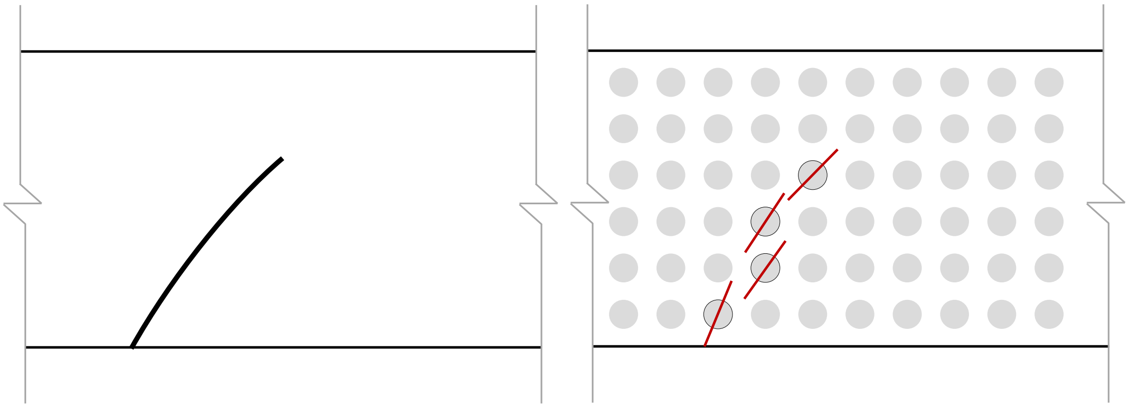

(a) (b)

Figure 8.1: (a) A possible crack path. (b) Discrete crack representation.

Before diving into the theory, it is important to clarify the procedure that will be followed once the fracture criterion is met at a particle. This is summarised in algorithm 6. Notice that, apart from steps 5-7, algorithm 6 is identical to the update steps in algorithm 5, i.e., an update of the reference configuration will be carried out in the same manner as discussed in chapter 5. However, now this is performed once fracture takes place and includes steps 5, 6 and 7, which deal with "breaking" the particles, updating the list of neighbours and providing the algorithm with the post-fracture velocities and the deformation state of the cracked particles.

**Algorithm 6:** Fracture update

```
if update at this step = TRUE (Fracture criterion met) then
    (1) COMPUTE the velocity as $\boldsymbol{v}_a = \frac{J_{\boldsymbol{\chi},a}\boldsymbol{p}_{\boldsymbol{\chi},a}}{\rho_0}$
    (2) ASSIGN $\boldsymbol{F}_{\boldsymbol{\chi},a} \leftarrow \boldsymbol{f}_a\boldsymbol{F}_{\boldsymbol{\chi},a}$, $\boldsymbol{H}_{\boldsymbol{\chi},a} \leftarrow \boldsymbol{h}_a\boldsymbol{H}_{\boldsymbol{\chi},a}$, $J_{\boldsymbol{\chi},a} \leftarrow \boldsymbol{j}_a\boldsymbol{J}_{\boldsymbol{\chi},a}$ and $\boldsymbol{\chi}_a \leftarrow \boldsymbol{x}_a$
    (3) UPDATE the linear momentum $\boldsymbol{p}_{\boldsymbol{\chi},a} = J^{-1}_{\boldsymbol{\chi},a}\rho_0\boldsymbol{v}_a$ and all other relevant variables
    (4) REINITIALISE $\boldsymbol{f}_a$, $\boldsymbol{h}_a$, $j_a$
    (5) SPLIT the cracked particles
    (6) UPDATE the list of neighbouring particles in the cracked region
    (7) COMPUTE post-fracture variables for the split particles, namely $\boldsymbol{v}_a^{\pm}$, $\boldsymbol{F}_a^{\pm}$
    (8) COMPUTE corrected kernel and gradient approximations at $\boldsymbol{\chi}_a$: $\tilde{W}_{ba}^{\boldsymbol{\chi}}$ and $\tilde{\boldsymbol{\nabla}}_{\boldsymbol{\chi}}W_{ba}^{\boldsymbol{\chi}}$
end
```

In the present approach, a cracked particle is split into two particles once a failure criterion is met, as illustrated in figure 8.2. The parent particle $a$, which has a volume $v_a$ and mass $m_a = \rho_a v_a$ is split creating two daughter particles, $a^+$ and $a^-$. Each daughter particle receives half of the mass of particle $a$, i.e., $m_a^+ = m_a^- = \frac{m_a}{2}$, also implying that the volume $v_a^+ = v_a^- = \frac{v_a}{2}$. Therefore, conservation of mass is satisfied.

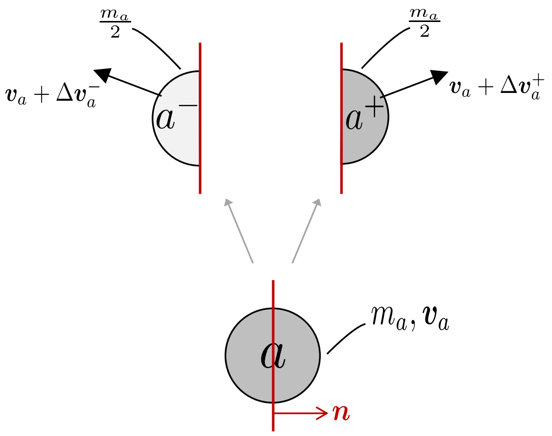

Figure 8.2: Particle splitting.

The post-fracture velocities for the daughter particles $a^+$ and $a^-$ are assumed as

$$\boldsymbol{v}_a^+ = \boldsymbol{v}_a + \Delta\boldsymbol{v}_a^+, \tag{8.1a}$$

$$\boldsymbol{v}_a^- = \boldsymbol{v}_a + \Delta\boldsymbol{v}_a^-, , \tag{8.1b}$$

where, $\Delta\boldsymbol{v}_a^+ = \Delta v_a^+\boldsymbol{n}_a$ and $\Delta\boldsymbol{v}_a^- = \Delta v_a^-\boldsymbol{n}_a$, with $\boldsymbol{n}_a$ being the normal of the fracture surface attached to particle $a$ in the current configuration. Note that, as soon as the fracture criterion is met for any particle, the reference configuration will be updated (see algorithm 6). Therefore, at this stage, the reference configuration will match the current configuration. The following derivations are performed taking this into account, i.e., the post-fracture quantities are computed at step 7 of algortithm 6.

Imposing conservation of linear momentum, and expressing it in terms of the material configuration

$$m_a\boldsymbol{v}_a = \rho_{0,a}V_a\boldsymbol{v}_a = \rho_{0,a}V_a^+\boldsymbol{v}_a^+ + \rho_{0,a}V_a^-\boldsymbol{v}_a^-, \tag{8.2a}$$

$$V_a\boldsymbol{v}_a = V_a^+\boldsymbol{v}_a^+ + V_a^-\boldsymbol{v}_a^-, \tag{8.2b}$$

$$= \frac{1}{2}V_a\left(\boldsymbol{v}_a + \Delta\boldsymbol{v}_a^+\right) + \frac{1}{2}V_a\left(\boldsymbol{v}_a + \Delta\boldsymbol{v}_a^-\right), \tag{8.2c}$$

where $\rho_{0,a}$ is the material density of particle $a$, $V_a$ is the volume of particle $a$ in the material configuration ($V_a = J_{\boldsymbol{\chi},a}^{-1}V_a^{\boldsymbol{\chi}} = J_a^{-1}v_a$) and $V_a^\pm = \frac{V_a}{2}$.

Note that equation 8.2c implies

$$\frac{1}{2}V_a\left(\Delta\boldsymbol{v}_a^+ + \Delta\boldsymbol{v}_a^-\right) = \frac{1}{2}V_a\left(\Delta v_a^+ + \Delta v_a^-\right)\boldsymbol{n}_a = \boldsymbol{0}, \tag{8.3}$$

and therefore, $\Delta v_a^+ = -\Delta v_a^- := \Delta v_a$.

Imposing conservation of energy

$$\left(k_a + \Psi_a\right)V_a = \left(k_a^+ + \Psi_a^+\right)V_a^+ + \left(k_a^- + \Psi_a^-\right)V_a^-, \tag{8.4a}$$

$$= \left(k_a^+ + \Psi_a^+ + k_a^- + \Psi_a^-\right)\frac{V_a}{2}, \tag{8.4b}$$

where $k_a$ is the kinetic energy per unit of material volume, $\Psi_a$ is the internal energy density in terms of material configuration.

Rearranging the above equation, one can write

$$\frac{1}{2}\left(k_a^+ + k_a^-\right) - k_a = \Psi_a - \frac{1}{2}\left(\Psi_a^+ + \Psi_a^-\right). \tag{8.5}$$

By further developing the LHS of equation 8.5

$$\frac{1}{2}\left(k_a^+ + k_a^-\right) - k_a = \frac{1}{4}\rho_{0,a}\left(\boldsymbol{v}_a^+\cdot\boldsymbol{v}_a^+ + \boldsymbol{v}_a^-\cdot\boldsymbol{v}_a^- - 2\boldsymbol{v}_a\cdot\boldsymbol{v}_a\right). \tag{8.6}$$

Note that

$$\boldsymbol{v}_a^+\cdot\boldsymbol{v}_a^+ = \left(\boldsymbol{v}_a + \Delta v_a\boldsymbol{n}_a\right)\cdot\left(\boldsymbol{v}_a + \Delta v_a\boldsymbol{n}_a\right) = \boldsymbol{v}_a\cdot\boldsymbol{v}_a + \left(\Delta v_a\right)^2 + 2\left(\boldsymbol{v}_a\cdot\boldsymbol{n}_a\right)\Delta v_a, \tag{8.7}$$

and

$$\boldsymbol{v}_a^-\cdot\boldsymbol{v}_a^- = \left(\boldsymbol{v}_a - \Delta v_a\boldsymbol{n}_a\right)\cdot\left(\boldsymbol{v}_a - \Delta v_a\boldsymbol{n}_a\right) = \boldsymbol{v}_a\cdot\boldsymbol{v}_a + \left(\Delta v_a\right)^2 - 2\left(\boldsymbol{v}_a\cdot\boldsymbol{n}_a\right)\Delta v_a. \tag{8.8}$$

Replacing 8.7 and 8.8 in equation 8.6 leads to

$$\frac{1}{2}\left(k_a^+ + k_a^-\right) - k_a = \frac{1}{2}\rho_{0,a}\left(\Delta v_a\right)^2, \tag{8.9}$$

which can be used in equation 8.5 to allow $\Delta v_a$ to be computed as

$$\Delta v_a = \left(\frac{\Psi_a - \frac{1}{2}\left(\Psi_a^+ + \Psi_a^-\right)}{\frac{\rho_{0,a}}{2}}\right)^{\frac{1}{2}}. \tag{8.10}$$

Upon solution of $\Delta v_a$, one can obtain $\boldsymbol{v}_a^- = \boldsymbol{v}_a - \Delta v_a \boldsymbol{n}_a$ and $\boldsymbol{v}_a^+ = \boldsymbol{v}_a + \Delta v_a \boldsymbol{n}_a$.

Recall that in a $[\boldsymbol{p}, \boldsymbol{F}]$ formulation, the internal energy density is given as $\Psi_a = \Psi\left(\boldsymbol{F}_a\right)$, and therefore, $\Psi_a^\pm = \Psi\left(\boldsymbol{F}_a^\pm\right)$. Moreover, $\boldsymbol{P}_a^\pm \boldsymbol{N}_a = \boldsymbol{0}$ holds for a free boundary, with $\boldsymbol{P}$ being the first Piola-Kirchhoff stress tensor and $\boldsymbol{N}_a$ the outward normal of the fracture surface in the material configuration ($\boldsymbol{N}_a = \boldsymbol{H}_a^{-1}\boldsymbol{n}_a\frac{da}{dA}$). Thus, $\boldsymbol{F}_a^\pm$ can be defined as

$$\boldsymbol{F}_a^\pm = \boldsymbol{F}_a + \Delta\boldsymbol{F}_a^\pm, \qquad \text{satisfying} \quad \boldsymbol{P}\left(\boldsymbol{F}_a + \Delta\boldsymbol{F}_a^\pm\right)\boldsymbol{N}_a = \boldsymbol{0}. \tag{8.11}$$

A rank-1 jump can be assumed for $\boldsymbol{F}$, that is

$$\boldsymbol{F}_a^\pm = \boldsymbol{F}_a - \boldsymbol{\beta} \otimes \boldsymbol{N}_a. \tag{8.12}$$

An equation to solve for $\boldsymbol{\beta}$ emerges from the fact that

$$\boldsymbol{P}_a^\pm \boldsymbol{N}_a = \boldsymbol{P}_a^\pm\left(\boldsymbol{F}_a^\pm\right)\boldsymbol{N}_a = \boldsymbol{P}_a^\pm\left(\boldsymbol{F}_a - \boldsymbol{\beta}\otimes\boldsymbol{N}_a\right)\boldsymbol{N}_a = \boldsymbol{0}. \tag{8.13}$$

Using an iterative Newton-Raphson technique

$$\underbrace{\boldsymbol{P}\left(\boldsymbol{F}_a - \boldsymbol{\beta}^{(k)}\otimes\boldsymbol{N}_a\right)\boldsymbol{N}_a}_{\boldsymbol{t}^k_{\boldsymbol{N},a}} - \underbrace{\boldsymbol{\mathcal{C}}_{\boldsymbol{NN}}\left(\boldsymbol{F}_a - \boldsymbol{\beta}^{(k)}\otimes\boldsymbol{N}_a\right)}_{\boldsymbol{\mathcal{C}}_{\boldsymbol{NN},a}}\left(\boldsymbol{\beta}^{(k+1)} - \boldsymbol{\beta}^{(k)}\right) = 0, \tag{8.14}$$

thus

$$\boldsymbol{\beta}^{(k+1)} = \boldsymbol{\beta}^{(k)} + \left[\boldsymbol{\mathcal{C}}^{(k)}_{\boldsymbol{NN},a}\right]^{-1}\boldsymbol{t}^{(k)}_{\boldsymbol{N},a}, \tag{8.15}$$

and, finally

$$\boldsymbol{F}_a^\pm = \boldsymbol{F}_a - \boldsymbol{\beta}^{(k+1)}\otimes\boldsymbol{N}_a. \tag{8.16}$$

For linear elasticity, $\boldsymbol{\mathcal{C}}^{(k)}_{\boldsymbol{NN},a} = \boldsymbol{\mathcal{C}}^{\text{lin}}_{\boldsymbol{NN},a}$ remains constant and therefore $\boldsymbol{\beta} = \boldsymbol{\mathcal{C}}^{\text{lin}}_{\boldsymbol{NN},a}\boldsymbol{t}_{\boldsymbol{N},a}$, and

$$\begin{aligned}
\boldsymbol{F}_a^\pm &= \boldsymbol{F}_a - \left[\boldsymbol{\mathcal{C}}^{\text{lin}}_{\boldsymbol{NN},a}\right]^{-1}\boldsymbol{t}_{\boldsymbol{N},a}\otimes\boldsymbol{N}_a, && \text{(8.17a)}\\
&= \boldsymbol{F}_a\left(\boldsymbol{I} - \boldsymbol{N}_a\otimes\boldsymbol{N}_a\right) + \left(\boldsymbol{F}_a\boldsymbol{N}_a - \left[\boldsymbol{\mathcal{C}}^{\text{lin}}_{\boldsymbol{NN},a}\right]^{-1}\boldsymbol{t}_{\boldsymbol{N},a}\right)\otimes\boldsymbol{N}_a. && \text{(8.17b)}
\end{aligned}$$

Considering linear elasticity

$$\begin{aligned}
\boldsymbol{\mathcal{C}}^{\text{lin}}_{\boldsymbol{NN},a} &= \left(\lambda+\mu\right)\boldsymbol{N}_a\otimes\boldsymbol{N}_a + \mu\boldsymbol{I}, && \text{(8.18a)}\\
&= \left(\lambda+2\mu\right)\boldsymbol{N}_a\otimes\boldsymbol{N}_a + \mu\boldsymbol{t}_1\otimes\boldsymbol{t}_1 + \mu\boldsymbol{t}_2\otimes\boldsymbol{t}_2, && \text{(8.18b)}
\end{aligned}$$

and therefore

$$\left[\boldsymbol{\mathcal{C}}^{\mathrm{lin}}_{\boldsymbol{NN},a}\right]^{-1} = \frac{1}{\lambda + 2\mu}\boldsymbol{N}_a \otimes \boldsymbol{N}_a + \frac{1}{\mu}\left(\boldsymbol{I} - \boldsymbol{N}_a \otimes \boldsymbol{N}_a\right). \tag{8.19}$$

The above equations lead to

$$\boldsymbol{F}^+_a = \boldsymbol{F}^-_a = \boldsymbol{F}_a - \boldsymbol{\beta} \otimes \boldsymbol{N}_a, \qquad \text{with} \quad \boldsymbol{\beta} = \left[\boldsymbol{\mathcal{C}}^{\mathrm{lin}}_{\boldsymbol{NN},a}\right]^{-1} \boldsymbol{t}_{\boldsymbol{N},a}. \tag{8.20}$$

**Remark 9** *Following the work of Belytschko et al. [69], a linear traction-displacement (cohesive) law, as the one shown in figure 8.3, is imposed across the discontinuity. The energy dissipation is chosen to match the fracture energy.*

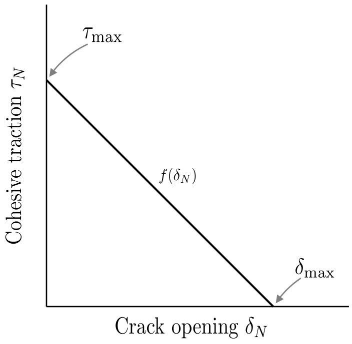

Figure 8.3: Linear cohesive model.

*The displacement jump* $\delta_N$ *is defined as*

$$\delta_N = \boldsymbol{n} \cdot [\![\boldsymbol{u}]\!] = \boldsymbol{n} \cdot \left(\boldsymbol{u}^+ - \boldsymbol{u}^-\right). \tag{8.21}$$

*By considering a cohesive law involving only the normal component of the traction, the maximum normal traction* $\tau_{max}$ *is defined as*

$$\tau_{max} = \boldsymbol{n} \cdot \boldsymbol{t}_{\boldsymbol{N}} = \boldsymbol{n} \cdot \boldsymbol{P}\boldsymbol{N}, \tag{8.22}$$

*while the critical crack opening* $\delta_{max}$ *is given by*

$$\delta_{max} = \frac{2G_f}{\tau_{max}}, \tag{8.23}$$

*with* $G_f$ *being the fracture energy. Therefore, the area under the cohesive law shown in figure 8.3 is the fracture energy.*

## 8.3 Particle split

Once any single particle reaches a failure criterion, fracture takes place and the particle is split into two daughter particles, as presented in the previous section. When new particles are introduced in the domain, and consequently new boundaries are created (the fracture surface), a special treatment is required to correctly take into account the contributions of the neighbouring particles in the SPH approximation.

The approach adopted in this work is similar to what is done elsewhere (the so-called visibility method [1, 61, 72]). Each of the two new particles formed after fracture have its neighbouring list updated, respecting the main restriction that no virtual-edge connecting a target particle to any of its neighbours can intersect the fracture plane, the same also applies to the neighbours of the neighbouring particles of the cracked particles. Figure 8.4 illustrates this concept. The orientation of the cutting plane is obtained according to the failure criterion used, and it will be discussed in the next section.

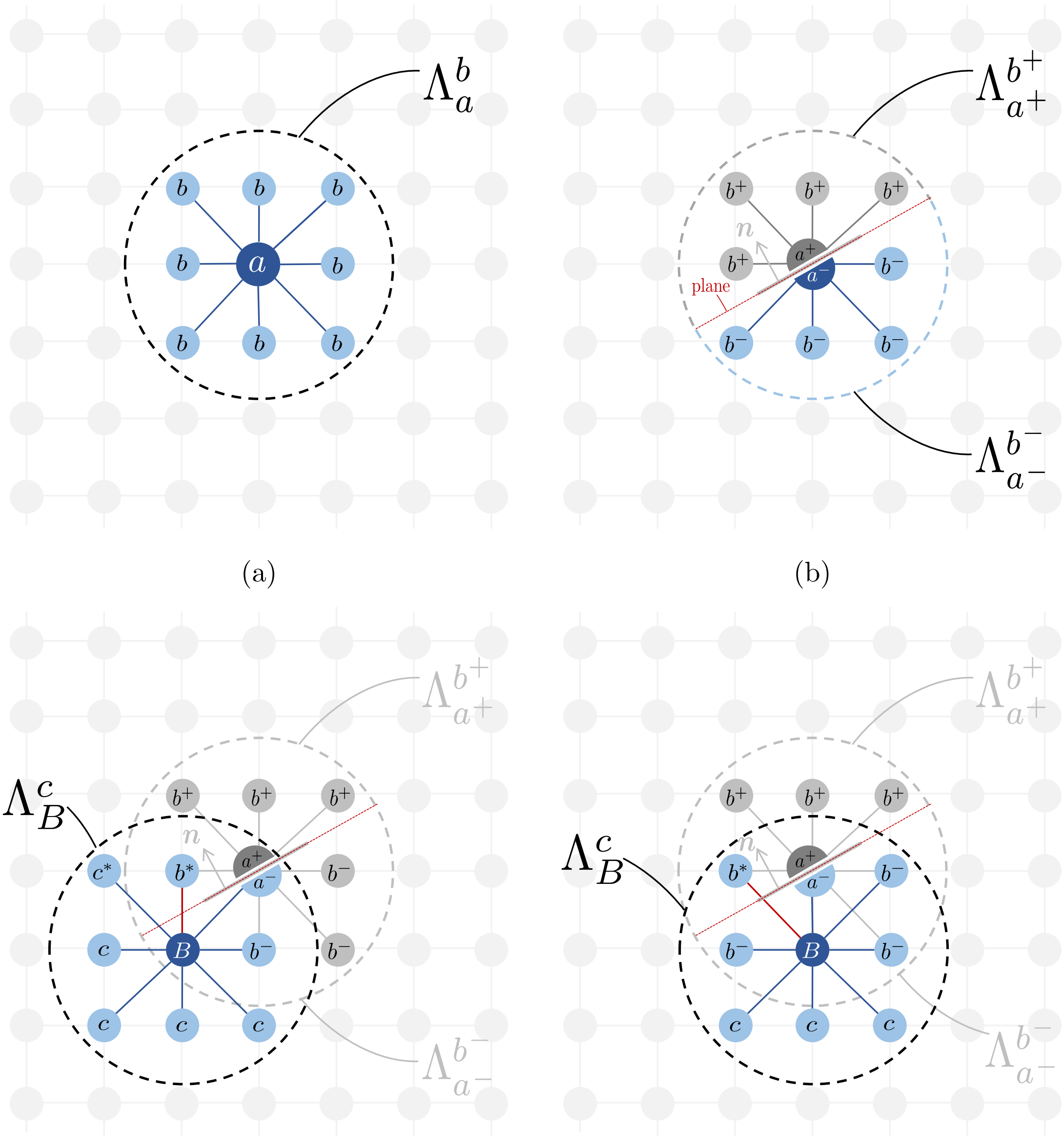

(a)

(b)

(c)

(d)

Figure 8.4: (a) Neighbouring particles of the cracked particle in the pre-fracture. (b) Neighbouring particles of the cracked particle in the post-fracture. (c) and (d) Neighbours of arbitrary particles in the vicinity of the cracked particle.

In figure 8.4a, $\Lambda_a^b$ represents the set of neighbouring particles $b$ belonging to the domain of influence of the target particle $a$ in the pre-fracture configuration. If particle $a$ reaches a failure threshold, it is split into two new particles $a^+$ and $a^-$, as represented in figure 8.4b. The neighbouring lists of the two new particles, as well as of the other particles lying within the set $\Lambda_a^b$, need to be redefined. For example, in figure 8.4b the target particle $a^+$ can only receive contributions of neighbouring particles $b^+$, i.e., neighbouring particles lying on the + side of the crack. The same concept applies to the target particle $a^-$, which can only take into account the neighbouring particles $b^-$. Moreover, a particle $b^+$ cannot have a particle $b^-$ as a neighbour as this would imply the intersection of the virtual-edge connecting the two particles with the fracture plane. Consider each of the particles $B$ highlighted in figures 8.4c and 8.4d, they need to be prevented of interacting with particles $b^*$ and vice-versa, i.e., the virtual-edge $\overline{Bb^*}$ needs to be eliminated. Notice however that the pair $\overline{Bc^*}$ is not removed, because particle $c^*$ lies outside of the domain of influence of the cracked particle $a$, i.e., particle $c^*$ was not a neighbour of particle $a$ and, in the present approach, the fracture region is limited to the cracked particle and its immediate neighbours.

Once fracture takes place, in order to define the neighbouring particles of $a^+$ and $a^-$ one can compute the dot product $(\boldsymbol{x}_b - \boldsymbol{x}_a) \cdot \boldsymbol{n}$ and classify in which side of the surface particle $b$ lies. On the other hand, to check if any two specific particles, say particle $b_1$ and particle $b_2$, fall on opposite sides of a crack surface centred at $a$, a possible approach is to find the intersection between the virtual-edge connecting the two particles and the cutting plane. This verification is done as soon as a new fracture surface is introduced, for all particles within the compact support of the cracked particle.

The intersection point is given as

$$\boldsymbol{x}_{\text{int}}\left(s_{\text{int}}\right) = \boldsymbol{x}_{b_1} + s_{\text{int}}\left(\boldsymbol{x}_{b_2} - \boldsymbol{x}_{b_1}\right), \tag{8.24}$$

where the intersection parameter $s_{\text{int}}$ is computed as

$$s_{\text{int}} = \frac{-\boldsymbol{n}_a \cdot \left(\boldsymbol{x}_{b_1} - \boldsymbol{x}_a\right)}{\boldsymbol{n}_a \cdot \left(\boldsymbol{x}_{b_2} - \boldsymbol{x}_{b_1}\right)}. \tag{8.25}$$

If $0 \leq s_{\text{int}} \leq 1$ the virtual-edge intersects the fracture plane. Notice that, in this approach the fracture plane cuts through the entire domain of influence of particle $a$. However, if desired, the fracture plane can be delimited by introducing an additional intersection criterion $\|\boldsymbol{x}_{\text{int}} - \boldsymbol{x}_a\| \leq \alpha r_a$. In this case, $r_a$ is the radius of a circle delimiting the fracture plane, computed as $r_a = \max_{b \in \Lambda_a^b}\left(\|\boldsymbol{x}_b - \boldsymbol{x}_a\|\right)$, and $\alpha$ is a scale factor.

Notice that once a particle has its list of neighbouring particles modified, a new smoothing length needs to be computed before corrected kernels and gradients are recomputed. The procedure is the same as the one performed for any (non-cracked) particle in the initial configuration, i.e., the distance between the target particle and its most distant neighbour, together with the smoothing factor $f_h$, will determine the new smoothing length (see equations 4.20 and 4.28 in chapter 4). The particle split discussed in this section is driven by the physics of the fracture phenomenon. The only purpose of splitting a particle in this formulation is to represent the fracture resorting to as few abstractions as possible (in contrast to enriched formulations [57, 59] or phase-field approaches[114]). The particle is split into two new particles. Conservation of mass, linear momentum and total energy are imposed. Even though not explored in this work, particle splits (refinements) such as those performed in

[115] or [61], could be performed prior to fracture, aiming at an increased accuracy at the crack front.

In order to illustrated a practical case, consider the schematic crack evolving in two steps, as illustrated in figure 8.5. In Step 1 particles $A$ and $B$ are cracked and need to be split. The pre-fracture and the post-fracture neighbouring particles for $A$ and $B$ are shown in figure 8.6. In Step 2, another two particles ($C$ and $D$) are also cracked, their neighbouring particles are highlighted in the pre and post-fracture in figure 8.7. Notice that once a particle is cracked, it is split into two daughter particles and each of these two new particles have their list of neighbours updated such that no virtual-edge intersects the fracture surface.

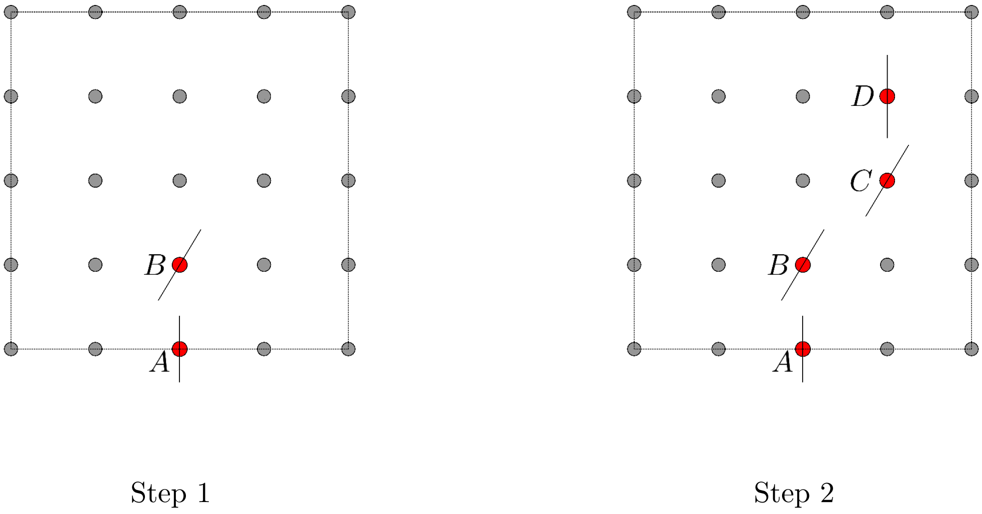

Step 1

Step 2

Figure 8.5: Sequence of time steps with cracked particles.

# 8.4 Failure criteria

## 8.4.1 Maximum principal stress criterion

For brittle fracture problems, the maximum principal stress criterion is considered to be valid [116]. This criterion can be represented as

$$f = \frac{\langle \sigma_{\max} \rangle}{\sigma^0_{\max}}, \tag{8.26}$$

where $\sigma^0_{\max}$ is a material parameter that defines the maximum allowable principal stress and the Macaulay bracket is used to imply that a purely compressive stress state does not initiate the fracture, i.e., $\langle \sigma_{\max} \rangle = 0$ if $\sigma_{\max} < 0$ and $\langle \sigma_{\max} \rangle = \sigma_{\max}$, where $\sigma_{\max} = \max(\sigma_1, \sigma_2, \sigma_3)$, with $\sigma_{1,2,3}$ being the principal stresses. Fracture is assumed to initiate when $f \geq 1$.

When the maximum principal stress criterion is used, the newly formed crack is always orthogonal to the maximum principal stress direction when the fracture criterion is satisfied.

A single particle is assumed to have a spherical shape, and therefore its volume satisfies $V = \frac{4}{3}\pi r^3$. With this assumption, the area of the fracture surface of a particle is given as $A_f = \frac{3V}{4r}$, where the radius $r = \left(\frac{3V}{4\pi}\right)^{\frac{1}{3}}$ delimits the local fracture surface.

## 8.5 Conclusion

This chapter presented a new dynamic fracture formulation that further extends the capabilities of the SPH framework developed in this work. A crack was represented as a set of contiguous cracked particles. A particle that achieved a failure criterion was split into two particles and the post-fracture velocities and deformation gradients were derived satisfying conservation of mass, linear momentum and total energy. An algorithm based on visibility methods was developed to split the SPH compact support without incurring in new particle searches. A standard cohesive law was imposed across the discontinuity in such a way that the dissipation matched the fracture energy.

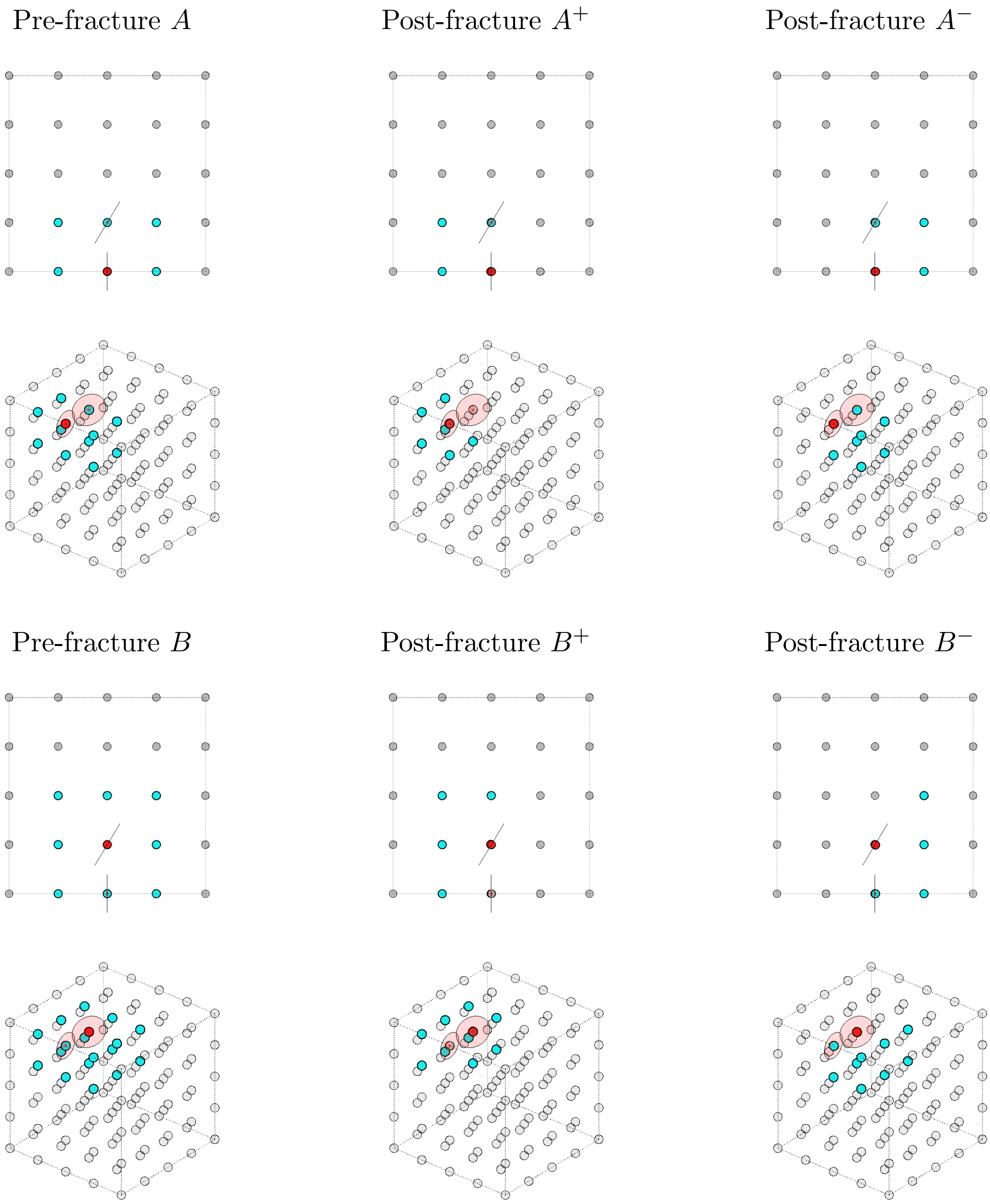

Figure 8.6: Domain of influence of cracked particles in step 1. First and second rows show different views of particle $A$ and its neighbours in the pre and post-fracture. Third and fourth rows show the same for particle $B$.

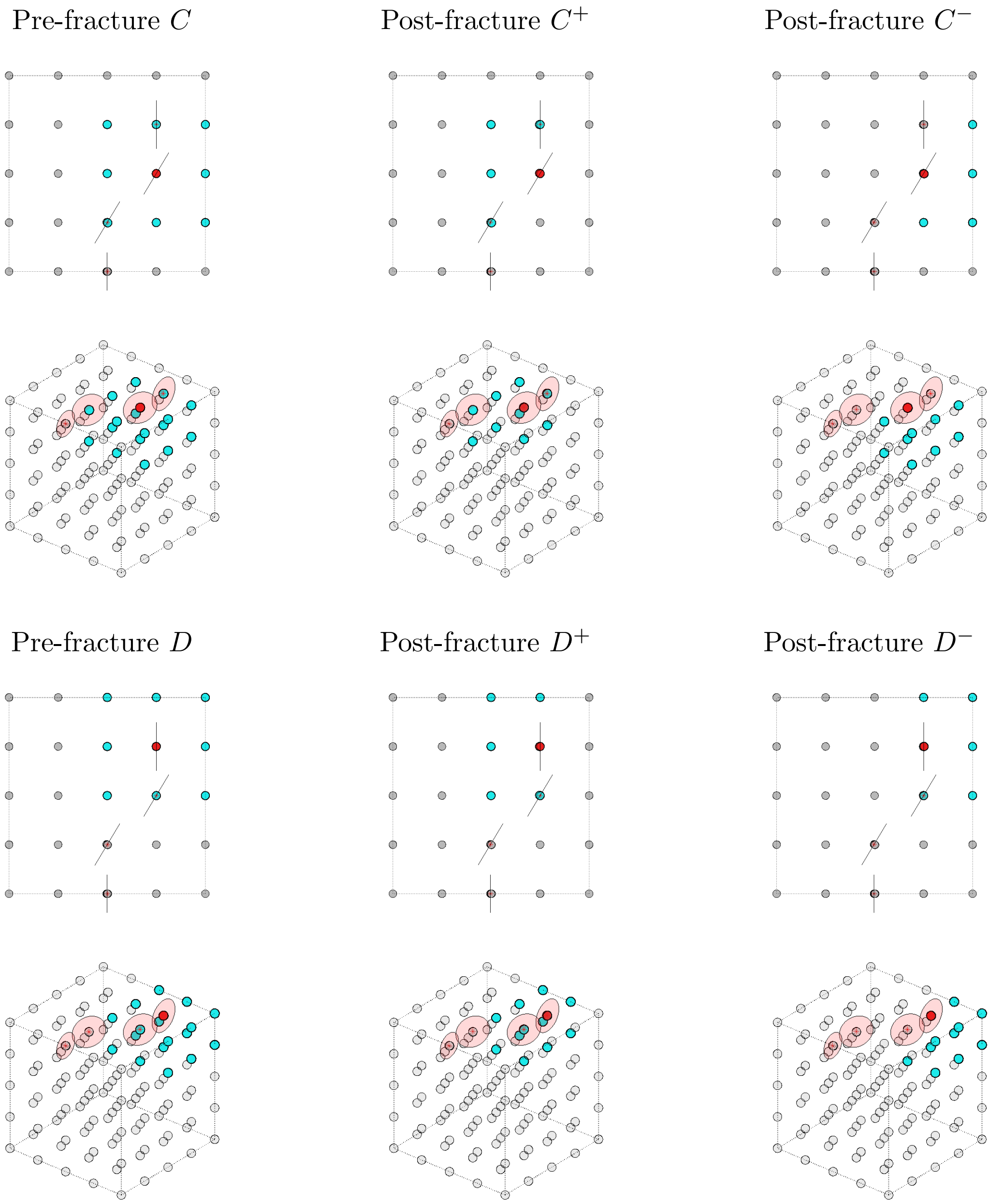

Figure 8.7: Domain of influence of cracked particles in step 2. First and second rows show different views of particle $C$ and its neighbours in the pre and post-fracture. Third and fourth rows show the same for particle $D$.

# Chapter 9

# Fracture mechanics numerical examples

## 9.1 Introduction

In this chapter, in continuation of the numerical examples presented so far, the potential of the formulation for applications in dynamic fracture is explored in classic 2D test cases. The obtained results are only briefly assessed aiming at checking the global behaviour of the formulation in dynamic fracture scenarios. Further investigations involving comparisons against experimental data (necessary for validation) were not carried out at this stage.

## 9.2 Mode-I dynamic fracture

This example illustrates the prediction of dynamic crack propagation in a plate, with an initiated crack, subjected to a tensile load. The objective is to test the particle splitting capability in a simple scenario and verify the behaviour of the algorithm with respect to the evolution of stresses and pressures as the crack propagates. The model presented herein consists of a two-dimensional (plane strain) rectangular plate with a length of $L = 0.2286\text{m}$ and width $W = 0.3048\text{m}$, the main characteristics of the model are illustrated in figure 9.1. Only half the domain is represented and appropriate symmetry conditions are applied. Notice in figure 9.1 that an initial crack with length 0.038m is introduced at the middle of the plate (half crack length appears in the figure). The tensile symmetric loading induces a mode I fracture in the specimen. Equal and opposite velocity boundary conditions were imposed in the horizontal ($X$) direction of the particles located at both ends of the plate:

$$V(t) = \begin{cases} \frac{V_0 t}{t_{\text{ramp}}} & t_{\text{ramp}} \geq t, \\ V_0 & \text{otherwise.} \end{cases} \tag{9.1}$$

with $V_0 = \pm 0.06\frac{\text{m}}{\text{s}}$ and $t_{\text{ramp}} = 1.96 \times 10^{-4}\text{s}$. A fixed $\alpha_{CFL} = 0.9$ was used for the simulations.

The particle distribution is uniform and a tributary volume distribution was used. One model (M1), containing 5741 particles, was studied. Notice that in the initial crack region (red line highlighted in figure 9.1) two particles occupy the same position

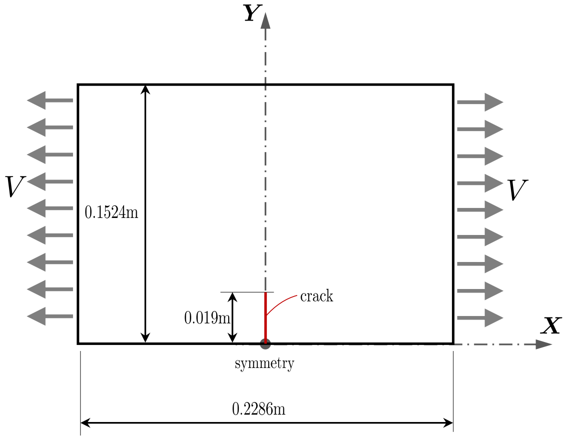

Figure 9.1: Mode I Crack propagation: tensile plate.

and do not interact with each other, representing a pre-existing discontinuity in the domain.

Initial density $\rho_0 = 2400\frac{\mathrm{kg}}{\mathrm{m}^3}$, Young's modulus $E = 31.37 \times 10^9 \frac{\mathrm{N}}{\mathrm{m}^2}$ and Poisson's ratio $\nu = 0.2$ were adopted as the material parameters for a nearly incompressible neo-Hookean constitutive model. The maximum principal stress failure criterion is used and the maximum allowable principal stress is $\sigma_0^{\max} = 10.45 \times 10^6 \frac{\mathrm{N}}{\mathrm{m}^2}$. Once the failure criterion is met, fracture takes place and triggers an update of the reference configuration. Dissipation across the discontinuity (fracture energy) is not taken into account in this example. A 2D cubic smoothing function is employed with a factor $f_h = 0.8$ for all the simulations.

Figure 9.2 shows results for the early stage of crack propagation and towards the end of the simulation. For different time-steps, the maximum principal stress is shown on the left and the corresponding fracture status (red for cracked particles and blue for non-cracked particles) is shown on the right. Figure 9.3 shows the magnitude of the velocity at different stages of the simulation. Finally, figures 9.4a and 9.4b show the evolution of the Y position and the magnitude of the velocity at the crack tip. Notice that the crack tip is identified as the non-cracked particle that interacts with the two sides of the crack, i.e., with the two sides of the last cracked particle.

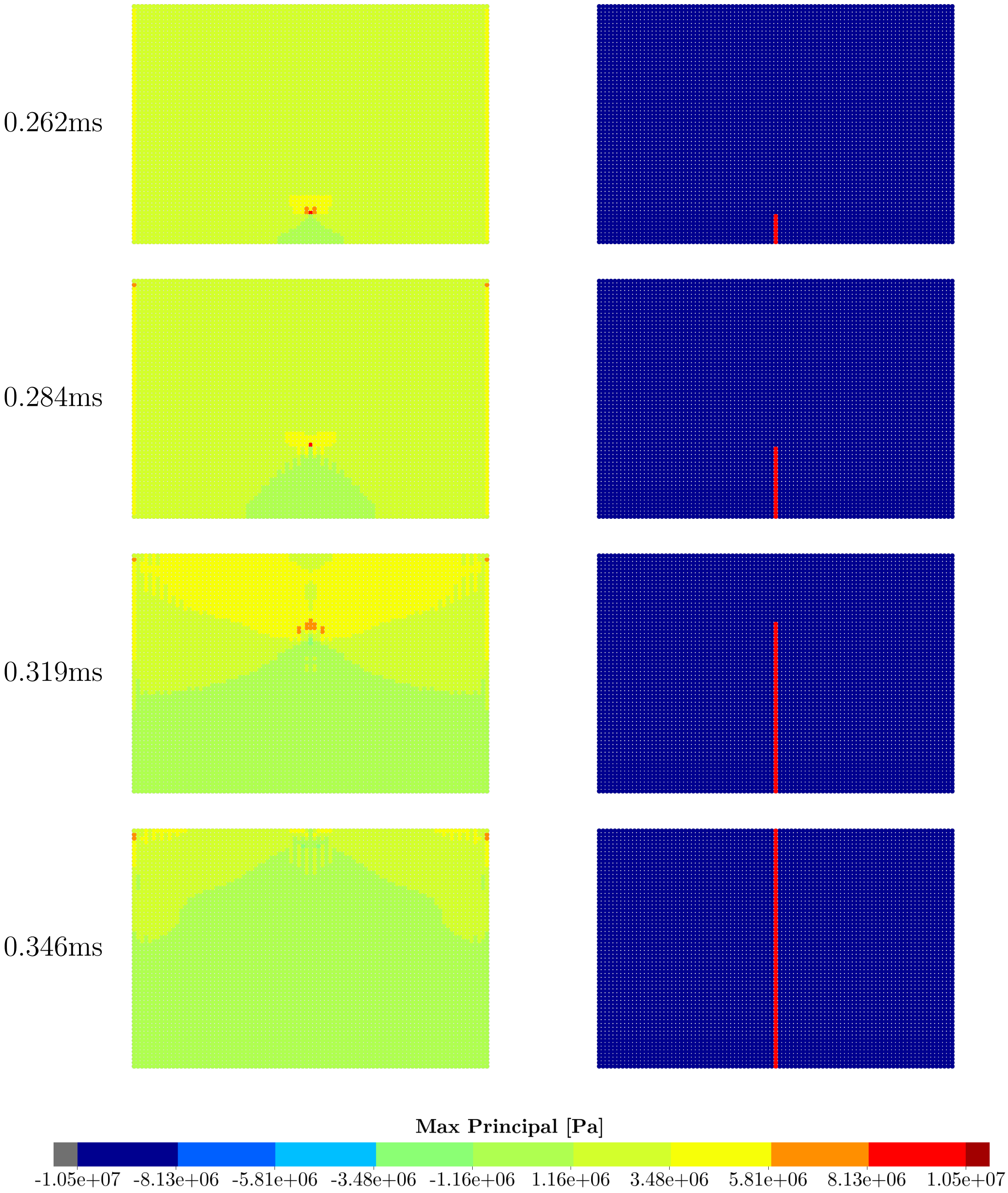

Figure 9.2: Mode I fracture: Maximum principal stresses on the left column and fracture status (cracked particles in red, non-cracked in blue) on the rigth.

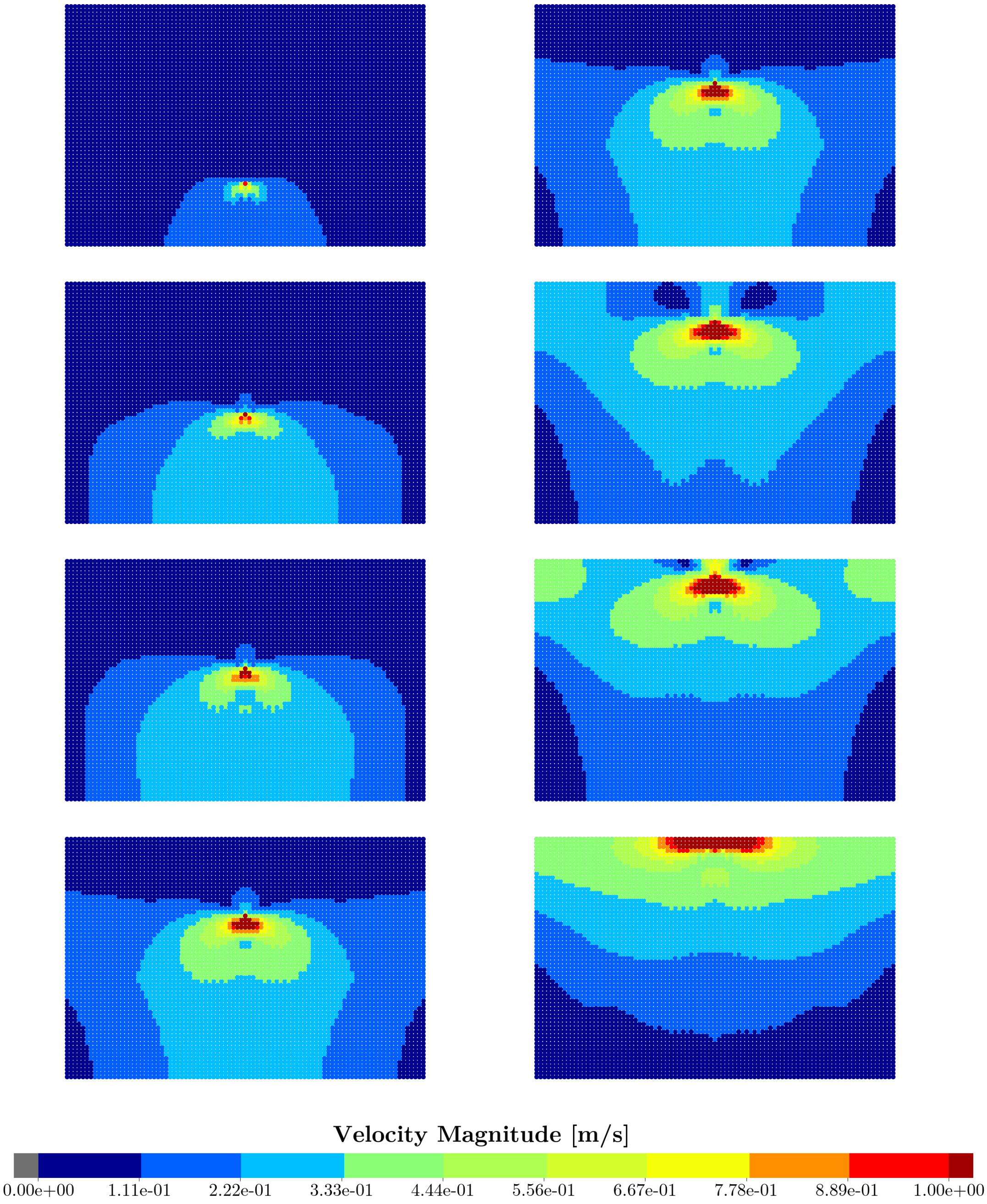

Figure 9.3: Mode I fracture: Magnitude of velocity at times {0.280, 0.298, 0.306, 0.316, 0.326, 0.330, 0.338, 0.346} ms (from top to bottom and left to right).

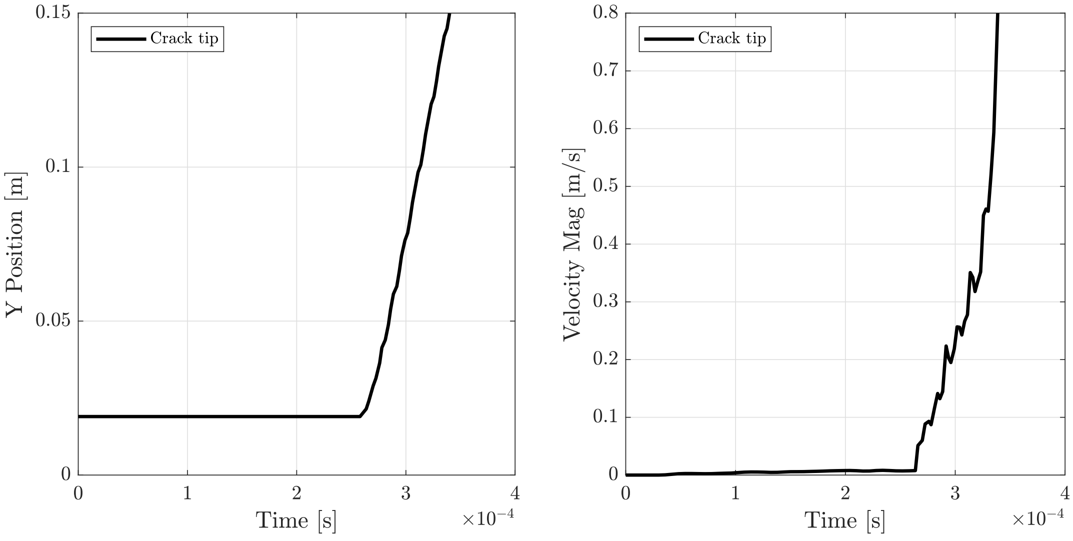

(a) (b)

Figure 9.4: Mode I crack propagation. (a) Y position of the crack tip. (b) Velocity magnitude of the crack tip.

## 9.3 Dynamic shear failure

This example illustrates the prediction of dynamic crack propagation in a plate, with an edge crack, subjected to a high rate shear impact load. Two versions of this experiment are widely studied in the literature and are known either as the Kalthoff-Winkler experiment (double notched plate) or the Zhou–Rosakis–Ravichandran experiment (single notched plate) [117]. Many authors have studied the problem in a variety of computational fracture mechanics approaches [1, 69, 114, 117–126]. The model presented herein consists of a double notched plate and follows the characteristics presented in [69, 114], i.e., a two-dimensional (plane strain) rectangular plate with a length of $L = 0.200$m, and width $W = 0.100$m, the main characteristics of the model are illustrated in figure 9.5. Notice in figure 9.5 that an initial crack with length 0.050m is introduced at the left edge of the plate. Only half the domain is represented with the particles located at the bottom face subjected to symmetric boundary conditions (movement constrained in the $Y$ direction) and the lower left part of the specimen receiving an impulse load in the horizontal ($X$) direction, modelled as a prescribed velocity as:

$$V(t) = \begin{cases} \frac{V_0 t}{t_{\text{ramp}}} & t_{\text{ramp}} \geq t, \\ V_0 & \text{otherwise.} \end{cases} \tag{9.2}$$

with $V_0 = 16.5\frac{\text{m}}{\text{s}}$ and $t_{\text{ramp}} = 1.0 \times 10^{-7}$s. A fixed $\alpha_{CFL} = 0.9$ was used for the simulations.

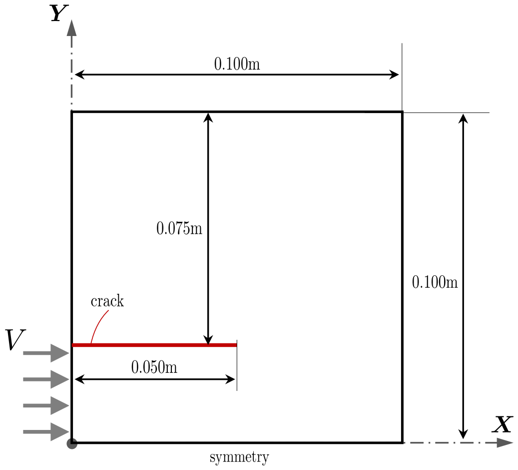

Figure 9.5: Dynamic shear failure.

The particle distribution is uniform and a tributary volume distribution was used. Two models (M1 containing 451 particles and M2 containing 1701 particles), were studied. Notice that in the initial crack region (red line highlighted in figure 9.5) two particles occupy the same position and do not interact with each other, representing a pre-existing discontinuity in the domain.

Initial density $\rho_0 = 8000\frac{\text{kg}}{\text{m}^3}$, Young's modulus $E = 190 \times 10^9\frac{\text{N}}{\text{m}^2}$ and Poisson's ratio $\nu = 0.3$ were adopted as the material parameters for a nearly incompressible neo-Hookean constitutive model. The maximum principal stress failure criterion is used and the maximum allowable principal stress is $\sigma_0^{\max} = 1.07 \times 10^9 \, \frac{\mathrm{N}}{\mathrm{m}^2}$. Once the failure criterion is met, fracture takes place and triggers an update of the reference configuration. A fracture energy of $2.213 \times 10^4 \, \frac{\mathrm{N}}{\mathrm{m}}$ was taken into account. The energy dissipation across the discontinuity is chosen to match the fracture energy via a standard implementation of a cohesive law, as proposed in [69]. A 2D cubic smoothing function is employed with a factor $f_h = 0.8$ for all the simulations.

Figure 9.6 shows results for the simulation at the early stage of crack propagation and towards the end of the simulation. The maximum principal stress is shown on the left and the corresponding fracture status (red for cracked particles and blue for non-cracked particles) is shown on the right. The average crack propagation angle is 65° measured with respect to the $X$ axis, which is in perfect agreement with the results reported in [69] and [114]. Only the pre-existing crack was allowed to propagate in this model, and crack branching was not permitted. Further investigations into this and other dynamic fracture examples are under preparation and will appear in future author's publications.

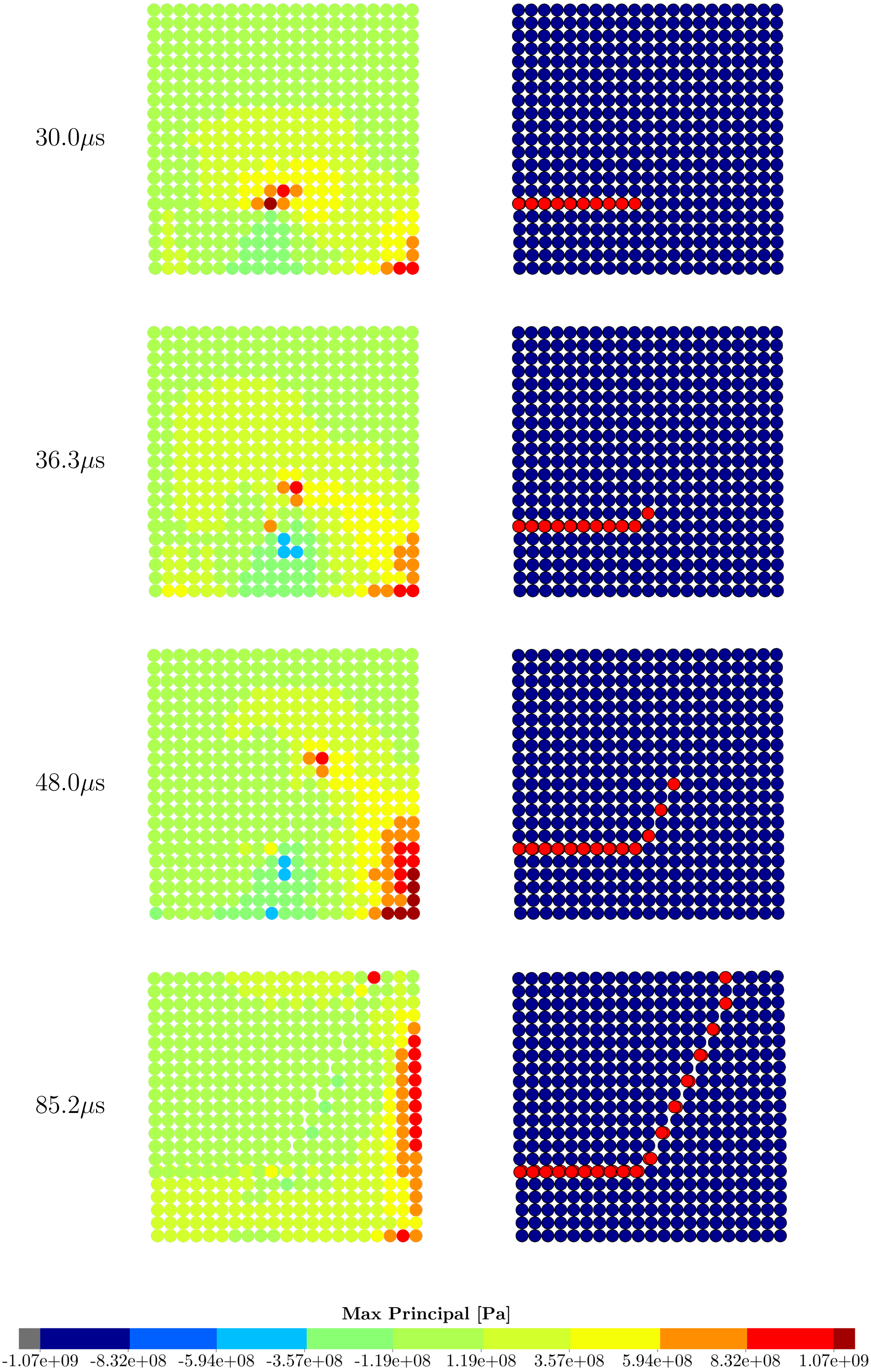

Figure 9.6: Dynamic shear failure Model M1: Maximum principal stresses on the left column and fracture status (cracked particles in red, non-cracked in blue) on the rigth.

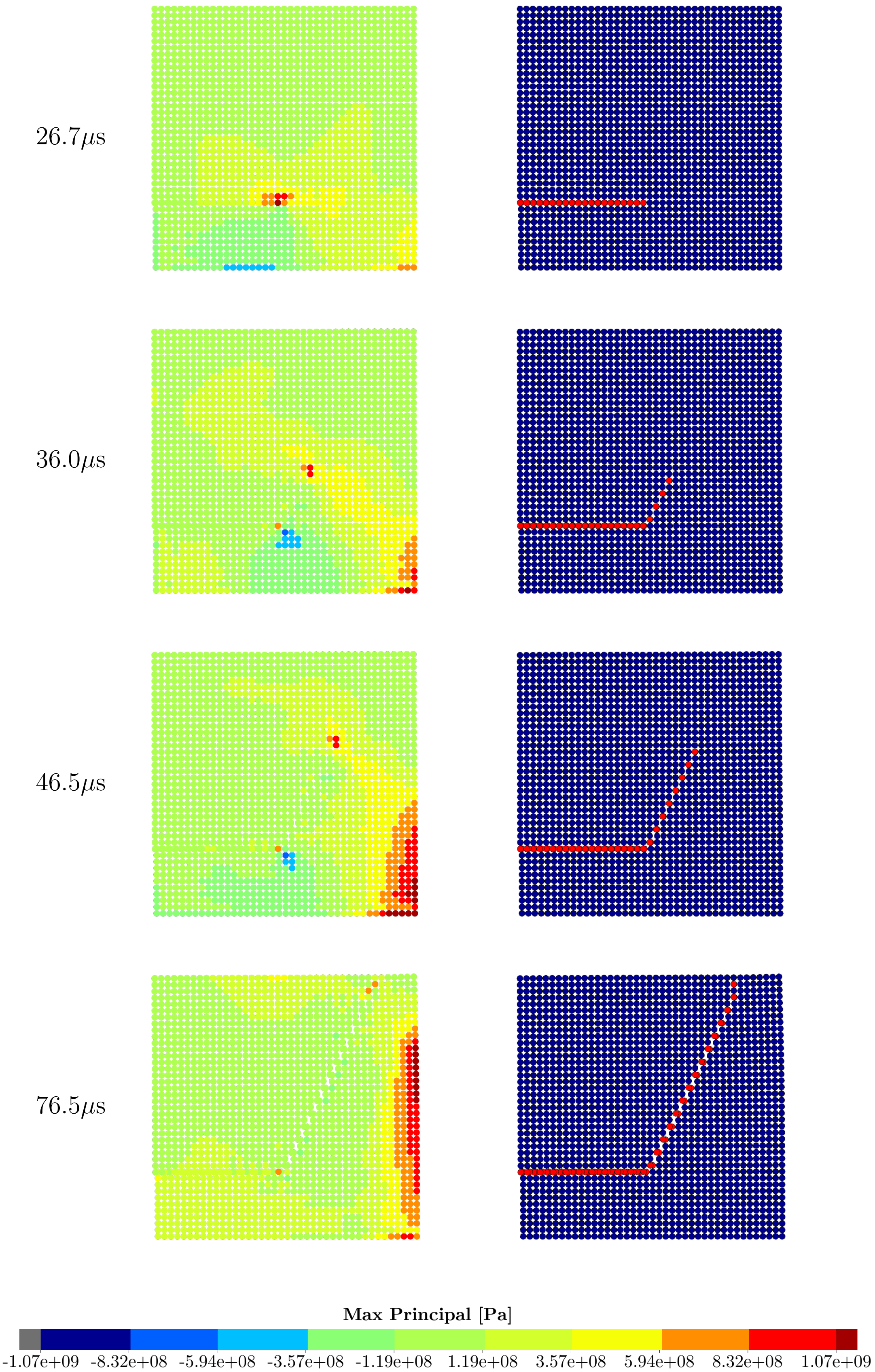

Figure 9.7: Dynamic shear failure Model M2: Maximum principal stresses on the left column and fracture status (cracked particles in red, non-cracked in blue) on the rigth.

## 9.4 Mixed-mode dynamic fracture

This example illustrates the prediction of dynamic crack propagation in a beam with an offset edge crack subjected to an impact load. Experimental data for this classic benchmark problem is available in [127], many authors have studied the same problem in computational mechanics ([1, 119, 122, 124, 125, 128–130]). The model presented herein consists of a two-dimensional (plane strain) rectangular beam with a length of $L = 0.2286$m and width $W = 0.0762$m, the main characteristics of the model are illustrated in figure 9.8. The distance between supports is 0.2032m. Regarding the boundary conditions, a particle located at 0.0127m from the left edge had its $X$ and $Y$ movements restricted (pinned) throughout the simulation. From the other side, i.e., the particle located at 0.0127m from the right edge of the beam, had its movement in the $Y$ direction restricted (roller). Notice in figure 9.8 that an initial crack with length 0.019m is introduced with an offset of 0.06604m measured from the midspan of the beam. This induces a mixed mode fracture in the specimen. To simulate the impact load, a velocity boundary condition was imposed in the vertical ($Y$) direction of the top particles located at the midspan:

$$V(t) = \begin{cases} \frac{V_0 t}{t_{\text{ramp}}} & t_{\text{ramp}} \geq t, \\ V_0 & \text{otherwise.} \end{cases} \tag{9.3}$$

with $V_0 = 0.06\frac{\text{m}}{\text{s}}$ and $t_{\text{ramp}} = 1.96 \times 10^{-4}$s. A fixed $\alpha_{CFL} = 0.9$ was used for the simulations.

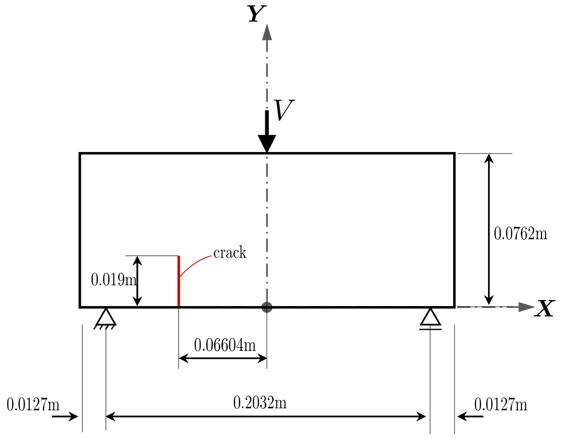

Figure 9.8: Crack propagation: Beam under impact load.

The particle distribution is non-uniform and a tributary volume distribution was used. The regions surrounding the initial crack, as well as the region of crack propagation, is refined. Only one model refinement (M1) containing 9465 particles was studied. Notice that in the initial crack region (red line highlighted in figure 9.8) two particles occupy the same position and do not interact with each other, representing a pre-existing discontinuity in the domain.

Initial density $\rho_0 = 2400\frac{\mathrm{kg}}{\mathrm{m}^3}$, Young's modulus $E = 31.37 \times 10^9 \frac{\mathrm{N}}{\mathrm{m}^2}$ and Poisson's ratio $\nu = 0.2$ were adopted as the material parameters for a nearly incompressible neo-Hookean constitutive model. The maximum principal stress failure criterion is used and the maximum allowable principal stress is $\sigma_0^{\max} = 10.45 \times 10^6 \frac{\mathrm{N}}{\mathrm{m}^2}$. Once the failure criterion is met, fracture takes place and triggers an update of the reference configuration. A fracture energy of $19.58\frac{\mathrm{N}}{\mathrm{m}}$ was taken into account. The energy dissipation across the discontinuity is chosen to match the fracture energy via a standard implementation of a cohesive law, as proposed in [69]. A 2D cubic smoothing function is employed with a factor $f_h = 0.8$ for all the simulations.

Figure 9.9 shows results for the simulation at the early stage of crack propagation and towards the end of the simulation. The maximum principal stress is shown on the left and the corresponding fracture status (red for cracked particles and blue for non-cracked particles) is shown on the right. The crack propagates (initially) at an angle of 63° measured with respect to the $X$ axis. Figure 9.10 shows similar results, but with a zoom in the crack tip region and with the colour legend set to half of the maximum allowable principal stress, so that it is easier to visualise the stress distribution around the crack tip.

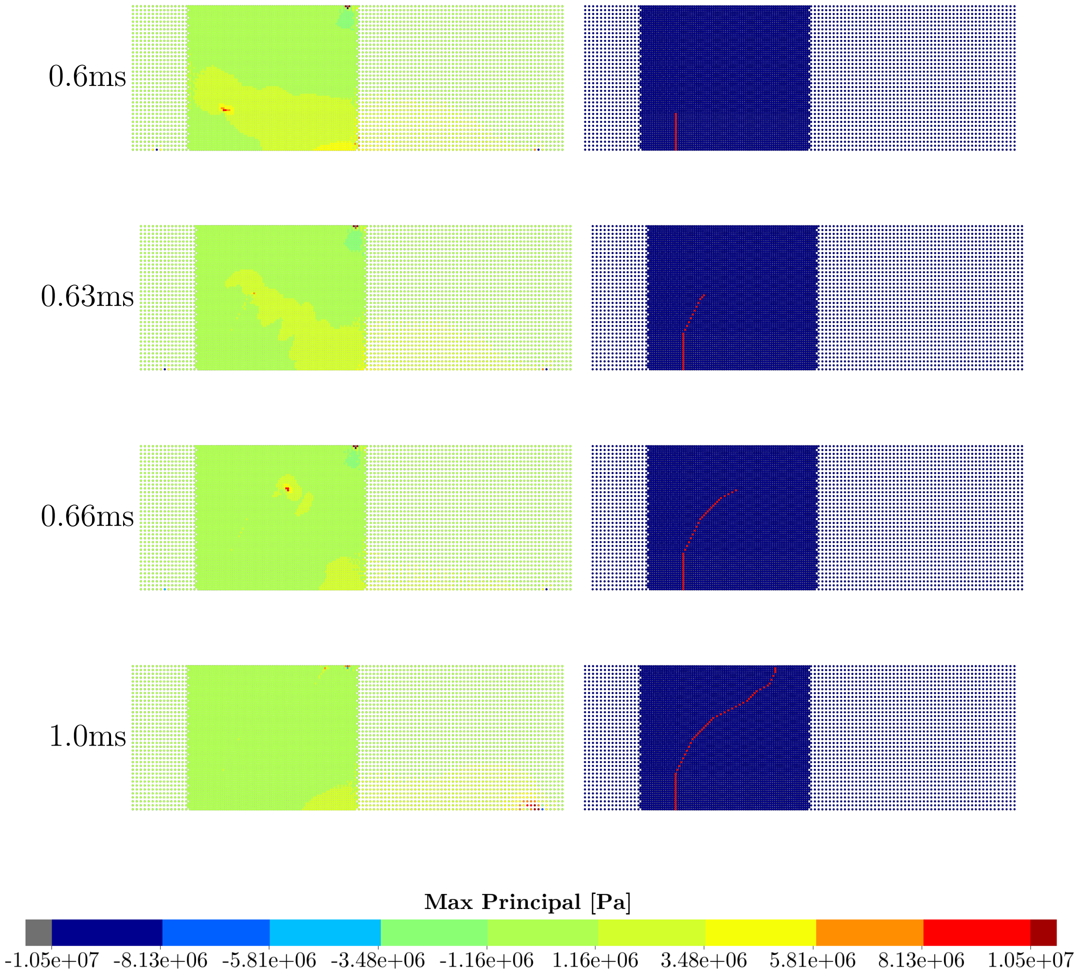

Figure 9.9: Mixed-mode dynamic fracture: Maximum principal stresses on the left column and fracture status (cracked particles in red, non-cracked in blue) on the rigth.

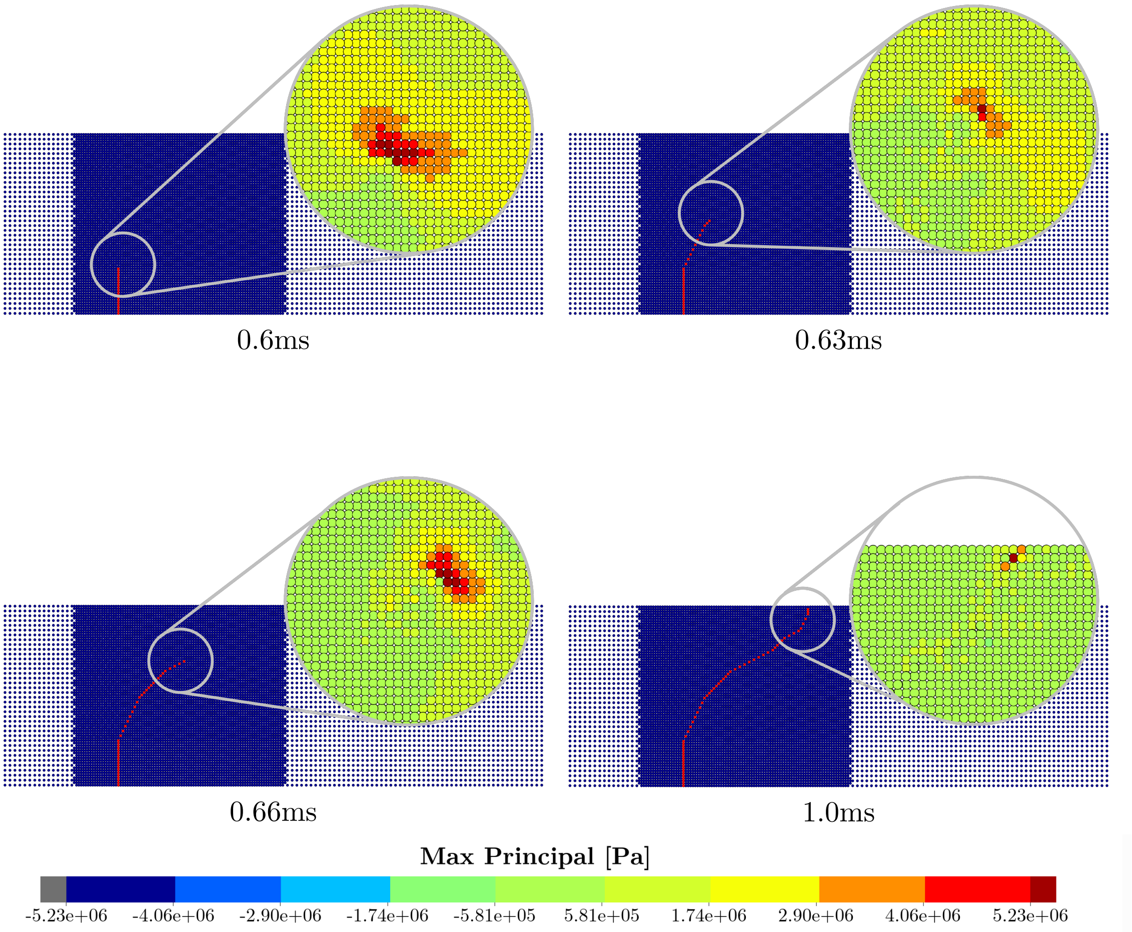

0.6ms

0.63ms

0.66ms

1.0ms

Figure 9.10: Mixed-mode dynamic fracture: Maximum principal stresses around the crack tip. Colour legend set to half of maximum allowable principal stress $\sigma_0^{\max}$ to ease visualisation.

These preliminary results show that the framework is suitable for mixed-mode dynamic fracture scenarios. The crack pattern, as well as the initial propagation angle of 63° are in good agreement with results available in the literature.

# Part V

# Conclusions

# Chapter 10

# Concluding Remarks

## 10.1 Conclusions

In this work, a new updated reference Lagrangian Smooth Particle Hydrodynamics algorithm for the analysis of large deformation elasticity and elasto-plasticity has been presented. Isothermal and thermally-coupled cases were considered. The new stabilised updated reference Lagrangian SPH framework is aimed to be a robust alternative tool for computer simulations in fast solid dynamics problems, prepared for the endeavour of handling problems with topological changes such as dynamic fracture. The Smooth Particle Hydrodynamics method is not new. Even the first applications to the context of solids and structures, which came much later, are no less than thirty years old. Therefore, an enormous amount of enhancements to the original technique have already been made. Some of these contributions were cited in this work, but by no means in an exhaustive manner. The purpose of the following paragraphs is to put together several observations about the main features that make the formulation proposed in this work unique and advantageous.

To start with, the motivation for developing an updated Lagrangian formulation came from the interest in realistic simulation of problems involving topological changes, namely dynamic fracture. The initial undeformed configuration of a body does not know anything about the new boundaries that will be formed when a crack propagates. The most natural and realistic manner to take this into account, is to look at the current configuration, where the crack actually exists. Updated Lagrangian formulations serve to this purpose, i.e., to use the information of the current configuration in the computations.

However, to work on the current configuration all the time (purely updated Lagrangian formulation) is computationally expensive. The possibility of updating the reference configuration only when required is appealing and was proposed for a displacement-based formulation in [24]. In the context of SPH, an update would be required, for example, when fracture or self contact or adaptive particle refinements take place. That is, any physically or numerically motivated event that requires a modification in the SPH compact support (by adding/subtracting particles to/from it) implies in the need of an update. An appropriate multiplicative decomposition of the conservation variables made in this work has resulted into an amenable mixed set of conservation equations which can be degenerated into a total Lagrangian system or into a purely updated Lagrangian system. This means that, in the proposed method, updates can be performed only when desired and this can be, for example, when a particle in the model is split (fracture). This feature was explored in several examples, including all test cases from chapter 9, where updates were triggered by fracture (particle split), but also in the bending column (6.2.2) and necking bar (6.3.2) examples, where the frequency of the updates was arbitrarily chosen.

In this work, the motion of a solid body was described by a mixed-based set of first order conservation laws. Namely, the equation of conservation of linear momentum and three geometric conservation laws (for the deformation gradient, its cofactor and its determinant). In a thermal context, the system is supplemented with the conservation equation of the total energy. This system of equations was explored before [27, 76], but never in an updated reference Lagrangian context. Out of the three geometric conservation laws, only the conservation law for the deformation gradient is strictly necessary, ensuring that strains and displacements converge with the same accuracy. The other two geometric conservation laws are optional and add flexibility to the scheme, allowing for example applications in the nearly incompressible regime. In the twisting column example (6.2.2) the Poisson's ratio was increased up to 0.4995 and no pressure instabilities were observed. Even though incompressibility is also present in the elasto-plastic numerical examples, the extra conservation laws are not necessary since the physical plastic dissipation by itself avoids the development of pressure instabilities.

The structure of the system of first-order conservation laws allowed the development of one of the most remarkable features of the framework: the upwinding Riemann-based stabilisation algorithm. This stabilisation technique was actually already used in the Total Lagrangian formulation of [27] and their outstanding results motivated the present work. Here, consistent and locally conservative stabilisation was derived in terms of the newly introduced incremental conservation variables and their work conjugates. The stabilisation tensors were derived in terms of physical pressure and shear wave speeds, requiring no artificial stabilisation parameters. A kernel-based linear reconstruction of the neighbouring states of the Riemann values was proposed to guarantee second order accuracy in space. With no exceptions, all the numerical examples presented in this work demonstrated the robustness of the stabilisation technique. From the simple bending column (6.2.2) with few or several updates of the reference configuration, through the challenging extremely large deformation of the twisting column (6.2.2) and punch tests (6.2.3,7.3), to the complex formation of shear bands in elasto-plasticity (6.3.3), the numerical dissipation was shown to be consistently added to the system in the correct amount to avoid instabilities, without adversely affecting the solution.

The higher accuracy resulting from the mixed-based formulation, combined with the fact that kernels and gradients of kernels were corrected to satisfy constant and linear completeness, permitted the use of coarser particle distributions, still maintaining good resolution of the results. Moreover, only a small number of particles per compact support were needed. In general, a particle in a standard 3D model will have between 8 (corner particle) and 27 (centre particle) neighbours. Since the SPH approximation requires looping over neighbouring particles, the less neighbours, the faster the algorithm will be. Another aspect of this work, is that in the simulation of solids, even for a truly updated Lagrangian formulation, there is no need to perform new searches of neighbouring particles unless a topological change took place. That is, the fact that the computational domain is deformed, does not imply that the list of neighbouring particles needs to be changed.

There should be no impediment for performing updates, and therefore recomputing kernels and gradients, in the deformed configuration while keeping the same original list of neighbours. Actually, performing new searches using standard spherical compact supports in deformed solids discretised with coarse particle distributions would potentially lead to inaccuracies. In particular, in the case of anisotropic changes in volume, a large number of particles could be present in one direction, while few or none particles would be found in other directions, leading to poor approximations. Keeping the original neighbours fixed in such scenario would result in a similar problem, i.e., the particles could be very far from each other in one direction, and very close in other, leading to potential discrepancies in the computation of gradients. To be able to keep the list of neighbours unchanged and still recompute kernels and gradients in deformed configurations maintaining good resolution, four different ways of combining anisotropic compact supports with SPH corrections were proposed in this work. The four options were shown to perform equally well across the variety of test cases performed. However, it is worth noticing that only two of these proposals are capable of handling topological changes, if they take place.

In this work a variety of constitutive models well-known from the literature were applied in both isothermal and thermal contexts. In elasticity a nearly-incompressible neo-Hookean model was considered. For elasto-plasticity a classic implementation of a Hencky-based von Mises model was chosen and applied with linear, nonlinear and also with the Johnson-Cook hardening laws. In the thermal context, the models were enhanced with the Mie-Grüneisen equation of state, allowing the coupling between pressure and temperature. It is worth noticing that the temperature update was possible thanks to the introduction of the conservation law for the total energy. Even though no special adaptations were made in the stabilisation algorithm for thermal scenarios, it is worth pointing out that the thermal examples were solved extremely well. When thermal shock was involved, such as in the thermal L-shaped block (7.2) it was observed that even though the pressure was well computed for coarse models, they did not perform so well from a thermal perspective. However, successive model refinements showed that the formulation can handle such problems if proper particle distributions are used. Moreover, the same problem when set-up without the thermal shock faced no difficulties even with the coarsest model (figure 7.10b).

Time integration is a vast research field and it was far from the scope of this project to go in such direction. Therefore, a well established [94] three-stage Runge-Kutta time integration method was implemented, resulting in values of the CFL stability restriction close to one. The use of such time integrator represents an improvement for this type of mixed-based SPH formulation. Previous works [27, 76] based on the same set of first order conservation laws employed a two-stage Runge-Kutta time integrator, having their CFL number restricted to 0.3. Moreover, the implementation of the new time integrator also implied in developing a new compatible angular momentum preserving algorithm, a capability that was demonstrated in the L-shaped block example, in both isothermal (6.2.4) and thermal (7.2) contexts. The computation of stable time increments as implemented in this work relies on the current deformed configuration (equation 5.40), a fact that may lead to very small time increments in advanced stages of the deformation process if the particle spacing gets very small. The proposed formulation also has the capability of working with non-uniform initial particle distributions, such as the ones used for the necking bar

(6.3.2) and strain localisation (6.3.3) examples. However, it must be noticed that this local refinement will also affect the size of the stable time increment.

Dynamic fracture is a complex not well understood phenomenon and computational dynamic fracture is relatively new. The formulation proposed in this work has a minimum level of abstractions and is established upon simple concepts. The objectives were to gain an initial understanding of this phenomenon and to evaluate the applicability of the proposed formulation to this context. The spark for fracture was chosen to be based on the maximum principal stresses, i.e., once the tensile maximum principal stress at a particle achieves a material dependent threshold, fracture takes place. This verification was performed locally per particle, meaning that the maximum principal stress of each particle was verified against the failure criterion. If a particle violated the criterion, it was split into two particles and the orientation of the fracture surface was given by the corresponding maximum principal direction. This is a very natural way of thinking about fracture, once the material cannot resist the applied stresses, it physically breaks.

With two new particles being created in the model, post-fracture velocities and deformation gradients had to be computed locally, and this was done ensuring satisfaction of conservation of mass, linear momentum and total energy. It was assumed that the fracture surface cuts through the entire compact support of the split particle. Therefore, a special treatment based on visibility methods was needed to take this into account. However, even for this case no new searches of neighbouring particles were needed, the approach taken in this work consisted of eliminating the interaction between particles that violated the visibility criterion. This process is purely geometric and independent of the formulation. Given a cloud of particles that interact with each other within a compact support and a surface of arbitrary orientation that cuts this compact support in two parts, the task was to find the pairs of particles that, if connected, would cross the surface. These particles must be prevented of interacting, i.e., they must be removed from each other's lists of neighbours. However, this is by no means of trivial implementation when 3D non-uniform particle distributions are considered in scenarios of complex dynamic fracture with fracture surfaces appearing anywhere in any orientation. The methodology proposed in this work was well suited to handle the 2D examples performed herein and can potentially be expanded for 3D applications. However, this was beyond the objectives of this work.

The entire framework presented in this thesis was implemented in MATLAB R2018b. All the examples presented were simulated using such implementation. Evidently, a MATLAB code created during PhD studies has no intentions of competing in computational performance. However, it is worth pointing out that the formulation imposes no limitations in terms of the size of the model (number of particles) or complexity of the simulated geometries. A fairly large model (around 170k particles) of the punch block was simulated (7.3) and its geometry is notably more complex than that of the other benchmarks studied. All examples were extensively detailed with the purpose of demonstrating the potential of the framework and also allowing reproduction by future readers. Great attention was given in reporting energies and strictly monitoring the numerical dissipation on each model. Many other quantities such as stresses, strains, pressure, etc. were reported too. This is of fundamental importance in order to demonstrate the consistency of the scheme. All the results obtained with this framework were very robust, correlated well with previously published results when available and were physically sound according to the hypothesis assumed for each case.

## 10.2 Recommendations for further research

As suggestions of continuation of this work, the following topics are strongly encouraged:

- Exploring the framework further in thermo-mechanical applications, in particular in the context of elasto-plastic and visco-plastic constitutive models. This topic was only briefly explored in this work. Nevertheless, due to its outstanding stability properties, the formulation is expected to perform extremely well in the case of thermally-coupled problems, from both the continuum and numerical standpoints. Applications in manufacturing processes such as hot forming, hot machining and friction welding would potentially benefit of the advantages of a meshless method, due to the extremely large level of deformations involved in these processes. Moreover, complex phenomena such as material removal (separation) and melting are involved in the later two. Therefore, an updated Lagrangian formulation would be required. The fundamental ingredients for moving in such direction were developed in this work, i.e., the updated Lagrangian formulation with thermal and fracture capabilities. The Johnson-Cook model included in the framework would be adequate for such applications. However, computational contact mechanics was not approached in this work and would be necessary for those applications.

- Developing the framework further for more complex applications in dynamic fracture. Firstly, from the point of view of the particle splitting algorithm, which may be extended to the context of 3D applications and also include adaptive local particle refinement for the fracture region. This would open-up a broader range of possible applications, including fragmentation, and also enhance the robustness of the method by ensuring that a sufficient number of neighbouring particles is always available for the cracked particles. A groundbreaking research topic would be one involving the developments made in this work and Fluid Structure Interaction (FSI). A vast spectrum of applications would be available, with shock-wave induced fracture and fragmentation probably being one of great interest. Evidently military applications would be interesting, but medical sciences is also appealing, the problem of comminution of kidney stones in extracorporeal shock-wave lithotripsy could be better understood via such numerical simulations. The essential ingredients from the solid standpoint were developed in this work, but the topic of fluids and a possible interaction was not considered.

- Implementing the formulation in an optimised SPH environment, such as SPHysics [92, 131] or DualSPHysics [132]. This would certainly open-up a wider range of applications taking advantage of the latest technology in multithreading, parallel computing and possibly graphics processing units (GPU) acceleration.

# Part VI

# Appendices

# Appendix A

# Mathematical foundations

## A.1 Introduction

This appendix summarises the mathematical concepts used throughout this work.

For general purposes, let $\boldsymbol{u}$, $\boldsymbol{v}$ and $\boldsymbol{x}$ denote arbitrary vectors in the three dimensional Euclidean space

$$\boldsymbol{u} = \begin{bmatrix} u_1 \\ u_2 \\ u_3 \end{bmatrix}, \qquad \boldsymbol{v} = \begin{bmatrix} v_1 \\ v_2 \\ v_3 \end{bmatrix}, \qquad \boldsymbol{x} = \begin{bmatrix} x_1 \\ x_2 \\ x_3 \end{bmatrix}. \tag{A.1}$$

In addition, let $\boldsymbol{P}$ and $\boldsymbol{S}$ be second-order tensors, which can be arranged in the form of $3 \times 3$ matrices as

$$\boldsymbol{P} = \begin{bmatrix} P_{11} & P_{12} & P_{13} \\ P_{21} & P_{22} & P_{23} \\ P_{31} & P_{32} & P_{33} \end{bmatrix}, \qquad \boldsymbol{S} = \begin{bmatrix} S_{11} & S_{12} & S_{13} \\ S_{21} & S_{22} & S_{23} \\ S_{31} & S_{32} & S_{33} \end{bmatrix}. \tag{A.2}$$

The same for the second-order tensors $\boldsymbol{A}$, $\boldsymbol{B}$ and $\boldsymbol{C}$.

## A.2 Scalar, cross and tensor products

The geometric definition of the scalar (or inner) product of two vectors in the three dimensional Euclidean space is

$$\boldsymbol{u} \cdot \boldsymbol{v} = \|\boldsymbol{u}\| \|\boldsymbol{v}\| \cos\theta, \tag{A.3}$$

where $\theta$ is the angle between $\boldsymbol{u}$ and $\boldsymbol{v}$. The inner product can be expressed using index notation as

$$\boldsymbol{u} \cdot \boldsymbol{v} = u_i v_i. \tag{A.4}$$

A geometric definition can also be provided for the cross (or vector) product of two vectors as

$$\boldsymbol{u} \times \boldsymbol{v} = \|\boldsymbol{u}\| \|\boldsymbol{v}\| \sin\theta \boldsymbol{n}, \tag{A.5}$$

where $\theta$ is the angle between $\boldsymbol{u}$ and $\boldsymbol{v}$ and $\boldsymbol{n}$ is a unit vector perpendicular to the plane containing $\boldsymbol{u}$ and $\boldsymbol{v}$. Alternatively, the cross product can be expressed as the following determinant

$$\boldsymbol{u} \times \boldsymbol{v} = \begin{vmatrix} \boldsymbol{e}_1 & \boldsymbol{e}_2 & \boldsymbol{e}_3 \\ u_1 & u_2 & u_3 \\ v_1 & v_2 & v_3 \end{vmatrix}, \tag{A.6}$$

where $\boldsymbol{e}_1, \boldsymbol{e}_2$ and $\boldsymbol{e}_3$ denote three unit base vectors.

The components of the cross product can be expressed using index notation as

$$(\boldsymbol{u} \times \boldsymbol{v})_i = \varepsilon_{ijk} u_j v_k, \tag{A.7}$$

where $\varepsilon_{ijk}$ is the permutation tensor, defined as

$$\varepsilon_{ijk} = \begin{cases} 1 & \text{i,j,k = 1,2,3; 2,3,1 or 3,1,2} \\ \text{-1} & \text{i,j,k = 3,2,1; 2,1,3 or 1,3,2} \\ 0 & \text{otherwise (any repeated index)} \end{cases} \tag{A.8}$$

Note that the permutation tensor applied to a vector $\boldsymbol{u}$ gives the skew-symmetric of $\boldsymbol{u}$ as

$$\widetilde{\boldsymbol{U}} = \operatorname{skew}(\boldsymbol{u}) = \begin{bmatrix} 0 & -u_3 & u_2 \\ u_3 & 0 & -u_1 \\ -u_2 & u_1 & 0 \end{bmatrix}. \tag{A.9}$$

Therefore, the cross product can be rewritten using the skew-symmetric operator as

$$\boldsymbol{u} \times \boldsymbol{v} = \widetilde{\boldsymbol{U}}\boldsymbol{v} = -\widetilde{\boldsymbol{V}}\boldsymbol{u}, \tag{A.10}$$

where $\widetilde{\boldsymbol{U}} = \operatorname{skew}(\boldsymbol{u})$ and $\widetilde{\boldsymbol{V}} = \operatorname{skew}(\boldsymbol{v})$.

The tensor product of two vectors $\boldsymbol{u}$ and $\boldsymbol{v}$ is defined as

$$\boldsymbol{u} \otimes \boldsymbol{v} = \boldsymbol{u}\boldsymbol{v}^T. \tag{A.11}$$

The components of the tensor product can be expressed using index notation as

$$(\boldsymbol{u} \otimes \boldsymbol{v})_{ij} = u_i v_j. \tag{A.12}$$

Analogous to the scalar product of two vectors, the double contraction ( : ) of two second order tensors is defined as

$$\boldsymbol{A} \colon \boldsymbol{B} = A_{ij} B_{ij}. \tag{A.13}$$

The trace of a second order tensor is well defined by

$$\operatorname{tr}\boldsymbol{S} = S_{ii}, \tag{A.14}$$

and satisfies:

$$\mathrm{tr}(\boldsymbol{u} \otimes \boldsymbol{v}) = \boldsymbol{u} \cdot \boldsymbol{v}. \tag{A.15}$$

In this work, the tensor cross product is also used. This operation was first introduced in the context of continuum mechanics by Bonet et al. [48] and further explained in [49]. The tensor cross product between a vector $\boldsymbol{v}$ and a second order tensor $\boldsymbol{S}$ is defined, in components, as

$$(\boldsymbol{v} \boldsymbol{\times} \boldsymbol{S})_{ij} = \varepsilon_{ikl} v_k S_{lj}. \tag{A.16}$$

This operation replaces each column of $\boldsymbol{S}$ by the cross product between $\boldsymbol{v}$ and each original column of $\boldsymbol{S}$.

On the other hand, the tensor cross product between a second order tensor $\boldsymbol{S}$ and a vector $\boldsymbol{v}$ is defined, in components, as

$$(\boldsymbol{S} \boldsymbol{\times} \boldsymbol{v})_{ij} = \varepsilon_{jkl} S_{ik} v_l. \tag{A.17}$$

This operation replaces each row of $\boldsymbol{S}$ by the cross product between each original row of $\boldsymbol{S}$ and $\boldsymbol{v}$.

Finally, the tensor cross product between two second order tensors $\boldsymbol{S}$ and $\boldsymbol{P}$ is defined, in components, as

$$(\boldsymbol{S} \boldsymbol{\times} \boldsymbol{P})_{ij} = \varepsilon_{ikl} \varepsilon_{jmn} S_{km} P_{ln}. \tag{A.18}$$

## A.3 Gradient, divergence and curl operators

Consider a scalar function $f(\boldsymbol{x})$, the change in $f$ in the direction of an arbitrary incremental vector $\boldsymbol{u}$ at a point $\boldsymbol{x}_0$ is called the gradient of $f$ at $\boldsymbol{x}_0$ and is defined as

$$\boldsymbol{\nabla} f(\boldsymbol{x}_0) \cdot \boldsymbol{u} = Df(\boldsymbol{x}_0)[\boldsymbol{u}], \tag{A.19}$$

where $Df(\boldsymbol{x}_0)[\boldsymbol{u}]$ is the directional derivative of $f(\boldsymbol{x})$ at $\boldsymbol{x}_0$ in the direction of $\boldsymbol{u}$, which is defined as

$$Df(\boldsymbol{x}_0)[\boldsymbol{u}] = \left.\frac{d}{d\epsilon}\right|_{\epsilon=0} (f(\boldsymbol{x}_0 + \epsilon\boldsymbol{u})). \tag{A.20}$$

Note that $\epsilon$ in equation A.20 is an artificial parameter used to perform the derivative. The components of the gradient of $f$ are the partial derivatives of function $f$ in each spatial direction, i.e., they are given by

$$(\mathrm{grad} f)_i = (\boldsymbol{\nabla} f)_i = \frac{\partial f}{\partial x_i}. \tag{A.21}$$

For a vector field $\boldsymbol{f}$, the gradient at a point $\boldsymbol{x}_0$ can be defined in terms of the directional derivative as

$$\boldsymbol{\nabla} \boldsymbol{f}(\boldsymbol{x}_0)\boldsymbol{u} = D\boldsymbol{f}(\boldsymbol{x}_0)[\boldsymbol{u}]. \tag{A.22}$$

The components of the gradient of $\boldsymbol{f}$ are simply the partial derivatives of the vector components, given by

$$(\mathrm{grad}\boldsymbol{f})_{ij} = (\boldsymbol{\nabla} \boldsymbol{f})_{ij} = \frac{\partial f_i}{\partial x_j}. \tag{A.23}$$

Similarly, the gradient can be defined for a second order tensor $\boldsymbol{S}$ as

$$\boldsymbol{\nabla S}\,(\boldsymbol{x}_0)\boldsymbol{u} = D\boldsymbol{S}\,(\boldsymbol{x}_0)\,[\boldsymbol{u}]\,, \tag{A.24}$$

with the components of the third-order tensor $\boldsymbol{\nabla S}\,(\boldsymbol{x}_0)$ given by

$$(\boldsymbol{\nabla S})_{ijk} = \frac{\partial S_{ij}}{\partial x_k}. \tag{A.25}$$

The divergence of a vector field $\boldsymbol{f}$ is defined as the scalar given by the trace of the gradient of that vector field

$$\mathrm{div}\boldsymbol{f} = \mathrm{tr}\boldsymbol{\nabla f} = \frac{\partial f_i}{\partial x_i}. \tag{A.26}$$

The divergence of a second order tensor $\boldsymbol{S}$ is given by

$$(\mathrm{div}\boldsymbol{S})_i = (\boldsymbol{\nabla S}\colon \boldsymbol{I})_i = \frac{\partial S_{ij}}{\partial x_j}. \tag{A.27}$$

The curl of a vector field $\boldsymbol{f}$ is defined as

$$(\mathrm{curl}\boldsymbol{f})_i = \varepsilon_{ijk}\frac{\partial f_k}{\partial x_j}. \tag{A.28}$$

Finally, the curl of a second order tensor $\boldsymbol{S}$ is given by

$$(\mathrm{curl}\boldsymbol{S})_{ij} = \varepsilon_{jkl}\frac{\partial S_{il}}{\partial x_k}. \tag{A.29}$$

## A.4 Further useful properties and definitions

Some properties of the scalar product are

$$\boldsymbol{u}\cdot\boldsymbol{v} = \boldsymbol{v}\cdot\boldsymbol{u}, \tag{A.30a}$$
$$\boldsymbol{u}\cdot(\boldsymbol{v}+\boldsymbol{x}) = \boldsymbol{u}\cdot\boldsymbol{v}+\boldsymbol{u}\cdot\boldsymbol{x}, \tag{A.30b}$$
$$\boldsymbol{u}\cdot\boldsymbol{v} = \boldsymbol{u}^T\boldsymbol{v} = \boldsymbol{v}^T\boldsymbol{u}. \tag{A.30c}$$

Some properties of the cross product are

$$\boldsymbol{u}\times\boldsymbol{v} = -\boldsymbol{v}\times\boldsymbol{u}, \tag{A.31a}$$
$$\boldsymbol{x}\times(\boldsymbol{u}+\boldsymbol{v}) = \boldsymbol{x}\times\boldsymbol{u}+\boldsymbol{x}\times\boldsymbol{v}, \tag{A.31b}$$
$$\boldsymbol{x}\times(\boldsymbol{u}\times\boldsymbol{v}) = \boldsymbol{u}\,(\boldsymbol{x}\cdot\boldsymbol{v})-\boldsymbol{v}\,(\boldsymbol{x}\cdot\boldsymbol{u})\,. \tag{A.31c}$$

The combination of a cross product and a dot product is called scalar triple product and has the following property

$$\boldsymbol{x}\cdot(\boldsymbol{u}\times\boldsymbol{v}) = \boldsymbol{u}\cdot(\boldsymbol{v}\times\boldsymbol{x}) = \boldsymbol{v}\cdot(\boldsymbol{x}\times\boldsymbol{u}). \tag{A.32}$$

Some properties of the tensor product are

$$(\boldsymbol{u} \otimes \boldsymbol{v})\, \boldsymbol{x} = (\boldsymbol{x} \cdot \boldsymbol{v})\, \boldsymbol{u}, \tag{A.33a}$$

$$(\boldsymbol{u} \otimes \boldsymbol{v})^T = (\boldsymbol{v} \otimes \boldsymbol{u}), \tag{A.33b}$$

$$(\boldsymbol{S} \otimes \boldsymbol{v})\, \boldsymbol{u} = (\boldsymbol{u} \cdot \boldsymbol{v})\, \boldsymbol{S}, \tag{A.33c}$$

$$(\boldsymbol{u} \otimes \boldsymbol{v})\, \boldsymbol{S} = \left(\boldsymbol{u} \otimes \boldsymbol{S}^T \boldsymbol{v}\right), \tag{A.33d}$$

$$(\boldsymbol{v} \otimes \boldsymbol{S})\, \boldsymbol{u} = \boldsymbol{v} \otimes (\boldsymbol{S}\boldsymbol{u}). \tag{A.33e}$$

Some properties of the double contraction are

$$\boldsymbol{A} \colon \boldsymbol{B} = \operatorname{tr}\left(\boldsymbol{A}^T \boldsymbol{B}\right) = \operatorname{tr}\left(\boldsymbol{B}\boldsymbol{A}^T\right) = \operatorname{tr}\left(\boldsymbol{B}^T \boldsymbol{A}\right) = \operatorname{tr}\left(\boldsymbol{A}\boldsymbol{B}^T\right), \tag{A.34a}$$

$$\boldsymbol{S} \colon (\boldsymbol{u} \otimes \boldsymbol{v}) = \boldsymbol{u} \cdot \boldsymbol{S}\boldsymbol{v}. \tag{A.34b}$$

The transpose of a tensor $\boldsymbol{S}$ is defined as the tensor $\boldsymbol{S}^T$, which for any two vectors $\boldsymbol{u}$ and $\boldsymbol{v}$ satisfies

$$\boldsymbol{u} \cdot \boldsymbol{S}\boldsymbol{v} = \boldsymbol{v} \cdot \boldsymbol{S}^T \boldsymbol{u}. \tag{A.35}$$

Therefore, it follows that

$$(\boldsymbol{S} + \boldsymbol{P})^T = \boldsymbol{S}^T + \boldsymbol{P}^T, \tag{A.36a}$$

$$(\boldsymbol{S}\boldsymbol{P})^T = \boldsymbol{P}^T \boldsymbol{S}^T, \tag{A.36b}$$

$$\left(\boldsymbol{S}^T\right)^T = \boldsymbol{S}. \tag{A.36c}$$

A tensor is symmetric if $\boldsymbol{S} = \boldsymbol{S}^T$ and skew-symmetric if $\boldsymbol{S} = -\boldsymbol{S}^T$. An orthogonal tensor is a tensor that presents the following properties

$$\boldsymbol{Q}^T = \boldsymbol{Q}^{-1}, \tag{A.37a}$$

$$\boldsymbol{Q}^T \boldsymbol{Q} = \boldsymbol{I}, \tag{A.37b}$$

where $\boldsymbol{I}$ is the identity tensor.

Some properties of the tensor cross product are

$$(\boldsymbol{v} \boldsymbol{\times} \boldsymbol{S})\, \boldsymbol{x} = \boldsymbol{v} \times (\boldsymbol{S}\boldsymbol{x}), \tag{A.38a}$$

$$(\boldsymbol{S} \boldsymbol{\times} \boldsymbol{v})\, \boldsymbol{x} = \boldsymbol{S}\, (\boldsymbol{v} \times \boldsymbol{x}), \tag{A.38b}$$

$$\boldsymbol{v} \cdot (\boldsymbol{S} \boldsymbol{\times} \boldsymbol{P})\, \boldsymbol{x} = (\boldsymbol{v} \boldsymbol{\times} \boldsymbol{S}) \colon (\boldsymbol{P} \boldsymbol{\times} \boldsymbol{x}), \tag{A.38c}$$

$$(\boldsymbol{A} \boldsymbol{\times} \boldsymbol{B} \colon \boldsymbol{C}) = (\boldsymbol{B} \boldsymbol{\times} \boldsymbol{C} \colon \boldsymbol{A}) = (\boldsymbol{A} \boldsymbol{\times} \boldsymbol{C} \colon \boldsymbol{B}), \tag{A.38d}$$

$$(\boldsymbol{A}_1 \boldsymbol{B}) \boldsymbol{\times} (\boldsymbol{A}_2 \boldsymbol{B}) = (\boldsymbol{A}_1 \boldsymbol{\times} \boldsymbol{A}_2)\, \operatorname{cof}\boldsymbol{B}. \tag{A.38e}$$

Note that $\operatorname{cof}\boldsymbol{B}$ in equation A.38e is the cofactor matrix of $\boldsymbol{B}$, usually defined as

$$(\operatorname{cof}\boldsymbol{B})_{ij} = (-1)^{i+j} \boldsymbol{M}_{ij}, \tag{A.39}$$

where $\boldsymbol{M}_{ij}$ is the reduced determinant formed by omitting $i$th row and $j$th column of $\boldsymbol{B}$.

Some properties of the gradient and divergence are

$$\boldsymbol{\nabla}(f\boldsymbol{v}) = f\boldsymbol{\nabla}\boldsymbol{v} + \boldsymbol{v}\otimes\boldsymbol{\nabla}f, \tag{A.40a}$$

$$\operatorname{div}(f\boldsymbol{v}) = f(\operatorname{div}\boldsymbol{v}) + \boldsymbol{v}\cdot\boldsymbol{\nabla}f, \tag{A.40b}$$

$$\operatorname{div}\big(\boldsymbol{S}^T\boldsymbol{v}\big) = \boldsymbol{S}\colon\boldsymbol{\nabla}\boldsymbol{v} + \boldsymbol{v}\cdot(\operatorname{div}\boldsymbol{S}), \tag{A.40c}$$

$$\operatorname{div}(\boldsymbol{u}\otimes\boldsymbol{v}) = \boldsymbol{u}(\operatorname{div}\boldsymbol{v}) + (\boldsymbol{\nabla}\boldsymbol{u})\,\boldsymbol{v}. \tag{A.40d}$$

## A.5 Divergence theorem

Also known as Gauss's theorem, the divergence theorem states that

$$\int_{\Omega_V}(\operatorname{div}\boldsymbol{S})\,dV = \int_{\partial\Omega_V}(\boldsymbol{S}\boldsymbol{N})\,dA, \tag{A.41}$$

where the left side is a volume integral over the volume $V$ and the right side is the surface integral over the boundary of $V$. $\boldsymbol{N}$ is the outward pointing unit normal vector of the boundary $\partial\Omega_V$.

# Appendix B

# Fundamentals of nonlinear solid mechanics

## B.1 Introduction

This appendix summarises the fundamental concepts of nonlinear solid mechanics used throughout this work. For a more comprehensive view of this topic, the works by Gurtin [133] and Bonet et al. [88] are particularly recommended.

## B.2 Kinematics

In figure B.1, the general motion of a three-dimensional deformable body is illustrated. A generic point $P$ representing a single particle is located at its original or initial configuration (Time = 0) by the position vector $\boldsymbol{X}$. This particle can be mapped into the current configuration (Time = $t$) by the evolution operator $\boldsymbol{\phi}$.

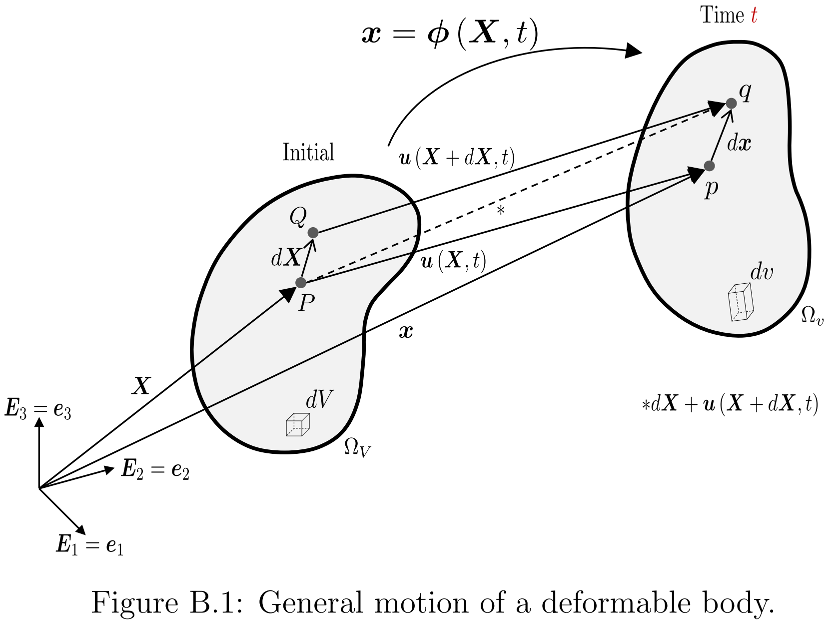

Figure B.1: General motion of a deformable body.

The motion is mathematically expressed by

$$\boldsymbol{x} = \boldsymbol{\phi}(\boldsymbol{X}, t), \tag{B.1}$$

where the position vector $\boldsymbol{x}$ provides the current position of the particle. Therefore, the velocity of the particle is a spatial vector, given by the time derivative of $\boldsymbol{\phi}$

$$\boldsymbol{v}\left(\boldsymbol{X},t\right)=\frac{\partial\boldsymbol{\phi}\left(\boldsymbol{X},t\right)}{\partial t}=\frac{\partial\boldsymbol{x}}{\partial t}. \tag{B.2}$$

The velocity can be alternatively expressed as a function of $\boldsymbol{x}$ and $t$ as

$$\boldsymbol{v}\left(\boldsymbol{x},t\right)=\boldsymbol{v}\left(\boldsymbol{\phi}^{-1}\left(\boldsymbol{x},t\right),t\right). \tag{B.3}$$

For a fixed value of $t$ equation B.1 represents the mapping between undeformed and deformed bodies. Relevant quantities can be described in terms of the configuration before the deformation (material description) or the configuration during deformation (spatial description).

By construction, from figure B.1 the displacement vectors $\boldsymbol{u}\left(\boldsymbol{X},t\right)$ and $\boldsymbol{u}\left(\boldsymbol{X}+d\boldsymbol{X},t\right)$ are given by

$$\boldsymbol{u}\left(\boldsymbol{X},t\right)=\boldsymbol{x}-\boldsymbol{X}=\boldsymbol{\phi}\left(\boldsymbol{X},t\right)-\boldsymbol{X}, \tag{B.4}$$

and

$$\boldsymbol{u}\left(\boldsymbol{X}+d\boldsymbol{X},t\right)=\left(\boldsymbol{x}+d\boldsymbol{x}\right)-\left(\boldsymbol{X}+d\boldsymbol{X}\right)=\boldsymbol{\phi}\left(\boldsymbol{X}+d\boldsymbol{X},t\right)-\left(\boldsymbol{X}+d\boldsymbol{X}\right). \tag{B.5}$$

Keeping $t$ fixed and taking the constant and linear terms from the Taylor's series[1] of $\boldsymbol{\phi}\left(\boldsymbol{X}+d\boldsymbol{X},t\right)$, in a neighbourhood of $\left(\boldsymbol{X},t\right)$, one can show that $\boldsymbol{\phi}\left(\boldsymbol{X}+d\boldsymbol{X},t\right)\approx\boldsymbol{\phi}\left(\boldsymbol{X},t\right)+\frac{\partial\boldsymbol{\phi}(\boldsymbol{X},t)}{\partial\boldsymbol{X}}d\boldsymbol{X}$. Therefore, it is possible to rewrite B.5 as

$$\boldsymbol{u}\left(\boldsymbol{X}+d\boldsymbol{X},t\right)=\boldsymbol{\phi}\left(\boldsymbol{X},t\right)+\frac{\partial\boldsymbol{\phi}\left(\boldsymbol{X},t\right)}{\partial\boldsymbol{X}}d\boldsymbol{X}-\boldsymbol{X}-d\boldsymbol{X}. \tag{B.6}$$

In finite deformation analysis it is possible to describe the relative spatial position of two particles after deformation in terms of the relative material position before deformation. For example, the single elemental spatial vector $d\boldsymbol{x}$ in figure B.1, is written in terms of material vector $d\boldsymbol{X}$ as follows

$$d\boldsymbol{x}=d\boldsymbol{X}+\boldsymbol{u}\left(\boldsymbol{X}+d\boldsymbol{X},t\right)-\boldsymbol{u}\left(\boldsymbol{X},t\right). \tag{B.7}$$

---

[1] Letting $x=x_0+\Delta x$ and $y=y_0+\Delta y$, the multi variable Taylor series of a real function $f(x,y)$ is given by

$$\begin{aligned}f(x,y)&=f(x_0+\Delta x,y_0+\Delta y)\\&=f(x_0,y_0)+f_x(x_0,y_0)(x-x_0)+f_y(x_0,y_0)(y-y_0)\\&+\frac{1}{2!}[f_{xx}(x_0,y_0)(x-x_0)^2+2f_{xy}(x_0,y_0)(x-x_0)(y-y_0)+f_{yy}(x_0,y_0)(y-y_0)^2]+\cdots\\&=f(x_0,y_0)+f_x(x_0,y_0)(\Delta x)+f_y(x_0,y_0)(\Delta y)\\&+\frac{1}{2!}[f_{xx}(x_0,y_0)(\Delta x)^2+2f_{xy}(x_0,y_0)(\Delta x)(\Delta y)+f_{yy}(x_0,y_0)(\Delta y)^2]+\cdots.\end{aligned}$$

where $f_{index}$ denote the partial derivatives of $f$ with respect to *index*.

Substituting B.4 and B.6 in equation B.7 gives

$$d\boldsymbol{x} = d\boldsymbol{X} + \boldsymbol{\phi}\left(\boldsymbol{X},t\right) + \frac{\partial \boldsymbol{\phi}\left(\boldsymbol{X},t\right)}{\partial \boldsymbol{X}} d\boldsymbol{X} - \boldsymbol{X} - d\boldsymbol{X} - \boldsymbol{\phi}\left(\boldsymbol{X},t\right) + \boldsymbol{X}, \tag{B.8a}$$

$$= \frac{\partial \boldsymbol{\phi}\left(\boldsymbol{X},t\right)}{\partial \boldsymbol{X}} d\boldsymbol{X}, \tag{B.8b}$$

$$= \boldsymbol{F} d\boldsymbol{X}. \tag{B.8c}$$

The definition of the deformation gradient tensor $\boldsymbol{F}$ emerges from B.8b as

$$\boldsymbol{F} = \frac{\partial \boldsymbol{\phi}\left(\boldsymbol{X},t\right)}{\partial \boldsymbol{X}} = \boldsymbol{\nabla}_{\boldsymbol{X}} \boldsymbol{\phi}\left(\boldsymbol{X},t\right) = \boldsymbol{\nabla}_{\boldsymbol{X}} \boldsymbol{\phi}, \tag{B.9}$$

where $\boldsymbol{\nabla}_{\boldsymbol{X}}$ is the gradient with respect to the initial configuration.

Equation B.9 is usually more conveniently written as

$$\boldsymbol{F} = \frac{\partial \boldsymbol{x}}{\partial \boldsymbol{X}} = \begin{bmatrix} \frac{\partial x_1}{\partial X_1} & \frac{\partial x_1}{\partial X_2} & \frac{\partial x_1}{\partial X_3} \\ \frac{\partial x_2}{\partial X_1} & \frac{\partial x_2}{\partial X_2} & \frac{\partial x_2}{\partial X_3} \\ \frac{\partial x_3}{\partial X_1} & \frac{\partial x_3}{\partial X_2} & \frac{\partial x_3}{\partial X_3} \end{bmatrix}. \tag{B.10}$$

Components of the deformation gradient tensor can be expressed using index notation as

$$F_{iI} = \frac{\partial x_i}{\partial X_I}; \qquad i, I = 1, 2, 3. \tag{B.11}$$

The inverse of $\boldsymbol{F}$ is:

$$\boldsymbol{F}^{-1} = \frac{\partial \boldsymbol{X}}{\partial \boldsymbol{x}} = \boldsymbol{\nabla} \boldsymbol{\phi}^{-1}, \tag{B.12}$$

noticing that $\boldsymbol{\nabla}$ is the gradient with respect to the current configuration.

The time derivative of the deformation gradient tensor is

$$\dot{\boldsymbol{F}} = \frac{d}{dt}\left(\frac{\partial \boldsymbol{\phi}}{\partial \boldsymbol{X}}\right) = \frac{\partial}{\partial \boldsymbol{X}}\left(\frac{\partial \boldsymbol{\phi}}{\partial t}\right) = \frac{\partial \boldsymbol{v}}{\partial \boldsymbol{X}} = \boldsymbol{\nabla}_{\boldsymbol{X}} \boldsymbol{v}, \tag{B.13}$$

The velocity was defined as a spatial vector and expressed in equation B.3 as a function of current coordinates. The derivative of $\boldsymbol{v}\left(\boldsymbol{x},t\right)$ with respect to $\boldsymbol{x}$ defines the velocity gradient tensor $\boldsymbol{l}$ as

$$\boldsymbol{l} = \boldsymbol{\nabla} \boldsymbol{v} = \frac{\partial \boldsymbol{v}\left(\boldsymbol{x},t\right)}{\partial \boldsymbol{x}} = \frac{\partial \boldsymbol{v}}{\partial \boldsymbol{X}} \frac{\partial \boldsymbol{X}}{\partial \boldsymbol{x}}. \tag{B.14}$$

Using the relationship between the velocity vector and the time derivative of the deformation gradient tensor allows equation B.14 to be rewritten as

$$\boldsymbol{l} = \dot{\boldsymbol{F}} \boldsymbol{F}^{-1}. \tag{B.15}$$

The determinant of $\boldsymbol{F}$ is denoted by Jacobian $J$ and relates differential volumes in initial and current configurations as

$$dv = J dV, \tag{B.16}$$

since a body is not allowed to penetrate itself, the only physically acceptable values of $J$ are $J > 0$.

Consider the initial and current volume elements given as

$$dV = d\boldsymbol{L} \cdot d\boldsymbol{A}, \tag{B.17}$$

$$dv = d\boldsymbol{l} \cdot d\boldsymbol{a}, \tag{B.18}$$

where $d\boldsymbol{L}$ is an arbitrary vector, which after deformation changes to $d\boldsymbol{l}$, $d\boldsymbol{A} = dA\boldsymbol{N}$ is an element of area in the initial configuration with normal $\boldsymbol{N}$, and $d\boldsymbol{a} = da\boldsymbol{n}$ is the deformed element of area, with normal $\boldsymbol{n}$. Using B.17 and B.18 in equation B.16 and noticing that $d\boldsymbol{l} = \boldsymbol{F}d\boldsymbol{L}$ gives

$$(\boldsymbol{F}d\boldsymbol{L}) \cdot d\boldsymbol{a} = Jd\boldsymbol{L} \cdot d\boldsymbol{A}. \tag{B.19}$$

Multiplying both sides of equation B.19 by $\boldsymbol{F}^{-1}$ and using the identity A.35 gives

$$d\boldsymbol{L} \cdot d\boldsymbol{a} = \boldsymbol{F}^{-1}Jd\boldsymbol{L} \cdot d\boldsymbol{A}, \tag{B.20a}$$

$$d\boldsymbol{L} \cdot d\boldsymbol{a} = d\boldsymbol{L} \cdot J\boldsymbol{F}^{-T}d\boldsymbol{A}, \tag{B.20b}$$

$$d\boldsymbol{a} = J\boldsymbol{F}^{-T}d\boldsymbol{A}, \tag{B.20c}$$

$$\boldsymbol{n}da = J\boldsymbol{F}^{-T}\boldsymbol{N}dA. \tag{B.20d}$$

Equation B.20d is also known as Nanson's formula and $J\boldsymbol{F}^{-T}$ is often referred to as the co-factor or adjoint tensor $\boldsymbol{H}$. Since a change in the scalar product of two elemental vectors involves a change in the length of each vector and a change in the angle between them (see the geometric definition of the scalar product in section A.1 of Appendix A), it can be used as a general measure of deformation. Let us write the scalar product of $d\boldsymbol{x}_1$ and $d\boldsymbol{x}_2$ in the deformed configuration in terms of the the material vectors $d\boldsymbol{X}_1$ and $d\boldsymbol{X}_2$ as

$$d\boldsymbol{x}_1 \cdot d\boldsymbol{x}_2 = \boldsymbol{F}d\boldsymbol{X}_1 \cdot \boldsymbol{F}d\boldsymbol{X}_2 = \boldsymbol{F}d\boldsymbol{X}_2 \cdot \boldsymbol{F}d\boldsymbol{X}_1, \tag{B.21a}$$

$$= d\boldsymbol{X}_1 \cdot \boldsymbol{F}^T\boldsymbol{F}d\boldsymbol{X}_2, \tag{B.21b}$$

$$= d\boldsymbol{X}_1 \cdot \boldsymbol{C}d\boldsymbol{X}_2, \tag{B.21c}$$

where $\boldsymbol{C}$ is the right Cauchy-Green deformation tensor, given by

$$\boldsymbol{C} = \boldsymbol{F}^T\boldsymbol{F}. \tag{B.22}$$

In an alternative way, $d\boldsymbol{X}_1$ and $d\boldsymbol{X}_2$ can be obtained in terms of the spatial vectors $d\boldsymbol{x}_1$ and $d\boldsymbol{x}_2$ as

$$d\boldsymbol{X}_1 \cdot d\boldsymbol{X}_2 = \boldsymbol{F}^{-1}d\boldsymbol{x}_1 \cdot \boldsymbol{F}^{-1}d\boldsymbol{x}_2 = \boldsymbol{F}^{-1}d\boldsymbol{x}_2 \cdot \boldsymbol{F}^{-1}d\boldsymbol{x}_1, \tag{B.23a}$$

$$= d\boldsymbol{x}_1 \cdot \boldsymbol{F}^{-T}\boldsymbol{F}^{-1}d\boldsymbol{x}_2, \tag{B.23b}$$

$$= d\boldsymbol{x}_1 \cdot \boldsymbol{b}^{-1}d\boldsymbol{x}_2, \tag{B.23c}$$

where $\boldsymbol{b}$ is the left Cauchy-Green or Finger tensor, given by

$$\boldsymbol{b} = \boldsymbol{F}\boldsymbol{F}^T. \tag{B.24}$$

The Lagrangian or Green strain tensor $\boldsymbol{E}$ can now be defined as the change in scalar product in terms of material vectors

$$\begin{aligned}
\frac{1}{2}\left(d\boldsymbol{x}_1 \cdot d\boldsymbol{x}_2 - d\boldsymbol{X}_1 \cdot d\boldsymbol{X}_2\right) &= \frac{1}{2}\left(d\boldsymbol{X}_1 \cdot \boldsymbol{C} d\boldsymbol{X}_2 - d\boldsymbol{X}_1 \cdot \boldsymbol{I} d\boldsymbol{X}_2\right), && \text{(B.25a)}\\
&= \frac{1}{2}\left(d\boldsymbol{X}_1 \cdot \left(\boldsymbol{C} - \boldsymbol{I}\right) d\boldsymbol{X}_2\right), && \text{(B.25b)}\\
&= d\boldsymbol{X}_1 \cdot \boldsymbol{E} d\boldsymbol{X}_2, && \text{(B.25c)}
\end{aligned}$$

with

$$\boldsymbol{E} = \frac{1}{2}\left(\boldsymbol{C} - \boldsymbol{I}\right). \tag{B.26}$$

Alternatively, the Eulerian or Almansi strain tensor $\boldsymbol{e}$ is given in terms of spatial vectors by

$$\begin{aligned}
\frac{1}{2}\left(d\boldsymbol{x}_1 \cdot d\boldsymbol{x}_2 - d\boldsymbol{X}_1 \cdot d\boldsymbol{X}_2\right) &= \frac{1}{2}\left(d\boldsymbol{x}_1 \cdot \boldsymbol{I} d\boldsymbol{x}_2 - d\boldsymbol{x}_1 \cdot \boldsymbol{b}^{-1} d\boldsymbol{x}_2\right), && \text{(B.27a)}\\
&= \frac{1}{2}\left(d\boldsymbol{x}_1 \cdot \left(\boldsymbol{I} - \boldsymbol{b}^{-1}\right) d\boldsymbol{x}_2\right), && \text{(B.27b)}\\
&= d\boldsymbol{x}_1 \cdot \boldsymbol{e} d\boldsymbol{x}_2, && \text{(B.27c)}
\end{aligned}$$

with

$$\boldsymbol{e} = \frac{1}{2}\left(\boldsymbol{I} - \boldsymbol{b}^{-1}\right). \tag{B.28}$$

Therefore, one can see that

$$\boldsymbol{e} = \boldsymbol{F}^{-T}\boldsymbol{E}\boldsymbol{F}^{-1}, \tag{B.29}$$

$$\boldsymbol{E} = \boldsymbol{F}^{T}\boldsymbol{e}\boldsymbol{F}. \tag{B.30}$$

The current rate of change of the scalar product in terms of initial elemental vectors can be obtained computing the time derivative of $\boldsymbol{E}$, which is known as Green-Lagrange strain rate tensor and is expressed in terms of $\boldsymbol{F}$ as

$$\dot{\boldsymbol{E}} = \frac{1}{2}\dot{\boldsymbol{C}} = \frac{1}{2}\left(\dot{\boldsymbol{F}}^T\boldsymbol{F} + \boldsymbol{F}^T\dot{\boldsymbol{F}}\right). \tag{B.31}$$

Another important quantity is the rate of deformation tensor $\boldsymbol{d}$, given by

$$\boldsymbol{d} = \boldsymbol{F}^{-T}\dot{\boldsymbol{E}}\boldsymbol{F}^{-1}, \tag{B.32}$$

which can also be written in terms of the velocity gradient as

$$\boldsymbol{d} = \frac{1}{2}\left(\boldsymbol{l} + \boldsymbol{l}^T\right). \tag{B.33}$$

Because $\det\boldsymbol{F} = J > 0$, it can be shown that there exist two positive-definite symmetric tensors $\boldsymbol{U}$ and $\boldsymbol{V}$ and an orthogonal tensor $\boldsymbol{R}$, such that

$$\boldsymbol{F} = \boldsymbol{R}\boldsymbol{U} = \boldsymbol{V}\boldsymbol{R}, \tag{B.34}$$

$\boldsymbol{U}$ and $\boldsymbol{V}$ are known, respectively, as the material and the spatial stretch tensors and $\boldsymbol{R}$ is a rotation tensor. The products in equation B.34 represent the polar decomposition of $\boldsymbol{F}$.

By using B.34 in B.8c, the current elemental vector $d\boldsymbol{x}$ can be written as

$$d\boldsymbol{x} = \boldsymbol{R}\boldsymbol{U}d\boldsymbol{X}, \tag{B.35}$$

or

$$d\boldsymbol{x} = \boldsymbol{V}\boldsymbol{R}d\boldsymbol{X}. \tag{B.36}$$

Expressions B.35 and B.36 allow us to think about the deformation process in two stages, the stretching followed by a rotation or a rotation followed by the stretching.

The stretch tensor $\boldsymbol{U}$ can be defined in terms of the right Cauchy-Green tensor $\boldsymbol{C}$ using the fact that $\boldsymbol{R}$ is orthogonal (see property A.37b in Appendix A) as

$$\boldsymbol{F} = \boldsymbol{R}\boldsymbol{U}, \tag{B.37a}$$
$$\boldsymbol{F}^T = \boldsymbol{U}^T\boldsymbol{R}^T, \tag{B.37b}$$
$$\boldsymbol{F}^T\boldsymbol{F} = \boldsymbol{U}^T\boldsymbol{R}^T\boldsymbol{R}\boldsymbol{U}, \tag{B.37c}$$
$$\boldsymbol{C} = \boldsymbol{U}^T\boldsymbol{U}. \tag{B.37d}$$

Following the same approach, $\boldsymbol{V}$ can be written in terms of the left Cauchy-Green or Finger tensor $\boldsymbol{b}$ as

$$\boldsymbol{F} = \boldsymbol{V}\boldsymbol{R}, \tag{B.38a}$$
$$\boldsymbol{F}^T = \boldsymbol{R}^T\boldsymbol{V}^T, \tag{B.38b}$$
$$\boldsymbol{F}\boldsymbol{F}^T = \boldsymbol{V}\boldsymbol{R}\boldsymbol{R}^T\boldsymbol{V}^T, \tag{B.38c}$$
$$\boldsymbol{b} = \boldsymbol{V}\boldsymbol{V}^T. \tag{B.38d}$$

The right Cauchy-Green tensor has the following spectral decomposition

$$\boldsymbol{C} = \sum_{i=1}^{3} \lambda_i^2 \boldsymbol{N}_i \otimes \boldsymbol{N}_i, \tag{B.39}$$

where $\lambda_1^2$, $\lambda_2^2$ and $\lambda_3^2$ are the eigenvalues of $\boldsymbol{C}$ and $\boldsymbol{N}_1$, $\boldsymbol{N}_2$ and $\boldsymbol{N}_3$ are the corresponding eigenvectors, representing the principal directions of $\boldsymbol{C}$. Substituting B.37d in B.39 and choosing $\boldsymbol{U}$ to be a symmetric tensor, results in

$$\boldsymbol{U} = \sum_{i=1}^{3} \lambda_i \boldsymbol{N}_i \otimes \boldsymbol{N}_i. \tag{B.40}$$

In a similar manner, the principal directions of $\boldsymbol{b}$ are given by the eigenvalues $\overline{\lambda}_1^2$, $\overline{\lambda}_2^2$ and $\overline{\lambda}_3^2$ and the corresponding eigenvectors $\boldsymbol{n}_1$, $\boldsymbol{n}_2$ and $\boldsymbol{n}_3$, which allows $\boldsymbol{V}$ to be written as

$$\boldsymbol{V} = \sum_{i=1}^{3} \overline{\lambda}_i \boldsymbol{n}_i \otimes \boldsymbol{n}_i. \tag{B.41}$$

From equation B.34 it is possible to write

$$\boldsymbol{V} = \boldsymbol{R}\boldsymbol{U}\boldsymbol{R}^T, \tag{B.42}$$

and by substituting equation B.40 for $\boldsymbol{U}$ in this expression gives

$$\boldsymbol{V} = \boldsymbol{R}\left(\sum_{i=1}^{3} \lambda_i \boldsymbol{N}_i \otimes \boldsymbol{N}_i\right)\boldsymbol{R}^T, \tag{B.43a}$$

$$= \sum_{i=1}^{3} \lambda_i (\boldsymbol{R}\boldsymbol{N}_i) \otimes (\boldsymbol{R}\boldsymbol{N}_i). \tag{B.43b}$$

Comparing B.43b with B.41 shows that

$$\lambda_i = \overline{\lambda}_i, \tag{B.44}$$

$$\boldsymbol{n}_i = \boldsymbol{R}\boldsymbol{N}_i. \tag{B.45}$$

Finally, substituting equation B.40 for $\boldsymbol{U}$ in B.34 and using B.44 and B.45 gives the deformation gradient in terms of the principal stretches and principal directions as

$$\boldsymbol{F} = \boldsymbol{R}\boldsymbol{U}, \tag{B.46a}$$

$$= \boldsymbol{R}\left(\sum_{i=1}^{3} \lambda_i \boldsymbol{N}_i \otimes \boldsymbol{N}_i\right), \tag{B.46b}$$

$$= \sum_{i=1}^{3} \lambda_i (\boldsymbol{R}\boldsymbol{N}_i) \otimes \boldsymbol{N}_i, \tag{B.46c}$$

$$= \sum_{i=1}^{3} \lambda_i \boldsymbol{n}_i \otimes \boldsymbol{N}_i. \tag{B.46d}$$

## B.3 Stress and equilibrium

Consider a general deformable body subjected to forces acting on its surface and suppose the body is cut by a fictitious plane $Q$, as shown in figure B.2. In addition, consider the element of area $da$ normal to $\boldsymbol{n}$ and the resultant force $d\boldsymbol{p}$ acting on this area.

The concept of stress at a point is obtained by letting $da$ become infinitesimal. The limiting ratio of $d\boldsymbol{p}/da$ as $da$ goes to zero defines the traction (or stress) vector $\boldsymbol{t}$ corresponding to the normal $\boldsymbol{n}$ as

$$\boldsymbol{t}(\boldsymbol{n}) = \lim_{da \to 0} \frac{d\boldsymbol{p}}{da}, \tag{B.47}$$

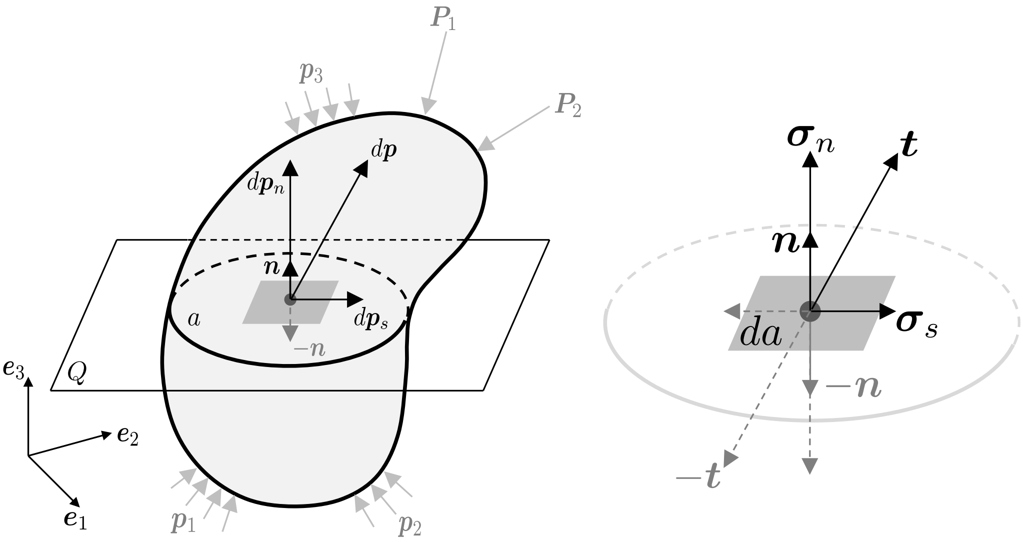

Figure B.2: The traction vector.

where the relationship between $\boldsymbol{t}$ and $\boldsymbol{n}$ must satisfy the principle of action and reaction, which is expressed in this case as

$$\boldsymbol{t}(-\boldsymbol{n}) = -\boldsymbol{t}(\boldsymbol{n}). \tag{B.48}$$

Similarly, the limiting ratios of $d\boldsymbol{p}_n/da$ and $d\boldsymbol{p}_s/da$, as $da$ goes to zero, define the normal stress vector $\boldsymbol{\sigma}_n$ and the shear stress vector $\boldsymbol{\sigma}_s$ at a point as

$$\boldsymbol{\sigma}_n = \lim_{da\to 0} \frac{d\boldsymbol{p}_n}{da}, \tag{B.49}$$

$$\boldsymbol{\sigma}_s = \lim_{da\to 0} \frac{d\boldsymbol{p}_s}{da}. \tag{B.50}$$

Therefore, the following relationships can be written

$$\boldsymbol{t} = \boldsymbol{\sigma}_n + \boldsymbol{\sigma}_s, \tag{B.51}$$

$$\boldsymbol{\sigma}_n = (\boldsymbol{t}\cdot\boldsymbol{n})\,\boldsymbol{n}, \tag{B.52}$$

$$\boldsymbol{\sigma}_s = \boldsymbol{t} - \boldsymbol{\sigma}_n. \tag{B.53}$$

Let us define a stress tensor $\boldsymbol{\sigma}$ as

$$\boldsymbol{\sigma} = \sum_{i,j=1}^{3} \sigma_{ij}\boldsymbol{e}_i \otimes \boldsymbol{e}_j, \tag{B.54}$$

$\boldsymbol{\sigma}$ is known as the Cauchy stress tensor, which relates the normal vector $\boldsymbol{n}$ to the traction vector $\boldsymbol{t}$ as

$$\boldsymbol{t}(\boldsymbol{n}) = \boldsymbol{\sigma}\boldsymbol{n} = \sum_{i,j=1}^{3} \sigma_{ij}\,(\boldsymbol{e}_j\cdot\boldsymbol{n})\,\boldsymbol{e}_i = \sum_{i,j=1}^{3} \sigma_{ij}\,(\boldsymbol{e}_i\otimes\boldsymbol{e}_j)\,\boldsymbol{n}. \tag{B.55}$$

In an alternative form, $\boldsymbol{\sigma}$ can be written as

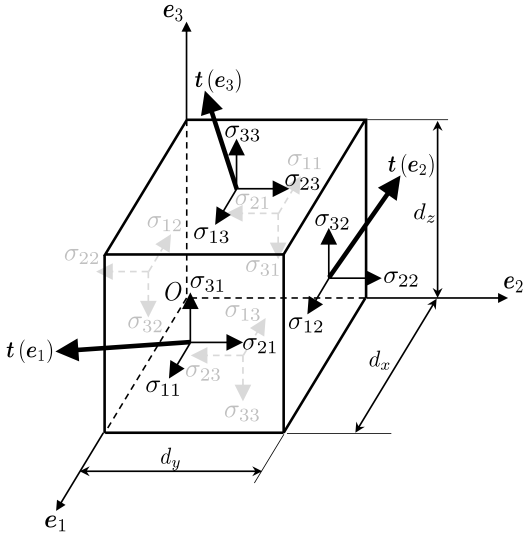

Figure B.3: Stress components at a point.

$$\boldsymbol{\sigma} = \sum_{i=1}^{3} \boldsymbol{t}(\boldsymbol{e}_i) \otimes \boldsymbol{e}_i, \tag{B.56}$$

giving a physical interpretation for the columns of $\boldsymbol{\sigma}$. They are formed by the components of the traction vectors acting on the planes normal to the Cartesian directions $\boldsymbol{e}_1$, $\boldsymbol{e}_2$ and $\boldsymbol{e}_3$ (see figure B.3). Summation of moments in figure B.3 leads to the symmetry of the Cauchy stress tensor. Due to its symmetry $\left(\boldsymbol{\sigma} = \boldsymbol{\sigma}^T\right)$, $\boldsymbol{\sigma}$ has three eigenvalues $\sigma_i$, $i = 1, 2, 3$ denominated principal stresses, which are normal stresses acting on planes normal to $\hat{\boldsymbol{e}}_i$, $i = 1, 2, 3$, i.e., normal to the eigenvectors of $\boldsymbol{\sigma}$.

In general terms, the Cauchy stresses give the current force per unit of current (deformed) area, that is why it is often called "true-stress". However, it can be of practical interest to develop alternative stress representations, for example, the so called Kirchhoff stress tensors, as follows.

Note that a relationship between the resultant force $d\boldsymbol{p}$, the traction force per unit of current area $\boldsymbol{t}$ and the traction force per unit of initial area $\boldsymbol{t}_0$ can be established as

$$d\boldsymbol{p} = \boldsymbol{t} da = \boldsymbol{t}_0 dA. \tag{B.57}$$

Then, the Nanson's formula introduced in equation B.20d, together with the definition of $\boldsymbol{t}$ in equation B.55, can be applied in order to rewrite B.57 as

$$\boldsymbol{\sigma}\boldsymbol{n} da = \boldsymbol{t}_0 dA, \tag{B.58a}$$

$$\boldsymbol{\sigma} J \boldsymbol{F}^{-T} \boldsymbol{N} dA = \boldsymbol{t}_0 dA, \tag{B.58b}$$

$$J \boldsymbol{\sigma} \boldsymbol{F}^{-T} \boldsymbol{N} = \boldsymbol{t}_0. \tag{B.58c}$$

Therefore, a tensor $\boldsymbol{P}$ can be defined such that

$$\boldsymbol{t}_0 = \boldsymbol{P}\boldsymbol{N}, \tag{B.59}$$

where $\boldsymbol{P}$ is named as the first Piola-Kirchhoff stress tensor, given by

$$\boldsymbol{P} = J\boldsymbol{\sigma}\boldsymbol{F}^{-T}. \tag{B.60}$$

The first Piola-Kirchhoff can be physically interpreted as the current force per unit of initial (undeformed) area. Note that $\boldsymbol{P}$ is unsymmetric and is not completely related to the initial configuration. Combining equations B.59 and B.57 leads to

$$\boldsymbol{t} = \boldsymbol{t}_0 \frac{dA}{da} = \boldsymbol{P}\boldsymbol{N}\frac{dA}{da}. \tag{B.61}$$

Nevertheless, a second Piola-Kirchhoff stress tensor $\boldsymbol{S}$, which is a truly material symmetric stress tensor, can be defined as

$$\boldsymbol{S} = \boldsymbol{F}^{-1}\boldsymbol{P} = J\boldsymbol{F}^{-1}\boldsymbol{\sigma}\boldsymbol{F}^{-T}. \tag{B.62}$$

A summary of the relations between different stress measures presented in this section is provided in table B.1.

| **Conversion between stress measures** | | | | |
|---|---|---|---|---|
| | $\boldsymbol{\sigma}$ | $\boldsymbol{\tau}$ | $\boldsymbol{P}$ | $\boldsymbol{S}$ |
| $\boldsymbol{\sigma} =$ | $\boldsymbol{\sigma}$ | $J^{-1}\boldsymbol{\tau}$ | $J^{-1}\boldsymbol{P}\boldsymbol{F}^T$ | $J^{-1}\boldsymbol{F}\boldsymbol{S}\boldsymbol{F}^T$ |
| $\boldsymbol{\tau} =$ | $J\boldsymbol{\sigma}$ | $\boldsymbol{\tau}$ | $\boldsymbol{P}\boldsymbol{F}^T$ | $\boldsymbol{F}\boldsymbol{S}\boldsymbol{F}^T$ |
| $\boldsymbol{P} =$ | $J\boldsymbol{\sigma}\boldsymbol{F}^{-T}$ | $\boldsymbol{\tau}\boldsymbol{F}^{-T}$ | $\boldsymbol{P}$ | $\boldsymbol{F}\boldsymbol{S}$ |
| $\boldsymbol{S} =$ | $J\boldsymbol{F}^{-1}\boldsymbol{\sigma}\boldsymbol{F}^{-T}$ | $\boldsymbol{F}^{-1}\boldsymbol{\tau}\boldsymbol{F}^{-T}$ | $\boldsymbol{F}^{-1}\boldsymbol{P}$ | $\boldsymbol{S}$ |
| with $J = \det \boldsymbol{F}$ | | | | |

Table B.1: Relationship between stress measures.

# Appendix C

# Conservation laws

## C.1 Introduction

This appendix summarises the principles of mechanics of deformable solids used throughout this work. For a comprehensive view of this topic, the works by Bonet et al. [88, 134] are particularly recommended.

## C.2 Basic definitions

Deformable solids are continuous medium in which the material points move in a three dimensional Euclidean space and the concepts related to time are absolute, i.e., are independent of the observer. For sake of simplicity, let us assume that the external forces that influence the movement of a deformable solid are restricted to body forces per unit of volume, distributed over the volume of the solid, and traction forces per unit of area, distributed over the external surface of the solid. Consider $\boldsymbol{b}$ as the vector of body forces and $\boldsymbol{t}$ as the traction vector, both acting in the current configuration. Thus, the following relations can be established

$$\boldsymbol{b}dv = \boldsymbol{b}_0 dV, \tag{C.1a}$$

$$\boldsymbol{b} = \frac{dV}{dv}\boldsymbol{b}_0 = J^{-1}\boldsymbol{b}_0, \tag{C.1b}$$

and,

$$\boldsymbol{t}da = \boldsymbol{t}_0 dA, \tag{C.2a}$$

$$\boldsymbol{t} = \boldsymbol{t}_0 \frac{dA}{da}, \tag{C.2b}$$

where $\boldsymbol{b}_0$ is the body force per unit of initial volume, $\boldsymbol{t}_0$ is the traction vector per unit of initial area and $J$ is the Jacobian defined in B.16.

The resultant of external forces $\boldsymbol{f}_{\text{ext}}$ and moments $\boldsymbol{m}_{\text{ext}}$ in the initial configuration can then be written as

$$\boldsymbol{f}_{\text{ext}} = \int_{\Omega_V} \boldsymbol{b}_0 \, dV + \int_{\partial\Omega_V} \boldsymbol{t}_0 \, dA, \tag{C.3}$$

$$\boldsymbol{m}_{\text{ext}} = \int_{\Omega_V} \boldsymbol{x} \times \boldsymbol{b}_0 \, dV + \int_{\partial\Omega_V} \boldsymbol{x} \times \boldsymbol{t}_0 \, dA. \tag{C.4}$$

The inertia principle applies, i.e., for a fixed reference frame all points within the solid body are at rest or in uniform rectilinear movement. Moreover, at each instant, for each single point there is a scalar function $\rho > 0$, named specific mass, such that the mass of the point is computed as

$$dm = \rho dv. \tag{C.5}$$

If $\rho_0$ is used to denote the specific mass of the material in the initial configuration, the principle of conservation of mass states that

$$\rho dv = \rho_0 dV, \tag{C.6a}$$

$$\rho = \frac{dV}{dv}\rho_0 = J^{-1}\rho_0. \tag{C.6b}$$

The linear momentum and the angular momentum about mass center are defined in the initial configuration as

$$\boldsymbol{L} = \int_{\Omega_V} \rho_0 \boldsymbol{v} \, dV, \tag{C.7}$$

$$\boldsymbol{A}_G = \int_{\Omega_V} \boldsymbol{x} \times \rho_0 \boldsymbol{v} \, dV, \tag{C.8}$$

where $\boldsymbol{v}$ is the velocity vector.

The power of the body and traction forces in the initial configuration can be written as

$$\dot{\Pi}_{\boldsymbol{b}_0} = \int_{\Omega_V} \boldsymbol{b}_0 \cdot \boldsymbol{v} \, dV, \tag{C.9}$$

$$\dot{\Pi}_{\boldsymbol{t}_0} = \int_{\partial\Omega_V} \boldsymbol{t}_0 \cdot \boldsymbol{v} \, dA. \tag{C.10}$$

$$\dot{\Pi}_{\text{ext}} = \dot{\Pi}_{\boldsymbol{b}_0} + \dot{\Pi}_{\boldsymbol{t}_0}. \tag{C.11}$$

In the current configuration, the power of internal forces is written in terms of the Cauchy stress tensor and the rate of deformation tensor (see Appendix B for more details) as

$$\dot{\Pi}_{\text{int}_{\boldsymbol{\sigma}}} = \int_{\Omega_v} \boldsymbol{\sigma} : \boldsymbol{d} \, dv. \tag{C.12}$$

In the initial configuration, the power of internal forces is written in terms of the first Piola-Kirchhoff stress tensor (see Appendix B for more details) as

$$\dot{\Pi}_{\mathrm{int}_{\boldsymbol{P}}} = \int_{\Omega_V} \boldsymbol{P} \colon \dot{\boldsymbol{F}} \, dV, \tag{C.13}$$

or alternatively, in terms of the second Piola-Kirchhoff stress tensor as

$$\dot{\Pi}_{\mathrm{int}_{\boldsymbol{S}}} = \int_{\Omega_V} \boldsymbol{S} \colon \dot{\boldsymbol{E}} \, dV. \tag{C.14}$$

Finally, the kinetic energy of a deformable solid is defined in the initial configuration as

$$K = \int_{\Omega_V} \frac{1}{2} \rho_0 \boldsymbol{v} \cdot \boldsymbol{v} \, dV. \tag{C.15}$$

## C.3 Linear momentum balance principle

The mathematical expression of the linear momentum balance principle, in terms of the initial configuration, is

$$\frac{d}{dt} \int_{\Omega_V} \rho_0 \boldsymbol{v} \, dV = \int_{\Omega_V} \boldsymbol{b}_0 \, dV + \int_{\partial\Omega_V} \boldsymbol{t}_0 \, dA. \tag{C.16}$$

Equation C.16 states that $\dot{\boldsymbol{L}} = \boldsymbol{f}_{\mathrm{ext}}$ and can be rewritten using $\boldsymbol{t}_0 = \boldsymbol{P}\boldsymbol{N}$ together with the divergence theorem (see section A.5 of Appendix A)

$$\frac{d}{dt} \int_{\Omega_V} \rho_0 \boldsymbol{v} \, dV = \int_{\Omega_V} \boldsymbol{b}_0 \, dV + \int_{\partial\Omega_V} \boldsymbol{P}\boldsymbol{N} \, dA, \tag{C.17a}$$

$$= \int_{\Omega_V} \boldsymbol{b}_0 \, dV + \int_{\Omega_V} \mathrm{DIV}\boldsymbol{P} \, dV, \tag{C.17b}$$

where $\boldsymbol{P} = \boldsymbol{P}(\boldsymbol{X}, t)$ is the first Piola-Kirchhoff stress tensor defined in section B.3 of Appendix B, $\boldsymbol{N}$ is the outward pointing unit normal in the initial configuration and DIV denotes the material divergence with respect to the material configuration.

Because the integral over initial volume is constant in time, equation C.17b can be rewritten leading to a local differential linear momentum conservation law

$$\frac{\partial \boldsymbol{p}}{\partial t} - \mathrm{DIV}\boldsymbol{P} = \boldsymbol{b}_0, \tag{C.18}$$

with $\boldsymbol{p} = \boldsymbol{p}(\boldsymbol{X}, t) = \rho_0 \boldsymbol{v}$ being the linear momentum per unit of initial volume.

## C.4 Angular momentum balance principle

The mathematical expression of the angular momentum balance principle, in terms of the initial configuration, is

$$\frac{d}{dt} \int_{\Omega_V} \boldsymbol{x} \times \rho_0 \boldsymbol{v} \, dV = \int_{\Omega_V} \boldsymbol{x} \times \boldsymbol{b}_0 \, dV + \int_{\partial\Omega_V} \boldsymbol{x} \times \boldsymbol{t}_0 \, dA. \tag{C.19}$$

Equation C.19 states that $\dot{\boldsymbol{A}}_G = \boldsymbol{m}_{\text{ext}}$ and can be rewritten using $\boldsymbol{t}_0 = \boldsymbol{PN}$ together with the divergence theorem (see section A.5 of Appendix A)

$$\frac{d}{dt}\int_{\Omega_V} \boldsymbol{x} \times \rho_0 \boldsymbol{v}\, dV = \int_{\Omega_V} \boldsymbol{x} \times \boldsymbol{b}_0\, dV + \int_{\partial\Omega_V} \boldsymbol{x} \times \boldsymbol{PN}\, dA, \tag{C.20a}$$

$$= \int_{\Omega_V} \boldsymbol{x} \times \boldsymbol{b}_0\, dV + \int_{\Omega_V} \mathrm{DIV}\,(\boldsymbol{x} \boldsymbol{\times} \boldsymbol{P})\, dV. \tag{C.20b}$$

Because the integral over initial volume is constant in time, equation C.20b can be rewritten leading to a local differential angular momentum conservation law

$$\frac{\partial}{\partial t}(\boldsymbol{x} \times \boldsymbol{p}) - \mathrm{DIV}(\boldsymbol{x} \boldsymbol{\times} \boldsymbol{P}) = \boldsymbol{x} \times \boldsymbol{b}_0, \tag{C.21}$$

with $\boldsymbol{p} = \boldsymbol{p}\,(\boldsymbol{X}, t) = \rho_0 \boldsymbol{v}$ being the linear momentum per unit of initial volume.

It is convenient to study the last term on the right side of equation C.20a in a component-wise form, as follows

$$\int_{\partial\Omega_V} \varepsilon_{ijk} x_j P_{kL} N_L\, dA = \int_{\Omega_V} \frac{\partial}{\partial X_L}\left(\varepsilon_{ijk} x_j P_{kL}\right) dV, \tag{C.22a}$$

$$= \int_{\Omega_V} \left(\varepsilon_{ijk} \frac{\partial x_j}{\partial X_L} P_{kL} + \varepsilon_{ijk} x_j \frac{\partial P_{kL}}{\partial X_L}\right) dV, \tag{C.22b}$$

$$= \int_{\Omega_V} \varepsilon_{ijk} F_{jL} P_{kL}\, dV + \int_{\Omega_V} \varepsilon_{ijk} x_j \frac{\partial P_{kL}}{\partial X_L}\, dV, \tag{C.22c}$$

$$= \int_{\Omega_V} \left(\boldsymbol{\epsilon} \colon \boldsymbol{FP}^T\right)_i dV + \int_{\Omega_V} (\boldsymbol{x} \times \mathrm{DIV}\boldsymbol{P})_i\, dV, \tag{C.22d}$$

where $\boldsymbol{\epsilon}$ is the permutation tensor, introduced here to represent the tensor cross product, as defined in equation A.16 in section A.2 of Appendix A.

Using the definition provided for the velocity vector $\boldsymbol{v}$ in equation B.2 and the definition of the linear momentum per unit of initial volume $\boldsymbol{p} = \rho_0 \boldsymbol{v}$, one can write

$$\frac{\partial \boldsymbol{x}}{\partial t} = \frac{\boldsymbol{p}}{\rho_0}. \tag{C.23}$$

Using C.23 and noticing from equation C.18 that

$$\frac{\partial \boldsymbol{p}}{\partial t} = \boldsymbol{b}_0 + \mathrm{DIV}\boldsymbol{P}, \tag{C.24}$$

allows equation C.21 to be rewritten as

$$\frac{\partial \boldsymbol{x}}{\partial t} \times \boldsymbol{p} + \boldsymbol{x} \times \frac{\partial \boldsymbol{p}}{\partial t} - \mathrm{DIV}\,(\boldsymbol{x} \boldsymbol{\times} \boldsymbol{P}) = \boldsymbol{x} \times \boldsymbol{b}_0, \tag{C.25a}$$

$$\frac{\boldsymbol{p}}{\rho_0} \times \boldsymbol{p} + \boldsymbol{x} \times (\boldsymbol{b}_0 + \mathrm{DIV}\boldsymbol{P}) - \mathrm{DIV}\,(\boldsymbol{x} \boldsymbol{\times} \boldsymbol{P}) = \boldsymbol{x} \times \boldsymbol{b}_0, \tag{C.25b}$$

$$\boldsymbol{x} \times (\mathrm{DIV}\boldsymbol{P}) = \mathrm{DIV}\,(\boldsymbol{x} \boldsymbol{\times} \boldsymbol{P})\,. \tag{C.25c}$$

Equation C.25c implies that the term $\boldsymbol{\epsilon} \colon \boldsymbol{FP}^T$ in equation C.22d must vanish. Indeed, back to section B.3 of Appendix B, one can see that $\boldsymbol{FP}^T = J\boldsymbol{\sigma}^T = J\boldsymbol{\sigma}$

(see table B.1) and as a consequence of symmetry of the Cauchy stress tensor, it can be verified that

$$\boldsymbol{\epsilon}\colon \boldsymbol{F}\boldsymbol{P}^T = \boldsymbol{\epsilon}\colon J\boldsymbol{\sigma}^T = J \begin{bmatrix} \sigma_{32} - \sigma_{23} \\ \sigma_{13} - \sigma_{31} \\ \sigma_{21} - \sigma_{12} \end{bmatrix} = \boldsymbol{0}. \tag{C.26}$$

## C.5 Energy balance principle

An energy equation can be derived by multiplying equation C.18 by the velocity vector $\boldsymbol{v}$, resulting in

$$\frac{\partial \boldsymbol{p}}{\partial t} \cdot \boldsymbol{v} - (\mathrm{DIV}\boldsymbol{P}) \cdot \boldsymbol{v} = \boldsymbol{b}_0 \cdot \boldsymbol{v}. \tag{C.27}$$

With the aid of the divergence theorem and the properties presented in equations A.35 and A.40c, integrating C.27 over the initial domain gives

$$\int_{\Omega_V} \frac{\partial(\rho_0 \boldsymbol{v})}{\partial t} \cdot \boldsymbol{v}\, dV + \int_{\Omega_V} \boldsymbol{P}\colon \boldsymbol{\nabla_X v}\, dV - \int_{\Omega_V} \mathrm{DIV}\big(\boldsymbol{P}^T\boldsymbol{v}\big)\, dV = \int_{\Omega_V} \boldsymbol{b}_0 \cdot \boldsymbol{v}\, dV, \tag{C.28a}$$

$$\int_{\Omega_V} \frac{\partial(\rho_0 \boldsymbol{v})}{\partial t} \cdot \boldsymbol{v}\, dV + \int_{\Omega_V} \boldsymbol{P}\colon \frac{\partial \boldsymbol{v}}{\partial \boldsymbol{X}}\, dV - \int_{\partial\Omega_V} \big(\boldsymbol{P}^T\boldsymbol{v}\big) \cdot \boldsymbol{N}\, dA = \int_{\Omega_V} \boldsymbol{b}_0 \cdot \boldsymbol{v}\, dV, \tag{C.28b}$$

$$\frac{d}{dt}\int_{\Omega_V} \frac{1}{2}\rho_0 \boldsymbol{v} \cdot \boldsymbol{v}\, dV + \int_{\Omega_V} \boldsymbol{P}\colon \frac{\partial \boldsymbol{v}}{\partial \boldsymbol{X}}\, dV - \int_{\partial\Omega_V} (\boldsymbol{P}\boldsymbol{N}) \cdot \boldsymbol{v}\, dA = \int_{\Omega_V} \boldsymbol{b}_0 \cdot \boldsymbol{v}\, dV, \tag{C.28c}$$

$$\frac{d}{dt}\int_{\Omega_V} \frac{1}{2}\rho_0 \boldsymbol{v} \cdot \boldsymbol{v}\, dV + \int_{\Omega_V} \boldsymbol{P}\colon \frac{\partial \boldsymbol{v}}{\partial \boldsymbol{X}}\, dV = \int_{\Omega_V} \boldsymbol{b}_0 \cdot \boldsymbol{v}\, dV + \int_{\partial\Omega_V} \boldsymbol{t}_0 \cdot \boldsymbol{v}\, dA. \tag{C.28d}$$

Noticing that the time derivative of $\boldsymbol{F}(\boldsymbol{X}, t)$ is related to the velocity vector $\boldsymbol{v}$ as

$$\frac{\partial \boldsymbol{F}}{\partial t} = \frac{\partial \boldsymbol{v}}{\partial \boldsymbol{X}} = \boldsymbol{\nabla_X v}. \tag{C.29}$$

C.28d can be rewritten as

$$\frac{d}{dt}\int_{\Omega_V} \frac{1}{2}\rho_0 \boldsymbol{v} \cdot \boldsymbol{v}\, dV + \int_{\Omega_V} \boldsymbol{P}\colon \dot{\boldsymbol{F}}\, dV = \int_{\Omega_V} \boldsymbol{b}_0 \cdot \boldsymbol{v}\, dV + \int_{\partial\Omega_V} \boldsymbol{t}_0 \cdot \boldsymbol{v}\, dA. \tag{C.30}$$

## C.6 Conservation laws for geometric quantities

Conservation of mass, linear and angular momentum are classic in mechanics. Following [44–47], conservation laws of geometric quantities such as the deformation gradient, the volume map (Jacobian of $\boldsymbol{F}$) and the area map (co-factor of $\boldsymbol{F}$) are now introduced aiming at the establishment of a mixed set of conservation laws.

The first presentation of this formulation in fast solid dynamics by Lee et al. [44, 45] had as unknowns the linear momentum, the deformation gradient and the total energy. With both the linear momentum and the deformation gradient tensor being primary variables of the problem, stresses converge at the same rate as the velocities and displacements. Moreover, the new formulation is shown to be efficient in nearly incompressible and bending dominated scenarios. However, in case of extreme deformations in the incompressible limit, the $\boldsymbol{p}-\boldsymbol{F}$ formulation lacks robustness. In [46], Gil et al. enhanced the formulation for nearly and truly incompressible deformations with the novelty of introducing a new conservation law for the Jacobian $J$ of the deformation gradient, providing extra flexibility to the scheme. In [47], a new geometric conservation law for the co-factor $\boldsymbol{H}$ of the deformation gradient was added to the framework leading to an enhanced mixed-formulation. The development of this new conservation equation was possible due to the simplification introduced by the use of a tensor cross product operation, presented for the first time in the context of solid mechanics in [48] and further explained in [49]. The evolution of works mentioned above resulted in a mixed methodology in the form of a system of first order conservation laws, where the equation of the conservation of the linear momentum $\boldsymbol{p}$ is supplemented with three geometric conservation laws, i.e., conservation of the deformation gradient $\boldsymbol{F}$, of the volume map $J$ (Jacobian) and of the area map $\boldsymbol{H}$ (co-factor).

As presented before, the volume map $J$ can be computed as

$$J = \det \boldsymbol{F}, \tag{C.31}$$

and the time derivative of $J$ coincides with the directional derivative of $J$ in the direction of the velocity $\boldsymbol{v}$ (see [88]), that is,

$$\dot{J} = DJ\,[\boldsymbol{v}] = D(\det \boldsymbol{F})\,[D\boldsymbol{F}\,[\boldsymbol{v}]]\,, \tag{C.32}$$

note that

$$D\boldsymbol{F}\,[\boldsymbol{v}] = \boldsymbol{\nabla_X v} = \boldsymbol{\nabla_X}\left(\frac{\boldsymbol{p}}{\rho_0}\right). \tag{C.33}$$

The tensor cross product introduced by Bonet et al. in [48, 49] (see Appendix A) plays a fundamental role in rewriting the area map $\boldsymbol{H} = J\boldsymbol{F}^{-T}$ defined in equation B.20d, which can now be written as

$$\boldsymbol{H} = \mathrm{cof}\boldsymbol{F} = \frac{1}{2}\boldsymbol{F} \times \boldsymbol{F}. \tag{C.34}$$

In addition, as presented in [25–27], a set of involutions needs to be satisfied by the conservation variables $\boldsymbol{F}$ and $\boldsymbol{H}$, they are: $\mathrm{CURL}\boldsymbol{F} = \boldsymbol{0}$ and $\mathrm{DIV}\boldsymbol{H} = \boldsymbol{0}$.

## C.6.1 Deformation gradient conservation principle

In order to derive the conservation of deformation gradient tensor, expression C.29 is alternatively written as (see the identity defined in equation A.40d)

$$\frac{\partial \boldsymbol{F}}{\partial t} - \mathrm{DIV}(\boldsymbol{v} \otimes \boldsymbol{I}) = \boldsymbol{0}, \tag{C.35}$$

where $\boldsymbol{I}$ is the identity tensor.

Integrating C.35 over the initial volume and with the aid of the divergence theorem and property A.33e, gives

$$\int_{\Omega_V} \frac{\partial \boldsymbol{F}}{\partial t}\, dV = \int_{\Omega_V} \mathrm{DIV}(\boldsymbol{v} \otimes \boldsymbol{I})\, dV, \tag{C.36a}$$

$$\frac{d}{dt}\int_{\Omega_V} \boldsymbol{F}\, dV = \int_{\partial\Omega_V} (\boldsymbol{v} \otimes \boldsymbol{I})\, \boldsymbol{N}\, dA, \tag{C.36b}$$

$$\frac{d}{dt}\int_{\Omega_V} \boldsymbol{F}\, dV = \int_{\partial\Omega_V} \boldsymbol{v} \otimes \boldsymbol{N}\, dA. \tag{C.36c}$$

### C.6.2 Area map conservation principle

The rate of change of $\boldsymbol{H}$ can be obtained by computing the directional derivative of $\boldsymbol{H}$ in the direction of velocity $\boldsymbol{v}$. The use of expression C.34 makes this operation easier, avoiding the need of computing derivatives of the inverse of the deformation gradient, as follows

$$\dot{\boldsymbol{H}} = D\boldsymbol{H}\,[\boldsymbol{v}] = D\left(\frac{1}{2}\boldsymbol{F} \times \boldsymbol{F}\right)[\boldsymbol{v}]\,, \tag{C.37a}$$

$$= \boldsymbol{F} \times D\boldsymbol{F}\,[\boldsymbol{v}], \tag{C.37b}$$

$$= \boldsymbol{F} \times \boldsymbol{\nabla}_{\boldsymbol{X}}\boldsymbol{v}. \tag{C.37c}$$

Alternatively, $\boldsymbol{H}$ can be defined as

$$\frac{1}{2}\boldsymbol{F} \times \boldsymbol{F} = \frac{1}{2}\mathrm{CURL}\,(\boldsymbol{x} \times \boldsymbol{F})\,. \tag{C.38}$$

In order to show the validity of the identity in C.38 it is convenient to express its terms in a component-wise form. The definition of the tensor cross product between two tensors (see equation A.18) can be particularised to the deformation gradient tensor, which is a second order two-point tensor, as

$$(\boldsymbol{F} \times \boldsymbol{F})_{iI} = \varepsilon_{ijk}\varepsilon_{IJK}F_{jJ}F_{kK}. \tag{C.39}$$

Writing the components of CURL($\boldsymbol{x} \times \boldsymbol{F}$) and using the fact that CURL$\boldsymbol{F} = \boldsymbol{0}$ shows the validity of the identity

$$(\mathrm{CURL}\,(\boldsymbol{x} \times \boldsymbol{F}))_{iI} = \varepsilon_{IJK}\frac{\partial\,(\boldsymbol{x} \times \boldsymbol{F})_{iK}}{\partial X_J} = \varepsilon_{IJK}\frac{\partial}{\partial X_J}(\varepsilon_{ijk}x_jF_{kK}), \tag{C.40a}$$

$$= \varepsilon_{ijk}\varepsilon_{IJK}\frac{\partial}{\partial X_J}(x_jF_{kK}), \tag{C.40b}$$

$$= \varepsilon_{ijk}\varepsilon_{IJK}\left(\frac{\partial x_j}{\partial X_J}F_{kK} + x_j\frac{\partial F_{kK}}{\partial X_J}\right), \tag{C.40c}$$

$$= \varepsilon_{ijk}\varepsilon_{IJK}F_{jJ}F_{kK}. \tag{C.40d}$$

Substituting C.38 in C.37a, leads to the following result

$$\frac{\partial \boldsymbol{H}}{\partial t} - \mathrm{CURL}\,(\boldsymbol{v} \times \boldsymbol{F}) = \boldsymbol{0}. \tag{C.41}$$

Integrating C.41 over the initial volume and with the aid of the divergence theorem gives

$$\int_{\Omega_V} \frac{\partial \boldsymbol{H}}{\partial t}\, dV = \int_{\Omega_V} \mathrm{CURL}\,(\boldsymbol{v} \times \boldsymbol{F})\, dV, \tag{C.42a}$$

$$\frac{d}{dt}\int_{\Omega_V} \boldsymbol{H}\, dV = -\int_{\partial\Omega_V} \boldsymbol{v} \times \boldsymbol{F} \times \boldsymbol{N}\, dA. \tag{C.42b}$$

Noticing that the minus sign in this equation comes from the permutation tensor

$$\int_{\Omega_V} \mathrm{CURL}\,(\boldsymbol{v} \times \boldsymbol{F})\, dV = \int_{\Omega_V} \varepsilon_{IJK} \frac{\partial}{\partial X_J} (\varepsilon_{ijk} v_j F_{kK})\, dV, \tag{C.43a}$$

$$= \int_{\Omega_V} \varepsilon_{IJK}\varepsilon_{ijk} \left( \frac{\partial}{\partial X_J} (v_j F_{kK}) \right) dV, \tag{C.43b}$$

$$= \int_{\partial\Omega_V} \varepsilon_{IJK}\varepsilon_{ijk} v_j F_{kK} N_J\, dA, \tag{C.43c}$$

$$= \int_{\partial\Omega_V} \varepsilon_{IJK} \left(\boldsymbol{v} \times \boldsymbol{F}\right)_{iK} N_J\, dA, \tag{C.43d}$$

$$= -\int_{\partial\Omega_V} \varepsilon_{IKJ} \left(\boldsymbol{v} \times \boldsymbol{F}\right)_{iK} N_J\, dA. \tag{C.43e}$$

### C.6.3 Volume map conservation principle

The mathematical expression of the conservation of the volume map, i.e., the Jacobian, can be easily obtained noticing that $J$ can be redefined as $J = \frac{1}{3}\boldsymbol{H} : \boldsymbol{F}$ (see [49]), this avoids computing the directional derivative of $\det \boldsymbol{F}$ in equation C.32, and therefore

$$\dot{J} = DJ\,[\boldsymbol{v}] = D\left(\frac{1}{3}\boldsymbol{H} : \boldsymbol{F}\right)[\boldsymbol{v}], \tag{C.44a}$$

$$= \frac{1}{3}\left[D\boldsymbol{H}\,[\boldsymbol{v}] : \boldsymbol{F} + \boldsymbol{H} : D\boldsymbol{F}\,[\boldsymbol{v}]\right], \tag{C.44b}$$

$$= \frac{1}{3}\left[(\boldsymbol{F} \times \boldsymbol{\nabla}_{\boldsymbol{X}}\boldsymbol{v}) : \boldsymbol{F} + \boldsymbol{H} : \boldsymbol{\nabla}_{\boldsymbol{X}}\boldsymbol{v}\right], \tag{C.44c}$$

$$= \frac{1}{3}\left[(\boldsymbol{F} \times \boldsymbol{F}) : \boldsymbol{\nabla}_{\boldsymbol{X}}\boldsymbol{v} + \boldsymbol{H} : \boldsymbol{\nabla}_{\boldsymbol{X}}\boldsymbol{v}\right], \tag{C.44d}$$

$$= \frac{1}{3}\left[2\boldsymbol{H} : \boldsymbol{\nabla}_{\boldsymbol{X}}\boldsymbol{v} + \boldsymbol{H} : \boldsymbol{\nabla}_{\boldsymbol{X}}\boldsymbol{v}\right], \tag{C.44e}$$

$$= \boldsymbol{H} : \boldsymbol{\nabla}_{\boldsymbol{X}}\left(\frac{\boldsymbol{p}}{\rho_0}\right), \tag{C.44f}$$

with $\boldsymbol{p} = \rho_0\boldsymbol{v}$.

Using the fact that $\mathrm{DIV}\boldsymbol{H} = \boldsymbol{0}$ together with the identity A.40c, equation C.44f can be rewritten leading to the expression for the conservation of $J$

$$\frac{\partial J}{\partial t} - \mathrm{DIV}\left(\boldsymbol{H}^T\boldsymbol{v}\right) = 0. \tag{C.45}$$

Integrating C.45 over the initial volume and with the aid of the divergence theorem gives

$$\int_{\Omega_V} \frac{\partial J}{\partial t}\, dV = \int_{\Omega_V} \mathrm{DIV}\left(\boldsymbol{H}^T \boldsymbol{v}\right) dV, \tag{C.46a}$$

$$\frac{d}{dt}\int_{\Omega_V} J\, dV = \int_{\partial\Omega_V} \left(\boldsymbol{H}^T \boldsymbol{v}\right) \cdot \boldsymbol{N}\, dA. \tag{C.46b}$$

## C.7 Lagrangian formulations

Let us consider a mixed-based formulation $[\boldsymbol{p}, \boldsymbol{F}, \boldsymbol{H}, J]$. The expressions for the conservation of linear momentum (equation C.18), deformation gradient tensor (equation C.35), area map (equation C.41) and volume map (equation C.45) were presented in terms of the initial configuration, in a Total Lagrangian Formulation (TLF). In order to write these equations in terms of the current configuration (see figure 2.1), in an Updated Lagrangian Formulation (ULF), one can push forward the TLF equations. Moreover, one may want to write the same equations in terms of the intermediate configuration $\Omega_{V\boldsymbol{x}}$, in this work this approach is called updated reference Lagrangian formulation.

The total Lagrangian local form of the conservation law of linear momentum can be integrated over the initial volume in order to obtain its global form. By applying the divergence theorem and using $J$ and $\boldsymbol{H}$, the updated Lagrangian conservation law of linear momentum is obtained as follows

$$\frac{\partial \boldsymbol{p}}{\partial t} - \mathrm{DIV}\boldsymbol{P} = \boldsymbol{b}_0, \tag{C.47}$$

where $\boldsymbol{p} = \rho_0 \boldsymbol{v}$.

Integrating over the initial volume and applying the divergence theorem

$$\int_{\Omega_V} \frac{\partial\left(\rho_0 \boldsymbol{v}\right)}{\partial t}\, dV = \int_{\Omega_V} \boldsymbol{b}_0\, dV + \int_{\Omega_V} \mathrm{DIV}\boldsymbol{P}\, dV, \tag{C.48a}$$

$$= \int_{\Omega_V} \boldsymbol{b}_0\, dV + \int_{\partial\Omega_V} \boldsymbol{P}\boldsymbol{N}\, dA. \tag{C.48b}$$

Using $J$ and $\boldsymbol{H}$ in this expression we have

$$\int_{\Omega_v} \frac{\partial\left(\rho_0 \boldsymbol{v}\right)}{\partial t} J^{-1}\, dv = \int_{\Omega_v} \boldsymbol{b}_0 J^{-1}\, dv + \int_{\partial\Omega_v} \boldsymbol{P}\boldsymbol{H}^{-1}\boldsymbol{n}\, da, \tag{C.49a}$$

$$= \int_{\Omega_v} \boldsymbol{b}\, dv + \int_{\partial\Omega_v} \boldsymbol{\sigma}\boldsymbol{n}\, da, \tag{C.49b}$$

$$= \int_{\Omega_v} \boldsymbol{b}\, dv + \int_{\Omega_v} \mathrm{div}\boldsymbol{\sigma}\, dv. \tag{C.49c}$$

The local form is then given as

$$J^{-1}\frac{\partial \boldsymbol{p}}{\partial t} - \mathrm{div}\boldsymbol{\sigma} = \boldsymbol{b}. \tag{C.50}$$

A similar procedure can be performed for the conservation law of the deformation gradient tensor. Starting from equation C.36b and using $J$ and $\boldsymbol{H}$ to change the domain gives

$$\begin{aligned}\int_{\Omega_v} \frac{\partial \boldsymbol{F}}{\partial t} J^{-1}\, dv &= \int_{\partial\Omega_v} (\boldsymbol{v} \otimes \boldsymbol{I})\, \boldsymbol{H}^{-1}\boldsymbol{n}\, da, && \text{(C.51a)}\\ &= \int_{\Omega_v} \operatorname{div}\big(\boldsymbol{v} \otimes \boldsymbol{H}^{-1}\big)\, dv. && \text{(C.51b)}\end{aligned}$$

The local form is then given as

$$J^{-1}\frac{\partial \boldsymbol{F}}{\partial t} - \operatorname{div}\big(\boldsymbol{v} \otimes \boldsymbol{H}^{-1}\big) = \boldsymbol{0}. \tag{C.52}$$

The same procedure can also be applied for the conservation law of the area map, i.e., the co-factor of the deformation gradient tensor. Starting from equation C.42b and using $J$ and $\boldsymbol{H}$ gives

$$\begin{aligned}\int_{\Omega_v} \frac{\partial \boldsymbol{H}}{\partial t} J^{-1}\, dv &= -\int_{\partial\Omega_v} \boldsymbol{v} \times \boldsymbol{F} \times \boldsymbol{H}^{-1}\boldsymbol{n}\, da, && \text{(C.53a)}\\ &= -\int_{\Omega_v} \operatorname{div}\left(\boldsymbol{v} \times \boldsymbol{F} \times \boldsymbol{H}^{-1}\right) dv. && \text{(C.53b)}\end{aligned}$$

The local form is then given as

$$J^{-1}\frac{\partial \boldsymbol{H}}{\partial t} + \operatorname{div}\left(\boldsymbol{v} \times \boldsymbol{F} \times \boldsymbol{H}^{-1}\right) = \boldsymbol{0}, \tag{C.54}$$

or after further manipulations as

$$J^{-1}\frac{\partial \boldsymbol{H}}{\partial t} - \operatorname{div}\left(\boldsymbol{F} \times \big(\boldsymbol{v} \otimes \boldsymbol{H}^{-1}\big)\right) = \boldsymbol{0}. \tag{C.55}$$

Finally, for the conservation law of the volume map, i.e., the Jacobian of the deformation gradient tensor, starting from equation C.46b and using $J$ and $\boldsymbol{H}$ gives

$$\begin{aligned}\int_{\Omega_v} \frac{\partial J}{\partial t} J^{-1}\, dv &= \int_{\partial\Omega_v} \big(\boldsymbol{H}^T\boldsymbol{v}\big) \cdot \boldsymbol{H}^{-1}\boldsymbol{n}\, da, && \text{(C.56a)}\\ &= \int_{\partial\Omega_v} \boldsymbol{v} \cdot \boldsymbol{H}\boldsymbol{H}^{-1}\boldsymbol{n}\, da, && \text{(C.56b)}\\ &= \int_{\Omega_v} \operatorname{div}\boldsymbol{v}\, dv. && \text{(C.56c)}\end{aligned}$$

The local form is then given as

$$J^{-1}\frac{\partial J}{\partial t} - \operatorname{div}\boldsymbol{v} = 0. \tag{C.57}$$

A summary of the equations in both formulation is presented in table C.1.

| **Total Lagrangian vs. Updated Lagrangian** | |
|---|---|
| TLF | ULF |
| $\frac{\partial \boldsymbol{p}}{\partial t} - \text{DIV}\boldsymbol{P} = \boldsymbol{b}_0$<br>$\int_{\Omega_V} \frac{\partial(\rho_0 \boldsymbol{v})}{\partial t}\, dV = \int_{\Omega_V} \boldsymbol{b}_0\, dV + \int_{\partial\Omega_V} \boldsymbol{P}\boldsymbol{N}\, dA$ | $J^{-1}\frac{\partial \boldsymbol{p}}{\partial t} - \text{div}\boldsymbol{\sigma} = \boldsymbol{b}$<br>$\int_{\Omega_v} J^{-1}\frac{\partial(J\rho\boldsymbol{v})}{\partial t}\, dv = \int_{\Omega_v} \boldsymbol{b}\, dv + \int_{\partial\Omega_v} \boldsymbol{\sigma}\boldsymbol{n}\, da$ |
| $\frac{\partial \boldsymbol{F}}{\partial t} - \text{DIV}(\boldsymbol{v}\otimes\boldsymbol{I}) = \boldsymbol{0}$<br>$\int_{\Omega_V} \frac{\partial \boldsymbol{F}}{\partial t}\, dV = \int_{\partial\Omega_V} (\boldsymbol{v}\otimes\boldsymbol{I})\,\boldsymbol{N}\, dA$ | $J^{-1}\frac{\partial \boldsymbol{F}}{\partial t} - \text{div}\big(\boldsymbol{v}\otimes\boldsymbol{H}^{-1}\big) = \boldsymbol{0}$<br>$\int_{\Omega_v} J^{-1}\frac{\partial \boldsymbol{F}}{\partial t}\, dv = \int_{\partial\Omega_v} \big(\boldsymbol{v}\otimes\boldsymbol{H}^{-1}\big)\,\boldsymbol{n}\, da$ |
| $\frac{\partial \boldsymbol{H}}{\partial t} - \text{CURL}\,(\boldsymbol{v}\times\boldsymbol{F}) = \boldsymbol{0}$<br>$\int_{\Omega_V} \frac{\partial \boldsymbol{H}}{\partial t}\, dV = -\int_{\partial\Omega_V} \boldsymbol{v}\times\boldsymbol{F}\times\boldsymbol{N}\, dA$ | $J^{-1}\frac{\partial \boldsymbol{H}}{\partial t} + \text{div}\,\big(\boldsymbol{v}\times\boldsymbol{F}\times\boldsymbol{H}^{-1}\big) = \boldsymbol{0}$<br>$\int_{\Omega_v} J^{-1}\frac{\partial \boldsymbol{H}}{\partial t}\, dv = -\int_{\partial\Omega_v} \boldsymbol{v}\times\boldsymbol{F}\times\boldsymbol{H}^{-1}\boldsymbol{n}\, da$ |
| $\frac{\partial J}{\partial t} - \text{DIV}\,\big(\boldsymbol{H}^T\boldsymbol{v}\big) = 0$<br>$\int_{\Omega_V} \frac{\partial J}{\partial t}\, dV = \int_{\partial\Omega_V} \big(\boldsymbol{H}^T\boldsymbol{v}\big)\cdot\boldsymbol{N}\, dA$ | $J^{-1}\frac{\partial J}{\partial t} - \text{div}\boldsymbol{v} = 0$<br>$\int_{\Omega_v} J^{-1}\frac{\partial J}{\partial t}\, dv = \int_{\partial\Omega_v} \boldsymbol{v}\cdot\boldsymbol{n}\, da$ |
| with $\boldsymbol{p} = \rho_0\boldsymbol{v},\ \rho_0 = J\rho$ | |

Table C.1: Summary of the conservation laws of $[\boldsymbol{p}, \boldsymbol{F}, \boldsymbol{H}, J]$.

Following the same procedures, the TLF equations can be pushed forward to the intermediate configuration. For this purpose, instead of using $\boldsymbol{F}$, $\boldsymbol{H}$ and $J$, one should use $\boldsymbol{F}_{\boldsymbol{\chi}}$, $\boldsymbol{H}_{\boldsymbol{\chi}}$ and $J_{\boldsymbol{\chi}}$, resulting in

$$J_{\boldsymbol{\chi}}^{-1}\frac{\partial \boldsymbol{p}}{\partial t} - \text{div}_{\boldsymbol{\chi}}\left(J_{\boldsymbol{\chi}}^{-1}\boldsymbol{P}\boldsymbol{F}_{\boldsymbol{\chi}}^T\right) = J_{\boldsymbol{\chi}}^{-1}\boldsymbol{b}_0, \tag{C.58}$$

$$J_{\boldsymbol{\chi}}^{-1}\frac{\partial \boldsymbol{F}}{\partial t} - \text{div}_{\boldsymbol{\chi}}\big(\boldsymbol{v}\otimes\boldsymbol{H}_{\boldsymbol{\chi}}^{-1}\big) = \boldsymbol{0}, \tag{C.59}$$

$$J_{\boldsymbol{\chi}}^{-1}\frac{\partial \boldsymbol{H}}{\partial t} - \text{div}_{\boldsymbol{\chi}}\left(\boldsymbol{F}\times\big(\boldsymbol{v}\otimes\boldsymbol{H}_{\boldsymbol{\chi}}^{-1}\big)\right) = \boldsymbol{0} \tag{C.60}$$

$$J_{\boldsymbol{\chi}}^{-1}\frac{\partial J}{\partial t} - \text{div}_{\boldsymbol{\chi}}\left(\boldsymbol{H}_{\boldsymbol{\chi}}^{-T}\boldsymbol{H}^T\boldsymbol{v}\right) = 0. \tag{C.61}$$

By noticing that $\boldsymbol{F} := \boldsymbol{f}\boldsymbol{F}_{\boldsymbol{\chi}}$, $\boldsymbol{H} := \boldsymbol{h}\boldsymbol{H}_{\boldsymbol{\chi}}$, $J := jJ_{\boldsymbol{\chi}}$ and with the use of appropriate involutions $(\text{curl}_{\boldsymbol{\chi}}\left(\boldsymbol{F}\boldsymbol{F}_{\boldsymbol{\chi}}^{-1}\right) = \boldsymbol{0}; \text{div}_{\boldsymbol{\chi}}\left(\boldsymbol{H}\boldsymbol{H}_{\boldsymbol{\chi}}^{-1}\right) = \boldsymbol{0})$, these equations can be rewritten in a much simpler way, in terms of the incremental quantities $\boldsymbol{f}$, $\boldsymbol{h}$ and $j$

$$\frac{\partial \boldsymbol{p}_{\boldsymbol{\chi}}}{\partial t} = \text{div}_{\boldsymbol{\chi}}\boldsymbol{\sigma}_{\boldsymbol{\chi}} + \boldsymbol{b}_{\boldsymbol{\chi}} \tag{C.62}$$

$$\frac{\partial \boldsymbol{f}}{\partial t} = \boldsymbol{\nabla}_{\boldsymbol{\chi}}\boldsymbol{v}, \tag{C.63}$$

$$\frac{\partial \boldsymbol{h}}{\partial t} = \boldsymbol{f}\times\boldsymbol{\nabla}_{\boldsymbol{\chi}}\boldsymbol{v}, \tag{C.64}$$

$$\frac{\partial j}{\partial t} = \boldsymbol{h} \colon \boldsymbol{\nabla}_{\boldsymbol{\chi}}\boldsymbol{v}, \tag{C.65}$$

where $\boldsymbol{b}_{\boldsymbol{\chi}} = J_{\boldsymbol{\chi}}^{-1}\boldsymbol{b}_0 = j\boldsymbol{b}$; $\boldsymbol{p}_{\boldsymbol{\chi}} = J_{\boldsymbol{\chi}}^{-1}\boldsymbol{p} = J_{\boldsymbol{\chi}}^{-1}\rho_0\boldsymbol{v} = \rho_{\boldsymbol{\chi}}\boldsymbol{v} = j\rho\boldsymbol{v}$ and the stress tensor $\boldsymbol{\sigma}_{\boldsymbol{\chi}} = J_{\boldsymbol{\chi}}^{-1}\boldsymbol{P}\boldsymbol{F}_{\boldsymbol{\chi}}^T$ can alternatively be seen as $\boldsymbol{\sigma}_{\boldsymbol{\chi}} = \boldsymbol{P}\boldsymbol{H}_{\boldsymbol{\chi}}^{-1} = \boldsymbol{P}\boldsymbol{H}^{-1}\boldsymbol{h} = \boldsymbol{\sigma}\boldsymbol{h}$.

It is interesting to notice the following algebraic manipulations performed in order to obtain these equations. Starting from C.29 and using $\boldsymbol{F} \coloneqq \boldsymbol{f}\boldsymbol{F}_{\boldsymbol{\chi}}$ results in

$$\begin{aligned}
\dot{\boldsymbol{F}} &= \dot{\boldsymbol{f}}\boldsymbol{F}_{\boldsymbol{\chi}} + \boldsymbol{f}\dot{\boldsymbol{F}}_{\boldsymbol{\chi}} = \dot{\boldsymbol{f}}\boldsymbol{F}_{\boldsymbol{\chi}} = \boldsymbol{\nabla}_{\boldsymbol{X}}\boldsymbol{v}, \\
\dot{\boldsymbol{f}} &= \left(\boldsymbol{\nabla}_{\boldsymbol{X}}\boldsymbol{v}\right)\boldsymbol{F}_{\boldsymbol{\chi}}^{-1} = \boldsymbol{\nabla}_{\boldsymbol{\chi}}\boldsymbol{v},
\end{aligned} \tag{C.66}$$

which is equal to C.63.

The curl free nature of $\boldsymbol{F}$ allowed equation C.37c to be rewritten as C.41, using $\boldsymbol{H} \coloneqq \boldsymbol{h}\boldsymbol{H}_{\boldsymbol{\chi}}$ and the property A.38e of the tensor cross product in C.37c results in

$$\dot{\boldsymbol{H}} = \dot{\boldsymbol{h}}\boldsymbol{H}_{\boldsymbol{\chi}} + \boldsymbol{h}\dot{\boldsymbol{H}}_{\boldsymbol{\chi}} = \dot{\boldsymbol{h}}\boldsymbol{H}_{\boldsymbol{\chi}} = \boldsymbol{F} \times \boldsymbol{\nabla}_{\boldsymbol{X}}\boldsymbol{v}, \tag{C.67a}$$

$$\dot{\boldsymbol{h}} = \left(\boldsymbol{F} \times \boldsymbol{\nabla}_{\boldsymbol{X}}\boldsymbol{v}\right)\boldsymbol{H}_{\boldsymbol{\chi}}^{-1}, \tag{C.67b}$$

$$\dot{\boldsymbol{h}} = \left(\boldsymbol{f}\boldsymbol{F}_{\boldsymbol{\chi}} \times \left(\boldsymbol{\nabla}_{\boldsymbol{\chi}}\boldsymbol{v}\right)\boldsymbol{F}_{\boldsymbol{\chi}}\right)\boldsymbol{H}_{\boldsymbol{\chi}}^{-1}, \tag{C.67c}$$

$$\dot{\boldsymbol{h}} = \boldsymbol{f} \times \boldsymbol{\nabla}_{\boldsymbol{\chi}}\boldsymbol{v}, \tag{C.67d}$$

which is equal to C.64.

The divergence free nature of $\boldsymbol{H}$ allowed equation C.44f to be rewritten as C.45, using $J \coloneqq jJ_{\boldsymbol{\chi}}$ and the property A.34a of the double contraction in C.44f results in

$$\dot{J} = \dot{j}J_{\boldsymbol{\chi}} + j\dot{J}_{\boldsymbol{\chi}} = \dot{j}J_{\boldsymbol{\chi}} = \boldsymbol{H} \colon \boldsymbol{\nabla}_{\boldsymbol{X}}\boldsymbol{v}, \tag{C.68a}$$

$$\dot{j} = \left(\boldsymbol{H} \colon \boldsymbol{\nabla}_{\boldsymbol{X}}\boldsymbol{v}\right)J_{\boldsymbol{\chi}}^{-1}, \tag{C.68b}$$

$$\dot{j} = \left(\boldsymbol{h}\boldsymbol{H}_{\boldsymbol{\chi}} \colon \left(\boldsymbol{\nabla}_{\boldsymbol{\chi}}\boldsymbol{v}\right)\boldsymbol{F}_{\boldsymbol{\chi}}\right)J_{\boldsymbol{\chi}}^{-1}, \tag{C.68c}$$

$$\dot{j} = \big(\boldsymbol{h}\boldsymbol{H}_{\boldsymbol{\chi}}\boldsymbol{F}_{\boldsymbol{\chi}}^{T} \colon \left(\boldsymbol{\nabla}_{\boldsymbol{\chi}}\boldsymbol{v}\right)\big)J_{\boldsymbol{\chi}}^{-1}, \tag{C.68d}$$

$$\dot{j} = \left(\boldsymbol{h}J_{\boldsymbol{\chi}} \colon \left(\boldsymbol{\nabla}_{\boldsymbol{\chi}}\boldsymbol{v}\right)\right)J_{\boldsymbol{\chi}}^{-1}, \tag{C.68e}$$

$$\dot{j} = \boldsymbol{h} \colon \boldsymbol{\nabla}_{\boldsymbol{\chi}}\boldsymbol{v}, \tag{C.68f}$$

which is equal to C.65.

## C.8 First law of thermodynamics

In a standard Total Lagrangian Formulation the first law of thermodynamics is written in terms of the total energy of the system $E$ as

$$\frac{\partial E}{\partial t} - \mathrm{DIV}\left(\boldsymbol{P}^{T}\boldsymbol{v} - \boldsymbol{Q}\right) = \boldsymbol{b}_0 \cdot \boldsymbol{v} + s_0, \tag{C.69}$$

where $E$ is the total energy per unit of undeformed volume, $\boldsymbol{P}$ represents the first Piola-Kirchhoff stress tensor, $\boldsymbol{Q}$ represents the Lagrangian heat flux vector, $s_0$ denotes a possible heat source term, $\boldsymbol{b}_0$ is the body force per unit of initial volume and $\boldsymbol{v} = \rho_0^{-1}\boldsymbol{p}$ is the velocity.

Equation C.69, in its integral form, is given as

$$\frac{d}{dt}\int_{\Omega_V} E\, dV = \int_{\partial\Omega_V} \left(\boldsymbol{P}^{T}\boldsymbol{v} - \boldsymbol{Q}\right) \cdot \boldsymbol{N}\, dA + \int_{\Omega_V} \left(\boldsymbol{b}_0 \cdot \boldsymbol{v} + s_0\right) dV. \tag{C.70}$$

The left hand side of equation C.70, as well as the second term on the right hand side can be rewritten in terms of the intermediate configuration by using $J_{\boldsymbol{\chi}}$, as follows

$$\frac{d}{dt}\int_{\Omega_V} E\,dV = \frac{d}{dt}\int_{\Omega_V^{\boldsymbol{\chi}}} J_{\boldsymbol{\chi}}^{-1} E\,dV^{\boldsymbol{\chi}} = \frac{d}{dt}\int_{\Omega_V^{\boldsymbol{\chi}}} E_{\boldsymbol{\chi}}\,dV^{\boldsymbol{\chi}}, \tag{C.71}$$

and

$$\int_{\Omega_V} (\boldsymbol{b}_0\cdot\boldsymbol{v} + s_0)\,dV = \int_{\Omega_V^{\boldsymbol{\chi}}} J_{\boldsymbol{\chi}}^{-1}(\boldsymbol{b}_0\cdot\boldsymbol{v} + s_0)\,dV^{\boldsymbol{\chi}} = \int_{\Omega_V^{\boldsymbol{\chi}}} (\boldsymbol{b}_{\boldsymbol{\chi}}\cdot\boldsymbol{v} + s_{\boldsymbol{\chi}})\,dV^{\boldsymbol{\chi}}. \tag{C.72}$$

The first term on the right hand side of equation C.70, on the other hand, can be obtained in terms of the intermediate configuration by making use of the Nanson's rule, i.e., using $\boldsymbol{H}_{\boldsymbol{\chi}}\boldsymbol{N}dA = \boldsymbol{N}^{\boldsymbol{\chi}}dA^{\boldsymbol{\chi}}$

$$\int_{\partial\Omega_V} \left(\boldsymbol{P}^T\boldsymbol{v} - \boldsymbol{Q}\right)\cdot\boldsymbol{N}\,dA = \int_{\partial\Omega_V^{\boldsymbol{\chi}}} \left(\boldsymbol{P}^T\boldsymbol{v} - \boldsymbol{Q}\right)\cdot\boldsymbol{H}_{\boldsymbol{\chi}}^{-1}\boldsymbol{N}^{\boldsymbol{\chi}}\,dA^{\boldsymbol{\chi}}, \tag{C.73a}$$

$$= \int_{\partial\Omega_V^{\boldsymbol{\chi}}} (\boldsymbol{v}\otimes\boldsymbol{N}^{\boldsymbol{\chi}}) : \left(\boldsymbol{P}\boldsymbol{H}_{\boldsymbol{\chi}}^{-1}\right)dA^{\boldsymbol{\chi}} - \int_{\partial\Omega_V^{\boldsymbol{\chi}}} \left(\boldsymbol{H}_{\boldsymbol{\chi}}^{-T}\boldsymbol{Q}\right)\cdot\boldsymbol{N}^{\boldsymbol{\chi}}\,dA^{\boldsymbol{\chi}}, \tag{C.73b}$$

$$= \int_{\partial\Omega_V^{\boldsymbol{\chi}}} \left(\boldsymbol{\sigma}_{\boldsymbol{\chi}}^T\boldsymbol{v}\right)\cdot\boldsymbol{N}^{\boldsymbol{\chi}}\,dA^{\boldsymbol{\chi}} - \int_{\partial\Omega_V^{\boldsymbol{\chi}}} \boldsymbol{Q}_{\boldsymbol{\chi}}\cdot\boldsymbol{N}^{\boldsymbol{\chi}}\,dA^{\boldsymbol{\chi}}, \tag{C.73c}$$

with

$$\boldsymbol{Q}_{\boldsymbol{\chi}} = -\boldsymbol{K}_{\boldsymbol{\chi}}\boldsymbol{\nabla}_{\boldsymbol{\chi}}\theta, \tag{C.74}$$

and

$$\boldsymbol{K}_{\boldsymbol{\chi}} = j^{-1}k\boldsymbol{h}^T\boldsymbol{h}. \tag{C.75}$$

Recalling that in TLF, $\boldsymbol{Q} = -\boldsymbol{K}\boldsymbol{\nabla}_{\boldsymbol{X}}\theta$ and $\boldsymbol{K} = J^{-1}k\boldsymbol{H}^T\boldsymbol{H}$, equations C.74 and C.75 can be demonstrated taking into account that

$$\boldsymbol{\nabla}_{\boldsymbol{X}}\theta = \boldsymbol{F}_{\boldsymbol{\chi}}^T\boldsymbol{\nabla}_{\boldsymbol{\chi}}\theta, \qquad J = jJ_{\boldsymbol{\chi}}, \quad \textbf{and} \quad \boldsymbol{H} = \boldsymbol{h}\boldsymbol{H}_{\boldsymbol{\chi}}. \tag{C.76}$$

Therefore, the term $\boldsymbol{H}_{\boldsymbol{\chi}}^{-T}\boldsymbol{Q}$ becomes

$$\boldsymbol{H}_{\boldsymbol{\chi}}^{-T}\boldsymbol{Q} = -\boldsymbol{H}_{\boldsymbol{\chi}}^{-T}\left(\boldsymbol{K}\boldsymbol{\nabla}_{\boldsymbol{X}}\theta\right), \tag{C.77a}$$

$$= -\left(\boldsymbol{H}_{\boldsymbol{\chi}}^{-T}\boldsymbol{K}\boldsymbol{F}_{\boldsymbol{\chi}}^T\right)\boldsymbol{\nabla}_{\boldsymbol{\chi}}\theta, \tag{C.77b}$$

$$= -\left(\boldsymbol{H}_{\boldsymbol{\chi}}^{-T}J^{-1}k\boldsymbol{H}^T\boldsymbol{H}\boldsymbol{F}_{\boldsymbol{\chi}}^T\right)\boldsymbol{\nabla}_{\boldsymbol{\chi}}\theta, \tag{C.77c}$$

$$= -\left(\boldsymbol{H}_{\boldsymbol{\chi}}^{-T}j^{-1}J_{\boldsymbol{\chi}}^{-1}k\boldsymbol{H}_{\boldsymbol{\chi}}^T\boldsymbol{h}^T\boldsymbol{h}\boldsymbol{H}_{\boldsymbol{\chi}}\boldsymbol{F}_{\boldsymbol{\chi}}^T\right)\boldsymbol{\nabla}_{\boldsymbol{\chi}}\theta, \tag{C.77d}$$

$$= -\left(j^{-1}k\boldsymbol{h}^T\boldsymbol{h}\right)\boldsymbol{\nabla}_{\boldsymbol{\chi}}\theta, \tag{C.77e}$$

$$= -\boldsymbol{K}_{\boldsymbol{\chi}}\boldsymbol{\nabla}_{\boldsymbol{\chi}}\theta = \boldsymbol{Q}_{\boldsymbol{\chi}}. \tag{C.77f}$$

Combining the derivations presented above gives

$$\frac{d}{dt}\int_{\Omega_V^{\boldsymbol{\chi}}} E_{\boldsymbol{\chi}}\, dV^{\boldsymbol{\chi}} = \int_{\partial\Omega_V^{\boldsymbol{\chi}}} \left(\boldsymbol{\sigma}_{\boldsymbol{\chi}}^T\boldsymbol{v} - \boldsymbol{Q}_{\boldsymbol{\chi}}\right) \cdot \boldsymbol{N}^{\boldsymbol{\chi}}\, dA^{\boldsymbol{\chi}} + \int_{\Omega_V^{\boldsymbol{\chi}}} \left(\boldsymbol{b}_{\boldsymbol{\chi}} \cdot \boldsymbol{v} + s_{\boldsymbol{\chi}}\right) dV^{\boldsymbol{\chi}}, \tag{C.78}$$

with the corresponding local form given as

$$\frac{\partial E_{\boldsymbol{\chi}}}{\partial t} - \operatorname{div}_{\boldsymbol{\chi}}\left(\boldsymbol{\sigma}_{\boldsymbol{\chi}}^T\boldsymbol{v} - \boldsymbol{Q}_{\boldsymbol{\chi}}\right) = \boldsymbol{b}_{\boldsymbol{\chi}} \cdot \boldsymbol{v} + s_{\boldsymbol{\chi}}. \tag{C.79}$$

# Appendix D

# Conservation of angular momentum

## D.1 Introduction

In this appendix the monolithic discrete angular momentum projection algorithm presented in section 5.5 is further detailed.

## D.2 Angular momentum projection algorithm

Specifically, the local internal nodal force $\boldsymbol{T}_{ab}$ is modified (in a least-square sense) in order to preserve the total angular momentum, whilst still ensuring the global conservation of linear momentum.

Firstly, equations 5.38 can be combined as:

$$\begin{aligned}
\boldsymbol{\mathcal{U}}_a^{n+1} &= \frac{1}{3}\boldsymbol{\mathcal{U}}_a^{n} + \frac{2}{3}\left(\boldsymbol{\mathcal{U}}_a^{\star\star} + \Delta_t \dot{\boldsymbol{\mathcal{U}}}_a^{\star\star}\right), && \text{(D.1a)}\\
&= \frac{1}{3}\boldsymbol{\mathcal{U}}_a^{n} + \frac{2}{3}\left[\frac{3}{4}\boldsymbol{\mathcal{U}}_a^{n} + \frac{1}{4}\left(\boldsymbol{\mathcal{U}}_a^{\star} + \Delta_t \dot{\boldsymbol{\mathcal{U}}}_a^{\star}\right) + \Delta_t \dot{\boldsymbol{\mathcal{U}}}_a^{\star\star}\right], && \text{(D.1b)}\\
&= \frac{5}{6}\boldsymbol{\mathcal{U}}_a^{n} + \frac{1}{6}\boldsymbol{\mathcal{U}}_a^{\star} + \frac{\Delta_t}{6}\left(\dot{\boldsymbol{\mathcal{U}}}_a^{\star} + 4\dot{\boldsymbol{\mathcal{U}}}_a^{\star\star}\right), && \text{(D.1c)}\\
&= \frac{5}{6}\boldsymbol{\mathcal{U}}_a^{n} + \frac{1}{6}\left(\boldsymbol{\mathcal{U}}_a^{n} + \Delta_t \dot{\boldsymbol{\mathcal{U}}}_a^{n}\right) + \frac{\Delta_t}{6}\left(\dot{\boldsymbol{\mathcal{U}}}_a^{\star} + 4\,\dot{\boldsymbol{\mathcal{U}}}_a^{\star\star}\right), && \text{(D.1d)}\\
&= \boldsymbol{\mathcal{U}}_a^{n} + \frac{\Delta_t}{6}\left(\dot{\boldsymbol{\mathcal{U}}}_a^{n} + \dot{\boldsymbol{\mathcal{U}}}_a^{\star} + 4\dot{\boldsymbol{\mathcal{U}}}_a^{\star\star}\right). && \text{(D.1e)}
\end{aligned}$$

Hence, the geometry update is given as

$$\boldsymbol{x}_a^{n+1} - \boldsymbol{x}_a^{n} = \frac{\Delta_t}{6}\left(\boldsymbol{v}_a^{n} + \boldsymbol{v}_a^{\star} + 4\boldsymbol{v}_a^{\star\star}\right). \tag{D.2}$$

Sufficient conditions for the global preservation of the discrete linear and angular momentum within a time step are enforced at each stage of the three-stage Runge

Kutta time integrator, as follows

$$
\begin{aligned}
\mathbf{0} &= \sum_a V_a^{\boldsymbol{\chi}} \boldsymbol{x}_a^{n+1} \times \boldsymbol{p}_a^{n+1} - \sum_a V_a^{\boldsymbol{\chi}} \boldsymbol{x}_a^{n} \times \boldsymbol{p}_a^{n}, && \text{(D.3a)}\\
&= \sum_a V_a^{\boldsymbol{\chi}} \left[ \boldsymbol{x}_a^{n} + \frac{\Delta_t}{6\rho_{\boldsymbol{\chi},a}} \left( \boldsymbol{p}_a^{n} + \boldsymbol{p}_a^{\star} + 4\boldsymbol{p}_a^{\star\star} \right) \right] \times \boldsymbol{p}_a^{n+1} - \sum_a V_a^{\boldsymbol{\chi}} \boldsymbol{x}_a^{n} \times \boldsymbol{p}_a^{n}. && \text{(D.3b)}
\end{aligned}
$$

Defining

$$
\boldsymbol{x}_a^{n+\frac{1}{6}} = \boldsymbol{x}_a^{n} + \frac{\Delta_t}{6\rho_{\boldsymbol{\chi},a}} \boldsymbol{p}_a^{n}, \tag{D.4}
$$

then

$$
\begin{aligned}
\mathbf{0} &= \sum_a V_a^{\boldsymbol{\chi}} \left[ \boldsymbol{x}_a^{n+\frac{1}{6}} + \frac{\Delta_t}{6\rho_{\boldsymbol{\chi},a}} \left( \boldsymbol{p}_a^{\star} + 4\boldsymbol{p}_a^{\star\star} \right) \right] \times \boldsymbol{p}_a^{n+1} - \sum_a V_a^{\boldsymbol{\chi}} \boldsymbol{x}_a^{n} \times \boldsymbol{p}_a^{n} && \text{(D.5a)}\\
&- \sum_a V_a^{\boldsymbol{\chi}} \frac{\Delta_t}{6\rho_{\boldsymbol{\chi},a}} \boldsymbol{p}_a^{n} \times \boldsymbol{p}_a^{n},\\
&= \sum_a V_a^{\boldsymbol{\chi}} \boldsymbol{x}_a^{n+\frac{1}{6}} \times \left( \boldsymbol{p}_a^{n+1} - \boldsymbol{p}_a^{n} \right) + \frac{\Delta_t}{6\rho_{\boldsymbol{\chi},a}} \sum_a V_a^{\boldsymbol{\chi}} (\boldsymbol{p}_a^{\star} + 4\boldsymbol{p}_a^{\star\star}) \times \boldsymbol{p}_a^{n+1}, && \text{(D.5b)}\\
&= \sum_a V_a^{\boldsymbol{\chi}} \left[ \boldsymbol{x}_a^{n+\frac{1}{6}} + \frac{\Delta_t}{6\rho_{\boldsymbol{\chi},a}} \left( \boldsymbol{p}_a^{\star} + 4\boldsymbol{p}_a^{\star\star} \right) \right] \times \left( \boldsymbol{p}_a^{n+1} - \boldsymbol{p}_a^{n} \right) && \text{(D.5c)}\\
&- \sum_a V_a^{\boldsymbol{\chi}} \frac{\Delta_t}{6\rho_{\boldsymbol{\chi},a}} \boldsymbol{p}_a^{\star} \times \left( \boldsymbol{p}_a^{\star} - \boldsymbol{p}_a^{n} \right)\\
&- \sum_a V_a^{\boldsymbol{\chi}} \frac{\Delta_t}{6\rho_{\boldsymbol{\chi},a}} 4\boldsymbol{p}_a^{\star\star} \times \left( \boldsymbol{p}_a^{\star\star} - \boldsymbol{p}_a^{n} \right).
\end{aligned}
$$

Notice that

$$
\begin{aligned}
\boldsymbol{p}_a^{n+1} - \boldsymbol{p}_a^{n} &= \frac{\Delta_t}{6} \left( \dot{\boldsymbol{p}}_a^{n} + \dot{\boldsymbol{p}}_a^{\star} + 4\dot{\boldsymbol{p}}_a^{\star\star} \right), && \text{(D.6a)}\\
\boldsymbol{p}_a^{\star} - \boldsymbol{p}_a^{n} &= \Delta_t \dot{\boldsymbol{p}}_a^{n}, && \text{(D.6b)}\\
\boldsymbol{p}_a^{\star\star} - \boldsymbol{p}_a^{n} &= \frac{\Delta_t}{4} \left( \dot{\boldsymbol{p}}_a^{n} + \dot{\boldsymbol{p}}_a^{\star} \right). && \text{(D.6c)}
\end{aligned}
$$

Using this, equation D.5c can be rewritten as

$$\begin{aligned}
\mathbf{0} = &\sum_a V_a^{\boldsymbol{\chi}} \left[ \boldsymbol{x}_a^{n+\frac{1}{6}} + \frac{\Delta_t}{6\rho_{\boldsymbol{\chi},a}} \left( \boldsymbol{p}_a^\star + 4\boldsymbol{p}_a^{\star\star} \right) \right] \times \frac{\Delta_t}{6} \left( \dot{\boldsymbol{p}}_a^n + \dot{\boldsymbol{p}}_a^\star + 4\dot{\boldsymbol{p}}_a^{\star\star} \right) && \text{(D.7a)} \\
&- \sum_a V_a^{\boldsymbol{\chi}} \frac{\Delta_t}{6\rho_{\boldsymbol{\chi},a}} \boldsymbol{p}_a^\star \times \Delta_t \dot{\boldsymbol{p}}_a^n - \sum_a V_a^{\boldsymbol{\chi}} \frac{\Delta_t}{6\rho_{\boldsymbol{\chi},a}} 4\boldsymbol{p}_a^{\star\star} \times \frac{\Delta_t}{4} \left( \dot{\boldsymbol{p}}_a^n + \dot{\boldsymbol{p}}_a^\star \right), \\
= &\frac{\Delta_t}{6} \sum_a V_a^{\boldsymbol{\chi}} \underbrace{\left[ \boldsymbol{x}_a^{n+\frac{1}{6}} + \frac{\Delta_t}{6\rho_{\boldsymbol{\chi},a}} \left( \boldsymbol{p}_a^\star + 4\boldsymbol{p}_a^{\star\star} \right) - \frac{\Delta_t}{\rho_{\boldsymbol{\chi},a}} \boldsymbol{p}_a^\star - \frac{\Delta_t}{\rho_{\boldsymbol{\chi},a}} \boldsymbol{p}_a^{\star\star} \right]}_{\text{“A”}} \times \dot{\boldsymbol{p}}_a^n && \text{(D.7b)} \\
&+ \frac{\Delta_t}{6} \sum_a V_a^{\boldsymbol{\chi}} \underbrace{\left[ \boldsymbol{x}_a^{n+\frac{1}{6}} + \frac{\Delta_t}{6\rho_{\boldsymbol{\chi},a}} \left( \boldsymbol{p}_a^\star + 4\boldsymbol{p}_a^{\star\star} \right) - \frac{\Delta_t}{\rho_{\boldsymbol{\chi},a}} \boldsymbol{p}_a^{\star\star} \right]}_{\text{“B”}} \times \dot{\boldsymbol{p}}_a^\star \\
&+ \frac{\Delta_t}{6} \sum_a V_a^{\boldsymbol{\chi}} \left[ \boldsymbol{x}_a^{n+\frac{1}{6}} + \frac{\Delta_t}{6\rho_{\boldsymbol{\chi},a}} \left( \boldsymbol{p}_a^\star + 4\boldsymbol{p}_a^{\star\star} \right) \right] \times 4\dot{\boldsymbol{p}}_a^{\star\star}.
\end{aligned}$$

Further manipulations in the first term (“A”) highlighted in equation D.7b leads to

$$\begin{aligned}
\text{“A”} &= \boldsymbol{x}_a^n + \frac{\Delta_t}{6\rho_{\boldsymbol{\chi},a}} \boldsymbol{p}_a^n - \frac{5\Delta_t}{6\rho_{\boldsymbol{\chi},a}} \boldsymbol{p}_a^\star - \frac{\Delta_t}{3\rho_{\boldsymbol{\chi},a}} \boldsymbol{p}_a^{\star\star}, && \text{(D.8a)} \\
&= \boldsymbol{x}_a^n + \frac{\Delta_t}{6\rho_{\boldsymbol{\chi},a}} \boldsymbol{p}_a^n - \frac{5\Delta_t}{6\rho_{\boldsymbol{\chi},a}} \boldsymbol{p}_a^\star - \frac{\Delta_t}{4\rho_{\boldsymbol{\chi},a}} \boldsymbol{p}_a^n - \frac{\Delta_t}{12\rho_{\boldsymbol{\chi},a}} \left( \boldsymbol{p}_a^\star + \Delta_t \dot{\boldsymbol{p}}_a^\star \right), && \text{(D.8b)} \\
&= \boldsymbol{x}_a^n - \frac{\Delta_t}{12\rho_{\boldsymbol{\chi},a}} \boldsymbol{p}_a^n - \frac{11\Delta_t}{12\rho_{\boldsymbol{\chi},a}} \boldsymbol{p}_a^\star - \frac{\Delta_t^2}{12\rho_{\boldsymbol{\chi},a}} \dot{\boldsymbol{p}}_a^\star, && \text{(D.8c)} \\
&= \boldsymbol{x}_a^n - \frac{\Delta_t}{\rho_{\boldsymbol{\chi},a}} \boldsymbol{p}_a^n - \frac{11\Delta_t^2}{12\rho_{\boldsymbol{\chi},a}} \dot{\boldsymbol{p}}_a^n - \frac{\Delta_t^2}{12\rho_{\boldsymbol{\chi},a}} \dot{\boldsymbol{p}}_a^\star. && \text{(D.8d)}
\end{aligned}$$

As for the second term (“B”) highlighted in equation D.7b

$$\begin{aligned}
\text{“B”} &= \boldsymbol{x}_a^n + \frac{\Delta_t}{6\rho_{\boldsymbol{\chi},a}} \boldsymbol{p}_a^n + \frac{\Delta_t}{6\rho_{\boldsymbol{\chi},a}} \boldsymbol{p}_a^\star - \frac{\Delta_t}{3\rho_{\boldsymbol{\chi},a}} \boldsymbol{p}_a^{\star\star}, && \text{(D.9a)} \\
&= \boldsymbol{x}_a^n + \frac{\Delta_t}{3\rho_{\boldsymbol{\chi},a}} \boldsymbol{p}_a^n + \frac{\Delta_t^2}{6\rho_{\boldsymbol{\chi},a}} \dot{\boldsymbol{p}}_a^n - \frac{\Delta_t}{12\rho_{\boldsymbol{\chi},a}} \left( 4\boldsymbol{p}_a^n + \Delta_t \dot{\boldsymbol{p}}_a^n + \Delta_t \dot{\boldsymbol{p}}_a^\star \right), && \text{(D.9b)} \\
&= \boldsymbol{x}_a^n + \frac{\Delta_t^2}{12\rho_{\boldsymbol{\chi},a}} \dot{\boldsymbol{p}}_a^n - \frac{\Delta_t^2}{12\rho_{\boldsymbol{\chi},a}} \dot{\boldsymbol{p}}_a^\star. && \text{(D.9c)} \\
& && \text{(D.9d)}
\end{aligned}$$

Finally

$$\begin{aligned}
\mathbf{0} = &\sum_a V_a^{\boldsymbol{\chi}} \left( \boldsymbol{x}_a^n - \frac{\Delta_t}{\rho_{\boldsymbol{\chi},a}} \boldsymbol{p}_a^n - \frac{\Delta_t^2}{12\rho_{\boldsymbol{\chi},a}} \dot{\boldsymbol{p}}_a^\star \right) \times \dot{\boldsymbol{p}}_a^n + \sum_a V_a^{\boldsymbol{\chi}} \left( \boldsymbol{x}_a^n + \frac{\Delta_t^2}{12\rho_{\boldsymbol{\chi},a}} \dot{\boldsymbol{p}}_a^n \right) \times \dot{\boldsymbol{p}}_a^\star \\
&+ \sum_a V_a^{\boldsymbol{\chi}} 4 \left[ \boldsymbol{x}_a^{n+\frac{1}{6}} + \frac{\Delta_t}{6\rho_{\boldsymbol{\chi},a}} \left( \boldsymbol{p}_a^\star + 4\boldsymbol{p}_a^{\star\star} \right) \right] \times \dot{\boldsymbol{p}}_a^{\star\star}.
\end{aligned} \tag{D.10}$$

Therefore

$$\sum_a V_a^{\boldsymbol{\chi}} \boldsymbol{x}_a^{n-1} \times \dot{\boldsymbol{p}}_a^n = \boldsymbol{0}, \tag{D.11a}$$

$$\sum_a V_a^{\boldsymbol{\chi}} \left( \boldsymbol{x}_a^n + \frac{\Delta_t^2}{6\rho_{\boldsymbol{\chi},a}} \dot{\boldsymbol{p}}_a^n \right) \times \dot{\boldsymbol{p}}_a^{\star} = \boldsymbol{0}, \tag{D.11b}$$

$$\sum_a 4V_a^{\boldsymbol{\chi}} \left[ \boldsymbol{x}_a^n + \frac{\Delta_t}{6\rho_{\boldsymbol{\chi},a}} \left( \boldsymbol{p}_a^n + \boldsymbol{p}_a^{\star} + 4\boldsymbol{p}_a^{\star\star} \right) \right] \times \dot{\boldsymbol{p}}_a^{\star\star} = \boldsymbol{0}, \tag{D.11c}$$

$$\sum_a V_a^{\boldsymbol{\chi}} \left( \boldsymbol{x}_a^n + \frac{\Delta_t}{6\rho_{\boldsymbol{\chi},a}} \left( \boldsymbol{p}_a^{\star} - \boldsymbol{p}_a^n \right) \right) \times \dot{\boldsymbol{p}}_a^{\star} = \boldsymbol{0}. \tag{D.11d}$$

In summary, the constrains are as follows

$$\sum_a V_a^{\boldsymbol{\chi}} \boldsymbol{\xi}_a \times \dot{\boldsymbol{p}}_a^{\alpha} = \boldsymbol{0}, \tag{D.12}$$

with

$$\boldsymbol{\xi}_a = \boldsymbol{x}_a^n - \frac{\Delta_t}{\rho_{\boldsymbol{\chi},a}} \boldsymbol{p}_a^n, \qquad \text{for} \quad \alpha = n, \tag{D.13a}$$

$$\boldsymbol{\xi}_a = \boldsymbol{x}_a^n + \frac{\Delta_t}{6\rho_{\boldsymbol{\chi},a}} \left( \boldsymbol{p}_a^{\star} - \boldsymbol{p}_a^n \right), \qquad \text{for} \quad \alpha = \star, \tag{D.13b}$$

$$\boldsymbol{\xi}_a = \boldsymbol{x}_a^n + \frac{\Delta_t}{6\rho_{\boldsymbol{\chi},a}} \left( \boldsymbol{p}_a^n + \boldsymbol{p}_a^{\star} + 4\boldsymbol{p}_a^{\star\star} \right), \qquad \text{for} \quad \alpha = \star\star\,. \tag{D.13c}$$

With the objective of illustrating the capability of the framework to globally preserve the linear and angular momentum, a cube of unit side length is left free rotating in space. A uniform distribution of (10 x 10 x 10) particles was used and all sides are free. A tributary volume distribution was employed. The cube is subjected to an initial constant angular velocity $\boldsymbol{\omega}$ relative to its centroid, with $\boldsymbol{\omega} = \Omega\,[0, 0, 1]^T$, where $\Omega = 105 \frac{\text{rad}}{\text{s}}$. Initial density $\rho_0 = 1100 \frac{\text{kg}}{\text{m}^3}$, Young's modulus $E = 1.7 \times 10^7 \frac{\text{N}}{\text{m}^2}$ and Poisson's ratio $\nu = 0.3$ were adopted as the material parameters for a nearly incompressible neo-Hookean constitutive model. A fixed $\alpha_{CFL} = 0.9$ was used for the simulation.

The time evolution of the components of the total linear and angular momenta are shown in figures D.1a and D.1b, respectively. As it should be expected, the block exhibits no change in angular momentum when activating the discrete momentum projection algorithm. The global linear momentum is zero to machine precision. For illustration purposes, the time evolution of the deformation of the block with its pressure distribution is shown in figure D.2.

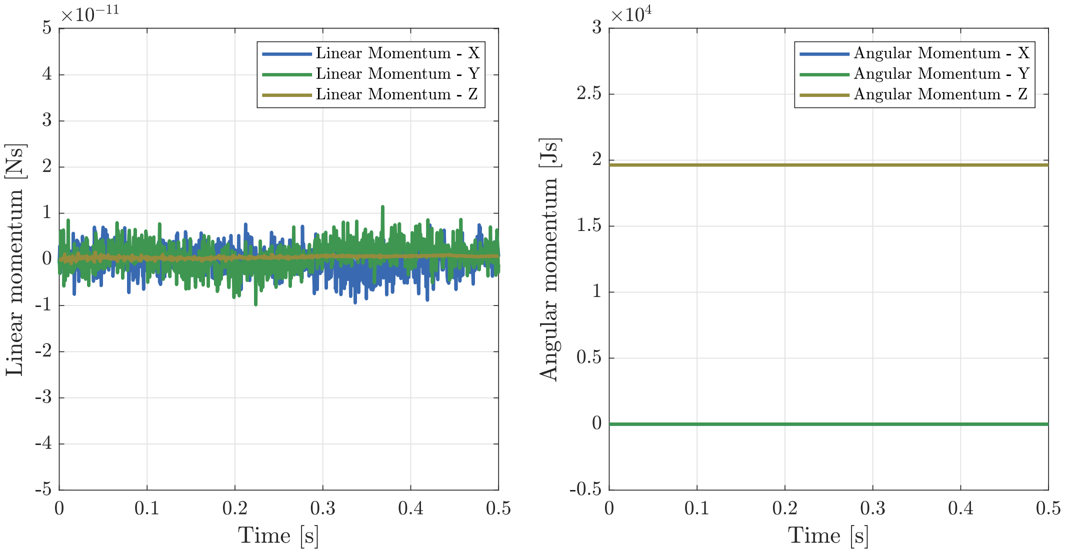

(a) (b)

Figure D.1: Spinning cube in an updated reference Lagrangian formulation, with updates performed at every time step, considering the angular momentum projection algorithm: (a) Evolution of the components of linear momentum. (b) Evolution of the components of angular momentum.

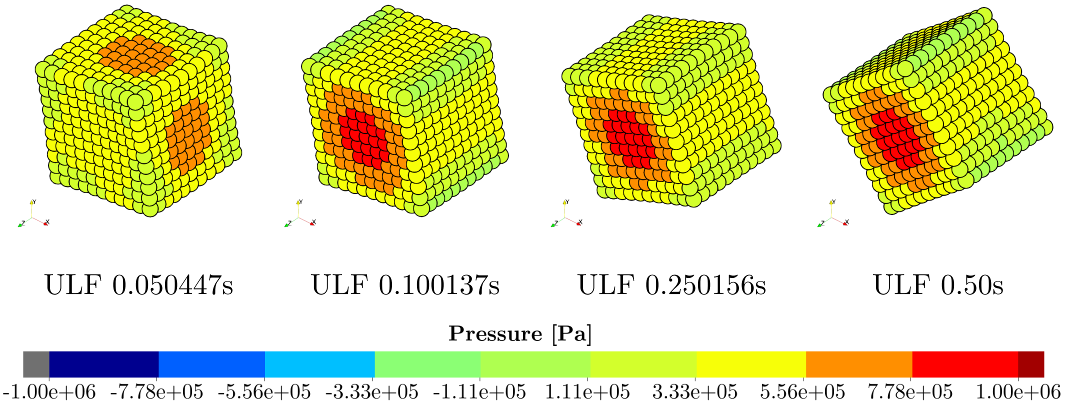

Figure D.2: Spinning cube pressure distribution.

# Bibliography

[1] T. Belytschko, Y. Krongauz, D. Organ, M. Fleming, and P. Krysl. "Meshless methods: An overview and recent developments". In: *Comput. Methods Appl. Mech. Engrg.* 139.1-4 (1996), pp. 3–47. DOI: `10.1016/S0045-7825(96)01078-X`.

[2] A. Huerta, T. Belytschko, S. Fernández-Méndez, T. Rabczuk, X. Zhuang, and M. Arroyo. "Meshfree methods". In: *Encyclopedia of Computational Mechanics Second Edition* 1.1 (2017). Ed. by R. Borst E. Stein and T. J. Hughes, pp. 1–38. DOI: `10.1002/9781119176817.ecm2005`.

[3] J. S. Chen, M. Hillman, and S. W. Chi. "Meshfree methods: Progress made after 20 years". In: *Journal of Engineering Mechanics* 143.4 (2017), pp. 1–38. DOI: `10.1061/(ASCE)EM.1943-7889.0001176`.

[4] R. A. Gingold and J. J. Monaghan. "Smoothed particle hydrodynamics: theory and application to non-spherical stars". In: *Monthly Notices of the Royal Astronomical Society* 181.3 (1977), pp. 375–389. DOI: `10.1093/mnras/181.3.375`.

[5] L. B. Lucy. "A numerical approach to the testing of the fission hypothesis". In: *The Astronomical Journal* 82.12 (1977), pp. 1013–1024.

[6] T. Belytschko, Y. Y. Lu, and L. GU. "Element-free Galerkin methods". In: *Int. J. Numer. Meth. Engng* 37.1 (1994), pp. 229–256. DOI: `10.1002/nme.1620370205`.

[7] G. D. Kenney, B. A. Levett, N. G. Thompson, N. Sridhar, H. A. Bratfos, and P. Bjerager. *Forensic examination of deepwater Horizon blowout preventer - Volume I final report.* Tech. rep. EP030842. Det Norske Veritas, 2011.

[8] A. Mota, J. Knap, and M. Ortiz. "Three-dimensional fracture and fragmentation of artificial kidney stones". In: *Journal of Physics: Conference Series* 46.1 (2006), pp. 299–303. DOI: `10.1088/1742-6596/46/1/041`.

[9] J. W. Swegle, D. L. Hicks, and S. W. Attaway. "Smoothed particle hydrodynamics stability analysis". In: *Journal of Computational Physics* 116.1 (1995), pp. 123–134.

[10] L. D. Libersky and A. G. Petschek. "Smooth particle hydrodynamics with strength of materials". In: *Lecture Notes in Physics* 395.1 (1991), pp. 248–257. DOI: `10.1007/3-540-54960-9_58`.

[11] L. D. Libersky, A. G. Petschek, T. C. Carney, J. R. Hipp, and F. A. Allahdadi. "High strain Lagrangian hydrodanymics: A three-dimensional SPH code for dynamic material response". In: *Journal of Computational Physics* 109.1 (1993), pp. 65–75. DOI: `10.1006/jcph.1993.1199`.

[12] J. J. Monaghan. “Smoothed particle hydrodynamics”. In: *Annual Review of Astronomy and Astrophysics* 30.1 (1992), pp. 543–574.

[13] J. W. Swegle, S. W. Attaway, M. W. Heinstein, F. J. Mello, and D. L. Hicks. *An analysis of smoothed particle hydrodynamics.* Tech. rep. SAND93-2513. Sandia National Laboratories, 1994.

[14] R. Vignjevic and J. Campbell. “Review of development of the smooth particle hydrodynamics (SPH) Method”. In: *Predictive Modeling of Dynamic Processes* 1.1 (2009). Ed. by S. Hiermaier, pp. 367–396. DOI: `10.1007/978-1-4419-0727-1_20`.

[15] C. T. Dyka and R. P. Ingel. *Addressing tension instability in SPH methods.* Tech. rep. NRL/MR/6384–94–7641. Naval Research Laboratory, 1994.

[16] C. T. Dyka and R. P. Ingel. “An approach for tension instability in smoothed particle hydrodynamics (SPH)”. In: *Computers & Structures* 57.4 (1995), pp. 573–580. DOI: `10.1016/0045-7949(95)00059-P`.

[17] J. P. Morris. “A study of the stability properties of smooth particle hydrodynamics”. In: *Publ. Astron. Soc. Aust.* 13.1 (1996), pp. 97–102. DOI: `10.1017/S1323358000020610`.

[18] P. W. Randles and L. D. Libersky. “Smoothed particle hydrodynamics: Some recent improvements and applications”. In: *Comput. Methods Appl. Mech. Engrg.* 139.1 (1996), pp. 375–408. DOI: `10.1016/S0045-7825(96)01090-0`.

[19] G. A. Dilts. “Moving least-squares particle hydrodynamics I: Consistency and stability”. In: *Int. J. Numer. Meth. Engng.* 44.1 (1999), pp. 1115–1155. DOI: `10.1002/(SICI)1097-0207(19990320)44:8<1115::AID-NME547>3.0.CO;2-L`.

[20] T. Belytschko, Y. Guo, W. K. Liu, and S. P. Xiao. “A unified stability analysis of meshless particle methods”. In: *Int. J. Numer. Meth. Engng* 1.48 (2000), pp. 1359–1400. DOI: `10.1002/1097-0207(20000730)48:9<1359::AID-NME829>3.0.CO;2-U`.

[21] J. Bonet and S. Kulasegaram. “Correction and stabilisation of smooth particle hydrodynamics methods with applications in metal forming simulations”. In: *Int. J. Numer. Meth. Engng* 47.1 (2000), pp. 1189–1214. DOI: `10.1002/(SICI)1097-0207(20000228)47:6<1189::AID-NME830>3.0.CO;2-I`.

[22] R. Vignjevic, J. Campbell, and L. Libersky. “A treatment of zero-energy modes in the smoothed particle hydrodynamics method”. In: *Comput. Methods Appl. Mech. Engrg.* 184.1 (2000), pp. 67–85. DOI: `10.1016/S0045-7825(99)00441-7`.

[23] J. Bonet and S. Kulasegaram. “Remarks on tension instability of Eulerian and Lagrangian corrected smooth particle hydrodynamics (CSPH) methods”. In: *Int. J. Numer. Meth. Engng* 52.1 (2001), pp. 1203–1220. DOI: `10.1002/nme.242`.

[24] Y. Vidal, J. Bonet, and A. Huerta. “Stabilized updated Lagrangian corrected SPH for explicit dynamics problems”. In: *Int. J. Numer. Meth. Engng* 69.1 (2007), pp. 2687–2710. DOI: `10.1002/nme.1859`.

[25] C. H. Lee, A. J. Gil, G. Greto, S. Kulasegaram, and J. Bonet. “A new Jameson-Schmidt-Turkel smooth particle hydrodynamics algorithm for large strain explicit fast dynamics”. In: *Comput. Methods Appl. Mech. Engrg.* 311.1 (2016), pp. 71–111. DOI: `10.1016/j.cma.2016.07.033`.

[26] C. H. Lee, A. J. Gil, O. I. Hassan, J. Bonet, and S. Kulasegaram. “A variationally consistent Strealine upwind Petrov-Galerkin smooth particle hydrodynamics algorithm for large strain solid dynamics”. In: *Comput. Methods Appl. Mech. Engrg.* 318.1 (2017), pp. 514–236. DOI: `10.1016/j.cma.2017.02.002`.

[27] C. H. Lee, A. J. Gil, A. Ghavamian, and J. Bonet. “A total Lagrangian upwind smooth particle hydrodynamics algorithm for large strain explicit solid dynamics”. In: *Comput. Methods Appl. Mech. Engrg.* 344.1 (2019), pp. 209–250. DOI: `10.1016/j.cma.2018.09.033`.

[28] Y. Krongauz and T. Belytschko. “Consistent pseudo-derivatives in meshless methods”. In: *Comput. Methods Appl. Mech. Engrg.* 146.1 (1997), pp. 371–386. DOI: `10.1016/S0045-7825(96)01234-0`.

[29] J. Bonet and T. -S. L. Lok. “Variational and momentum preservation aspects of smooth particle hydrodynamics formulations”. In: *Comput. Methods Appl. Mech. Engrg.* 180.1 (1999), pp. 97–115. DOI: `10.1016/S0045-7825(99)00051-1`.

[30] G. A. Dilts. “Moving least-squares particle hydrodynamics II: Conservation and boundaries”. In: *Int. J. Numer. Meth. Engng.* 48.1 (2000), pp. 1503–1524. DOI: `10.1002/1097-0207(20000810)48:10<1503::AID-NME832>3.0.CO;2-D`.

[31] W. G. Hoover, C. G. Hoover, and E. C. Merritt. “Smooth-particle applied mechanics: Conservation of angular momentum with tensile stability and velocity averaging”. In: *Phys. Rev* 69.1 (2004), p. 016702. DOI: `10.1103/PhysRevE.69.016702`.

[32] T. Belytschko and S. P. Xiao. “Stability analysis of particle methods with corrected derivatives”. In: *Computers and Mathematics with Applications* 1.43 (2002), pp. 329–350. DOI: `10.1016/S0898-1221(01)00290-5`.

[33] J. P. Gray, J. J. Monaghan, and R. P. Swift. “SPH elastic dynamics”. In: *Comput. Methods Appl. Mech. Engrg.* 190.49-50 (2001), pp. 6641–6662. DOI: `10.1016/S0045-7825(01)00254-7`.

[34] G. C. Ganzenmüller. “An hourglass control algorithm for Lagrangian Smooth Particle Hydrodynamics”. In: *Comput. Methods Appl. Mech. Engrg.* 286.1 (2015), pp. 87–106. DOI: `10.1016/j.cma.2014.12.005`.

[35] G. C. Ganzenmüller, M. Sauer, M. May, and S. Hiermaier. “Hourglass control for Smooth Particle Hydrodynamics removes tensile and rank-deficiency instabilities”. In: *Eur. Phys. J. Spec. Top.* 225.1 (2016), pp. 385–395. DOI: `10.1140/epjst/e2016-02631-x`.

[36] G. Greto and S. Kulasegaram. “An efficient and stabilised SPH method for large strain metal plastic deformations”. In: *Computational Particle Mechanics* 7.1 (2019), pp. 523–539. DOI: `10.1007/s40571-019-00277-6`.

[37] S. Mohseni-Mofidi and C. Bierwisch. “Application of hourglass control to Eulerian smoothed particle hydrodynamics”. In: *Computational Particle Mechanics* 8.1 (2020), pp. 51–67. DOI: `10.1007/s40571-019-00312-6`.

[38] H. Karim Serroukh, M. Mabssout, and M. I. Herreros. “Updated Lagrangian Taylor-SPH method for large deformation in dynamic problems”. In: *Applied Mathematical Modelling* 80.1 (2020), pp. 238–256. DOI: `10.1016/j.apm.2019.11.046`.

[39] S. Leroch, M. Varga, S. J. Eder, A. Vernes, M. Rodriguez Ripoll, and G. C. Ganzenmüller. “Smooth particle hydrodynamics simulation of damage induced by a spherical indenter scratching a viscoplastic material”. In: *International Journal of Solids andStructures* 81.1 (2016), pp. 188–202. DOI: `10.1016/j.ijsolstr.2015.11.025`.

[40] A. Khayyer, Y. Shimizu, H. Gotoh, and K. Nagashima. “A coupled incompressible SPH-Hamiltonian SPH solver for hydroelastic FSI corresponding to composite structures”. In: *Applied Mathematical Modelling* 94.1 (2021), pp. 242–271. DOI: `10.1016/j.apm.2021.01.011`.

[41] A. Khayyer, Y. Shimizu, H. Gotoh, and S. Hattori. “Multi-resolution ISPH-SPH for accurate and efficient simulation of hydroelastic fluid-structure interactions in ocean engineering”. In: *Ocean Engineering* 226.1 (2021), p. 108652. DOI: `10.1016/j.oceaneng.2021.108652`.

[42] A. M. A. Nasar, B. D. Rogers, A. Revell, and P. K. Stansby. “Flexible slender body fluid interaction: Vector-based discrete element method with Eulerian smoothed particle hydrodynamics”. In: *Computers & Fluids* 179.1 (2019), pp. 563–578. DOI: `10.1016/j.compfluid.2018.11.024`.

[43] M. McLoone and N. J. Quinlan. “Coupling of the meshless finite volume particle method and the finite element method for fluid–structure interaction with thin elastic structures”. In: *European Journal of Mechanics - B/Fluids* 92.1 (2022), pp. 117–131. DOI: `10.1016/j.euromechflu.2021.12.001`.

[44] C. H. Lee, A. J. Gil, and J. Bonet. “Development of a cell centred upwind finite volume algorithm for a new conservation law formulation in structural dynamics”. In: *Computers and Structures* 118.1 (2013), pp. 13–38. DOI: `10.1016/j.compstruc.2012.12.008`.

[45] C. H. Lee, A. J. Gil, and J. Bonet. “Development of a stabilised Petrov–Galerkin formulation for conservation laws in Lagrangian fast solid dynamics”. In: *Comput. Methods Appl. Mech. Engrg.* 268.1 (2014), pp. 40–64. DOI: `10.1016/j.cma.2013.09.004`.

[46] A. J. Gil, C. H. Lee, J. Bonet, and M. Aguirre. “A stabilised Petrov–Galerkin formulation for linear tetrahedral elements in compressible, nearly incompressible and truly incompressible fast dynamics”. In: *Comput. Methods Appl. Mech. Engrg.* 276.1 (2014), pp. 659–690. DOI: `10.1016/j.cma.2014.04.006`.

[47] J. Bonet, A. J. Gil, C. H. Lee, M. Aguirre, and R. Ortigosa. “A first order hyperbolic framework for large strain computational solid dynamics. Part I: Total Lagrangian isothermal elasticity”. In: *Comput. Methods Appl. Mech. Engrg.* 283.1 (2015), pp. 689–732. DOI: `10.1016/j.cma.2014.09.024`.

[48] J. Bonet, A. J. Gil, and R. Ortigosa. “A computational framework for polyconvex large strain elasticity”. In: *Comput. Methods Appl. Mech. Engrg.* 283.1 (2015), pp. 1061–1094. DOI: `10.1016/j.cma.2014.10.002`.

[49] J. Bonet, A. J. Gil, and R. Ortigosa. “On a tensor cross product based formulation of large strain solid mechanics”. In: *International Journal of Solids and Structures* 84.1 (2016), pp. 49–63. DOI: `10.1016/j.ijsolstr.2015.12.030`.

[50] W. Benz and E. Asphaug. “Impact simulations with fracture. I. Methods and tests”. In: *ICARUS* 107.1 (1994), pp. 98–116. DOI: `10.1006/icar.1994.1009`.

[51] D. A. Mandell and C. A. Wingate. *Prediction of material strenght and fracture of glass using the SPHINX smooth particle hydrodynamics code.* Tech. rep. LA-12830. Los Alamos National Lab., 1994. DOI: `10.2172/29427`.

[52] W. Benz and E. Asphaug. “Simulations of brittle solids using smooth particle hydrodynamics”. In: *Computer Physics Communications* 87.1 (1995), pp. 253–265. DOI: `10.1016/0010-4655(94)00176-3`.

[53] R. Das and P. W. Cleary. “Effect of rock shapes on brittle fracture using smoothed particle hydrodynamics”. In: *Theoretical and Applied Fracture Mechanics* 53.1 (2010), pp. 47–60. DOI: `10.1016/j.tafmec.2009.12.004`.

[54] T. De Vuyst and R. Vignjevic. “Total Lagrangian SPH modelling of necking and fracture in electromagnetically driven ring”. In: *International Journal of Fracure* 180.1 (2013), pp. 53–70. DOI: `10.1007/s10704-012-9801-4`.

[55] S. Chakraborty and A. Shaw. “Crack propagation in bi-material system via pseudo-spring smoothed particle hydrodynamics”. In: *International Journal for Computational Methods in Engineering Science and Mechanics* 15.3 (2014), pp. 294–301. DOI: `10.1080/15502287.2014.882436`.

[56] J. Young. “Modelling elastic dynamics and fracture with coupled mixed correction Eulerian Total Lagrangian SPH”. PhD thesis. The University of Edinburgh, May 2018.

[57] T. Rabczuk and T. Belytschko. “Cracking particles: a simplified meshfree method for arbitrary evolving cracks”. In: *Int. J. Numer. Meth. Engng* 1.61 (2004), pp. 2316–2343. DOI: `10.1002/nme.1151`.

[58] T. Rabczuk, P. M. A. Areias, and T. Belytschko. “A meshfree thin shell method for non-linear dynamic fracture”. In: *Int. J. Numer. Meth. Engng* 1.72 (2007), pp. 524–548. DOI: `10.1002/nme.2013`.

[59] T. Rabczuk and T. Belytschko. “A three-dimensional large deformation meshfree method for arbitrary evolving cracks”. In: *Comput. Methods Appl. Mech. Engrg.* 1.196 (2007), pp. 2777–2799. DOI: `10.1016/j.cma.2006.06.020`.

[60] H. X. Wang and S. X. Wang. “Analysis of dynamic fracture with cohesive crack segment method”. In: *CMES - Computer Modeling in Engineering and Sciences* 35.3 (2008), pp. 253–274.

[61] T. Rabczuk, G. Zi, S. Bordas, and H. Nguyen-Xuan. “A simple and robust three-dimensional cracking-particle method without enrichment”. In: *Comput. Methods Appl. Mech. Engrg.* 199.37-40 (2010), pp. 2437–2455. DOI: `10.1016/j.cma.2010.03.031`.

[62] T. Rabczuk, J. H. Song, X. Zhuang, and C. Anitescu. *Extended Finite Element and Meshfree Methods.* 1st ed. London: Elsevier Science Publishing Co Inc, 2019.

[63] N. Moës, J. Dolbow, and T. Belytschko. “A finite element method for crack growth without remeshing”. In: *Int. J. Numer. Meth. Engng.* 46.1 (1999), pp. 131–150. DOI: `10.1002/(SICI)1097-0207(19990910)46:1<131::AID-NME726>3.0.CO;2-J`.

[64] N. Sukumar, J. E. Dolbow, and N. Moës. “Extended finite element method in computational fracture mechanics: a retrospective examination”. In: *Int J Fract* 196.1 (2015), pp. 189–206. DOI: `10.1007/s10704-015-0064-8`.

[65] S. A. Silling. “Reformulation of elasticity theory for discontinuities and long-range forces”. In: *Journal of the Mechanics and Physics of Solids* 48.1 (2000), pp. 175–209. DOI: `10.1016/S0022-5096(99)00029-0`.

[66] S. A. Silling, O. Weckner, E. Askari, and F. Bobaru. “Crack nucleation in a peridynamic solid”. In: *Int J Fract* 162.1 (2010), pp. 219–227. DOI: `10.1007/s10704-010-9447-z`.

[67] S. A. Silling and A. Askari. *Peridynamic model for fatigue cracking.* Tech. rep. SAND2014-18590. Sandia National Laboratories, 2014.

[68] G. C. Ganzenmüller, S. Hiermaier, and M. May. “On the similarity of meshless discretizations of Peridynamics and Smooth-Particle Hydrodynamics”. In: *Computer & Structures* 150.1 (2015), pp. 71–78. DOI: `10.1016/j.compstruc.2014.12.011`.

[69] T. Belytschko, H. Chen, J. Xu, and G. Zi. “Dynamic crack propagation based on loss of hyperbolicity and a new discontinuous enrichment”. In: *Int. J. Numer. Meth. Engng* 58.1 (2003), pp. 1873–1905. DOI: `10.1002/nme.941`.

[70] T. Belytschko, W. Kam Liu, B. Moran, and K. I. Elkhodary. *Nonlinear finite elements for continua and structures.* 2nd ed. West Sussex: John Wiley & Sons Inc, 2014.

[71] J. J. C. Remmers, R. de Borst, and A. Needleman. “A cohesive segments method for the simulation of crack growth”. In: *Computational Mechanics* 1.31 (2003), pp. 69–77. DOI: `10.1007/s00466-002-0394-z`.

[72] D. Organ, M. Fleming, T. Terry, and T. Belytschko. “Continuous meshless approximations for nonvonvex bodies by difraction and transparency”. In: *Computational Mechanics* 1.18 (1996), pp. 225–235. DOI: `10.1007/BF00369940`.

[73] T. Rabczuk and X. Zhuang. “Meshless Discretization Methods”. In: *Encyclopedia of Continuum Mechanics* 1.1 (2018). Ed. by H. Altenbach and A. Öchsner, pp. 1–15. DOI: `10.1007/978-3-662-53605-6_15-1`.

[74] J. Haider, C. H. Lee, A. J. Gil, A. Huerta, and J. Bonet. “An upwind cell centred Total Lagrangian finite volume algorithm for nearly incompressible explicit fast solid dynamic applications”. In: *Comput. Methods Appl. Mech. Engrg.* 1.340 (2018), pp. 684–727. DOI: `10.1016/j.cma.2018.06.010`.

[75] E. A. de Souza Neto and D. Perić. *Computational methods for plasticity: theory and applications.* West Sussex: John Wiley & Sons Ltd, 2008.

[76] A. Ghavamian, C. H. Lee, A. J. Gil, J. Bonet, T. Heuzé, and L. Stainier. “An entropy-stable Smooth Particle Hydrodynamics algorithm for large strain thermo-elasticity”. In: *Comput. Methods Appl. Mech. Engrg.* 379.1 (2021), p. 113736. DOI: `10.1016/j.cma.2021.113736`.

[77] G. R. Johnson and W. H. Cook. “A constitutive model and data for metals subjected to large strains, high strain rates and high temperature”. In: *Proc. 7th Int. Symp. on Ballistics* 1.1 (1983), pp. 541–547.

[78] G. R. Johnson and W. H. Cook. “Fracture characteristics of three metals subjected to various strains, strain rates, temperatures and pressures”. In: *Engineering Fracture Mechanics* 21.1 (1985), pp. 31–48. DOI: `10.1016/0013-7944(85)90052-9`.

[79] G. R. Johnson and W. H. Cook. “Evaluation of cylinder-impact test data for constitutive model constants”. In: *Journal of Applied Physics* 64.8 (1988), p. 3901. DOI: `10.1063/1.341344`.

[80] L. Gambirasio and E. Rizzi. “On the calibration strategies of the Johnson–Cook strength model: Discussion and applications to experimental data”. In: *Materials Science & Engineering A* 610.1 (2014), pp. 370–413. DOI: `10.1016/j.msea.2014.05.006`.

[81] A. He, G. Xie, H. Zhang, and X. Wang. “A comparative study on Johnson–Cook, modified Johnson–Cook and Arrhenius-type constitutive models to predict the high temperature flow stress in 20CrMo alloy steel”. In: *Materials and Design* 52.1 (2013), pp. 677–685. DOI: `10.1016/j.matdes.2013.06.010`.

[82] E. Kreyszig. *Advanced Engineering Mathematics*. 10th ed. New York: John Wiley & Sons Inc, 2010.

[83] R. J. Thacker, E. R. Tittley, F. R. Pearce, H. M. P. Couchman, and P. A. Thomas. “Smoothed Particle Hydrodynamics in cosmology: a comparative study of implementations”. In: *Monthly Notices of the Royal Astronomical Society* 319.2 (2000), pp. 619–648. DOI: `10.1111/j.1365-8711.2000.03927.x`.

[84] G. R. Johnson, R. A. Stryk, and S. R. Beissel. “SPH for high velocity impact computations”. In: *Comput. Methods Appl. Mech. Engrg.* 139.1 (1996), pp. 347–373. DOI: `10.1016/S0045-7825(96)01089-4`.

[85] M. Robinson. “Turbulence and Viscous Mixing using Smoothed Particle Hydrodynamics”. PhD thesis. Monash University, July 2009.

[86] W. Dehnen and H. Aly. “Improving convergence in smoothed particle hydrodynamics simulations without pairing instability”. In: *Monthly Notices of the Royal Astronomical Society* 425.2 (2012), pp. 1068–1082. DOI: `10.1111/j.1365-2966.2012.21439.x`.

[87] J. M. Owen, J. V. Villumsen, P. R. Shapiro, and H. Martel. “Adaptive Smoothed Particle Hydrodynamics: Methodology II”. In: *Astrophysical Journal, Supplement Series* 116.2 (1998), pp. 155–209. DOI: `10.1002/nme.684`.

[88] J. Bonet, A. J. Gil, and R. D. Wood. *Nonlinear solid mechanics for finite element analysis: statics*. Cambridge: Cambridge University Press, 2016.

[89] A. N. Parshikov, S. A. Medin, I. I. Loukashenko, and V. A. Milekhin. “Improvements in SPH method by means of interparticle contact algorithm and analysis of perforation tests at moderate projectile velocities”. In: *International Journal of Impact Engineering* 24.8 (2000), pp. 779–796. DOI: `10.1016/S0734-743X(99)00168-2`.

[90] A. N. Parshikov and S. A. Medin. “Smoothed Particle Hydrodynamics Using Interparticle Contact Algorithms”. In: *Journal of Computational Physics* 180.1 (2002), pp. 358–382. DOI: `10.1006/jcph.2002.7099`.

[91] B. D. Rogers, R. A. Dalrymple, and P. K. Stansby. “Simulation of caisson breakwater movement using 2-D SPH”. In: *Journal of Hydraulic Research* 48.1 (2010), pp. 135–141. DOI: `10.1080/00221686.2010.9641254`.

[92] M. Gomez-Gesteira, B. D. Rogers, A. J. C. Crespo, R. A. Dalrymple, M. Narayanaswamy, and J. M. Dominguez. “SPHysics - development of a free-surface fluid solver- Part 1: Theory and Formulations”. In: *Computers & Geosciences* 48.1 (2010), pp. 289–299. DOI: `10.1016/j.cageo.2012.02.029`.

[93] C. H. Lee. “Development of a cell centred upwind finite volume algorithm for a new conservation law formulation in structural dynamics”. PhD thesis. Swansea University, Feb. 2012.

[94] C. W. Shu and S. Osher. “Efficient implementation of essentially non-oscillatory shock-capturing schemes”. In: *Journal of Computational Physics* 1.77 (1988), pp. 439–471. DOI: `10.1016/0021-9991(88)90177-5`.

[95] J. Haider, C. H. Lee, A. J. Gil, and J. Bonet. “A first-order hyperbolic framework for large strain computational solid dynamics: An upwind cell centred Total Lagrangian scheme”. In: *Int. J. Numer. Meth. Engng* 109.3 (2016), pp. 407–456. DOI: `10.1002/nme.5293`.

[96] G. Scovazzi, B. Carnes, X. Zeng, and S. Rossi. “A simple, stable, and accurate linear tetrahedral finite element for transient, nearly and fully incompressible solid dynamics: A dynamic variational multiscale approach”. In: *International Journal for Numerical Methods in Engineering* 106 (2016), pp. 799–839. DOI: `10.1002/nme.5138`.

[97] S. Rossi, N. Abboud, and G. Scovazzi. “Implicit finite incompressible elastodynamics with linear finite elements: A stabilized method in rate form”. In: *Computer Methods in Applied Mechanics and Engineering* 311 (2016), pp. 208–249. DOI: `10.1016/j.cma.2016.07.015`.

[98] G. Scovazzi, T. Song, and X. Zeng. “A velocity/stress mixed stabilized nodal finite element for elastodynamics: Analysis and computations with strongly and weakly enforced boundary conditions”. In: *Computer Methods in Applied Mechanics and Engineering* 325 (2017), pp. 532–576. DOI: `10.1016/j.cma.2017.07.018`.

[99] S. Fernández-Méndez, J. Bonet, and A. Huerta. “Continuous blending of SPH with finite elements”. In: *Computers and Structures* 1.83 (2005), pp. 1448–1458. DOI: `10.1016/j.compstruc.2004.10.019`.

[100] M. Franke, A. Janz, M. Schiebl, and P. Betsch. "An energy momentum consistent integration scheme using a polyconvexity-based framework for nonlinear thermo-elastodynamics". In: *International Journal for Computational Methods in Engineering Science and Mechanics* 115.5 (2018), pp. 549–577. DOI: `10.1002/nme.5816`.

[101] P. Betsch and M. Schiebl. "Energy-momentum-entropy consistent numerical methods for large-strain thermoelasticity relying on the GENERIC formalism". In: *International Journal for Computational Methods in Engineering Science and Mechanics* 119.12 (2019), pp. 1216–1244. DOI: `10.1002/nme.6089`.

[102] J. Bonet, C. H. Lee, A. J. Gil, and A. Ghavamian. "A first order hyperbolic framework for large strain computational solid dynamics. Part III: Thermoelasticity". In: *Comput. Methods Appl. Mech. Engrg.* 373 (2021). DOI: `10.1016/j.cma.2020.113505`.

[103] A. Huerta and F. Casadei. "New ALE applications in non-linear fast-transient solid dynamics". In: *Engineering Computations* 11.4 (1994), pp. 317–345.

[104] J. Bonet and A. J. Burton. "A simple average nodal pressure tetrahedral element for incompressible and nearly incompressible dynamic explicit applications". In: *Commun. Numer. Meth. Engng* 14.1 (1998), pp. 437–449. DOI: `10.1002/(SICI)1099-0887(199805)14:5<437::AID-CNM162>3.0.CO;2-W`.

[105] J. C. Simo. "A framework for finite strain elastoplasticity based on maximum plastic dissipation and the multiplicative decomposition. Part II: computational aspects". In: *Comput. Methods Appl. Mech. Engrg.* 68.1 (1988), pp. 1–31. DOI: `10.1016/0045-7825(88)90104-1`.

[106] A. Rodrígues-Ferran, F. Casadei, and A. Huerta. "ALE stress update for transient and quasistatic processes". In: *Int. J. Numer. Meth. Engng* 43.1 (1998), pp. 241–262. DOI: `10.1002/(SICI)1097-0207(19980930)43:2<241::AID-NME389>3.0.CO;2-D`.

[107] A. Rodrígues-Ferran, A. Pérez-Foguet, and A. Huerta. "Arbitrary Lagrangian–Eulerian (ALE) formulation for hyperelastoplasticity". In: *Int. J. Numer. Meth. Engng* 53.1 (2002), pp. 1831–1851. DOI: `10.1002/nme.362`.

[108] F. Armero and E. Love. "An arbitrary Lagrangian–Eulerian finite element method for finite strain plasticity". In: *Int. J. Numer. Meth. Engng* 57.1 (2003), pp. 471–508. DOI: `10.1002/nme.684`.

[109] N. Abboud and G. Scovazzi. "Elastoplasticity with linear tetrahedral elements: A variational multiscale method". In: *Int. J. Numer. Meth. Engng* 115.1 (2018), pp. 913–955. DOI: `10.1002/nme.5831`.

[110] J. C. Simo and F. Armero. "Geometrically non-linear enhanced strain mixed methods and the method of incompatible modes". In: *Int. J. Numer. Meth. Engng* 33.1 (1992), pp. 1413–1449. DOI: `10.1002/nme.1620330705`.

[111] E. A. de Souza Neto, D. Perić, M. Dutko, and D. R. J. Owen. "Design of simple low order finite elements for large strain analysis of nearly incompressible solids". In: *International Journal of Solids and Structures* 33.20-22 (1996), pp. 3277–3296. DOI: `10.1016/0020-7683(95)00259-6`.

[112] Dassault Systèmes. *ABAQUS Benchmarks Guide, Version 2016.* United States, 2016.

[113] J. Amani, E. Oterkus, P. Areias, G. Zi, T. Nguyen-Thoi, and T. Rabczuk. "A non-ordinary state-based peridynamics formulation for thermoplastic fracture". In: *International Journal of Impact Engineering* 87.1 (2016), pp. 83–94. DOI: `doi.org/10.1016/j.ijimpeng.2015.06.019`.

[114] M. J. Borden, C. V. Verhoosel, M. A. Scott, T. J. R. Hughes, and C. M. Landis. "A phase-field description of dynamic brittle fracture". In: *Comput. Methods Appl. Mech. Engrg.* 217-220.1 (2012), pp. 77–95. DOI: `10.1016/j.cma.2012.01.008`.

[115] J. Feldman. "Dynamic refinement and boundary contact forces in smoothed particle hydrodynamics with applications in fluid flow problems". PhD thesis. Swansea University, Feb. 2006.

[116] A. P. Boresi, R. J. Schmidt, and O. M. Sidebottom. *Advanced mechanics of materials.* 5th ed. New York: John Wiley & Sons Inc, 1993.

[117] S. Li, W. K. Liu, A. J. Rosakis, T. Belytschko, and W. Hao. "Mesh-free Galerkin simulations of dynamic shear band propagation and failure mode transition". In: *International Journal of Solids and Structures* 39.1 (2002), pp. 1213–1240. DOI: `10.1016/j.ijsolstr.2015.12.030`.

[118] R. C. Batra and M. V. S. Ravinsankar. "Three-dimensional numerical simulation of the Kalthoff experiment". In: *International Journal of Fracture* 105.1 (2000), pp. 161–186. DOI: `10.1023/A:1007658224458`.

[119] J. H. Song, P. M. A. Areias, and T. Belytschko. "A method for dynamic crack and shear band propagation with phantom nodes". In: *Int. J. Numer. Meth. Engng.* 67.1 (2006), pp. 868–893. DOI: `10.1002/nme.1652`.

[120] R. de Borst J. J. C. Remmers and and A. Needleman. "The simulation of dynamic crack propagation using the cohesive segments method". In: *Journal of the Mechanics and Physics of Solids* 56.1 (2008), pp. 70–92. DOI: `10.1016/j.jmps.2007.08.003`.

[121] L. Chen, B. Li, and R. de Borst. "Energy conservation during remeshing in the analysis of dynamic fracture". In: *Int. J. Numer. Meth. Engng.* 120.4 (2019), pp. 433–446. DOI: `10.1002/nme.6142`.

[122] K. Zhang, S. L. Shen, and A. Zhou. "Dynamic brittle fracture with eigenerosion enhanced material point method". In: *Int. J. Numer. Meth. Engng.* 121.17 (2019), pp. 3768–3794. DOI: `10.1002/nme.6381`.

[123] H. L. Ren, X. Y. Zhuang, C. Anitescu, and T. Rabczuk. "An explicit phase field method for brittle dynamic fracture". In: *Engineering Fracture Mechanics* 217.1 (2019), pp. 45–56. DOI: `10.1016/j.compstruc.2019.03.005`.

[124] S. Patnaik and F. Semperlotti. "Variable-order fracture mechanics and its application to dynamic fracture". In: *Computational Materials* 7.27 (2021). DOI: `10.1038/s41524-021-00492-x`.

[125] F. Yan, W. Zhang, P. Z. Pan, and S. J. Li. "Dynamic crack propagation analysis combined the stable scheme and continuous-discontinuous cellular automaton". In: *Engineering Fracture Mechanics* 241.1 (2021), p. 107390. DOI: `10.1016/j.engfracmech.2020.107390`.

[126] M. Bybordiani and D. Dias-da-Costa. “A consistent finite element approach for dynamic crack propagation with explicit time integration”. In: *Comput. Methods Appl. Mech. Engrg.* 376.1 (2021), p. 113652. DOI: `10.1016/j.cma.2020.113652`.

[127] R. John and S. P. Shah. “Mixed-Mode Fracture of Concrete Subjected to Impact Loading”. In: *Journal of Structural Engineering* 116.3 (1990), pp. 585–602. DOI: `10.1061/(ASCE)0733-9445(1990)116:3(585)`.

[128] T. Belytschko, D. Organ, and C. Gerlach. “Element-free galerkin methods for dynamic fracture in concrete”. In: *Comput. Methods Appl. Mech. Engrg.* 187.3-4 (2000), pp. 385–399. DOI: `10.1016/S0045-7825(00)80002-X`.

[129] Z. Zhang and Y. Chen. “Modeling nonlinear elastic solid with correlated lattice bond cell for dynamic fracture simulation”. In: *Comput. Methods Appl. Mech. Engrg.* 279.1 (2014), pp. 325–347. DOI: `10.1016/j.cma.2014.06.036`.

[130] Z. Fan, H. Liao, H. Jiang, H. Wang, and B. Li. “A dynamic adaptive eigenfracture method for failure in brittle materials”. In: *Engineering Fracture Mechanics* 244.1 (2021), p. 107540. DOI: `10.1016/j.engfracmech.2021.107540`.

[131] A. J. C. Crespo, J. M. Dominguez, A. Barreiro, M. Gomez-Gesteira, and B. D. Rogers. “GPUs, a new tool of acceleration in CFD: Efficiency and reliability on Smoothed Particle Hydrodynamics methods”. In: *PLoS ONE* 6.6 (2011), e20685. DOI: `10.1371/journal.pone.0020685`.

[132] J. M. Dominguez, G. Fourtakas, C. Altomare, R. B. Canelas, A. Tafuni, O. Garcia-Feal, I. Martinez-Estevez, A. Mokos, R. Vacondio, A. J. C. Crespo, B. D. Rogers, P. K. Stansby, and M. Gomez-Gesteira. “DualSPHysics: from fluid dynamics to multiphysics problems”. In: *Computational Particle Mechanics* 9.5 (2022), pp. 867–895. DOI: `10.1007/s40571-021-00404-2`.

[133] M. E. Gurtin. *An introduction to continuum mechanics.* New York: Academic Press, 1981.

[134] J. Bonet, A. J. Gil, and R. D. Wood. *Nonlinear solid mechanics for finite element analysis: dynamics.* Cambridge: Cambridge University Press, 2020.